



HAL
open science

Réponse sismique des tunnels dans les sols : du déterministe à des approches probabilistes

Qiangqiang Sun

► **To cite this version:**

Qiangqiang Sun. Réponse sismique des tunnels dans les sols : du déterministe à des approches probabilistes. Materials Science [cond-mat.mtrl-sci]. Université Grenoble Alpes [2020-..], 2020. English. NNT : 2020GRALI067 . tel-03155419

HAL Id: tel-03155419

<https://theses.hal.science/tel-03155419>

Submitted on 1 Mar 2021

HAL is a multi-disciplinary open access archive for the deposit and dissemination of scientific research documents, whether they are published or not. The documents may come from teaching and research institutions in France or abroad, or from public or private research centers.

L'archive ouverte pluridisciplinaire **HAL**, est destinée au dépôt et à la diffusion de documents scientifiques de niveau recherche, publiés ou non, émanant des établissements d'enseignement et de recherche français ou étrangers, des laboratoires publics ou privés.

THÈSE

Pour obtenir le grade de

DOCTEUR DE L'UNIVERSITE GRENOBLE ALPES

Spécialité : **2MGE : Matériaux, Mécanique, Génie civil, Electrochimie**

Arrêté ministériel : 25 mai 2016

Présentée par

Qiangqiang SUN

Thèse dirigée par **Daniel DIAS**
et codirigée par **Orianne JENCK**

préparée au sein du **Laboratoire Sols, Solides, Structures et Risques**
dans l'**École Doctorale I-MEP2 – Ingénierie – Matériaux, Mécanique, Environnement, Energétique, Procédés, Production**

Seismic response of tunnels in soils: From deterministic to probabilistic approaches

Thèse soutenue publiquement le **26/11/2020**,
devant le jury composé de:

M. Gopal MADABHUSHI

Professeur, University of Cambridge (Rapporteur)

M. Ioannis ANASTASOPOULOS

Professeur, ETH Zurich (Rapporteur)

M. Fernando LOPEZ-CABALLERO

Maître de Conférences, Université Paris-Saclay (Examinateur)

M. Marwan SADEK

Professeur, Lebanese University of Beirut (Examinateur)

M. Frédéric DONZE

Professeur, Université Grenoble Alpes (Examinateur, Président du jury)

M. Daniel DIAS

Professeur, Université Grenoble Alpes (Directeur de thèse)

Mme. Orianne JENCK

Maître de Conférences, Université Grenoble Alpes (Co-directeur)



Abstract

Tunnels are an essential part of infrastructure systems and play an ever-increasing role in the process of urbanization. Nevertheless, severe damage, including collapse, occurred and was reported worldwide in recent decades. Therefore, the research on the design of tunnel against seismic events to effectively mitigate risks and reduce large socio-economic losses due to earthquake disasters received increasing attention. On the other hand, new challenges such as large shield-driven tunnelling in multi-layered formations, tunnelling-induced stress perturbation, as well as uncertain soil property lead to the need for detailed investigation of their potential influences.

This dissertation aims at investigating the tunnel seismic response using deterministic and probabilistic approaches. The analyses are based on two-dimensional nonlinear simulations using the explicit finite difference code *FLAC*. First, a critical assessment of the Rayleigh damping use in nonlinear numerical models is conducted to highlight its significant importance and to provide a selection guideline for the subsequent analyses. Then, the tunnel construction impact is incorporated in the numerical models with the convergence-confinement method. The tunnel seismic responses for various initial stress states are then presented. Next, theoretical and numerical studies are performed to reveal the mechanical mechanism of an underlying soft soil layer for the tunnel seismic protection. Finally, the uncertainty of the soil parameters is introduced into the model as random variables. The sparse polynomial chaos expansion based Global Sensitivity Analysis and the conventional Monte Carlo simulations are respectively utilized to identify the most important variables and quantify the variability in the tunnel seismic deformations. The presented work considers a more realistic soil-tunnel system, thus it provides valuable insights for the behavior of tunnels under seismic loadings.

Résumé

Les tunnels constituent une des parties essentielles des systèmes d'infrastructure et jouent un rôle de plus en plus important dans le processus d'urbanisation. Néanmoins, de graves dommages, dont des effondrements, se sont produits et ont été recensés dans le monde entier au cours des dernières décennies. Par conséquent, la recherche sur la conception des tunnels notamment en zone sismique afin d'atténuer efficacement les risques et de réduire les pertes socio-économiques importantes dues aux tremblements de terre a reçu une attention croissante. D'autre part, de nouveaux défis tels que les tunnels de grande section excavés à l'aide de tunneliers dans des horizons multicouches, la perturbation du champ de contraintes induit par les tunnels, ainsi que l'incertitude des propriétés des sols, nécessitent une étude détaillée de leurs influences potentielles.

Cette thèse vise à étudier la réponse sismique de tunnels à l'aide d'approches déterministes et probabilistes. Les analyses sont basées sur des simulations non linéaires bidimensionnelles utilisant le code de différences finies explicite *FLAC*. Tout d'abord, une évaluation critique de l'utilisation de l'amortissement de Rayleigh dans les modèles numériques non linéaires est menée afin de mettre en évidence son importance et de fournir des règles pour les analyses ultérieures. L'impact de la construction des tunnels a ensuite été intégré dans les modèles numériques en utilisant la méthode convergence-confinement. La réponse sismique des tunnels pour divers états de contrainte initiaux est ensuite présentée. Des études théoriques et numériques sont effectuées pour contribuer à une meilleure compréhension des mécanismes liés à la présence d'une couche de sol compressible sous-jacente pour la protection sismique des ouvrages souterrains. Enfin, l'incertitude des paramètres du sol est introduite dans les modèles numériques sous forme de variables aléatoires. La méthode probabiliste Sparse Polynomial Chaos Expansion combinée à une analyse de sensibilité globale et des simulations de type Monte Carlo sont utilisées pour identifier les variables les plus importantes et quantifier la variabilité des déformations sismiques en tunnel. Le travail présenté considère un système d'interaction sol/tunnel réaliste qui permet de fournir des informations précieuses sur le comportement des tunnels sous chargement sismique.

Acknowledgments

This thesis work would not have been achieved without the support, guidance, encouragement, and dedication of numerous people.

First, I would like to express my sincere gratitude to my thesis supervisor, Professor Daniel Dias for his support and guidance throughout my research work. His extensive knowledge, academic curiosity, and efficient problem solving was invaluable and will have a continuous influence on my future career path. Many thanks also to my co-supervisor Dr. Orianne Jenck for her generosity with her time. She was so kind and helped me a lot during the preparation of the yearly report and this thesis work.

Second, I wish to thank the members of the jury, namely Professor Gopal Madabhushi and Professor Ioannis Anastasopoulos for their careful reading and insightful comments. I also thank Professor Marwan Sadek, Professor Frédéric Donze, Dr. Fernando Lopez-Caballero for having accepted to be part of the committee and for their significant guidance.

Third, I would like to thank the China Scholarship Council for financial support and the two former members of the geomechanics team, namely Dianchun Du and Xiangfeng Guo for their help. They provided me great advice for improving my research and found interesting topics to work together. I also thank them for the discussion about life, society, and the future. Besides, I have had the great pleasure to meet plenty of nice friends and fellow students. This was a happy time.

Finally, I am thankful to my parents. All these experiences would not have been possible without their endless love and support. I thank them for inspiring me to follow my dream and for teaching me to be a kind person.

Contents

| | |
|--|-----------|
| Chapter 1 Introduction | 15 |
| 1.1 Background | 15 |
| 1.2 Objectives..... | 17 |
| 1.3 Thesis outline | 17 |
| | |
| Chapter 2 Literature Review | 21 |
| 2.1 Introduction..... | 21 |
| 2.2 Viscous damping at small strains | 21 |
| 2.2.1 Frequency domain vs time domain | 21 |
| 2.2.2 Rayleigh damping formulation | 24 |
| 2.2.3 Rayleigh damping determination | 26 |
| 2.3 Deterministic models..... | 32 |
| 2.3.1 Pseudo-static method..... | 33 |
| 2.3.2 Dynamic time-history method..... | 39 |
| 2.4 Probabilistic models | 47 |
| 2.4.1 Uncertainty quantification | 47 |
| 2.4.2 Probabilistic analysis of tunnels under static conditions | 50 |
| 2.4.3 Probabilistic analysis of tunnels under seismic conditions | 53 |
| 2.5 Conclusion | 55 |
| | |
| Chapter 3 Rayleigh damping in nonlinear numerical models | 57 |
| 3.1 Introduction..... | 57 |
| 3.2 Methods..... | 58 |
| 3.2.1 Damping determination approaches | 58 |
| 3.2.2 Input ground motions..... | 59 |
| 3.2.3 Two-dimensional numerical modelling..... | 59 |
| 3.3 Numerical results | 62 |

| | |
|---|------------|
| 3.4 Conclusion | 73 |
| Chapter 4 Influence of stress relief during excavation on the seismic response of tunnels..... | 75 |
| 4.1 Introduction..... | 75 |
| 4.2 Tunnel excavation simulation | 77 |
| 4.2.1 Convergence-confinement method | 77 |
| 4.2.2 Stress relief process | 79 |
| 4.3 Numerical modelling of soil-tunnel system..... | 79 |
| 4.4 Analysis results | 83 |
| 4.4.1 Static analysis..... | 84 |
| 4.4.2 Seismic analysis | 88 |
| 4.4.3 Surface ground motions..... | 95 |
| 4.4.4 Depth-dependent G/G_{\max} curve..... | 96 |
| 4.5 Conclusions..... | 98 |
| Chapter 5 Underlying soft soil layer-tunnel seismic interaction | 101 |
| 5.1 Introduction..... | 101 |
| 5.2 Plane SH wave propagation in a three-layered elastic medium..... | 103 |
| 5.2.1 Analytical solution | 103 |
| 5.2.2 Parametric analysis | 105 |
| 5.3 Soft soil layer-tunnel system..... | 109 |
| 5.3.1 Outline of the idealized problem..... | 109 |
| 5.3.2 Model details | 111 |
| 5.4 Numerical results | 113 |
| 5.4.1 Free-field case | 113 |
| 5.4.2 Soil-tunnel system..... | 116 |
| 5.5 Discussion..... | 123 |
| 5.6 Conclusion | 126 |
| Chapter 6 Probabilistic seismic response of tunnels in random soils: Sensitivity analysis ... | 129 |

| | |
|---|------------|
| 6.1 Introduction..... | 129 |
| 6.2 Method | 131 |
| 6.2.1 Polynomial chaos expansion | 131 |
| 6.2.2 Sobol' indices | 132 |
| 6.2.3 Error estimation..... | 133 |
| 6.2.4 Numerical procedure | 133 |
| 6.3 Computational model | 134 |
| 6.3.1 Deterministic numerical model | 134 |
| 6.3.2 Probabilistic modelling of variables | 136 |
| 6.4 Method verification | 139 |
| 6.4.1 <i>SPCE</i> model | 139 |
| 6.4.2 Sensitivity indices | 142 |
| 6.5 Sensitivity analysis | 143 |
| 6.5.1 Soil type and motion intensity..... | 143 |
| 6.5.2 Coefficient of variation..... | 146 |
| 6.6 Discussion | 148 |
| 6.6.1 Variability in the computed Sobol' indices..... | 148 |
| 6.6.2 Input ground motion characteristics | 152 |
| 6.7 Conclusions..... | 153 |
| | |
| Chapter 7 Probabilistic seismic response of tunnels in random soils: Statistical analysis | 155 |
| 7.1 Introduction..... | 155 |
| 7.2 Monte Carlo simulation..... | 156 |
| 7.2.1 Latin hypercube sampling | 156 |
| 7.2.2 Sample size | 157 |
| 7.2.3 Probabilistic models..... | 158 |
| 7.3 Results of the reference case..... | 158 |
| 7.4 Parametric study | 160 |
| 7.4.1 Soil type and lining stiffness | 160 |
| 7.4.2 Correlation between c and ϕ | 164 |

| | |
|---|------------|
| 7.4.3 Probability distribution and <i>COV</i> | 168 |
| 7.5 Implications on tunnel seismic design | 172 |
| 7.6 Conclusions..... | 173 |
| Chapter 8 Conclusion | 177 |
| 8.1 Summary and results | 177 |
| 8.2 Outlook..... | 180 |
| Appendix A..... | 183 |
| Appendix B..... | 185 |
| Reference | 187 |

Nomenclature

Abbreviations

| | |
|-------------|--|
| <i>CCM</i> | Convergence-confinement method |
| <i>CDF</i> | Cumulative distribution function |
| <i>COV</i> | Coefficient of variation |
| <i>EL</i> | Equivalent-linear |
| <i>FORM</i> | First order reliability method |
| <i>FS</i> | Factor of safety |
| <i>GSA</i> | Global sensitivity analysis |
| <i>K-S</i> | Kolmogorov-Smirnov |
| <i>LB</i> | Lower bound |
| <i>LHS</i> | Latin hypercube sampling |
| <i>LSA</i> | Local sensitivity analysis |
| <i>MCSR</i> | Modified cross-section racking deformation |
| <i>MF</i> | Mean frequency |
| <i>NL</i> | Nonlinear |
| <i>PDF</i> | Probability density function |
| <i>PF</i> | Predominant frequency |
| <i>PGA</i> | Peak ground acceleration |
| <i>POE</i> | Probability of exceedance |
| <i>SF</i> | Site fundamental frequency |
| <i>SPCE</i> | Sparse Polynomial Chaos Expansion |
| <i>UB</i> | Upper bound |

Roman Symbols

| | |
|-------------|--------------------------------|
| A_{loop} | Area of the stress-strain loop |
| A_3/A_1 | Transmission coefficient |
| c | Cohesion |
| D | Tunnel diameter |
| d | Thickness of a soft soil layer |
| E | Young's modulus |
| f_{min} | Center frequency |
| f_n | Soil n^{th} mode frequency |
| f_2 | First matching frequency |
| G | Shear modulus |
| G/G_{max} | Shear modulus reduction |
| H | Tunnel buried depth |
| h | Location of a soft soil layer |
| K | Bulk modulus |
| K_n | Normal spring stiffness |
| K_s | Shear spring stiffness |

| | |
|---------|--|
| K_0 | Lateral earth pressure factor |
| M | Bending moment |
| M_s | Modulus reduction factor |
| N | Sample size |
| p_r | Reference pressure |
| p' | Mean effective pressure |
| p | Polynomial degree |
| q | q -norm in PCE |
| r | Tunnel radius |
| S_i | First order Sobol' index of variable i |
| S_i^T | Total Sobol' index of variable i |
| T | Axial force |
| t | Tunnel thickness |
| V_s | Shear wave velocity |

Greek Symbols

| | |
|---------------------|---------------------------------------|
| ρ | Density |
| α | Mass-proportional coefficient |
| β | Stiffness-proportional coefficient |
| γ | Shear strain |
| γ_{ff} | Fried field shear strain |
| γ_m | Yield shear strain |
| γ_{max} | Maximum shear strain |
| γ_{ref} | Reference shear strain |
| ΔD | Tunnel deformation |
| ΔZ_{min} | Minimum mesh size |
| ε_{LOO} | Leave-one-out error |
| ε_{VAL} | Validation error |
| λ | Stress relaxation coefficient |
| λ_w | Wavelength |
| μ | Mean value |
| ν | Poisson's ratio |
| ξ_{tar} | Target damping ratio |
| ξ_{min} | Critical damping ratio |
| $\rho_{c,\varphi}$ | Correlation between c and φ |
| σ | Standard deviation |
| σ^0 | Initial radial stress |
| σ_r | Radial stress |
| σ_1 | Maximum stress |
| σ_3 | Minimum stress |
| τ | Shear stress |
| φ | Internal friction angle |
| $\Psi_\alpha(\xi)$ | Multivariate polynomials in PCE |
| ω | Angular frequency |

Other Symbols

| | |
|---------------------|---|
| $[C]$ | Viscous damping matrix |
| $\mathbb{E}[\cdot]$ | Expectation |
| $\{I\}$ | Unit vector |
| $[K]$ | Stiffness matrix |
| $[M]$ | Mass matrix |
| $\{\ddot{u}\}$ | Vector of nodal relative acceleration |
| $\{\dot{u}\}$ | Vector of nodal relative velocities |
| \ddot{u}_g | Acceleration at the base of the soil column |
| $Var[\cdot]$ | Variance |

Chapter 1

Introduction

1.1 Background

Tunnels are an important part of civil infrastructures and can have diverse uses such as subways, highways, and water transport. Traditionally, tunnels were considered to be less severely affected by earthquakes than other structures, the seismic vulnerability was thus seldom considered (Hashash *et al.*, 2001; St John and Zahrah, 1987; Wang, 1993). In recent years, however, severe damage, including collapse, occurred and was reported worldwide (Kontoe *et al.*, 2008; Lu and Hwang, 2018; Shen *et al.*, 2014; Uenushi and Sakurai, 2000). Therefore, the research on the design of tunnel against seismic activities to effectively mitigate risks and reduce large socio-economic losses due to earthquake-induced tunnel damage has attracted increasing attention.

The seismic analysis and design of tunnels are currently based on analytical solutions, numerical analyses, and experimental studies. Characterizing the seismic behaviour of a tunnel (e.g., identifying its deformation or internal forces) is not an easy task for analytical and experimental studies since they are limited to the necessarily adopted simplifications, budget constraint, and data acquisition. Numerical analyses considered continuum media have then to be employed, such as the finite difference or the finite element method.

Numerical approaches allow the analysts to examine the earthquake effects on the tunnels considering various levels of complexity and using high-fidelity modelling of the soil-tunnel

systems. Over the past two decades, numerical investigations have contributed to answering fundamental questions on the seismic response of tunnels considering the site conditions and soil parameters. However, new challenges such as large shield-driven tunnelling in multi-layered formations, tunnelling-induced stress perturbation, as well as uncertain soil property lead to the need for detailed investigation of their potential influences.

Tunnel numerical analyses are subjected to several uncertainty sources, including uncertainty of seismic ground motions, uncertainty of geotechnical parameters, and uncertainty of seismic analysis models. When a simple constitutive soil model is employed, the frequency-dependent Rayleigh damping is generally required to provide damping at small strains or to remain numerical stability. Various criteria and approaches for dealing with the inherent limitations (i.e., frequency-dependent) of Rayleigh damping have been proposed. However, there is no consensus regarding the best approach for determining Rayleigh damping parameters in dynamic analyses.

Moreover, the accurate characterization of geotechnical parameters remains a challenging task due to the natural heterogeneity of geomaterials, measurement methods, modelling errors, and the quality of the available limited data. All the geotechnical parameters exhibit a distribution around their mean value and these distributions can be represented in numerical analyses by random variables or random fields. Uncertainties of geotechnical parameters directly contribute to the increase of the response variability and can affect the tunnel seismic design.

Deterministic models are the most commonly utilized procedure in the current practice, but they neglect to consider the uncertainty of geotechnical parameters that can only be examined within a probabilistic framework. Probabilistic analysis serves as an opportunity to explicitly reflect the effects of the uncertainties, and to distinguish important from unimportant variables. Probabilistic analyses are therefore necessary to be conducted to rationally quantify the variability in the tunnel seismic response, although it has received little attention in the literature.

1.2 Objectives

The previous section demonstrates that the safety of tunnels is of major importance in earthquake-prone areas and remains a challenging problem for design. Indeed, the analyses often use simplified cases (e.g., homogeneous soil conditions, excavation is assumed to take place simultaneously with the lining set up) or ignore the geotechnical parameter uncertainty by accounting for their average values that may underestimate the earthquake effects on tunnels.

Considering all the previous statements, the present work aims at numerically investigating the seismic behaviour of tunnels addressing these assumptions that are often not representative of real conditions. The main objectives of this work include the following:

- Highlight the significant importance of the Rayleigh damping on the numerical predictions, which is commonly utilized in nonlinear numerical models.
- Investigate the tunnel seismic response considering the construction consequence that is generally neglected in numerical models.
- Present both the theoretical and numerical reasons of how an underlying soft soil layer is of benefit to the tunnel seismic protection as a natural damper.
- Identify the most important variable that has an important contribution to the variability in the tunnel seismic deformation.
- Examine the seismic deformation statistical characteristics caused by the uncertainties of the geotechnical parameters.

1.3 Thesis outline

From these objectives, the document is organized into six chapters that are now presented.

After an introduction of the considered problem, Chapter 2 contains a review of the numerical models considered for the seismic analysis of tunnels in the deterministic and probabilistic frameworks. The general aspects of the viscous damping employed at small strains in

dynamic time-history analyses and the existing approaches for determining the Rayleigh damping matrix are first addressed. Then two categories of numerical models, namely quasi-static and dynamic time-history analyses are described. Finally, the probabilistic analyses of tunnels under both static and seismic conditions are briefly described.

Chapter 3 investigates the variability in the tunnel seismic behaviour (i.e., axial forces) caused by different Rayleigh damping models. Five practical damping determination approaches and six commonly adopted target damping ratios are selected. Two groups of ground motions with diverse frequency characteristics are considered. The maximum axial forces calculated by these five approaches are compared. The reduction levels of the normalized axial forces caused by different target damping ratios, as well as the variability in the calculated axial forces induced by five approaches are investigated in detail.

Chapter 4 explores the influence of the excavation-induced stress disturbance on the seismic response of tunnels. The tunnel excavation is simulated using a 2D plane strain numerical model considering the convergence-confinement method. Dynamic time-history analyses are subsequently performed assuming both the no-slip and full-slip conditions between the soil and the tunnel lining. The upper and lower limit relationships between the stress relaxation coefficients and the seismic internal force increments are presented. The influences of the stress redistribution on the surface ground motions and of the depth-dependent modulus reduction curves on the calculated internal forces are also discussed.

Chapter 5 investigates the underlying soft soil layer-tunnel interaction under seismic loadings. In an attempt to obtain a better understanding of the soft interlayer influence on the wave propagations, a theoretical study is first conducted assuming a plane SH wave vertically propagating through a three-layered elastic medium. Then parametric numerical analyses are conducted to investigate the seismic response of tunnels with the variation of the soft layer parameters including its thickness, shear wave velocity, and position.

Chapter 6 deals with probabilistic analyses. It attempts to explore the efficiency of the sparse

polynomial chaos expansions combined with a global sensitivity analysis (*SPCE-GSA*) for the tunnel seismic response analysis in strong nonlinearity and high dimensional. This method permits us to figure out the parameters that have the most or least influence on the tunnel seismic deformations variability. The basic principles behind the *SPCE-GSA* method are introduced. Then, the accuracy of the *SPCE* model as well as the efficiency of the *SPCE-GSA* method is respectively presented. Sensitivity analyses are performed for a wide range of shear wave velocities, motion intensities, and coefficients of variation. Finally, the sensitivity indices variability caused by the sampling size, polynomial degree (to train the *SPCE* model), and input ground motion characteristics are evaluated.

Chapter 7 aims to quantify the variability in the tunnel seismic deformations caused by seven uncertain geotechnical parameters. The statistical characteristics in terms of mean, variance, and coefficient of variation of the tunnel deformations are examined through Monte Carlo simulations. To address some limitations of the existing studies, analyses are performed considering a variety of uncertain scenarios. Finally, the impact of the uncertainty of the geotechnical parameters on a reliability-based seismic design of tunnels is discussed.

Chapter 2

Literature review

2.1 Introduction

In this chapter, a literature review of numerical models for the seismic analysis of tunnels in deterministic and probabilistic frameworks is presented. Several issues related to their application are discussed. Section 2.2 describes the general aspects of the viscous damping employed at small strains in dynamic time-history analyses and the existing approaches for determining the Rayleigh damping matrix. Two categories of tunnel seismic analysis methods, namely the quasi-static and dynamic time-history analyses are described in Section 2.3. Finally, an overview of the probabilistic analysis of tunnels under both static and seismic conditions is presented in Section 2.4.

2.2 Viscous damping at small strains

2.2.1 Frequency domain vs time domain

In earthquake engineering practice, seismic wave propagation from the bedrock to the ground surface can be quantified either by an equivalent-linear (*EL*) analysis in the frequency-domain or by a nonlinear (*NL*) analysis in the time-domain. To improve the understanding of the viscous damping role in *NL* numerical models, differences between the *EL* analysis and the *NL* analysis are presented.

Frequency-domain *EL* analyses are based on closed-form solutions of the wave equation for shear waves propagate vertically through a layered continuous medium (Lysmer *et al.*, 1971; Kramer, 1996). The soil properties needed for each soil layer are shear wave velocity V_s , mass density ρ , and curves for modulus reduction (G/G_{\max}) and damping (D) versus the shear strain (γ), as shown in Fig. 2.1a. The analysis with an *EL* modelling is an iterative procedure in which effective shear strain-compatible shear modulus and damping are adopted at each calculation step. In this way, the soil nonlinearity is approximately simulated using the *EL* approach, as schematically shown in Fig. 2.1b. It should be noted that frequency-domain analyses are essentially the linear dynamic analyses and they model soil damping using a strain-compatible curve, i.e., damping independent of frequency. *EL* analysis requires small computational cost and few input parameters, thus this method has successfully been utilized to predict the seismic response of a given site. However, the limitations of *EL* analysis are broadly recognized, e.g., total stress approach, one-dimensional, poor performance for deep soil deposits and high strain cases (Griffiths *et al.*, 2016).

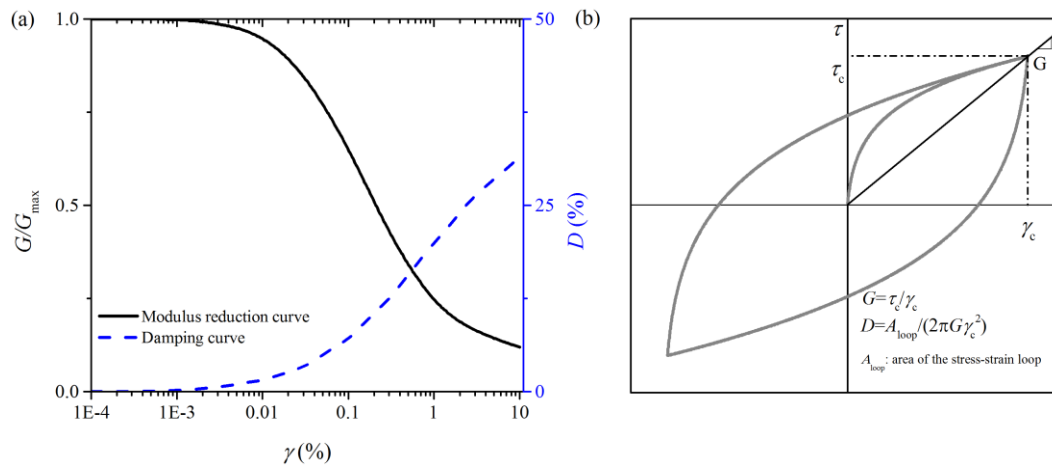


Fig. 2.1 (a) $G/G_{\max} \sim \gamma$ and $D \sim \gamma$ curves; and (b) stress-strain loops of soil in shear illustrating measurement of secant shear modulus and damping ratio.

NL response analyses in the time-domain can effectively address the limitations of the *EL* approach (Clough and Penzien, 1993). They provide a more accurate characterization of the nonlinear soil behaviour under cyclic loading using constitutive models with different levels of complexity. On the other hand, *NL* analyses allow considering directly the soil-structure

interaction effect under various conditions, e.g., large-scale, multi-dimensional, and multi-directional ground motion conditions. In essence, the dynamic calculation in the time-domain is to solve the equations of motion. *NL* dynamic analysis system is represented by a series of lumped masses or is discretized into elements. The system of equations is discretized temporally and a time-stepping scheme such as the Newmark- β method is employed to solve the equations and to obtain the response at each time step. A detailed numerical model for seismic analysis requires at least an accurate constitutive model for the materials, an adequate model dimension, an appropriate boundary condition, and a reasonable specification of the earthquake input motions. Among these necessary points, accurate energy dissipation modelling is one of the most important issues (Priestly and Grant, 2005).

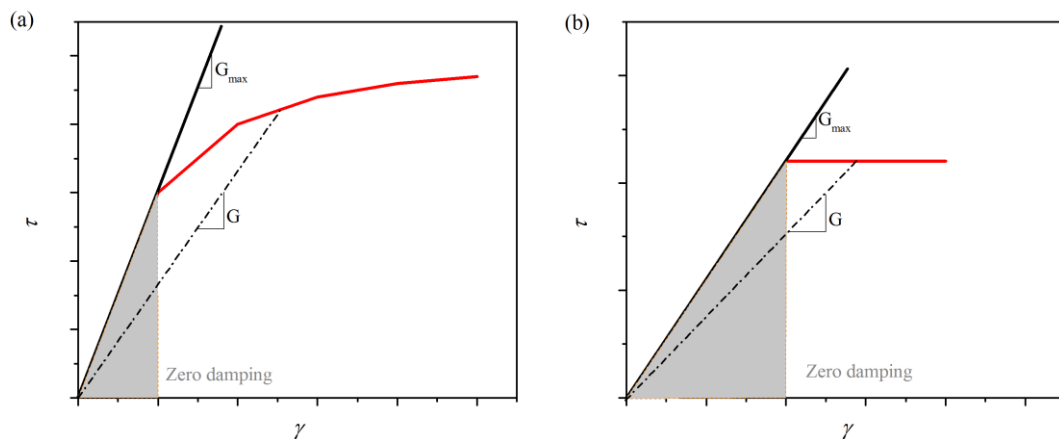


Fig. 2.2 Schematic representation of the zero damping: (a) at very small strains; and (b) in the elastic ranges.

In the *NL* time-domain models, there are two sources of soil damping (Kwok *et al.*, 2007): the first one is the hysteretic damping associated with the area bounded by the stress-strain loops, which strongly depends on the soil constitutive model and the level of nonlinearity. However, some soil constitutive models (e.g. linear elasticity with perfect plasticity, Fig. 2.2b) adopted for dynamic analyses induce no energy dissipation in the linear elastic range, which is incompatible with the soil damping properties measured in the laboratory. Furthermore, varieties of nonlinear models commonly utilized in current analyses cannot produce sufficient damping at very small strains (lower than 10^{-6} to 10^{-4}), due to the nearly linear backbone curve (Fig. 2.2a). The soil damping underestimation will lead to an overestimation of propagated ground motion. Thus, there is a necessity to incorporate viscous damping into most *NL*

numerical models, in order not only to avoid unrealistic responses for problems involving small strains but also to ensure numerical stability (i.e., resonance and high frequency noise).

2.2.2 Rayleigh damping formulation

In the *NL* analysis, the following dynamic equation of motion is solved (Clough and Penzien, 1993):

$$[M]\{\ddot{u}\} + [C]\{\dot{u}\} + [K]\{u\} = -[M]\{I\}\ddot{u}_g \quad (2.1)$$

where $[M]$ is the mass matrix; $[C]$ is the viscous damping matrix; $[K]$ is the stiffness matrix; $\{\ddot{u}\}$ is the vector of nodal relative acceleration; $\{\dot{u}\}$ is the vector of nodal relative velocities; and $\{u\}$ is the vector of nodal relative displacements; \ddot{u}_g is the acceleration at the base of the soil column and $\{I\}$ is the unit vector.

Viscous damping is assumed to be of Rayleigh type as being straightforward to implement in numerical procedures. It can be expressed as follows:

$$[C] = \alpha[M] + \beta[K] \quad (2.2)$$

where α and β are respectively the mass-proportional and stiffness-proportional coefficients.

The coefficients can be obtained based on the following equations:

$$\begin{Bmatrix} \alpha \\ \beta \end{Bmatrix} = \frac{2\xi_{tar}}{\omega_1 + \omega_2} \begin{bmatrix} \omega_1\omega_2 \\ 1 \end{bmatrix} \quad (2.3)$$

$$\xi = \frac{1}{2} \left(\frac{\alpha}{\omega} + \beta\omega \right) \quad (2.4)$$

$$\omega = 2\pi f \quad (2.5)$$

$$\xi_{min} = \sqrt{\alpha\beta} \quad (2.6)$$

$$f_{min} = \frac{\sqrt{\alpha/\beta}}{2\pi} \quad (2.7)$$

where ω_1 and ω_2 are the two parameters which ensure the frequency range, ξ_{tar} is the target damping ratio, f_{min} represents the central position of the approximate frequency-independent range, and ξ_{min} is the corresponding critical damping ratio. The above equations illustrate the basic form of a full Rayleigh damping formulation, as plotted in Fig. 2.3.

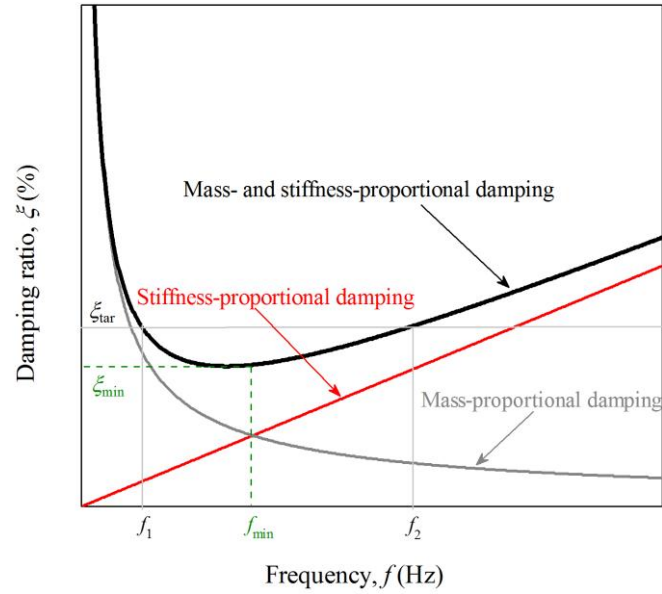


Fig. 2.3 Full Rayleigh damping formulations.

The figure demonstrates the dependency of the Rayleigh damping on the frequency. There are three critical issues for the Rayleigh damping (Hall, 2006; Kausel, 2014):

- The choice of the type of damping model.
- The value of the target damping ratio ξ_{tar} .
- The two matching frequencies f_1 and f_2 .

For the type of damping model, the simplified (stiffness-proportional only) and full (mass- and stiffness-proportional) Rayleigh damping matrices are commonly utilized in practical analysis. Concerning the value of ξ_{tar} , which is always selected according to the small strain damping or on the smallest value to obtain a stable solution, a small damping ratio ranges from 1% to 5% is often employed. Higher or lower damping ratios are also adopted in some studies, depending on the soil constitutive model, input motion characteristic, and analysis strategy (Bilotta *et al.*, 2014; Kontoe *et al.*, 2011; Madabhushi *et al.*, 2018). However, it is tricky to select two matching frequencies, to define an approximate frequency-independent damping range. As shown in Fig. 2.3, Rayleigh damping ratios match the target damping only at two frequency points: f_1 and f_2 . It will underestimate the damping at frequencies between f_1 and f_2 and overestimate damping at frequencies lower than f_1 and higher than f_2 . Thus, one of the major difficulties in nonlinear dynamic analyses is the determination of the appropriate

frequency range. Otherwise, unreasonable damping ratios utilized will significantly influence the numerical predictions (Hall, 2006, 2018; Jehel, 2014; Luco, 2008; Nielsen, 2009).

Over the past years, many studies investigated the viscous damping modelling considering an appropriate Rayleigh damping formulation, as well as the numerical predictions that employed different Rayleigh damping models. In practice, the lower matching frequency f_1 is generally taken as the site fundamental frequency SF (1st natural mode), which can be estimated as follows (Kramer, 1996):

$$f_n = (2n - 1) \frac{V_{se}}{4H} \quad (2.8)$$

$$V_{se} = \frac{H}{\sum(H_i/V_{si})} \quad (2.9)$$

where n is the n -order natural mode of soil and f_n is the corresponding mode frequency, H is the soil deposit thickness, H_i and V_{si} are respectively the thickness and shear wave velocity of the soil layer i ; V_{se} is equivalent shear wave velocity of the soil. However, different guidelines can be found in the literature for selecting the higher matching frequency f_2 .

2.2.3 Rayleigh damping determination

Formerly, only the SF was used for formulating the damping model which referred to a single frequency method ($f_{\min}=f_1=f_2=SF$, $\xi_{\min}=\xi_{\text{tar}}$). It has been implemented into the code *QUAD4* (Idriss *et al.*, 1973). Conceptually, this method overestimated the overall damping except at frequency equals to SF , and resulted in a significant underestimation of the numerical response in all the frequency range. Then, Hudson *et al.* (1994) stated that using the odd-integer multiplier of the SF (e.g., 3,5,7) as the larger matching frequency with an overwhelming advantage over the single frequency method. They could reduce the frequency-dependent of the Rayleigh damping. The computer program *QUAD4* was extended to capture this concept and finally, an updated program *QUAD4M* was developed. In this code, the Rayleigh damping was assumed to be of the full Rayleigh type with two matching frequencies. The larger matching frequency $f_2=nSF$ with n being the smallest odd integer larger than the ratio of PF/SF was suggested (PF is the predominant frequency of the input

motions).

Subsequently, [Matasovic \(1993\)](#) developed a nonlinear site response analysis code (i.e., *D_MOD*) to evaluate the local site effects on the propagated ground motion with a modified hyperbolic soil model. This soil constitutive model produced nearly no damping at small strains thus a stiffness-proportional damping formulation was utilized. The damping matrix in Eqs. 2.2 and 2.3 will then be rewritten as follows:

$$[C] = \frac{2\xi_{tar}}{\omega} [K] \quad (2.10)$$

A confining pressure-independent ξ_{tar} was assumed in the model, which was inconsistent with the laboratory tests. This defect resulted in poor applicability of this code for deep soil deposits since an overestimated damping ratio was considered for the deep soil layers. The stiffness-proportional damping formulation could filter out a significant portion of the high frequency content of the ground motion.

To improve the applicability of this damping formulation, [Hashash and Park \(2001\)](#) introduced a confining pressure-dependent target damping ratio at zero strain to better estimate the ground motions of deep soil deposits (i.e., up to 1000 m). The target damping ratio was expressed, as follows:

$$\xi_{tar} = \frac{c}{(\sigma')^d} \quad (2.11)$$

where c and d are material parameters and σ' is the vertical effective stress.

The above equation was extended to a full Rayleigh damping formulation to further improve nonlinear site response analyses at short periods ([Hashash and Park, 2002](#)). By comparing various soil deposits, they suggested that the soil higher mode was better to consider to optimize the frequency f_2 particularly for soil deposits greater than 50 m thick. In their study, the 8th soil mode was employed for a 1000 m soil deposit. To further reduce the frequency-dependent, [Park and Hashash \(2004\)](#) proposed an extended Rayleigh formulation (*ERF*) for preserving the frequencies higher than the matching frequency f_2 . By utilizing four matching frequencies, the Eq. 2.2 was expanded to approximately model the

frequency-independent damping in a larger frequency range (Fig. 2.4), as follows:

$$[C] = \alpha[M] + \beta[K] + \zeta\{[K][M]^{-1}[K]\} + \delta\{[K][M]^{-1}[K][M]^{-1}[K]\} \quad (2.12)$$

where ζ, δ are the additional coefficients.

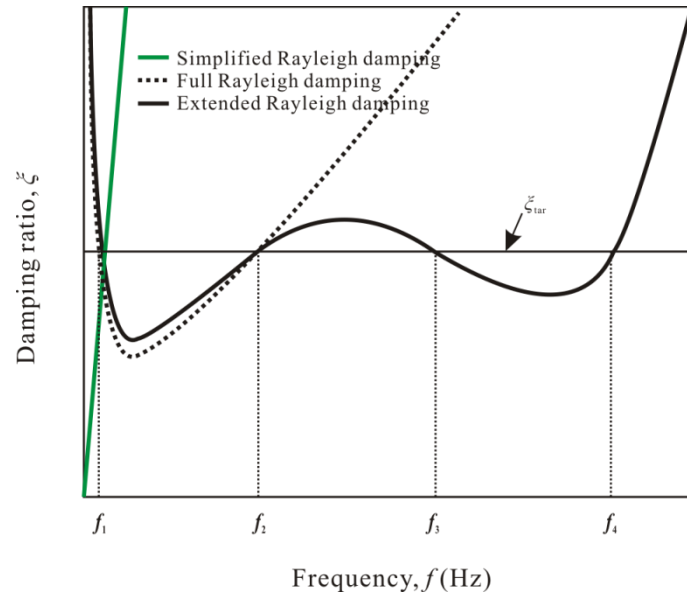


Fig. 2.4 Damping ratios using different Rayleigh damping formulations.

However, the *ERF* has only been implemented in the *DEEPSOIL* code. To investigate its effectiveness, three site conditions and four input motions were considered. The comparison showed that the *ERF* was able to better capture the high frequency content than the full Rayleigh damping but in general such improvement was negligible when a 5% damped spectral acceleration was calculated (Park and Hashash, 2004; Phillips and Hashash, 2009). They concluded that the additional frequencies f_3 and f_4 should be selected through an iterative process (calibrated with the 1D frequency-domain linear analysis), which was related to the site conditions and input motions. Thus, the additional two frequencies introduce more variability in the Rayleigh damping and it is seldom used in practice.

Visone *et al.* (2009) suggested that the Rayleigh damping formulation could be calibrated according to the results of the *EL* analysis procedure. The final profiles of shear modulus and soil damping ratios calculated by the *EL* analysis will then be used as the input material parameters in the *NL* models for visco-elastic analysis. The frequency range was determined

using SF and $3SF$ in their study. Their results showed that NL predictions matched well with those of the EL analysis, in terms of amplification functions and maximum acceleration profiles. This calibration procedure permits to provide a reliable ξ_{tar} if the nonlinear soil properties of a site are accurately characterized.

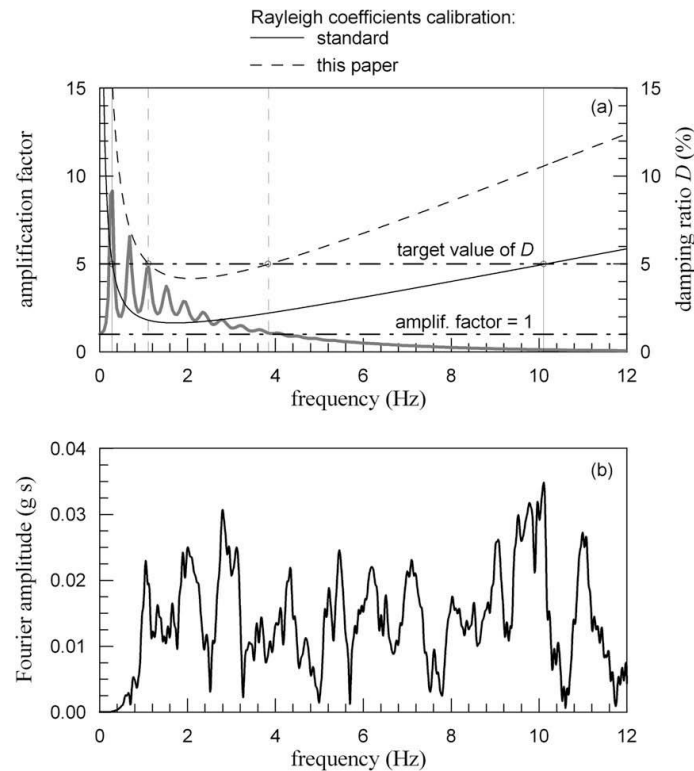


Fig. 2.5 Determination of the frequency range for the Rayleigh coefficients (Amorosi *et al.*, 2010).

Amorosi *et al.* (2010) followed a similar calibration procedure to select the viscous and linear elastic parameters for a FE analysis. In their study, the first matching frequency f_1 was identified by comparing the elastic amplification function of the EL analysis and the Fourier spectrum of the input motion. As shown in Fig. 2.5, the sample motion had low energy content for the first two natural frequencies of the deposit, such that the third natural frequency ($5SF$, equal to 1.12 Hz) was selected as f_1 . The frequency corresponding to an amplification function lower than one (around 3.8 Hz) was set as f_2 . The authors stated that the differences between the peak accelerations of adopting this method and the EL solutions were always lower than 10%. In contrast, the $QUAD4M$'s method appeared to overestimate the acceleration response when increasing the soil thickness and the PF/SF ratio. This

conclusion was later been confirmed by other researchers (Suwal *et al.*, 2014). They reported an overestimation of around 20% of the spectral acceleration caused by the *QUAD4M*'s method, particularly for high frequency input motions. Moreover, the study stated that the viscous damping influence seemed to depend on the nonlinear soil constitutive model, as the *D-MOD* code resulted in a higher overestimation than the *DEEPSOIL* code for the same Rayleigh damping formulation.

Lanzo *et al.* (2003) evaluated the impact of the viscous damping formulations (full and simplified) on the seismic response of three uniform soil deposits ($H=30, 100, 300$ m; $V_s=300$ m/s, $\xi_{tar}=3\%$). For the simplified form, only the *SF* was adopted for the stiffness-proportional damping while the *SF* and *nSF* (*QUAD4M*'s method) was used for the full damping formulation. The results of the analyses showed that the use of the simplified Rayleigh damping formulation could significantly underestimate the response, especially for deep deposits and high frequency motions. This could be attributed to the increasing relative importance of the higher modes in the response of deep deposits and the linearly increased effective damping ratio of higher modes.

Kwok *et al.* (2007) presented a comprehensive investigation into the viscous damping influence on the site seismic response. Both the simplified ($f_1=f_2=SF$, *PF*, and mean frequency *MF*) and full Rayleigh ($f_1= SF$, $f_2=3SF$, and $5SF$) damping formulations were compared for three real sites (*SF* ranges from 0.45 Hz to 6.4 Hz). They recommended that the full Rayleigh formulation rather than the simplified one should be used to estimate the viscous damping. As a first approximation, the *SF* and $5SF$ should be used to define the frequency range. While for simplified Rayleigh damping formulation, the *MF* of the input motion generally produced acceptable results whereas the other methods underestimated the response at short periods, particularly for deep sites. However, their recommendation was based on only one broadband synthetic acceleration history.

Papaspiliou *et al.* (2012) investigated the influence of viscous damping formulations on the probabilistic seismic hazard analyses using nonlinear time-domain analysis. In their study, the

smaller possible level of viscous damping (0.5%) was selected so as not to aggravate the tendency of overestimating the damping at high strains. The simplified (i.e., $f_1=f_2=SF$) and full ($f_1=SF, f_2=3SF, 5SF$) damping formulations were utilized. The analyses revealed significant numerical noise at high frequencies due to the damping underestimation (Fig. 2.6). Severe numerical noise can modify the shape of the spectral accelerations and even lead to numerical instabilities.

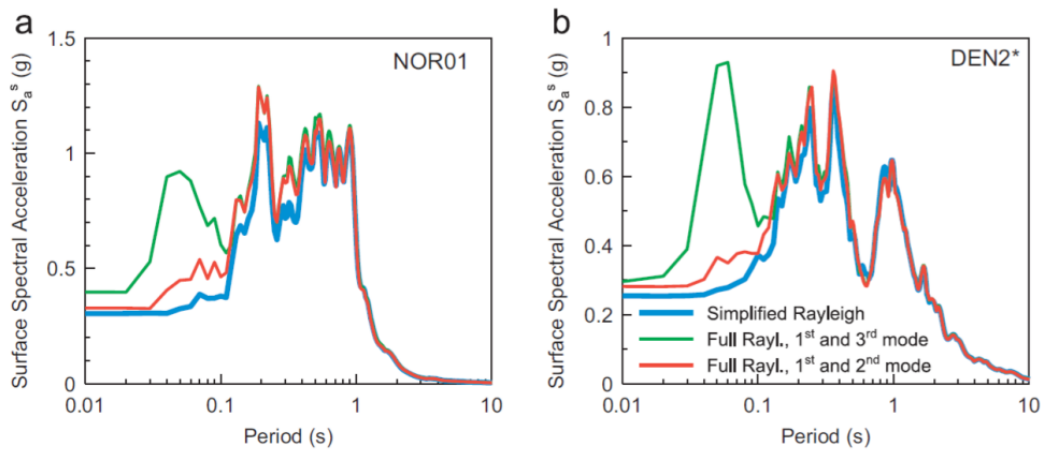


Fig. 2.6 Spectral accelerations obtained from site response analysis using records NOR01 and DEN2* for different Rayleigh damping formulations (Papasiliou *et al.*, 2012).

Mánica *et al.* (2014) evaluated the Rayleigh damping in the code *FLAC* through the visco-elastic response analysis of a given site in Mexico City. Similarly, a calibration procedure (Visone *et al.*, 2009) was utilized to obtain the target damping ratio and reduced the soil shear modulus, then the central frequency f_{\min} was randomly selected to minimize the difference (i.e., residual error sum of squares) of each calculated spectral acceleration with the original record (Fig. 2.7). The results demonstrated that the Rayleigh damping could be a suitable method to represent the soil energy dissipation when a proper parameter selection was adopted.

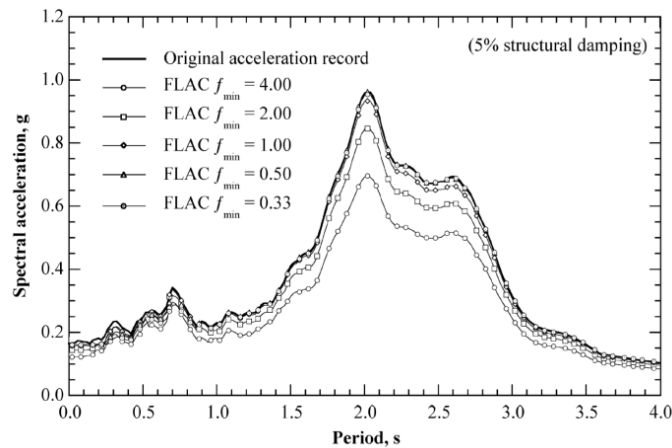


Fig. 2.7 Surface spectral acceleration using Rayleigh damping for different f_{\min} values (Mánica *et al.*, 2014).

Tasi *et al.* (2014) demonstrated that using SF and $5SF$ as the optimal frequencies was applicable for shallow soil deposits while selecting PF or MF of the input motion as the matching frequency f_2 could improve the time-domain predictions for deep soil deposits. They also suggested that the optimal f_2 should be selected as the maximum between $\{PF, MF, 5SF\}$. However, the method appeared to poorly perform for high frequency input motions especially with a significant difference in PF and MF .

This section reviews the literature related to the viscous damping at small strains, the different selection criteria, and the potential influences on the site seismic response analyses. The purpose of these studies was to provide or recommend an optimal approach that can effectively reduce the undesirable effects encountered by the misuse of the viscous damping for dynamic analyses.

2.3 Deterministic models

The seismic design of tunnels is currently based on analytical solutions, quasi-static numerical analyses, and time-domain dynamic time-history analyses (Hashash *et al.*, 2001). In this section, the representative numerical works on the seismic response of tunnels in dry soils are presented. This section focuses on presenting the current knowledge state of the tunnel seismic response based on quasi-static and dynamic time-history numerical analyses. It does not cover issues related to the tunnel seismic behaviour associated with ground failures such

as slope instabilities, liquefactions, and faults crossing.

2.3.1 Pseudo-static method

In general, seismic design loads for tunnels are characterized in terms of deformations and strains imposed on the tunnel lining by the surrounding soil mass. In contrast, the influence of tunnel inertial forces caused by the ground accelerations is secondary due to the deeply buried depth and relatively large inertia of the surrounding ground. It is widely accepted that three deformation modes describe the response of circular tunnels to ground shaking (St John and Zahrah, 1987): (a) axial deformation along the tunnel, (b) longitudinal bending, and (c) ovaling deformation. The latter one, as schematically illustrated in Fig. 2.8, is considered as the most critical deformation mode since the shear wave propagates normally or nearly normally to the tunnel axis. This can be simulated through two-dimensional plane strain numerical models.

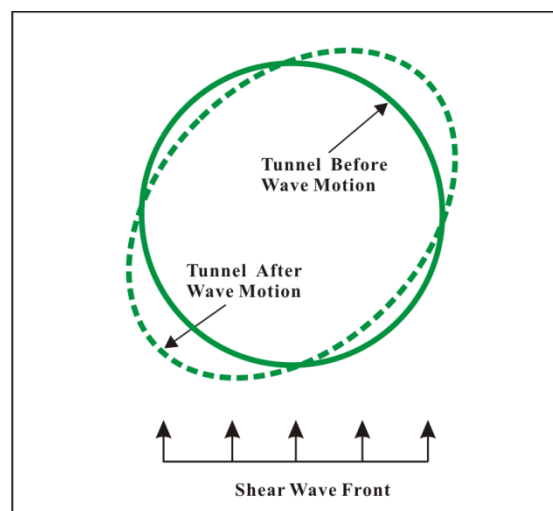


Fig. 2.8 Ovaling deformation of the circular tunnels under seismic waves (Owen and Scholl, 1987).

In the pseudo-static approach, the ground deformations are imposed as a static load and the soil-tunnel interaction (*SSI*) does not include dynamic or wave propagation effects. It can either be deformation-based: the model is subjected to a shear strain or force-based: the seismic-induced inertia force is applied as a constant body force (the seismic force is

progressively applied to the soil-structure system until the target displacement is reached). The imposed shear strain or the body force can be estimated by a one-dimensional site seismic response analysis or by empirical relations (Katona, 2010).

The simplest quasi-static approaches ignore the interaction of the underground structure with the surrounding ground. St John and Zahrah (1987) stated that the amount of racking imposed on the tunnel (Δ_{tunnel}) could be taken equal to the difference between the soil deformations (Δ_{ff}) at the top and the one at the tunnel bottom. This approach was satisfactory for low shaking levels or when the underground facility was excavated in a stiff medium. However, it resulted in conservative designs if the tunnel was very stiff relative to the soil due to the important *SSI* effect. Subsequently, Wang (1993) recommended two simplified frame analysis models for rectangular tunnels (Fig. 2.9), one was the pseudo-concentrated force for deep tunnels, and another one was the pseudo-triangular pressure distribution for shallow tunnels.

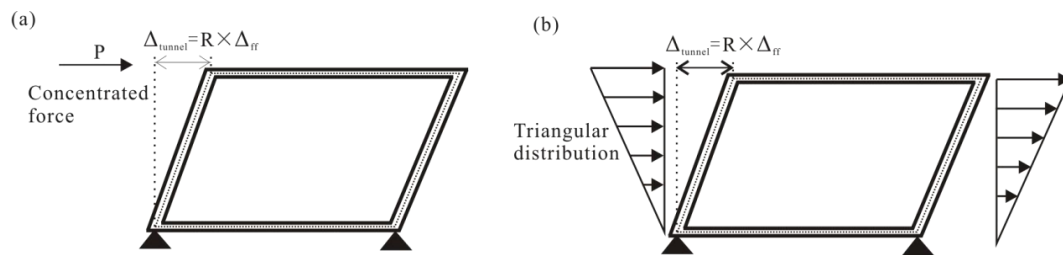


Fig. 2.9 Simplified frame analysis models: (a) concentrated load at the corner, and (b) triangular distributed load on the side walls (Wang, 1993).

To account for the *SSI* effect, a relationship was suggested to estimate tunnel distortion as follow:

$$\Delta_{\text{tunnel}} = R \times \Delta_{\text{ff}} \quad (2.13)$$

where R is the racking ratio that can be determined according to the R - F relationship (F is the flexibility ratio).

Iai (2005) proposed a simplified equivalent static analysis for buried structures, in which the seismic action was specified as the maximum relative displacement. Relative to previous models (St John and Zahrah, 1987; Wang, 1993), the inertia force of structure, and the

interface shear stresses were incorporated into the model through a series of normal and tangential springs (Fig. 2.10). However, the difficulty of this model in practical applications lied in the determination of the spring stiffness.

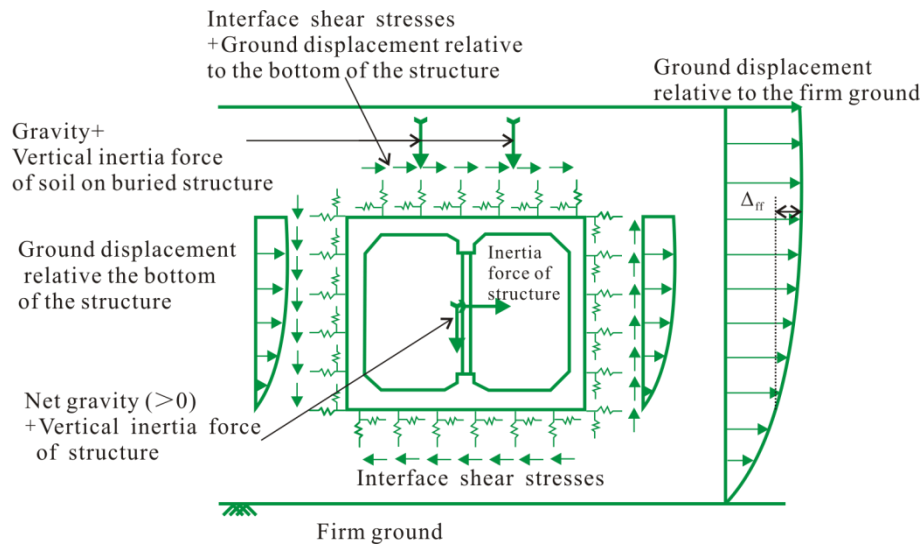


Fig. 2.10 Seismic actions on the buried structure for simplified equivalent static analysis (Lai, 2005).

Hwang and Lu (2007) proposed a modified cross-section racking deformation (*MCSR*D) method to investigate the allowable peak ground velocity for the old Sanyi tunnel. This deformation-based analysis method considered the *SSI* effect and nonlinear soil behaviour. Their analysis revealed that the presence of a tunnel restrained the local soil displacement and it became more significant as the applied strain increased (Fig. 2.11). The lining forces predicted by the quasi-static model matched well with the ones of the dynamic analysis in a small shear strain range (i.e., the maximum shear strain of $\gamma_{\max}=2 \times 10^{-4}$), with a maximum difference lower than 20%. However, the quasi-static model failed to estimate the lining forces for shallow buried tunnels, while for this situation a dynamic analysis was suggested (Lu and Hwang, 2019). The authors further developed a nonlinear model for the tunnel lining and, used this model to highlight the importance of a second lining reinforcement on the tunnel seismic stability (Lu and Hwang, 2017, 2018).

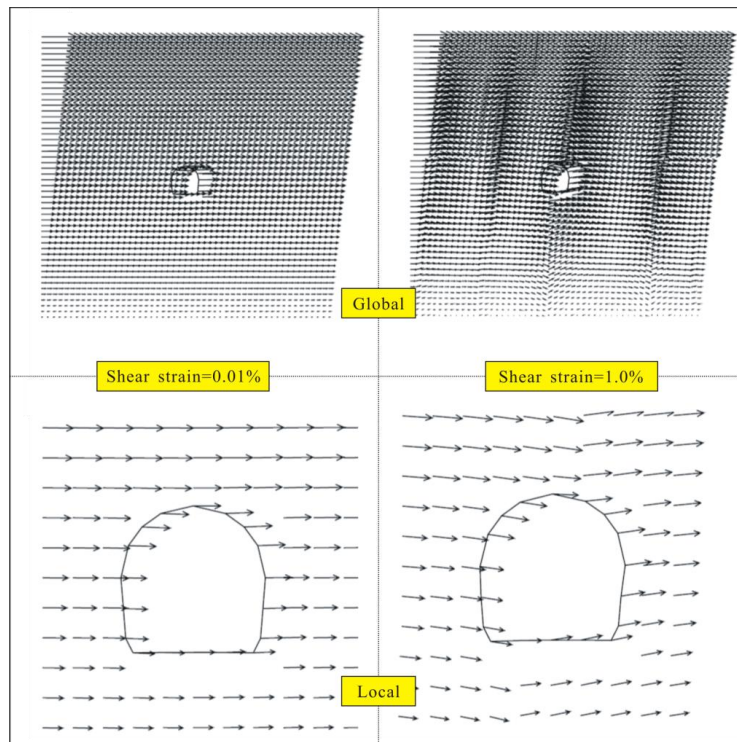


Fig. 2.11 The global (upper row) and local (lower row) displacement fields under small and large seismic shear strains (Huang and Lu, 2007).

Debiasi *et al.* (2013) investigated the effects of the soil-structure interaction, the geometry of the structure, overburden depth, and motion intensity on the seismic deformations of a rectangular tunnel. The applied horizontal body forces at the model boundary were uniformly distributed and the amplitude was determined based on the bedrock motion amplitude after multiplication by an amplification coefficient (i.e., 1.8). The results underlined the significant role of the soil-tunnel interface for shallow stiff structures and the non-negligible rotation response for low aspect ratio structures. Liu *et al.* (2014) compared three types of force distribution (i.e., inverted triangular, uniform, and parabolic) on the numerical predictions. The results stated that the inverted triangular distribution was the more practical one. Zou *et al.* (2017) incorporated the structural nonlinearities into this approach to be able to perform the seismic damage analysis of tunnels. The analysis revealed that the quasi-static analysis could reproduce the failure evolution of an underground structure: first the collapse of the central column then the top slab.

Gomes *et al.* (2015) utilized a concentrated force-based pseudo-static model to investigate the

seismic response of a circular tunnel in two-layered soils. In their study, an external static load was applied at the model upper nodes that induced a ground distortion related to the calculated free-field shear strains (i.e., 10^{-3}). The accuracy of the quasi-static model was verified by comparison with an analytical solution and dynamic analyses. Besides, this study has emphasized the significant influence of the soil stratification on the tunnel seismic behaviour. In conjunction with the lower/upper bound limit analysis, the pseudo-static method could also be utilized to assess the seismic stability of an unsupported/supported circular tunnel in terms of the stability coefficient (Chakraborty and Kumar, 2013; Sahoo and Kumar, 2012, 2014). The tunnel stability decreased with the increase of the horizontal seismic coefficient.

Tsinidis *et al.* (2015) compared the efficiency of the force-based and the deformation-based pseudo-static model with centrifuge tests. They found that the quasi-static analysis generally underestimated the bending moments relative to the dynamic time-history analysis: 20% to 40% lower for the elastic analysis and up to 60% lower for nonlinear soils. Compared to force-based analysis, the deformation-based analysis further reduced the predicted bending moments since a greater amount of induced ground strain was artificially absorbed by the soil elements, thus “relieving” the tunnel. However, other studies (Kontoe *et al.*, 2008) as well as the author’s subsequent research (Tsinidis *et al.*, 2016a) showed that the deformation-based analysis could also predict larger bending moments than force-based ones, and probably larger than the dynamic analysis ones. Therefore, it is difficult to draw a general conclusion on whether the quasi-static analysis results can be reasonably compared with those obtained by the dynamic analysis. It is a site-specific function of the flexibility ratio, tunnel depth, *SSI* effect, soil nonlinearity and, input ground motions.

Do *et al.* (2015a) investigated the effect of lining joints on the seismic behaviour of tunnels using deformation-based quasi-static analysis (Fig. 2.12). The soil-tunnel system was respectively built using the *FDM* numerical method (i.e., *FLAC*). The study has demonstrated that the calculated bending moments decreased with the decrease of the joint’s rotational stiffness, due to the increased tunnel flexibility.

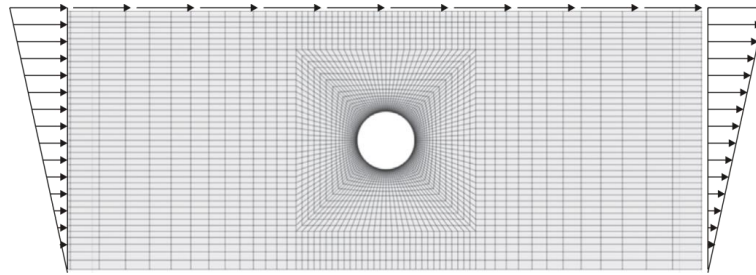


Fig. 2.12 Geometry and boundary conditions in the quasi-static model (Do *et al.*, 2015a).

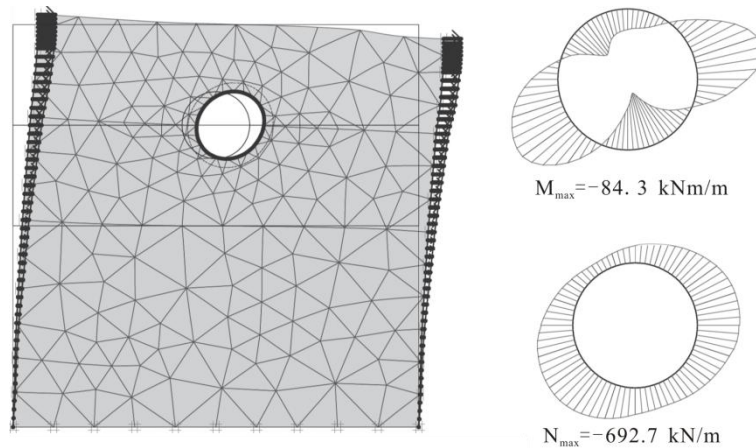


Fig. 2.13 Example of 2D quasi-static analysis: left is the deformed mesh and the right is the computed lining forces. (Argyroudis and Ptilakis, 2012).

Recently, there is an increasing interest in applying the quasi-static method to build fragility curves for tunnels since it is relatively cost-effective when compared with more complex dynamic time-history analyses. Argyroudis and Ptilakis (2012) were the first one, to the authors' knowledge, who developed and applied the quasi-static analysis for this purpose. The applied seismic ground deformation was calculated through a 1D equivalent linear analysis considering various motion characteristics, intensities, and soil conditions. Strain compatible soil shear stiffness was then used in 2D quasi-static analyses (Fig. 2.13), in which the soil nonlinearity was characterized by a linear elastic perfectly plastic constitutive model (Mohr-Coulomb shear failure criterion). Following the theoretical framework presented by Argyroudis and Ptilakis (2012), the quasi-static model has been utilized for the seismic vulnerability assessment of various types of tunnels (Huh *et al.*, 2017; Lee *et al.*, 2016; Nguyen *et al.*, 2019).

Another application of the quasi-static method is to validate the accuracy of analytical solutions since it is consistent with the assumptions of the analytical solutions (i.e., deformation-based analysis, pure shear state). For instance, Hashash *et al.* (2005) evaluated two analytical solutions (Penzien, 2000; Wang, 1993) for the no-slip case using a 2D numerical model, assuming elastic soil behaviour. The comparison demonstrated that the Penzien's solution significantly underestimated axial forces. Bobet *et al.* (2008) improved an existing analytical solution (Huo *et al.*, 2006) by incorporating soil-stiffness degradation. They stated that the improved solution was in good agreement with the quasi-static predictions in terms of deformations and stress responses for the no-slip case. Sedarat *et al.* (2009) highlighted the importance of the realistic representation of the soil-tunnel interface condition and the limitations of the analytical solution (Wang, 1993) for preliminary tunnel seismic designs. Kontoe *et al.* (2014) provided further numerical validations of four analytical solutions (Bobet, 2010; Park *et al.*, 2009a; Penzien, 2000; Wang, 1993) for a wide range of flexibility ratios, slippage conditions at the soil-tunnel interface based on the deformation-based quasi-static analysis.

In summary, the quasi-static method is a very attractive tool for the preliminary design, as it provides a quick and easy calculation of the seismic design loads in the tunnel lining. When a seismic action is directly imposed at the tunnel structures (i.e., common for rectangular ones), the *SSI* effect can be implicitly accounted through the empirical *R-F* relationships whereas it can be explicitly considered through the interface springs in a 2D soil-tunnel numerical model. However, it should be noted that the quasi-static models essentially include, to some extent, simplifications such as the distribution types of the applied deformations or forces, and the rough estimation of some parameters (applied deformation or forces).

2.3.2 Dynamic time-history method

Dynamic time-history analyses permit to consider the true soil nonlinearity and inertial interaction. A large number of existing studies were performed to investigate the tunnel seismic response. The majority of them focusing on 2D models, the minority focusing on

three-dimensional (3D) ones. To simulate rigorously all the three deformation tunnel modes as mentioned previously, a 3D analysis is needed. In current research studies, 3D tunnel models are seldom utilized, unless for modelling jointed segments, non-uniform or multi-directional seismic inputs, and special geological considerations like slopes, and faults. There are four basic issues in the dynamic time-history analysis of tunnels:

- Specification of the input motions.
- Constitutive models of the soils.
- Simulation of the soil-tunnel interface.
- Modelling of the tunnel lining.

Each of these issues is discussed below.

2.3.2.1 Input ground motions

Previous studies commonly utilized one ground motion in their numerical analyses or three ground motions to simply consider the influence of the input motion characteristics. Ground motions recorded in several well-known earthquakes (i.e., Kobe, Friuli, Nice, and Northridge) were frequently utilized in academic cases. These studies aimed at providing a better understanding of seismic response characteristics of tunnels for various conditions. On the other hand, some researchers investigated the influence of (1) near-field and far-field, (2) uniform and non-uniform, (3) horizontal and multi-directional, and (4) mainshock-aftershock ground motions, on the tunnel seismic response. They aimed at specifying the most unfavourable seismic input scenarios, and defining the relationship between the ground motion parameters and the tunnel seismic response. Sometimes they provided practical guidelines for appropriately specifying the input rock motions. For instance, [Chen and Wei \(2013\)](#) and [Cui *et al.* \(2018\)](#) have stated that the tunnel seismic damage was highly dependent on the velocity-related parameters and the presence of a velocity pulse could lead to more pronounced damage. [Huang *et al.* \(2020\)](#) confirmed this conclusion for *P* waves with large incident angles, whereas for small incident angles (<30 °) the motion intensity (*PGA*) tended to increase significantly the tunnel response (Fig. 2.14).

Concerning the spatial variation of ground motions, the general conclusion of past studies (Bi and Hao, 2012; Fabozzi *et al.*, 2018; Park *et al.*, 2009b; Yu *et al.*, 2013b; Zerva *et al.*, 1988) showed that:

- Non-uniform ground motions in general induced larger tunnel responses compared to uniform ones, particularly under discontinuous soil conditions (soil properties change in the longitudinal direction).
- Partially correlated input motions predicted high differential tunnel axial displacements compared to perfectly correlated ones. All vibration modes could be excited thus resulting in relatively high stresses.
- The influence was more evident for weak joint stiffness and large incident angles for segmental tunnels.

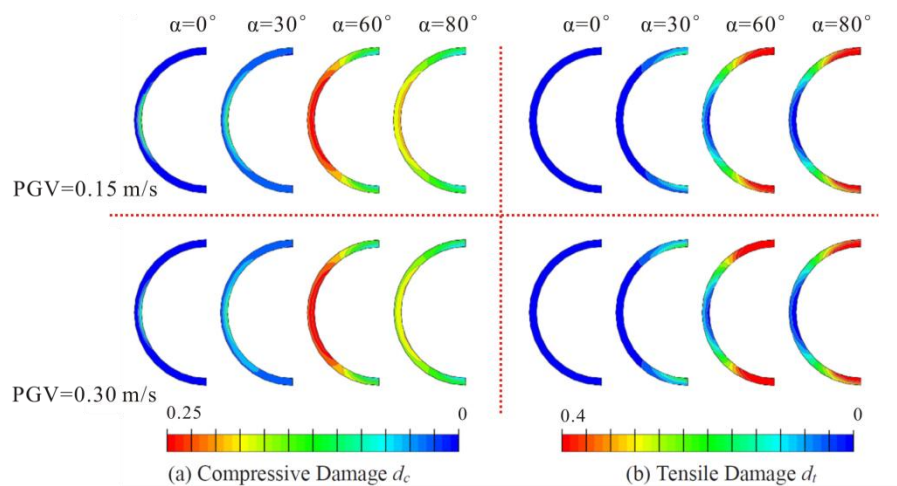


Fig. 2.14 Damage contours of ground motions with $PGV=0.15$ m/s and with $PGV=0.30$ m/s. (Huang *et al.*, 2020).

Multi-directional input motions have seldom been considered in seismic analyses and design of tunnels before the 1995 Kobe earthquake. However, the collapse of the Daikai subway station has demonstrated the great importance of the vertical ground motions (Iida *et al.*, 1996). The vertical ground motion could cause seismic damage to the underground structure in terms of additional compressive and tensile stresses. It is one of the fundamental reasons for the failure of the central column of the subway station and the tunnel lining cracks (Hashash *et al.*, 2001; Uenishi and Sakurai, 2000). Singh *et al.* (2018) and Sun *et al.* (2020a)

have investigated the tunnel damage under mainshock-aftershock ground motion sequences. They reported that the aftershock ground motion could cause severe cumulative damage and considered mainshocks only could underestimate the tunnel seismic response (Fig. 2.15).

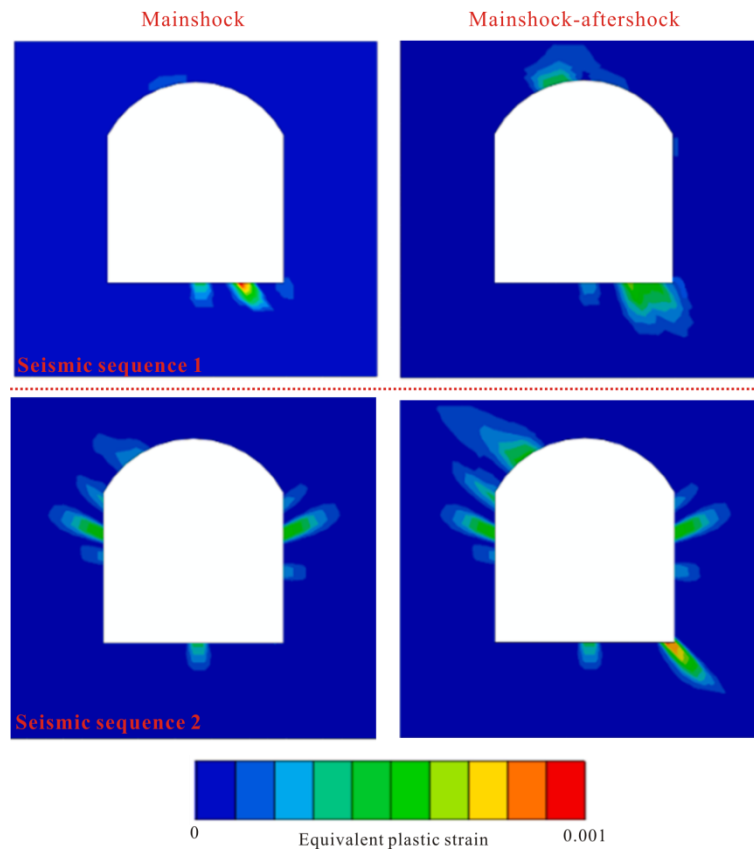


Fig. 2.15 Equivalent plastic strains of surrounding rock under mainshock and mainshock-aftershock sequence. (Sun *et al.*, 2020a).

2.3.2.2 Soil constitutive models

It is essential to develop and use constitutive models that can appropriately simulate the soil behaviour under cyclic loading and, to capture the tunnel seismic response accurately. For the tunnel seismic analysis, equivalent linear models and simple elasto-plastic models are often used, although their shortcomings are well-known. For instance, Cilingir and Madabhushi (2011a, 2011b) used a hardening non-associated elasto-plastic model (Mohr-Coulomb, *MC*) to study the effect of the frequency, amplitude, duration of the input motion, and depth on the dynamic behaviour of circular tunnels. Amorosi and Boldini (2009) studied the transverse

dynamic behaviour of tunnels in stiff and soft soils respectively adopting visco-elastic and *MC* models. The results underlined that soil plasticity produced a substantial modification of the loads acting in the lining, leading to permanent increments of both axial forces and bending moments. [Shen *et al.* \(2014\)](#) and [Wang *et al.* \(2019b\)](#) respectively adopted *MC* models for analyzing the failure mechanisms of a mountain tunnel that was damaged during the 2008 Wenchuan earthquake. [Patil *et al.* \(2018\)](#) and [Naseem *et al.* \(2020\)](#) also utilized the *MC* model to examine the influence of the tunnel shape on the lining forces.

On the other hand, sophisticated constitutive models are always preferred for tunnel seismic analysis since they reproduce more accurately the stress-strain behaviour of soils under various stress states. For instance, [Kontoe *et al.* \(2008\)](#) investigated the seismic damage of the Bolu tunnel using a two-surface kinematic hardening model. They compared the applicability of four soil constitutive models (modified Cam-clay with or without Rayleigh damping, modified Cam-clay coupled with a cyclic nonlinear, and the two-surface kinematic hardening model) for the same tunnel case ([Kontoe *et al.*, 2011](#)). The comparison highlighted the importance of the Rayleigh damping for a simple soil constitutive model. [Shahrour *et al.* \(2010\)](#) conducted a numerical analysis of the tunnel seismic response based on a cyclic elastoplastic constitutive soil model involving isotropic and kinematic hardening (*MODSOL* model). The results showed that the soil plasticity reduced the tunnel bending moments while the soil dilatancy had a moderate effect. [Zhuang *et al.* \(2019\)](#) adopted a visco-plastic memorial nested yield surface model to investigate the inter-story drift angle of underground structures considering different soil conditions and motion intensities. Utilizing a kinematic hardening model, [Cabangon *et al.* \(2019\)](#) underlined for the first time the importance of the initial structure of clay and its degradation in controlling the magnitude of the tunnel lining forces. [Kampas *et al.* \(2020\)](#) adopted the Hardening Soil model with small-strain stiffness to examine the seismic response of a horseshoe-shaped tunnel in cohesive and non-cohesive soils. They stated that the most conservative model regarding the tunnel seismic design would be considering a no-slip interface, zero soil cohesion, and negligible excavation-induced volume loss.

An important work regarding the soil constitutive model influence was the numerical Round Robin on Tunnel Tests (*RRTT*), organized by *TC204, ISSMGE* (Bilotta *et al.*, 2014). The predictive capacity of several numerical models with different levels of complexity was validated against centrifuge tests (Amorosi *et al.*, 2014; Conti *et al.*, 2014; Gomes, 2014; Hleibieh *et al.*, 2014; Tsinidis *et al.*, 2014). The comparison revealed that different constitutive models could provide a satisfactory agreement with experimental data in terms of ground acceleration responses but failed to reproduce permanent changes in lining forces. The simulations highlighted that sophisticated constitutive models were not always performing better than simplified ones, mainly due to the input parameter uncertainties (i.e., soil-tunnel interface, model calibration, and damping). The most severe drawback associated with sophisticated models is related to the larger number of required parameters, some of them cannot be determined from tests. All these models have their advantages and limitations; the utilization of models depends, to a large degree, on design purposes.

2.3.2.3 Soil-tunnel interface

One of the key issues regarding the soil-tunnel system is the contact between the tunnel lining and the soil. As mentioned previously, many simplified and analytical solutions assumed either a zero friction (i.e., full-slip condition) or a perfect bond between the tunnel and the surrounding soil (i.e., no-slip condition). However, the real interface condition is somewhere between the no-slip and full-slip for most of the cases. As suggested by many studies (Bobet, 2010; Kontoe *et al.*, 2014), the interface condition significantly affects the computed internal forces and, the axial forces in particular. A full-slip condition results in significantly lower axial forces and slightly larger bending moments. Oppositely, a no-slip condition predicts much larger axial forces and relatively smaller bending moments. Moreover, the soil-tunnel interface behaviour may affect the soil yielding response in the adjacent area to the tunnel (Tsinidis *et al.*, 2016b). As shown in Fig. 2.16, a more ‘rigid’ connection of the tunnel with the soil resulted in a higher constraint of the adjacent soil by the tunnel while a weaker interface increased deformations and strains of the adjacent soil.

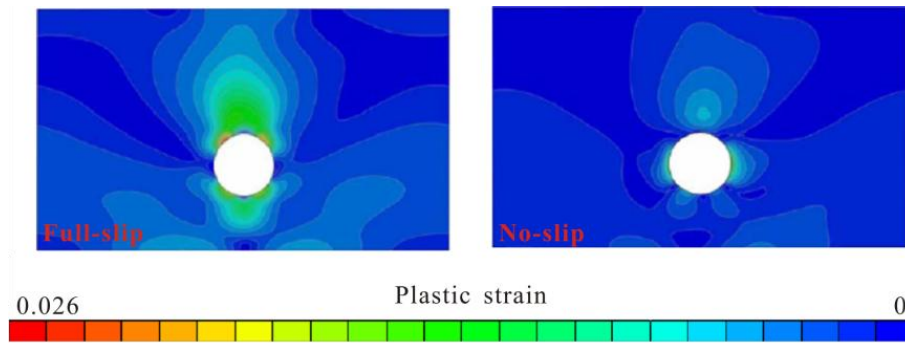


Fig. 2.16 Soil plastic strain around a flexible tunnel. (Tsinidis *et al.*, 2016).

The interface between the tunnel lining and the soil is generally simulated in two ways according to the numerical codes utilized. One is using the normal and tangential springs (i.e., *FLAC*), another one adopting a frictional coefficient (i.e., *ABAQUS*). It should be noted that the Mohr-Coulomb failure criterion is used to simulate the slippage and separation at the interface. In some numerical models, beam or liner elements were used to simulate the tunnel lining and were directly bonded to the nodes of the surrounding soil (no interface elements were utilized). Considering no soil/structure interface was acceptable for rock tunnels or weak ground motions since the *SSI* effect could be neglected (Hatzigeorgiou and Beskos, 2010; Kouretzis *et al.*, 2013; Sedarat *et al.*, 2009). The importance of the soil-tunnel interface was also highlighted in the *RRTT* campaign (Bilotta *et al.*, 2014). They demonstrated the necessity to conduct more experimental studies to properly qualify the interface friction property, which will permit to improve the numerical predictions against centrifuge test results. Since its important influence on the tunnel seismic response, a reliable estimation of the soil-tunnel interface response under seismic loads should be done.

2.3.2.4 Tunnel linings

Most previous studies regarding the tunnel seismic response focused on the elastic behavior of the tunnel lining and simulated it using a continuous beam or liner element (Amorosi and Boldini, 2009; Cilingir and Madabhushi, 2011a, 2011b; Kontoe *et al.*, 2008, 2011; Shahrour *et al.*, 2010; Tsinidis *et al.*, 2014; Zhuang *et al.*, 2019). Some authors have considered the tunnel lining nonlinearity, and a plastic-damage constitutive model was commonly utilized to

investigate the damage evolution and collapse of tunnels (Sun *et al.*, 2020a; Wang *et al.*, 2019b). A simple nonlinear structural model accounting for the stiffness degradation and ultimate capacity was employed, to obtain the fragility curves of tunnels for various site conditions and motion intensities (Argyroudis and Pitilakis, 2012; Nguyen *et al.*, 2019). Recently, Kampas *et al.* (2019) demonstrated how the structural modelling approach can affect the tunnel seismic response. In their study, three models of *RC* lining were assessed: (1) linear elastic using the section geometric stiffness, (2) linear elastic with a bending stiffness matching the uncracked stiffness, and (3) nonlinear model incorporating the stiffness degradation and ultimate capacity. An idealized elasticity approach can probably be appropriate for tunnels subjected to weak ground motions. The tunnel lining nonlinearity should be properly considered for strong ground motions, although it is not popular in the current analysis practices.

Another issue concerning the tunnel lining is the joints when a segmental lining is adopted. Case histories have demonstrated the good performance of the segmental tunnels during several seismic events (Hashash *et al.*, 2001). Therefore, the seismic behaviour of the segmental tunnels has only received limited attention. Yu *et al.* (2013a, 2013b) performed a 3D *FE* dynamic analysis on the seismic behaviour of a long tunnel incorporating the tunnel joints (Fig. 2.17). Their study revealed that the presence of flexible joints could decrease the stresses on the tunnel lining by 17% due to the flexibility of joints which allowed axial and curvature deformations and dissipate more energy.

Do *et al.* (2015b) stated that the presence of joints generally decreased the lining forces in terms of axial forces and bending moments, depending on the joint's number, location, stiffness, and tunnel radius. Lower seismic demand of the segmental lining compared to the continuous lining was also reported by other researchers (Fabozzi and Bilotta, 2016; Wang *et al.*, 2019a). However, it should be noted that the relative rotation between segments occurred at the end of shaking, suggesting a permanent loss of water-tightness of the lining (Fabozzi and Bilotta, 2016; Yu *et al.*, 2013b). Hence, the seismic design of a segmental lining requires careful consideration. More researches on the seismic analysis and design of segmental

tunnels are required since they are nowadays frequently constructed in seismic prone areas.

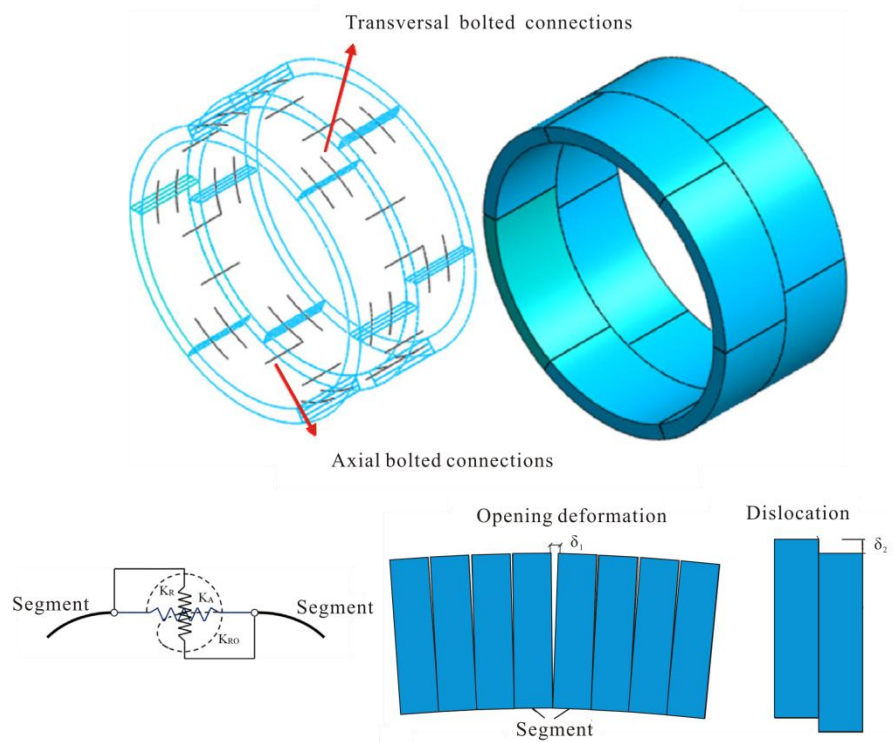


Fig. 2.17 Schematic representation of the segmental tunnel, joint connection scheme, opening deformation, and dislocation. (Yu *et al.*, 2013b; Do *et al.*, 2015b; Wang *et al.*, 2019a).

2.4 Probabilistic models

In this section, the basic theoretical framework of the adopted probabilistic analysis (i.e., uncertainty quantification) and, an overview of the probabilistic analysis of tunnels under static and seismic conditions are presented. Besides, the statistical parameters of some geotechnical properties utilized in the literature are summarized.

2.4.1 Uncertainty quantification

The probabilistic analysis aims at quantifying the input parameters uncertainties effects on the system outputs. An uncertainty quantification requires generally three aspects: the source and scale of uncertainty inputs, a computational model, and the uncertainty propagation process

(Lataniotis *et al.*, 2018a), as schematically illustrated in Fig. 2.18.

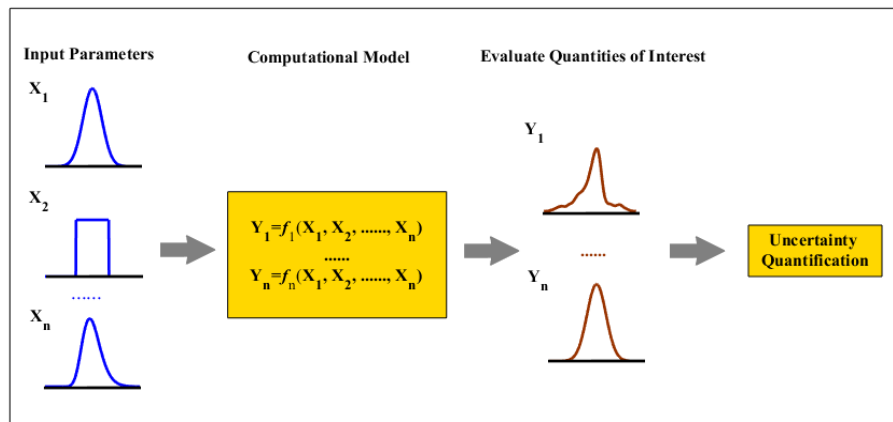


Fig. 2.18 Theoretical framework of uncertainty quantification.

The identification and modelling of the uncertainty sources are the crucial steps for the solution of any uncertainty quantification problems. There are three basic sources of uncertainties for the seismic analysis and design of tunnels:

- Specification of seismic ground motions.
- Uncertainty of material parameters.
- Selection of the seismic analysis and design methods.

In this thesis, the variability in the tunnel seismic response is quantified considering only the uncertainty of the geotechnical parameters. It should be emphasized here that in any probabilistic analysis, it is necessary to identify and quantify the uncertainty sources using the collected data or expert judgment. Although this step is extremely important for the site-specific analysis, it will be not considered in this thesis. The statistical parameters of the soil properties used in the analysis are taken from the literature.

After having properly quantified the uncertainties of the input parameters, the next step is to quantify their influences on the model output through a computational model. The computational model can be an analytic function, a simplified method, or a numerical model that will propagate a set of input parameters to a set of output quantities of interest. In the

geotechnical engineering field, simplified methods such as the limit analysis method were widely applied to evaluate the geo-structures stability (i.e., slope, embankment, tunnel face) in random soils since they permitted to obtain accurate results with lower computational costs (Pan and Dias, 2017, 2018). While for more complex physical phenomena, e.g., the seismic response of tunnels here, which cannot be investigated precisely by simplified methods, advanced numerical models (e.g. finite difference or finite element schemes) are necessary. In this thesis, a dynamic time-history analysis will be used.

The quantities of interest of a probabilistic response can either be the mean value and variance of the model response, or the probability of exceedance of a prescribed threshold (i.e., probability of failure). Historically, the Monte Carlo simulation can be employed to solve these problems. It is a very efficient tool but it usually requires a high number of deterministic calculations. Its computational cost may be unaffordable if the study aims to estimate small failure probabilities in the range between 10^{-3} and 10^{-5} since massive time-consuming will be needed. Under this circumstance, meta-modelling techniques, e.g., Polynomial Chaos Expansion, Kriging, Support Vector Machines, are promising ways in which computational expensive models can be substituted by inexpensive surrogate models (Mollon *et al.*, 2009, 2013; Pan and Dias, 2017). Therefore, Monte Carlo simulation is generally used as a means to get a reference solution or to calculate the mean value and variance of the model response.

The uncertainty quantification performed in this thesis is based on simulation-based techniques, utilizing two probabilistic methods. The Sparse Polynomial Chaos Expansion combined with the global sensitivity analysis is adopted for identifying the key variables that have the most or least influence on the tunnel seismic response. Then, in the framework of the Monte Carlo simulation, the statistical moments (mean, variance, coefficient of variation) of tunnel seismic response will be investigated.

2.4.2 Probabilistic analysis of tunnels under static conditions

So far, the probabilistic analysis of tunnels focuses mainly on the stability of tunnels (i.e., lining structure, tunnel face) under static conditions. For instance, [Schweiger *et al.* \(2001\)](#) presented a reliability analysis of a tunnel by combining probabilistic concepts and deterministic finite element methods. In their study, the internal friction angle (φ), cohesion (c), and Young's modulus (E) were considered as random variables with a lognormal distribution. A design chart for optimizing the lining thickness at a given probability of failure was provided. [Goh and Kulhawy \(2003\)](#) suggested a back-propagation neural network algorithm to develop a mathematical expression relating to the input and output variables. Then they used this method to investigate the vertical displacement of an existing tunnel in random soils. [Emeriault *et al.* \(2004\)](#) quantified the uncertainty of geotechnical parameters using the collected data from the Lyon subway site. The results underlined that not only the measurement errors but also the expert judgment significantly contributed to the uncertainty of the urban soil parameters. Therefore, a risk-oriented analysis was suggested to account for the uncertainties affecting tunnel design.

[Mollon *et al.* \(2009, 2011\)](#) presented a comprehensive investigation into the tunnel face stability considering the uncertainty of the soil shear strength parameters (c and φ). For the probability distribution of the random variables, c and φ were respectively considered as normal and non-normal variables. The negative correlation between the two variables ($\rho_{c,\varphi}=-0.5$) was also considered. The main conclusions included:

- The assumption of a negative correlation between the c and φ induced higher stability of the tunnel face.
- The normal distribution predicted a greater failure probability relative to non-normal distribution.
- The failure probability was much more influenced by the coefficient of variation of φ than that of c .

Following this study, the tunnel face stability problem was broadly investigated for various uncertainty scenarios, utilizing different probabilistic methods ([Li and Yang, 2018](#); [Pan and](#)

Dias, 2017, 2018).

Li and Low (2010) confirmed some of the above findings in their reliability analysis considering a circular tunnel under a hydrostatic stress field. In addition to normal and lognormal distributions, beta distributions were also adopted to characterize the uncertainty of the c , φ , and E . They stated that a beta distribution was able to predict an equivalent reliability index with a normal distribution, but both were lower than the lognormal distribution one. Song *et al.* (2011) showed that the deformations and plastic zones around a tunnel increased as the geotechnical property uncertainty increased. A higher tunnel face pressure was then necessary to remain the system at the stability. The results demonstrated that the parameter E had the most influence on the tunnel inward deformation in comparison with the c , and φ influences.

Cai (2011) proposed the probability density distributions of rock properties using field data. Then they utilized the proposed probability input models, to analyze the deformations of a rock tunnel. Lv *et al.* (2011, 2013, 2017a) investigated the influence of the rock properties uncertainty on the failure probability of circular tunnels considering the plastic zones and deformations. The methods used in their analysis were the first order and the second order reliability method (*FORM*, *SORM*), artificial neural network, quadratic polynomial chaos expansion, moving least squares response surface method, and Monte Carlo Simulation method. The uniform design and Latin hypercube sampling methods were used for the generation of the input variables. Their studies highlighted the limitations of the simple reliability methods such as *FORM*, *SORM* for complicated and nonlinear systems in which the limit state functions cannot be explicitly represented in terms of random variables. In such cases, a meta-modelling technique was recommended to construct performance functions (Li *et al.*, 2014).

Tiwari *et al.* (2017) considered the uncertainty in both the peak and residual shear strength to predict the tunnel deformations. They stated that the predicted displacements were matching well with the measured deformations whereas underestimated displacements appeared when

the residual strength uncertainty was ignored. Then, an optimization support design was proposed using the probabilistic analysis method (Tiwari *et al.*, 2018). Kroetz *et al.* (2018) performed a reliability-based tunnel lining design considering uncertain soil properties, using different reliability algorithms, e.g., *FORM*, Important sampling, Subset simulation, and Monte Carlo simulation. Recently, Hamrouni *et al.* (2019) adopted a genetic algorithm optimized surface response method to investigate the relationship between the stress relief and tunnel reliability index. The study demonstrated that increasing the stress relief reduced the ground settlement-based reliability index whereas increased the lining force-based one.

Table 2.1 Statistical parameters of the soil property used for tunnel static analysis.

| Author | c | φ | E | Ground |
|-----------------------------------|---------------------------------------|--------------------------------------|---------------------------------------|-----------|
| Schweiger <i>et al.</i> (2001) | 33.3%, <i>LN</i> | 9.5%, <i>LN</i> | 33.3%, <i>LN</i> | Soil |
| | 18.75%, <i>LN</i> | 6.8%, <i>LN</i> | 15.6%, <i>LN</i> | Rock |
| | 16.65%, <i>LN</i> | 5%, <i>LN</i> | 16.7%, <i>LN</i> | Weak rock |
| Goh and Kulhawy (2003) | - | - | 15%, 6.7%, <i>N</i> | Soil |
| Emeriault <i>et al.</i> (2004) | - | - | 35% ^{<i>a</i>} | Soil |
| | - | - | 8.2% ^{<i>a</i>} | Soil |
| Mollon <i>et al.</i> (2009, 2011) | 20%, <i>N</i> , <i>LN</i> | 10%, <i>N</i> , β | 15%, <i>N</i> , <i>LN</i> | Soil |
| Li and Low (2010) | 29.6%, <i>N</i> , <i>LN</i> , β | 5.7%, <i>N</i> , <i>LN</i> , β | 12.9%, <i>N</i> , <i>LN</i> , β | Rock |
| Song <i>et al.</i> (2011) | 10%~40%, <i>N</i> | 10%~40%, <i>N</i> | 10%~40%, <i>N</i> | Rock |
| Lv <i>et al.</i> (2011) | 13.2%, <i>N</i> , <i>LN</i> , β | 9.7%, <i>N</i> , <i>LN</i> , β | 12.9%, <i>N</i> , <i>LN</i> , β | Rock |
| Cai (2011) | 25.1%, <i>W</i> , <i>N</i> | 4.7%, <i>W</i> , <i>N</i> | 16.5%, <i>N</i> | Rock |
| Li <i>et al.</i> (2014) | - | - | 15%, <i>LN</i> | Rock |
| Tiwari <i>et al.</i> (2017, 2018) | - | - | 13.5%~20.96%, <i>LN</i> | Rock |
| Pan and Dias (2017) | 20%, <i>LN</i> | 10%, <i>LN</i> | | Soil |
| Chakraborty and Majumder (2018) | 30%, <i>LN</i> | 24%, <i>UN</i> | 15%, <i>LN</i> | Rock |
| Gong <i>et al.</i> (2018) | 33%, <i>LN</i> | 10%, <i>LN</i> | - | Soil |
| Kroetz <i>et al.</i> (2018) | 20%, <i>LN</i> | 20%, β | 15%, <i>LN</i> | Soil |
| Hamrouni <i>et al.</i> (2019) | - | - | 15%, <i>N</i> , <i>LN</i> | Soil |

Note: *N*=normal distribution; *LN*=lognormal distribution; *UN*=Uniform distribution; *W*= Weibull distribution; β = Beta distribution; *a* =unknown distribution type.

In summary, the tunnel face stability and lining structure stability are the two main subjects of the previous studies regarding the tunnel probabilistic analysis. For the tunnel face stability, authors aimed to estimate the face collapse or the blow-out failure modes of different ultimate limit states and eventually, to provide a rational support pressure for a target failure

probability. For the lining stability, the objectives are to estimate the lining failure probability for a specific uncertainty scenario and to provide an optimization design of a tunnel (i.e., lining thickness, bolt length, support location) for different target failure probabilities. These analyses generally consider the uncertainty of the c , φ , and E , considering different coefficients of variation (COV) and distribution types. The adopted parameters of the presented studies are summarized in Table 2.1. Other parameters such as density (ρ), Poisson's ratio (ν_s) were commonly assumed as constants due to their low variation level or insignificant influence on the tunnel response (Phoon and Kulhawy, 1999).

2.4.3 Probabilistic analysis of tunnels under seismic conditions

Traditionally, seismic analysis and design of tunnels are based on deterministic methods considering only the average or mean soil properties, probabilistic tunnel seismic responses were thus rarely investigated. Karakostas and Manolis (2000, 2002) presented the first investigation, on the dynamic response of an unlined tunnel in random elastic soils subjected to P and SH waves using a stochastic boundary element method. In their studies, the wave velocity was considered as a normally distributed random variable. Recently, probabilistic analyses were performed to assess the influence of the soil spring stiffness (k_{soil}) uncertainty on the eigenfrequency values of a buried pipeline (Manolis *et al.*, 2020). The random k_{soil} was characterized using uniform, normal, and lognormal distributions respectively.

Nedjar *et al.* (2007) investigated the randomness effects of two parameters (i.e., k_{soil} , and density ρ) on a pipeline bending stress and relative deformation responses. Their results indicated that the k_{soil} had a more pronounced influence on the computed response, while the mass influence was secondary. Also, an additional bending stress was induced due to the heterogeneity of soil property in the pipeline axial direction. Liu and Li (2008) investigated the stochastic seismic response of corroded pipelines based on the Markov process. They defined the corrosion percentage as a random variable. Yue and Ang (2016, 2017) studied the spatial variation effect of the elastic modulus on the rock tunnel reliability using the probability density evolution method, considering two- and three-dimensional numerical

models. They stated that the results obtained with a deterministic analysis using the mean values were usually higher than considering the random variation of the soil. Based on the target reliability, the thickness of the concrete lining was recommended for the tunnel design.

Chen et al. (2017) conducted a stochastic seismic performance of an immersed tunnel. They concluded that the elastic modulus variation has a minor influence on the bending moments, whereas it could increase the axial forces sharply. Assuming that the variable followed a lognormal distribution, Zhang and Liu (2020) performed a random finite element analysis to investigate the influence of the shear modulus uncertainty (as well as the spatial variability, random field method was utilized) on the seismic-induced internal forces of a rectangular tunnel. They found the maximum lateral deformation was significantly influenced by the randomness soil stiffness, where the maximum difference in the lateral deformation response between the deterministic and probabilistic analyses was approximately equal to 60%.

Table 2.2 Statistical parameters of the soil property used for tunnel seismic analysis.

| Author | G | ρ | V_s | Ground |
|-------------------------------------|-------------------------------|----------------|----------|--------|
| Karakostas and Manolis (2000, 2002) | | | 32%, N | Rock |
| Nedjar et al. (2007) | | 10%~100%, LN | | Soil |
| Yue and Ang (2016, 2017) | 23% ^{<i>b</i>} , N | | | Rock |
| Chen et al. (2017) | 20% ^{<i>c</i>} , N | | | Soil |
| Zhang and Liu (2020) | 30%, LN | | | Soil |

Note: *b*=estimated value according to 3σ rule; *c* =determined according to the *COV* of the *E*.

In summary, the most commonly utilized variables in the tunnel seismic analysis are the soil stiffness-related parameters. The *COV* and the corresponding distribution types are summarized in Table 2.2. The literature review has demonstrated that the stochastic seismic response of tunnels considering uncertain soil properties is still very limited. The common limitations of previous studies are associated with:

- The application of a linear constitutive soil model.
- The small number of random soil parameters considered.
- The uncertainty of parameter characterization considering only one distribution type.

- The limited uncertainty scenarios consideration.
- The insufficient studies on the statistical characteristics of the tunnel deformations.

To address these limitations, this thesis will consider dynamic time-history analyses to quantify the variability of seismic-induced tunnel deformations.

2.5 Conclusion

Various determination methods are reviewed in this chapter for overcoming the frequency-dependent of the Rayleigh damping. They are historically based on the site fundamental frequency in combination with a simplified damping formulation, which may lead to a significant underestimation of the response in the case of deep soils and high frequency ground motions. To relieve the adverse influence of the misuse of the Rayleigh damping, a full Rayleigh damping formulation accounting for the site high modes or ground motion characteristics is recommended.

Then, two kinds of quasi-static analyses are briefly described, namely the deformation-based and force-based quasi-static numerical methods. They permit to provide a quick and easy calculation of the seismic design loads in the tunnel lining. Furthermore, the soil-tunnel interaction can be implicitly considered through empirical $R-F$ relationships or be explicitly incorporated in a numerical model by a series of interface springs. However, the quasi-static method has some pitfalls, thus the numerical models should be properly prepared.

A literature review on the dynamic time-history analyses of tunnels is presented. Dynamic time-history analyses can effectively address several limitations of the quasi-static analysis, e.g., inertial interaction, wave effects. On the other hand, they require careful consideration of the input ground motions, soil constitutive models, soil-tunnel interface behaviour and, tunnel lining constitutive models.

Finally, the probabilistic analyses of tunnels under both static and seismic conditions have been reviewed. They aim to estimate the mean or variance of the model response or, to

compute the failure probability of a rare event. For the tunnel stability problem, the soil shear strength parameters are commonly considered as uncertain parameters while for the tunnel seismic analysis, the soil stiffness-related parameters are the uncertain ones. Various simulation techniques such as Monte Carlo simulation, and Sparse Polynomial Chaos Expansion (*SPCE*), can be utilized to propagate the uncertainty from the input variables to the model outputs. These two techniques will be used in this thesis to characterize the statistical characteristics of the tunnel seismic response, as well as to compute the *SPCE*-based Sobol indices that identify the contribution of each uncertain parameter in the variability of the model response.

Chapter 3

Rayleigh damping in nonlinear numerical models

3.1 Introduction

There are two sources of soil damping in nonlinear seismic analyses of tunnels. The first one is the frequency-independent hysteretic damping associated with the area bounded by stress-strain loops, which strongly depends on the soil constitutive model and the level of nonlinearity. The second one is the viscous damping that captures the soil damping at very small strains. When a simple elasto-plastic model (like linear elasticity with perfect plasticity) is adopted, it generally induces no energy dissipation at small strains. The full or the simplified Rayleigh damping models are commonly utilized to provide additional damping or to remain numerical stability.

However, Rayleigh damping can lead to an overdamping or an underdamping of the wave propagation due to its frequency-dependent. It further could result in substantial differences in the seismic responses of structures (Priestley and Grant, 2005). The negative effects caused by the improper use of the Rayleigh damping in time-history analyses, revealing the need for a reasonable determination of the damping models. To circumvent this issue, several practical methods are suggested to select the frequency interval so that the damping can approximately remain constant in the frequency range of interest.

There is no consensus regarding the best approach for determining the Rayleigh damping parameters in seismic analyses of tunnels. The users have then to determine the damping

parameters with a certain degree of arbitrariness and consequently, it can affect the numerical predictions and sometimes lead to erroneous results. Although the use of Rayleigh damping is common in numerical models, the influences of different damping models on tunnel seismic response are till now not well known. This chapter investigates the variability in the tunnel seismic behaviour (i.e., axial forces) caused by the use of different damping determination methods through a nonlinear time-history analysis. The commonly used five approaches are compared, considering a variety of cases including different ground motions, nonlinearity levels, and target damping ratios.

3.2 Methods

3.2.1 Damping determination approaches

The full Rayleigh damping formulation is adopted here, as shown in Fig. 2.3. The main issues in applying Rayleigh damping are the selection of the appropriate target viscous damping ratio ξ_{tar} , and of the frequency interval $[f_1, f_2]$. Concerning the value of ξ_{tar} , previous studies generally adopted a small damping ratio ranges from 1% to 5%. Higher or lower damping ratios were also utilized according to the soil constitutive models, input ground motions (Bilotta *et al.*, 2014; Kontoe *et al.*, 2011). In this work, ξ_{tar} ratio is assumed to vary from 0.2% to 10%, to cover a variety of cases.

Consistent with the previous studies, the site fundamental frequency (SF) is taken as the first matching frequency f_1 while the values of f_2 , are determined by five approaches, including:

- M1: the site fundamental frequency (SF).
- M2: the five times the site fundamental frequency ($5SF$).
- M3: the predominant frequency of ground motions (PF).
- M4: the mean frequency of ground motion (MF).
- M5: the n times the site fundamental frequency with n being the smallest odd integer larger than the ratio of PF/SF .

The details of these approaches can be found in Chapter 2.

3.2.2 Input ground motions

To consider the influence of ground motion characteristics and motion intensities, 50 ground motions are adopted in this work. These records are obtained from the NGA-West 2 Ground-Motion Database using the following search criteria: the magnitude ranges from 5 to 9, fault distance varies from 2 to 200 km, rupture distance changes from 2 to 500 km, and the soil shear wave velocity (at the top 30 m) ranges from 500 to 1500 m/s. The detailed information of these records is presented in Table. A.1 (see Appendix A). Furthermore, the seismic records are grouped into two categories based on the predominant frequency of ground motions. For Group A, it contains 17 ground motions that have rich high frequency components, and the corresponding PFs are less than 0.23 s. The left 33 ground motions belong to Group B and have relatively large PFs (>0.23 s). In general, Group B has a larger spectral acceleration (S_a), as shown in Fig. 3.1.

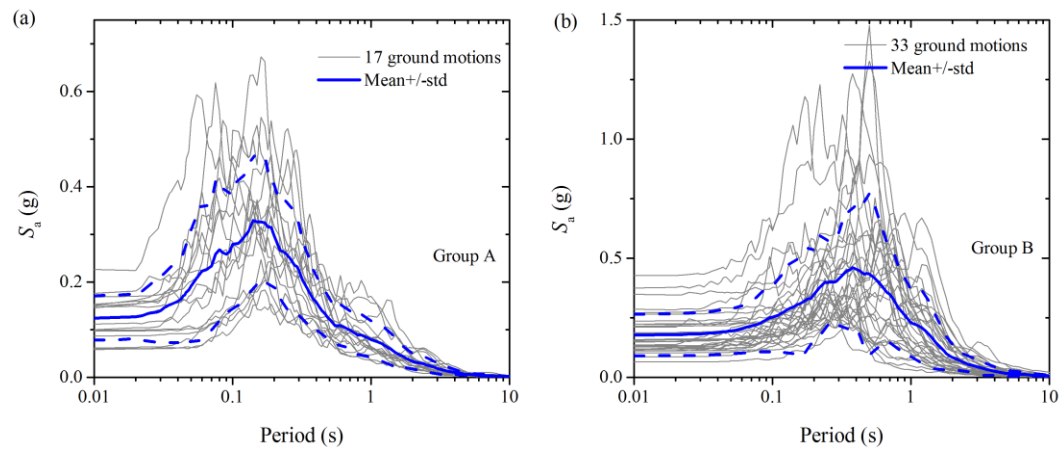


Fig. 3.1 Spectral accelerations of input motions for Group A and Group B.

3.2.3 Two-dimensional numerical modelling

The Bologna-Florence high-speed railway tunnel project in Italy is adopted as the reference case. This project is part of the Italian high-speed railway network. Some works have been recently performed to investigate the internal forces and stability of this tunnel during the construction and operation stages (Croce, 2011; Do *et al.*, 2014).

Fig. 3.2 shows the two-dimensional numerical model using the *FLAC* finite difference element code (Itasca, 2011). It is assumed that the behaviour of the tunnel lining is linear-elastic and the behaviour of the surrounding soil is simulated with an elastic-perfectly plastic constitutive model following the Mohr-Coulomb (*MC*) failure criterion. This criterion is frequently used in the nonlinear seismic analyses of tunnels, as demonstrated in Chapter 2. Parameters of the tunnel support and the soil adopted in this study are taken from the literature (Do *et al.*, 2014), as presented in Table 3.1.

Table 3.1 Properties of the soil and tunnel lining (Croce, 2011; Do *et al.*, 2014).

| Parameters | Symbol | Value | Unit |
|--|---------|--------|----------|
| <i>Properties of the clayey sand</i> | | | |
| Unit weight | ρ | 17 | kN/m^3 |
| Initial Young's modulus | E_s | 150 | MPa |
| Poisson's ratio | ν_s | 0.3 | - |
| Internal friction angle | ϕ | 37 | $^\circ$ |
| Dilatancy angle | ϕ | 0 | $^\circ$ |
| Cohesion | c | 5 | kPa |
| Lateral earth pressure factor | K_0 | 0.5 | - |
| Depth | H | 20 | m |
| <i>Properties of the tunnel lining</i> | | | |
| Young's modulus | E_l | 35,000 | MPa |
| Poisson's ratio | ν_l | 0.15 | - |
| Lining thickness | t | 0.4 | m |
| External diameter | D | 9.1 | m |

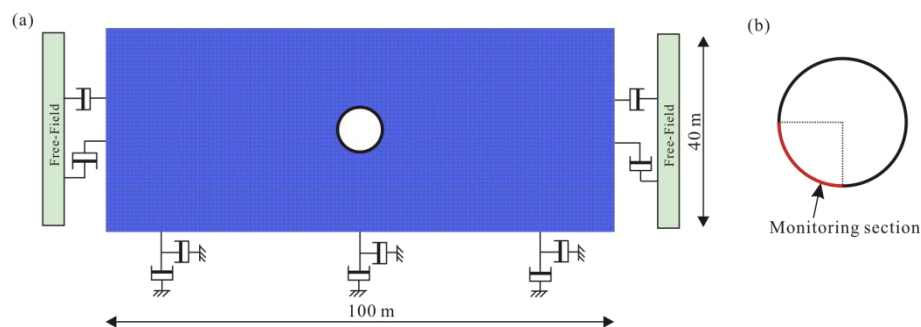


Fig. 3.2 Two-dimensional numerical model.

A necessary step in both static and dynamic numerical analyses is to determine the model boundary dimensions. The results obtained from the sensitivity analysis indicate that a numerical model width of 100 m is sufficient to avoid the boundary effects, as shown in Fig.

3.2. Finally, the model has a height of 40 m and a width of 100 m. The mesh size of 0.8×0.8 m is determined according to the well-known equations of [Kuhlemeyer and Lysmer \(1976\)](#). Concerning the soil-tunnel interface, the relative movement and separation between the soil and the tunnel are not allowed to simulate the most unfavourable axial force scenarios.

Before all the seismic analysis, a static analysis is conducted to determine the initial state of stresses. For the static analysis, both the horizontal and vertical displacements are restricted along the model bottom while horizontal displacements are restricted along the lateral boundaries. For the dynamic analysis, the free field boundaries are applied along the lateral boundaries to properly absorb the outward waves while and a quiet boundary is applied at the base of the model to simulate the elastic bedrock. For a single ground motion, the acceleration amplitude is scaled from 0.1 to 0.5 g to consider different soil nonlinearity levels (i.e., hysteretic damping levels). After high frequency (15 Hz) cutoff and baseline correction, the scaled acceleration time-history is integrated into the velocity time-history and then is transformed into a shear stress time-history (to match the model base condition). It is applied at the model base considering the vertical propagation of the ground motion.

Table 3.2 shows the values of f_2 calculated based on different methods and ground motion characteristics. In total, 1250 time-history analyses are performed to investigate the influence of Rayleigh damping models on the maximum seismic induced axial force acting on the tunnel lining (the studied lining section is shown in Fig. 3.2b). Similar findings observed for the bending moments and the tunnel deformations are not presented for the sake of brevity.

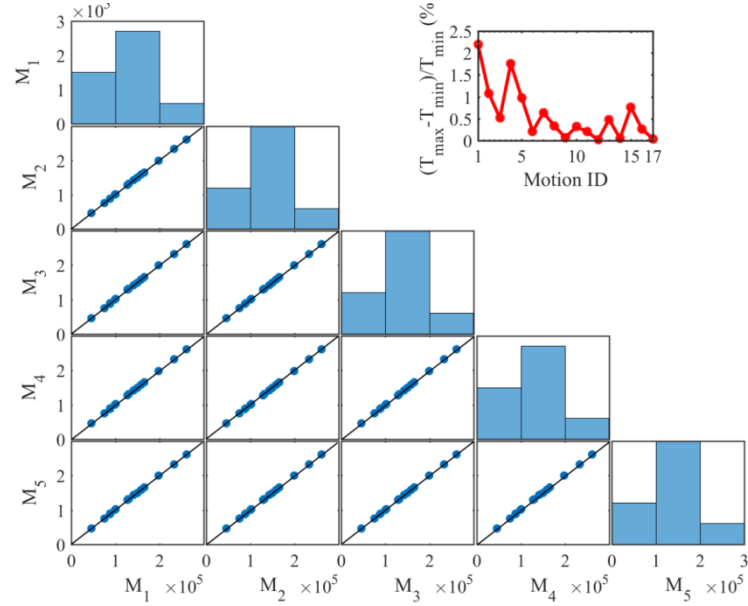
Table 3.2 The values of f_2 calculated by five damping determination approaches.

| <i>ID</i> | Group A | | | | | Group B | | | | |
|-----------|-------------------|--------------------|-------------------|-------------------|-----------------------|-------------------|--------------------|-------------------|-------------------|-----------------------|
| | <i>SF</i> (Hz) | <i>SSF</i> (Hz) | <i>PF</i> (Hz) | <i>MF</i> (Hz) | <i>nPF/SF</i> (Hz) | <i>SF</i> (Hz) | <i>SSF</i> (Hz) | <i>PF</i> (Hz) | <i>MF</i> (Hz) | <i>nPF/SF</i> (Hz) |
| 1 | 1.13 | 5.65 | 7.14 | 4.0 | 7.91 | 1.13 | 5.65 | 1.47 | 1.37 | 3.39 |
| 2 | 1.13 | 5.65 | 7.14 | 4.18 | 7.91 | 1.13 | 5.65 | 2.63 | 1.57 | 3.39 |
| 3 | 1.13 | 5.65 | 6.25 | 2.03 | 7.91 | 1.13 | 5.65 | 2.78 | 1.34 | 3.39 |
| 4 | 1.13 | 5.65 | 10.0 | 4.72 | 10.17 | 1.13 | 5.65 | 1.67 | 1.22 | 3.39 |
| 5 | 1.13 | 5.65 | 5.0 | 2.72 | 5.65 | 1.13 | 5.65 | 1.11 | 1.03 | 1.13 |
| 6 | 1.13 | 5.65 | 12.5 | 3.19 | 14.69 | 1.13 | 5.65 | 2.78 | 1.51 | 3.39 |
| 7 | 1.13 | 5.65 | 6.25 | 2.19 | 7.91 | 1.13 | 5.65 | 3.57 | 1.13 | 5.65 |
| 8 | 1.13 | 5.65 | 6.25 | 1.07 | 7.91 | 1.13 | 5.65 | 2.08 | 1.32 | 3.39 |
| 9 | 1.13 | 5.65 | 6.25 | 3.44 | 7.91 | 1.13 | 5.65 | 3.13 | 2.02 | 3.39 |
| 10 | 1.13 | 5.65 | 12.5 | 4.81 | 14.69 | 1.13 | 5.65 | 1.43 | 1.49 | 3.39 |
| 11 | 1.13 | 5.65 | 12.5 | 4.48 | 14.69 | 1.13 | 5.65 | 4.17 | 1.61 | 5.65 |
| 12 | 1.13 | 5.65 | 4.55 | 1.81 | 5.65 | 1.13 | 5.65 | 2.38 | 1.96 | 3.39 |
| 13 | 1.13 | 5.65 | 8.33 | 2.90 | 10.17 | 1.13 | 5.65 | 2.63 | 2.26 | 3.39 |
| 14 | 1.13 | 5.65 | 6.25 | 1.27 | 7.91 | 1.13 | 5.65 | 4.55 | 1.60 | 5.65 |
| 15 | 1.13 | 5.65 | 12.5 | 2.02 | 14.69 | 1.13 | 5.65 | 2.38 | 2.46 | 3.39 |
| 16 | 1.13 | 5.65 | 10.0 | 2.02 | 10.17 | 1.13 | 5.65 | 1.35 | 1.30 | 3.39 |
| 17 | 1.13 | 5.65 | 8.33 | 2.58 | 10.17 | 1.13 | 5.65 | 2.38 | 2.07 | 3.39 |
| 18 | | | | | | 1.13 | 5.65 | 2.27 | 1.31 | 3.39 |
| 19 | | | | | | 1.13 | 5.65 | 1.85 | 1.74 | 3.39 |
| 20 | | | | | | 1.13 | 5.65 | 1.79 | 1.58 | 3.39 |
| 21 | | | | | | 1.13 | 5.65 | 2.63 | 1.15 | 3.39 |
| 22 | | | | | | 1.13 | 5.65 | 2.63 | 2.02 | 3.39 |
| 23 | | | | | | 1.13 | 5.65 | 1.72 | 1.28 | 3.39 |
| 24 | | | | | | 1.13 | 5.65 | 2.63 | 1.68 | 3.39 |
| 25 | | | | | | 1.13 | 5.65 | 1.92 | 1.91 | 3.39 |
| 26 | | | | | | 1.13 | 5.65 | 3.85 | 2.87 | 5.65 |
| 27 | | | | | | 1.13 | 5.65 | 4.17 | 2.75 | 5.65 |
| 28 | | | | | | 1.13 | 5.65 | 4.17 | 2.19 | 5.65 |
| 29 | | | | | | 1.13 | 5.65 | 3.85 | 2.10 | 5.65 |
| 30 | | | | | | 1.13 | 5.65 | 2.63 | 3.33 | 3.39 |
| 31 | | | | | | 1.13 | 5.65 | 3.57 | 2.34 | 5.65 |
| 32 | | | | | | 1.13 | 5.65 | 3.85 | 2.05 | 5.65 |
| 33 | | | | | | 1.13 | 5.65 | 2.78 | 2.6 | 3.39 |

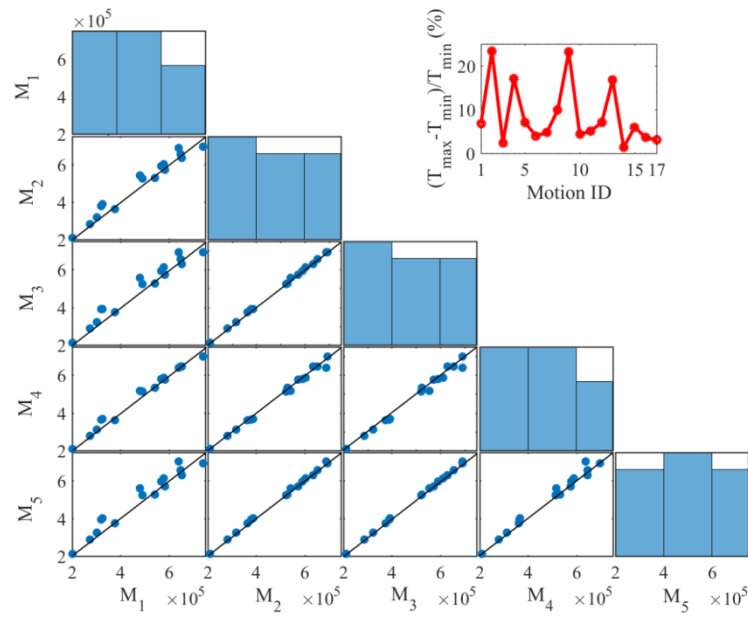
3.3 Numerical results

In this section, representative results of the tunnel seismic response analyses for different damping determination approaches and target damping ratios, including the: (1) seismic axial

force increments T , (2) normalized T , and (3) variation of the T , are thoroughly presented and discussed.



(a) $PGA=0.1$ g, $\zeta_{tar}=0.2\%$, Group A



(b) $PGA=0.5$ g, $\zeta_{tar}=10\%$, Group A

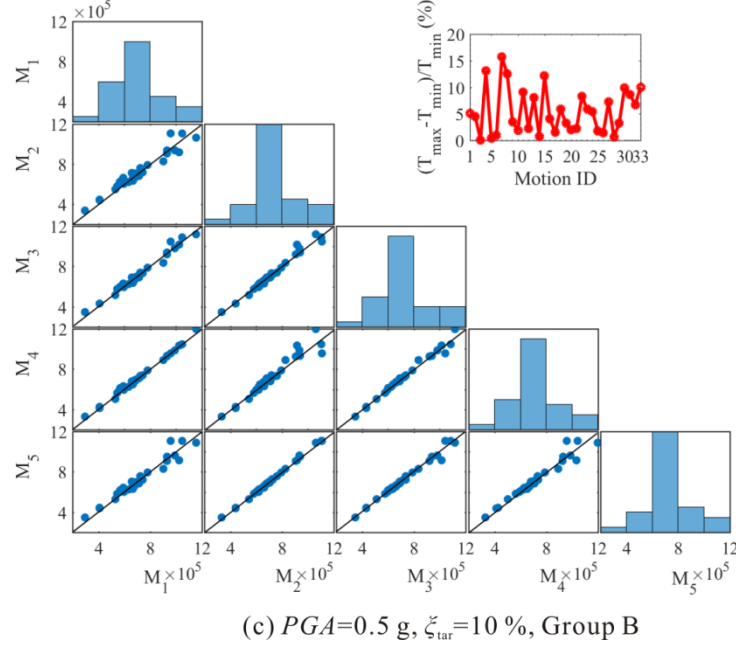


Fig. 3.3 Comparison of the seismic axial force increments calculated by different damping models: (a) $PGA=0.1$ g, $\zeta_{tar}=0.2\%$, Group A; (b) $PGA=0.5$ g, $\zeta_{tar}=10\%$, Group A; and (c) $PGA=0.5$ g, $\zeta_{tar}=10\%$, Group B.

Fig. 3.3 compares the seismic axial force increments computed by five damping determination approaches. These results correspond to $PGA=0.1$ g, $\zeta_{tar}=0.2\%$, Group A, and $PGA=0.5$ g, $\zeta_{tar}=10\%$, Groups A and B. For a given ground motion, the maximum relative difference of the axial force between five approaches is also calculated, as presented in the subplots. Fig. 3.3a demonstrates that different approaches compute almost the same results, with the largest relative difference of around 2%. When large target damping ratio and motion intensity are considered, an obvious difference (around 25%) of the calculated axial force appears. In general, using the site fundamental frequency only (i.e., M1) tends to underestimate almost all the responses, as shown in Fig. 3.3b. It is not surprising because this method produces a high damping ratio in the high frequency range, and shows a significant influence on the high frequency ground motions in particular. For the case considered, methods M2, M3, and M5 predict similar results. This is due to the relatively larger values of f_2 for these three methods (see Table 3.2). However, the results of using MF (i.e., M4) to determine the Rayleigh damping do not match the other four approaches very well. This is due to the calculated f_2 value by this method is quite different from other methods, especially for ground motions with the great difference between the PF and MF (i.e., the ratios of PF to MF are greater than 2 for most ground motions in Group A, Table 3.2). It should be noted that

the underestimation or overestimation is concluded based on the calculated tunnel axial forces of different methods, since the real response of this tunnel is not available (i.e., no experimental results to make a comparison).

However, the relationships between different methods become unclear for Group B, as shown in Fig. 3.3c. Overall, each method appears to have the probability to calculate the largest axial force. For instance, M1 (*SF* only) conceptually underestimates the response, but it appears to overestimate the response for some ground motions in comparison with other approaches. This could be attributed to high damping that may inhibit soil yielding. When plastic failure occurs, some energy may be dissipated through the hysteretic damping. Recent works have revealed that soil plasticity could modify the internal force distributions and tend to reduce the internal forces (Amorosi and Boldini, 2009; Shahrour *et al.*, 2010). In comparison with Fig. 3.3b, the significant effect of the input motions on the selection of a proper damping method is underlined. As a summary, it is difficult to get a general conclusion regarding which damping determination method predicts the conservative results for some cases. It is related to the target damping ratio, ground motion intensity, and ground motion characteristic.

To quantify the influence of the target damping ratio on the calculated axial forces, a dimensionless parameter, $T/T_{0.2}$, is introduced. It is the ratio of the seismic axial force increment at the specific ξ_{tar} compared to the one in the case of $\xi_{tar}=0.2\%$, for a given ground motion and damping determination approach. Thus, for each ξ_{tar} ratio, there are respectively 165 (33 ground motions \times 5 methods) and 85 (17 ground motions \times 5 methods) normalized values for Group B and Group A.

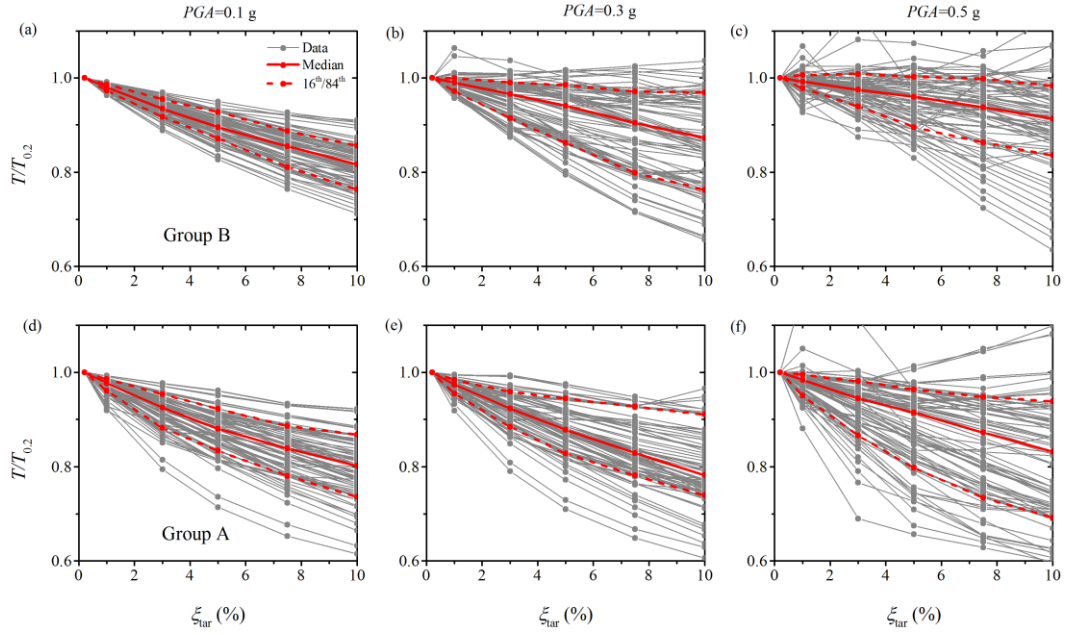


Fig. 3.4 Normalized axial force increments versus target damping ratios for three motion intensities: (a)~(c) Group A; and (d)~(f) Group B.

The evolutions of the normalized axial forces with the increasing target damping ratios are presented in Fig. 3.4, for the case of $PGA=0.1, 0.3,$ and 0.5 g. Figs. 3.4a~3.4c show the $T/T_{0.2}$ values for Group B while the results for Group A are shown in Figs. 3.4d~3.4f. Figs. 3.4a and 3.4c demonstrate that the axial forces decrease with increasing target damping ratio for all the analyses when the ground motion intensity is small (i.e., $PGA=0.1$ g). Further increase in the motion intensity, some $T/T_{0.2}$ values that are greater than 1.0 appear, especially for Group B subjected to 0.5 g earthquake loadings. In other words, a higher axial force is calculated for a larger ξ_{tar} value relative to the case of $\xi_{tar}=0.2\%$. This may be attributed to the fact that the soil state around the tunnel is modified by the value of the ξ_{tar} , as previously mentioned. Due to the nonlinear soil behaviour, the linear decreasing relationship between the parameter $T/T_{0.2}$ and ξ_{tar} disappear for some cases.

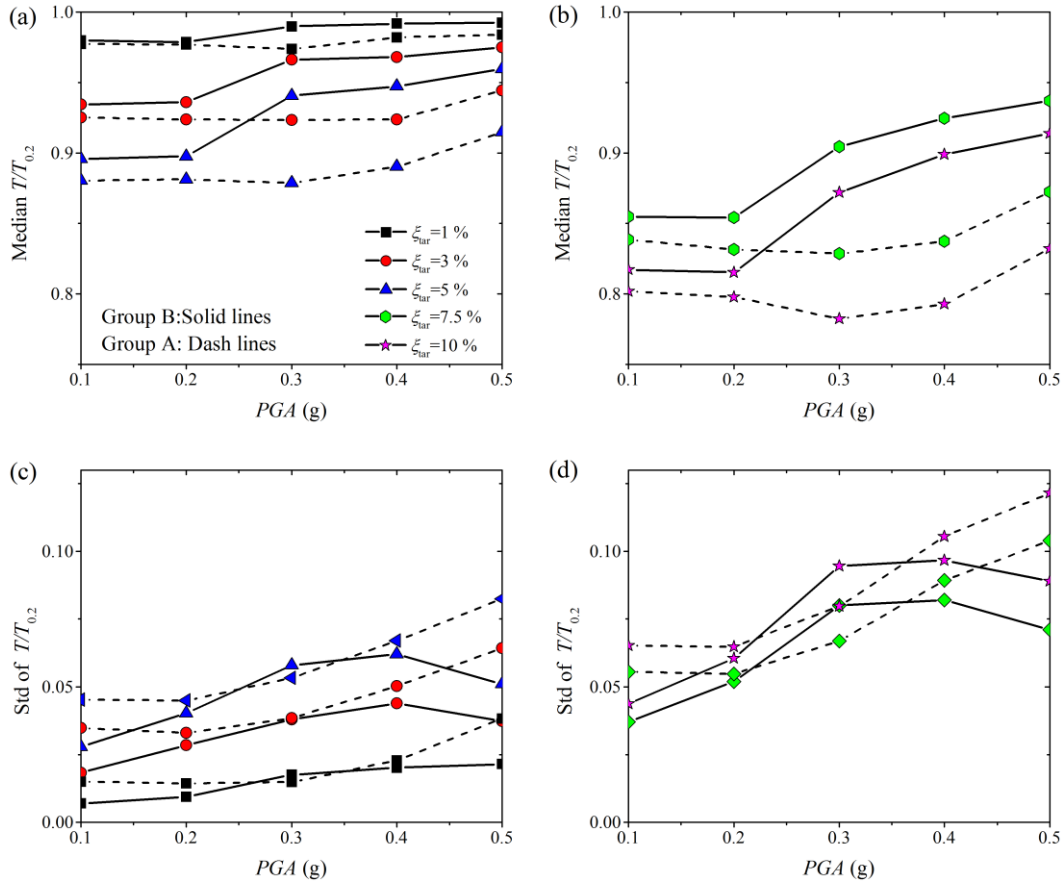


Fig. 3.5 Median and standard deviation of the normalized axial forces for different target damping ratios and motion intensities.

Fig. 3.5 displays the median and standard deviation of the $T/T_{0.2}$ computed from all the analyses with different target damping ratios and motion intensities. Increasing values of target damping ratio cause a decrease in the median normalized axial forces, with the reduction occurring predominantly at motion intensity less than 0.2 g for Group B. The reduction ranges from about 0.98 for $\xi_{tar}=1\%$ to about 0.82 for $\xi_{tar}=10\%$. This reduction is more evident in Group A. This is caused by the overestimated damping, which reduces the response at high frequency. Furthermore, Figs. 3.5a and 3.5b demonstrate how soil nonlinearity affects the median value of the $T/T_{0.2}$. In general, the normalized axial forces increase with increasing levels of soil nonlinearity. For Group B, the normalized axial forces for PGA less than 0.2 g are less affected by the motion intensity for all the target damping ratios. This range is wider (<0.4 g) for Group A due to the relatively low energy of ground motions (Fig. 3.1).

Figs. 3.5c and 3.5d show that the variability about the median value increases with the increase of the target damping ratio, identifying an increased influence on the tunnel seismic response for high target damping ratio. Increasing motion intensity causes a constant increase in the standard deviation for Group A, while for Group B a maximum standard deviation appears at around $PGA=0.3$ g. The change in standard deviation is caused by nonlinear soil behaviour (i.e., hysteretic damping). At weaker motions, soil nonlinearity is unimportant and the standard deviation is more influenced by ground motion characteristics (i.e., Group A has a bigger standard deviation than Group B for $PGA=0.1$ g). Increase the motion intensity to 0.2 and 0.3 g, the calculated axial force is scattered due to the different levels of induced strain and damping for different ground motions (Figs. 3.4b and 3.4e). At stronger motions, soil nonlinearity is significant and an “average effect” appears, leading to a reduced variability, (Fig. 3.4c). To conclude, the results of Fig. 3.5 reveal that large ξ_{tar} causes a significant reduction in the tunnel seismic response and the nonlinear soil behaviour tends to reduce this influence.

To quantify the influence of the damping determination approaches on the calculated axial forces, the variability in the results is quantified in terms of coefficient of variation (COV). It is calculated based on the following expression:

$$COV=\sigma/u \quad (3.1)$$

where σ is the standard deviation, u is the mean value of the calculated axial forces of five damping determination approaches for specified ground motion, motion intensity, and target damping ratio. Thus, for each PGA with a specific ξ_{tar} , there are respectively 17 and 33 COV values for Group A and Group B.

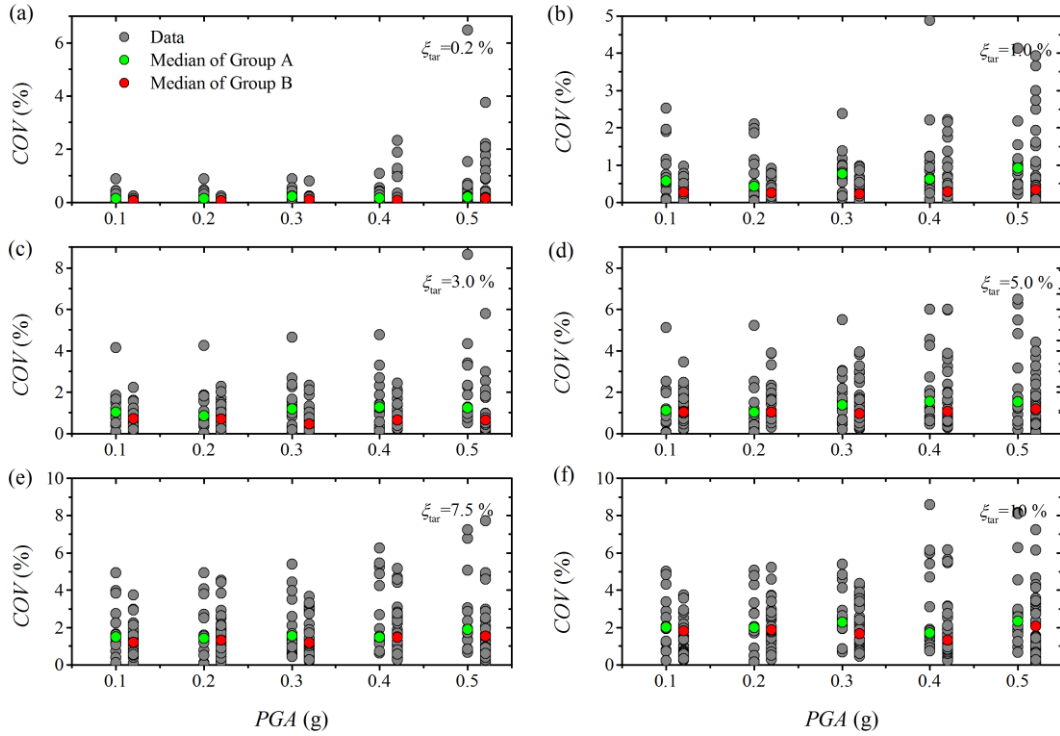


Fig. 3.6 COV of axial forces caused by five damping determination approaches for each ground motion and the median values (the results of Group B are shifted a little right to avoiding overlapping).

Fig. 3.6 displays the COVs of the calculated axial forces caused by five damping determination approaches with different levels of target damping ratio and ground motion intensity. The increased value of the target damping ratio causes an increase in the COV, with the maximum COV occurring at PGA larger than 0.3 g. In comparison with strong ground motions, the COVs for weaker ground motions are more sensitive to the value of the target damping ratio. For instance, the maximum COV changes from 1% for $\xi_{tar}=0.2\%$ to 5% for $\xi_{tar}=10\%$, in the case of $PGA=0.1$ g, Group A. This is due to the fact that the actual damping ratio used in the numerical model is related directly to the value of ξ_{tar} while the effect of ξ_{tar} is more significant for the low soil nonlinearity level, as previously stated (Fig. 3.5). On average, the median COV is less influenced by the intensity of ground motion, particularly for small ξ_{tar} cases. The maximum median COV is observed with a value of about 2.3%, for the case of $\xi_{tar}=10\%$, $PGA=0.5$ g, and Group A. A similar trend is observed for Group B, but with a slightly small COV.

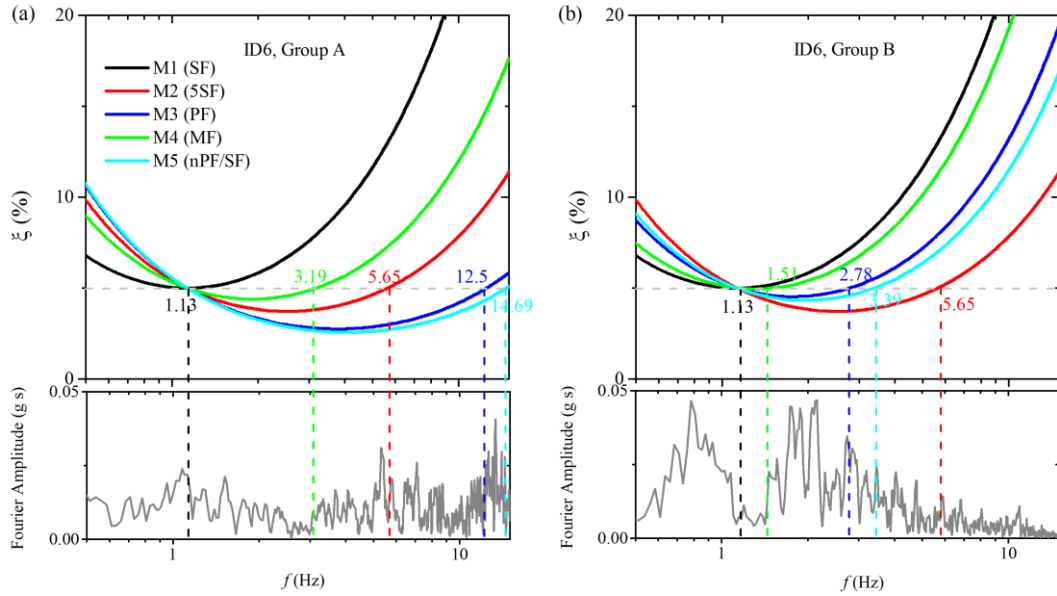


Fig. 3.7 Actual Rayleigh damping ratios calculated by five approaches.

To provide a better understanding, Fig. 3.7 shows the difference of the Rayleigh damping ratios in dynamic analysis for different damping determination approaches, corresponding to $\xi_{\text{tar}}=5\%$, and two ground motions that are respectively selected from two groups. For Group A, the frequency intervals determined by five approaches vary greatly (from 1.13 Hz to 14.69 Hz), leading to a substantial difference in the damping in the main frequency range (high frequency) of ground motions. Concerning Group B, the frequency intervals obtained by five approaches are relatively close (from 1.13 Hz to 5.65 Hz) and the damping ratios in the main frequency of ground motions differ moderately (relative to Group A). The results highlight that selecting reasonable target damping ratios and proper frequency determination approaches are necessary to obtain accurate numerical predictions.

Apart from the influence on the accuracy of numerical simulation, Rayleigh damping parameters significantly affect the computational cost. Fig. 3.8 displays the timestep for various damping parameters (f_{min} and ξ_{min} , calculated based on Eqs. 2.6 and 2.7), corresponding to the free-field case. Note that when the structural elements, soil-tunnel interface elements, and the irregular meshes are employed in the numerical model, the timestep is expected to be further reduced.

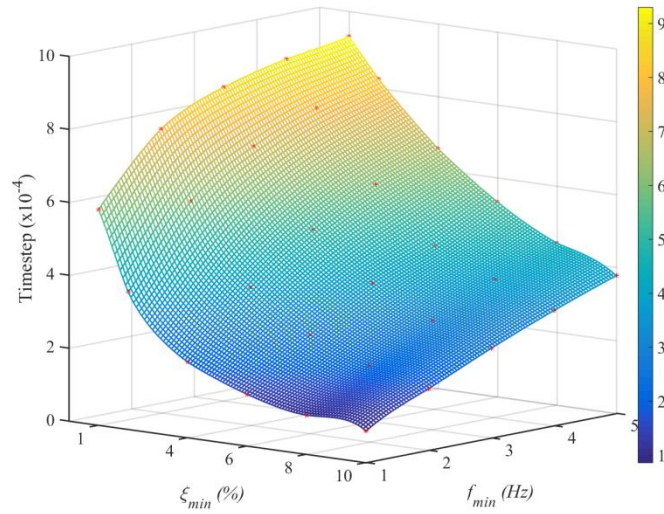


Fig. 3.8 Timestep for various damping parameters in the free-field case.

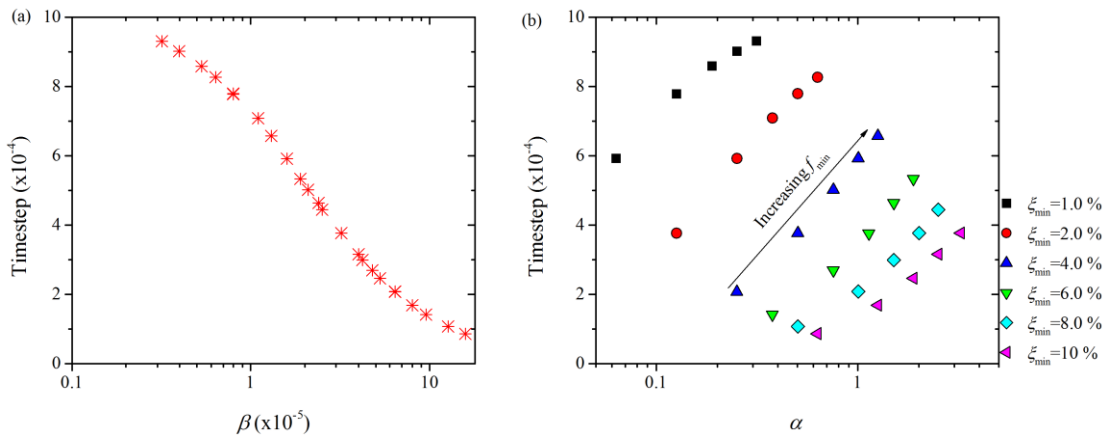


Fig. 3.9 Effects of stiffness-proportional and mass-proportional coefficients on timestep.

The utilization of Rayleigh damping reduces the timestep for the explicit solution scheme, resulting in higher calculation time. The reduction degree depends on the value of ξ_{\min} and f_{\min} . Taking $f_{\min}=2$ Hz as an example, the timestep with $\xi_{\min}=1\%$ is about 4 times the one when $\xi_{\min}=10\%$. A small timestep is required when high ξ_{\min} or small f_{\min} is employed. The relationships between the timestep and the mass-proportional damping coefficients α and stiffness-proportional damping coefficients β are presented, as shown in Fig. 3.9. Essentially, stiffness-proportional damping causes a reduction in the critical timestep for numerical stability. As the damping ratio corresponding to the high frequency is increased, the timestep is reduced. In other words, the steeper the damping curve in the high frequency range, the

longer the calculation time.

To further illustrate how the Rayleigh damping affects the propagation of ground motions, the surface acceleration time histories and the hysteretic loops at the tunnel center position for the free-field case (without tunnel) are calculated. The Nice ground motion with an amplitude of 0.249 g is used. The corresponding Fourier amplitude spectra, the amplification ratios (the Fourier amplitude of the surface acceleration to the input motion) are also presented in Fig. 3.10.

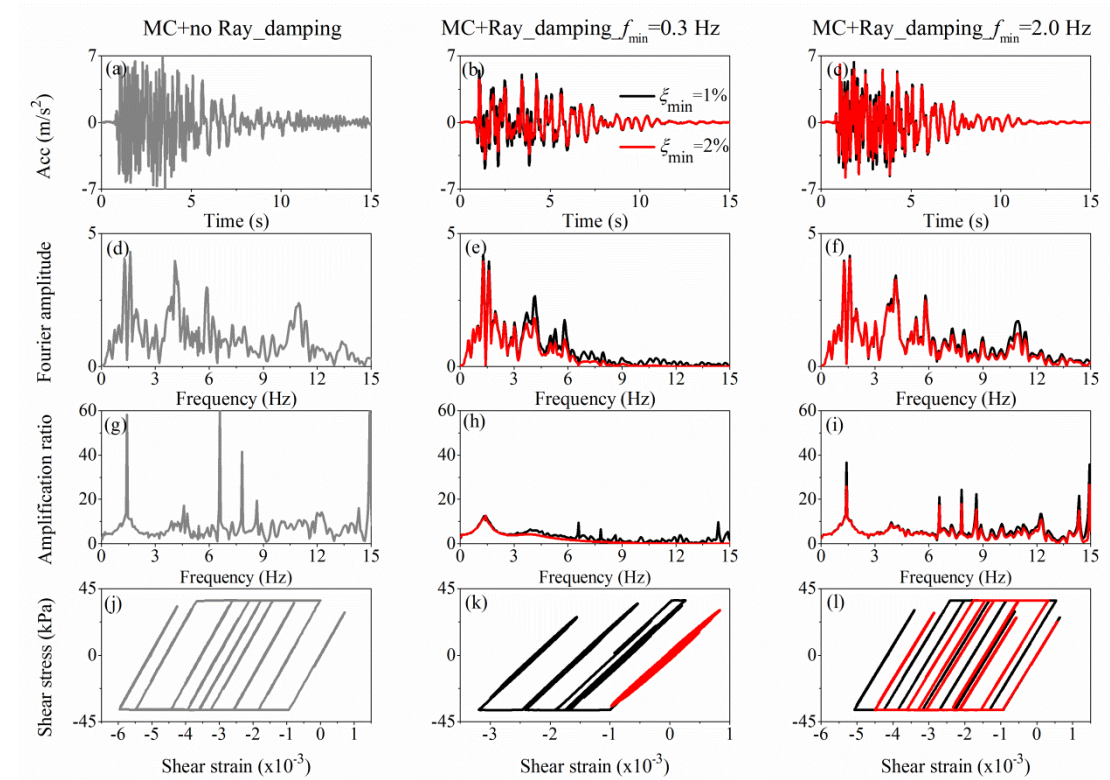


Fig. 3.10 Comparison of: (a)-(c) surface acceleration time histories, (d)-(f) Fourier amplitude, (g)-(i) Fourier amplitude amplification ratio of surface acceleration to the input, (j)-(l) stress-strain loops.

Rayleigh damping inhibits the response of peak ground accelerations, Fourier amplitude, and maximum strain. When Rayleigh damping is not incorporated in the model, the maximum *PGA* is equal to 9.12 m/s². The maximum *PGAs* are respectively 5.45, 6.34 m/s² when f_{min} is equal to 0.3, 2.0 Hz in the case of $\xi_{min}=1\%$. A higher frequency noise appeared in the time interval (10-15 s) of acceleration time histories when no additional Rayleigh damping is

added, as shown in Fig. 3.10a. The frequencies greater than 9 Hz of the input motion are filtered when $f_{\min}=0.3$ Hz and $\xi_{\min}=2\%$, resulting in a linear soil behaviour (Figs. 3.10h and 3.10k).

3.4 Conclusion

This chapter explores the role that plays the Rayleigh damping in nonlinear tunnel seismic analyses. Rayleigh damping models are commonly utilized to provide additional damping at small strains or to remain numerical stability when a simple constitutive soil model is adopted. The inherent limitation of the Rayleigh damping is its frequency-dependent, which could result in substantial differences in the tunnel seismic responses, as well as the increased computational cost.

Different criteria exist to guide the selection of the two matching frequencies to minimize the adverse effects of the dependency on the frequency of the Rayleigh damping. The Rayleigh damping specification is an issue that has often been treated with a certain degree of arbitrariness. To estimate the effects caused by a possible improper use, five damping determination approaches are compared in this chapter, considering a variety of intensities and characteristics of ground motions and target damping ratios.

On average, the calculated axial forces decrease with the target damping ratios increase. The maximum reduction occurs for the weaker ground motions with high frequency components (Group A). Nevertheless, higher target damping ratios result in large tunnel response is also observed for some cases due to the different levels of soil nonlinearity. The nonlinear soil behavior tends to reduce the target damping ratio influence. Oppositely, the soil nonlinearity increases the influence of the damping determination approach. A large *COV* caused by the damping determination approaches is generally observed for strong, high frequency ground motions, and large target damping (i.e., the maximum *COV* is equal to 2.3%).

The conventional method that only uses the soil fundamental frequency tends to

underestimate the tunnel seismic response, particularly for high frequency ground motions. However, it is difficult to recommend an appropriate approach for high target damping ratio and strong nonlinearity cases (Fig. 3.3c), since each approach appears to give the maximum tunnel response. Furthermore, the improper use of the Rayleigh damping results in a substantial increase in the time calculation. Stiffness-proportional damping controls the reduction degree: the steeper the damping curve in the high frequency range, the longer the calculation time.

Chapter 4

Influence of stress relief during excavation on the seismic response of tunnels

4.1 Introduction

Tunnel excavation leads to significant perturbations of the stress state in the surrounding soil. It thus will inevitably affect the tunnel lining response in terms of internal forces and deformations (Dias and Kastner, 2013; Do et al., 2014). Tunnelling in soft ground is generally accompanied by the deformation of the surrounding soil. The safety of the nearby structures such as pipelines, residual buildings can also be modified (Franza and Marshall, 2019).

Historical earthquakes have repeatedly demonstrated that the safety of tunnels is of major importance in the seismic prone areas, particularly for shallowly buried ones in soft soils. The seismic response of tunnels was the subject of intense research by a variety of analytical (Bobet, 2010; Park *et al.*, 2009a; Penzien, 2000; Wang, 1993), experimental (Bilotta et al., 2014; Lanzano et al., 2012, 2015), and numerical (Argyroudis and Pitilakis, 2012; Fabozzi *et al.*, 2018; Kontoe *et al.*, 2008; Tsinidis *et al.*, 2015, 2016a, 2016b) studies.

Analytical solutions are very attractive tools for the preliminary tunnel seismic design of tunnels. However, one of the well-known limitations is that they do not consider the construction consequence effect. The tunnel excavation process can be properly simulated through laboratory or centrifuge tests, as reported in the literature (Franza and Marshall, 2019). However, to the authors' knowledge, no previous centrifuge and shaking table tests

have considered the tunnel excavation process. This could be attributed to the difficulty in determining the true stress state in the surrounding soil and capturing precisely the stress relaxation coefficient (or volume loss ratio). Oppositely, numerical simulation is an alternative method for addressing the limitations of the analytical and experimental studies as they allow capturing the soil and tunnel lining stress and deformation responses at each excavation step.

Few studies have investigated the tunnel construction process in numerical modelling, but they are not focused on the stress relief effect assessment on the seismic behaviour of tunnels. For instance, [Corigliano *et al.* \(2011\)](#) analyzed the seismic response of the Serro Montefalco tunnel (Italy) using the nonlinear quasi-static approach. In their study, a stress relaxation coefficient of 0.75 was adopted to simulate the tunnel construction stages before the earthquake loading. [Sedarat *et al.* \(2009\)](#) and [Kontoe *et al.* \(2014\)](#) respectively verified the analytical solutions against the deformation-based quasi-static numerical method, both considering 50% of stress relaxation. [Ma *et al.* \(2018\)](#) performed a numerical analysis to investigate the burial depth influence on the seismic behaviour of a subway station, a volume loss ratio of 0.5% was assumed before the dynamic time-history analysis. However, all these studies failed to derive the relationship between the stress relaxation coefficients and the seismic internal force increments. More recently, [Gomes \(2013\)](#) provided the only investigation on the seismic response of tunnels using a dynamic time-history analysis that considered the stress disturbance effect induced by the tunnel excavation. This study assumed no relative movements and separation between the tunnel and the surrounding soil since no interface elements were employed. Conceptually, the presence of the soil-tunnel interface, to some extent, will provide an additional influence on the tunnel seismic response due to the different initial stresses (i.e., normal and tangential) acting at the interface. The stress relief process during tunnel excavation is an important phenomenon and its influence on the tunnel seismic behaviour requires further studies.

This chapter will explore how the initial stress state (caused by tunnel excavation) affects the seismic behaviour of tunnels using nonlinear dynamic time-history analyses. Before the

seismic analysis, the tunnel excavation is simulated in a two-dimensional plane strain model considering the convergence-confinement method to obtain the initial stress state in the surrounding soil, as well as the internal forces and deformations of the tunnel lining. Six ground motions are employed accounting for different input motion intensities and frequency characteristics. The developed numerical models consider both the no-slip and full-slip conditions between the soil and the lining, which is consistent with the commonly used assumption in analytical solutions. It allows predicting the upper and lower limit relationships between the stress relaxation coefficients and the seismic internal force increments. The possible influences of the stress redistribution on the surface ground motions and of the modulus reduction curves on the calculated internal forces are discussed.

4.2 Tunnel excavation simulation

4.2.1 Convergence-confinement method

Only a three-dimensional model can accurately simulate the tunnel excavation due to the tunnel advancement which induces a stress redistribution and three-dimensional deformation. However, due to the complexity and the time-consuming of this type of model, the tunnelling process is often modelled under two-dimensional plane strain conditions (Do *et al.*, 2014; Karakus, 2007).

The convergence-confinement method (CCM) which accounts for the 3D effects by replacing the ground to be excavated by a fictitious pressure is the one that has been widely used among the available equivalent approaches. The radial stress, σ_r , acting on the tunnel periphery is given as follows:

$$\sigma_r = (1 - \lambda)\sigma^0 \quad (4.1)$$

$$\lambda = \frac{U_r^{(x)}}{U_r^\infty} \quad (4.2)$$

$$U_r^\infty = \frac{1+\nu_s}{E_s} \sigma^0 r \quad (4.3)$$

where λ is the stress relaxation coefficient; σ^0 is the initial radial stress; $U_r^{(x)}$ is the radial

component of displacement at a distance x behind the face; U_r^∞ is the radial component of displacement at a distance behind the face considered as infinite; E_s and ν_s are respectively the elastic modulus and Poisson's ratio of the ground; r is the tunnel radius.

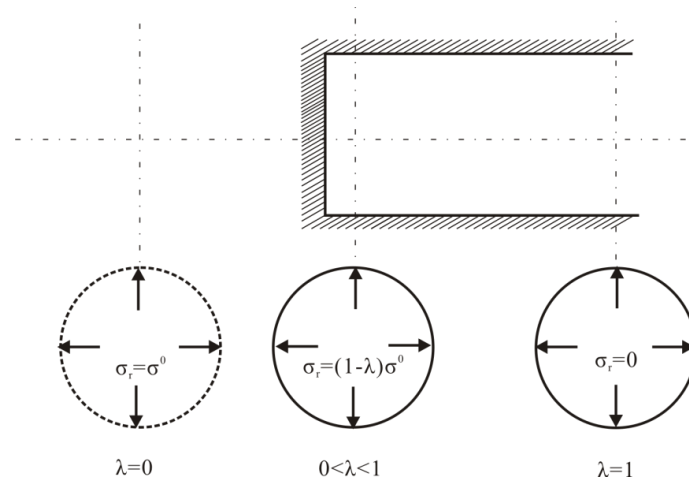


Fig. 4.1 Evolution of tunnel convergence with face advance.

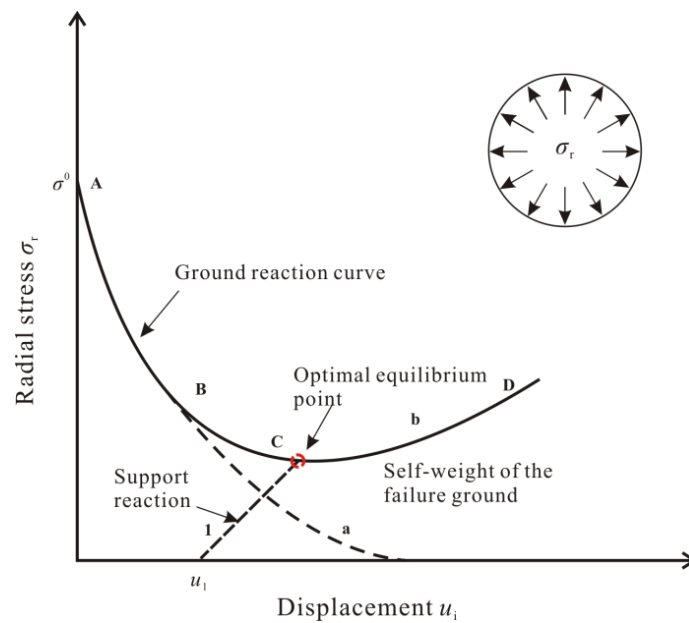


Fig. 4.2 Ground reaction curve of a tunnel and reaction line of the support: u_1 is the tunnel boundary displacement before the installation of the tunnel support.

The two-dimensional tunnelling problem is illustrated in Fig. 4.1. The tunnelling process is represented by increasing the λ value from 0 to 1. Fig. 4.2 shows the main characteristics of the convergence-confinement method. The convergence curve corresponds to the internal pressure versus the tunnel radial displacement. The tunnel radial displacement increases as the

internal pressure decreases. The tunnel can be self-stabilized without a liner (curve [a](#)) or the surrounding ground can fail which leads to an increase in the ground load acting on the tunnel lining (curve [b](#)). In the latter case, support should be installed to keep the stability of the tunnel.

4.2.2 Stress relief process

The tunnelling-induced stress relief process is simulated using the convergence-confinement method through the following steps ([Do et al., 2014](#); [Karakus and Fowell, 2003](#); [Karakus, 2007](#)):

- Generation of the initial geostatic stress under the gravity loads and the lateral earth pressure.
- The full tunnel face is excavated and a radial pressure is simultaneously applied to the tunnel boundaries. The radial pressure is then reduced step by step until it reaches the specified stress relaxation coefficient λ , and achieve a new equilibrium state.
- Installation of the tunnel lining then completely releases the residual radial pressure.

In practice, the stress relaxation coefficients are usually specified according to the back analysis of experimental or field monitoring data obtained during the tunnelling process. In the present study, four λ values of 0, 0.35, 0.5, and 0.7 are adopted parametrically. A value of $\lambda=0$ means that the tunnelling process is not taken into account in the analysis, which is consistent with most of the previous numerical studies and analytical solutions. It should be noted that the complete stress relief process ($\lambda=1.0$) is not adopted because the calculation cannot reach an equilibrium state (soil large deformation occurs), which is also not realistic for shallow tunnels constructed in soft soil.

4.3 Numerical modelling of soil-tunnel system

The Bologna-Florence high-speed railway tunnel project in Italy is also adopted as the reference case. The properties of soil and tunnel lining, and their constitutive models, are the

same as the ones utilized in Chapter 3. Fig. 4.3 shows the two-dimensional numerical model, with a height of 60 m and a width of 150 m. It should be noted that a larger model is built, to get rid of the boundary effect caused by the simulation of tunnel excavation (Do *et al.*, 2014). The boundaries conditions used in the numerical models are the same with ones used in Chapter 3, except the bottom boundary condition for dynamic analysis. The vertical velocity along the model bottom is fixed to simulate a rigid base condition. In other words, the bedrock is assumed to 60 m below the ground surface.

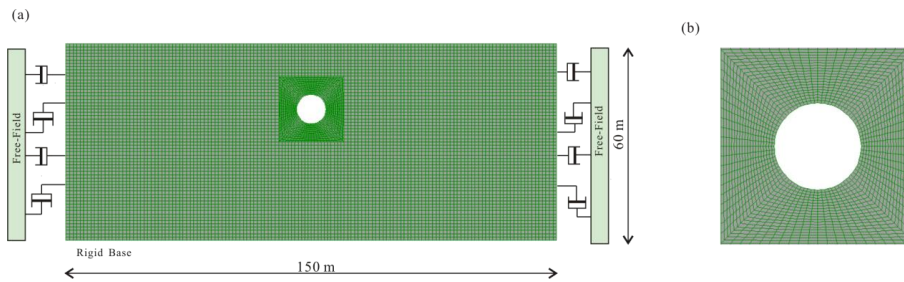


Fig. 4.3 Soil-tunnel numerical model: (a) meshes, geometry, and boundary conditions; (b) refined meshes.

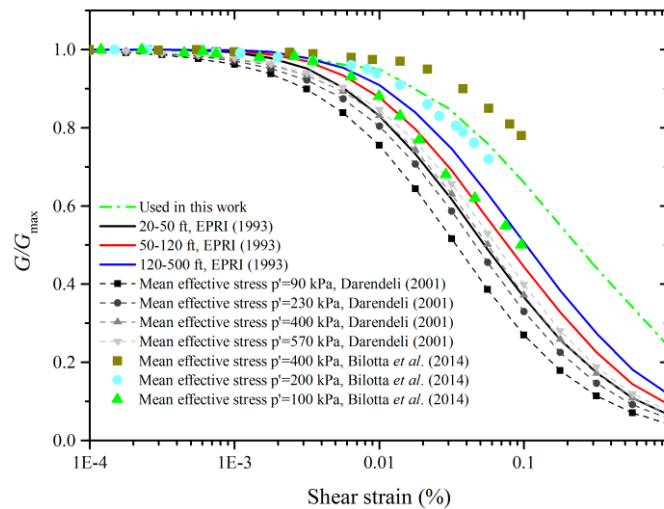


Fig. 4.4 Shear modulus reduction curves.

Hysteretic damping models used in the dynamic analysis impose the shear-modulus reduction and damping ratios as a function of cyclic shear strains. A built-in hysteretic damping model (Itasca, 2011) is also selected for the dynamic analysis, as follows:

$$G_{secant} = s^2(3 - 2s) \quad (4.4)$$

$$s = \frac{L_2 - L}{L_2 - L_1} \quad (4.5)$$

where L is the logarithmic strain and L_1 and L_2 are the extreme values of logarithmic strain.

Shear modulus reduction curves under different mean effective pressures, p' , or depths reported by several researchers (Bilotta *et al.*, 2014; Darendeli, 2001, EPRI, 1993) are presented in Fig. 4.4. It can be found that these curves are strongly influenced by mean effective pressure and different curves are obtained for the same pressure (e.g., $p'=400$ kPa). It should be clarified that the hysteretic damping used here is not as a primary way to simulate yielding, but as a supplement to the nonlinear constitutive model (linear elastic perfectly plastic in this study). In the absence of laboratory data, the modulus reduction curve suggested by Sun *et al.* (1988) is used. This curve is close to the data of Bilotta *et al.* (2014) for $p'=200$ kPa which corresponds to the location of the tunnel springline.

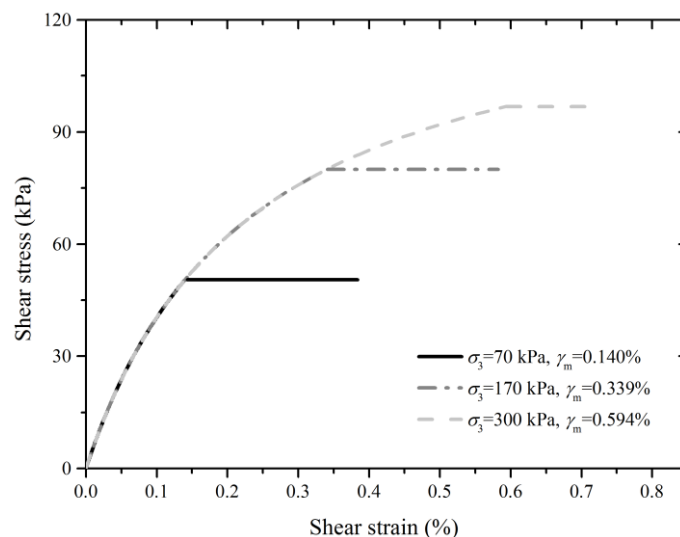


Fig. 4.5 Shear stress/strain curves: linear elastic perfectly plastic (Mohr-Coulomb shear failure criteria) constitutive model with hysteretic damping under different confinement pressures.

Fig. 4.5 presents the shear stress/strain curves under different confinement pressures (σ_3) when hysteretic damping is combined with the linear elastic perfectly plastic *MC* model. The *MC* model has a constant elastic shear modulus and constant yield stress. It is not able to simulate the soil modulus degradation in the elastic range. Hence, hysteretic damping permits to induce energy dissipation below the yield strain (γ_m). Whereas, the dissipated energy (area enclosed in the shear stress/strain loop) in the plastic range, can be attributed to both the hysteretic damping and *MC* model itself. Compared to the *MC* model only, the inclusion of

hysteretic damping increases the overall damping ratio during the dynamic analysis, which monotonically increases with the shear strain amplitude.

Besides the hysteretic damping, the frequency-dependent viscous damping is introduced utilizing the Rayleigh formulation in dynamic analysis. Owing to the inherent limitation of the Rayleigh damping, it is determined according to the recommendation of [Kwok *et al.* \(2007\)](#). The site fundamental frequency and five times the site fundamental frequency are selected to determine the center frequency, leading to $f_{\min}=1.8$ Hz in this study. Concerning the minimum damping ratio ξ_{\min} , a value of 3% is used. A relatively larger damping ratio used in this chapter because a rigid base is used (high-frequency noise is difficult to be filtered out) and it is expected to adopt a smaller one when a quiet boundary is employed at the model bottom ([Itasca, 2011](#)).

The soil-tunnel interfaces are modelled as a linear spring-slider system following the Mohr-Coulomb shear failure criterion. The relative movement and separation are controlled by the normal stiffness K_n and the shear stiffness K_s . The apparent stiffness of a zone in the normal direction is ([Itasca, 2011](#)):

$$\max \left[\frac{K + \frac{4}{3}G}{\Delta Z_{\min}} \right] \quad (4.6)$$

where K and G are the bulk and shear modulus respectively, and ΔZ_{\min} is the smallest width of the adjoining zone in the normal direction. According to the Users' manual ([Itasca, 2011](#)), nearly ten times the equivalent stiffness of the stiffest neighboring zone is generally used to calculate the normal stiffness. By the sensitivity analysis, $K_n=4 \times 10^9$ N/m³ is adopted here. A larger normal stiffness value is not recommended because of the increased computational cost. The shear stiffness depends on the degree of the slippage, and a very high stiffness value prevents movement on the interface. Through checking the soil-tunnel interface states in the sensitivity analysis, the shear stiffness of 4×10^9 N/m³ can properly present the no-slip condition. For the full-slip case, a nominal value of the shear stiffness ($K_s=1 \times 10^3$ N/m³) is used as recommended in [Kontoe *et al.* \(2014\)](#).

Six real ground motions (Table 4.1) with diverse frequency components are used as the seismic input motions to capture the influence of the frequency characteristics on the tunnel seismic behaviour, as plotted in Fig. 4.6. To reduce the computational cost, the ground motion duration time is set to 25 s, which contains the peak acceleration and critical frequency characteristics of the original ground motions. All the input ground motions are scaled to three amplitudes ($PGA=0.1, 0.2,$ and 0.4 g) to account for the effect of the input motion intensities. A low-pass filter is applied to remove the frequency higher than 15 Hz to ensure the numerical stability and the accuracy of the wave propagation within the model (otherwise, a fine mesh is necessary). The acceleration time histories are applied along the model bottom to simulate the vertically propagating ground motions.

Table 4.1 Six input ground motions.

| Number | Earthquake event | Station name | PGA (g) | Predominant frequency (Hz) |
|--------|------------------|-----------------------|-----------|----------------------------|
| GM1 | Imperial Valley | USGS station 5115 | 0.3152 | 7.1 |
| GM2 | Friuli | Tolmezzo (000) | 0.3513 | 3.9 |
| GM3 | Hollister | USGS station 1028 | 0.1948 | 2.5 |
| GM4 | Kobe | Kakogawa (cue90) | 0.3447 | 6.3 |
| GM5 | Loma Prieta | 090CDMG station 47381 | 0.3674 | 4.5 |
| GM6 | Northridge | 090CDMG station 24278 | 0.5683 | 3.8 |

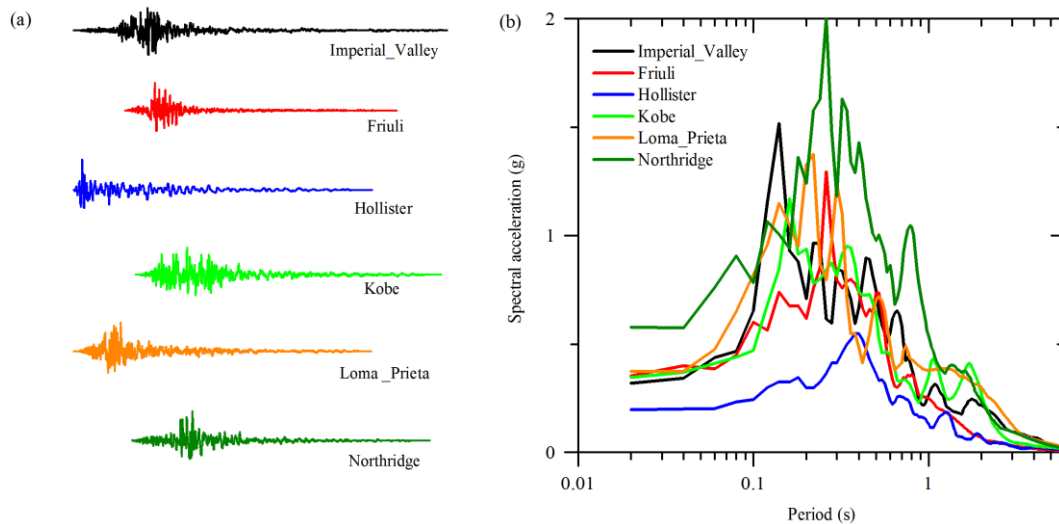


Fig. 4.6 Input ground motions: (a) acceleration time-histories; and (b) spectral accelerations.

4.4 Analysis results

4.4.1 Static analysis

Before the dynamic analyses, the static analyses are performed first to determine the initial stress states in the surrounding soils and the static lining forces and deformations. Fig. 4.7 shows the distribution of the static lining forces with different stress relaxation coefficients for the two soil-tunnel interface conditions at the end of the static analysis.

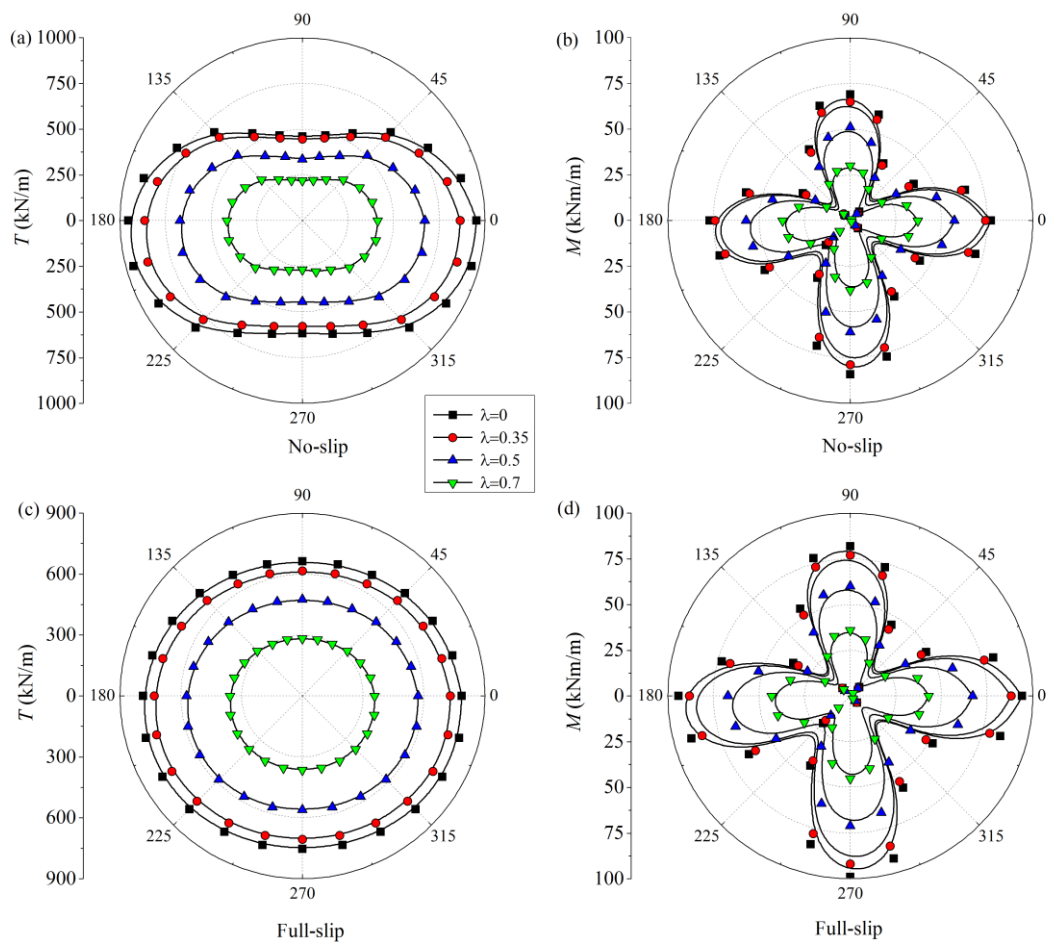
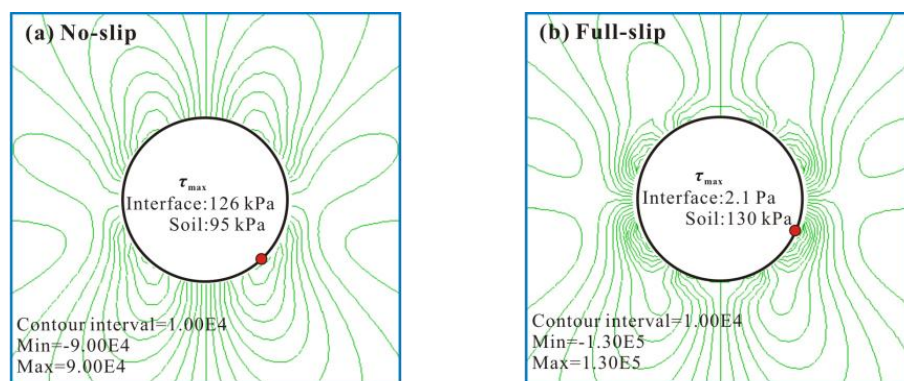


Fig. 4.7 Lining forces after the lining installed: (a) axial forces, no-slip; (b) bending moments, no-slip; (c) axial forces, full-slip; and (d) bending moments, full-slip.

An increase in the stress relaxation coefficient results in a reduction in the lining forces. Besides, the distributions of bending moment are similar for both the no-slip and full-slip cases. For the no-slip case, the maximum axial forces appeared at the two tunnel sides (Fig. 4.7a) due to the low value of the lateral earth pressure coefficient at rest (i.e., 0.5); while for the full-slip case, the axial forces seem to be almost constant in the lining. This can be

contributed to the slippage and separation that occurred between the soil and the tunnel due to the very small shear stiffness in the full-slip condition (Sedarat *et al.*, 2009).

Fig. 4.8 shows the maximum shear stress in the surrounding soil and at the interface. In the no-slip condition, the maximum interface shear stress (126 kPa) is larger than the maximum soil shear stress (95 kPa) for the no-slip condition, preventing the occurrence of the slippage at the soil-tunnel interface. Oppositely, the maximum interface shear stress is significantly smaller (2.1 Pa) than the one in the surrounding soil (130 kPa) for the full-slip condition, providing a negligible shear resistance to the slippage. It illustrates that the interface parameters selected in this study are appropriate to respectively simulate the no-slip and full-slip conditions.



Note: red point presents the location of the soil maximum shear stress

Fig. 4.8 Maximum soil shear stress without considering stress relief: (a) no-slip; and (b) full-slip.

To further validate the accuracy of the soil-tunnel interface parameters, Table 4.2 presents the comparison of the calculated maximum axial forces and bending moments by the numerical analysis and two analytical solutions (Bakker, 2003; Erdmann, 1983) for the no-slip condition without considering stress relief. The equations employed by the two analytical solutions are summarized in Appendix B. Both the analytical solutions over-estimate the lining forces, particularly for the axial forces calculated by the Erdmann (1983) solution (+43%). In general, analytical solutions assume a uniform stress field for a deep tunnel in an elastic soil. However, the tunnel in this study cannot be considered as a deep tunnel, and the stress at the tunnel crown ($\sigma_v=258$ kPa) is smaller than the one at the tunnel invert ($\sigma_v=408$ kPa). It thus leads to a

non-uniform stress field. Furthermore, the nonlinear soil behaviour affects the lining forces in the numerical predictions, as stated in the literature (Zhao *et al.*, 2017).

Table. 4.2 Comparison of the calculated axial forces and bending moments by numerical analysis and analytical solutions for the no-slip and no stress relief conditions.

| | This study | Bakker (2003) | Erdmann (1983) |
|-----------------------------|-------------------|----------------------|-----------------------|
| Axial force, T (kN/m) | 959 | 1233 (+26%) | 1374 (+43%) |
| Bending moment, M (kNm/m) | 84 | 86 (+2%) | 117 (+39%) |

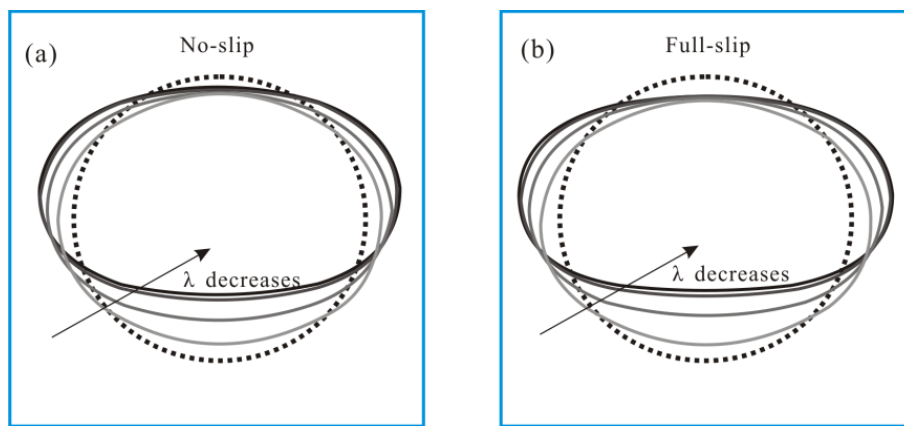


Fig. 4.9 Tunnel deformation modes for different stress relaxation coefficients: (a) no-slip; and (b) full-slip (Magnification factor: 300).

Fig. 4.9 compares the tunnel deformations for different stress relaxation coefficients, showing that the tunnel lining deforms less when a larger amount of stress is released, in terms of both the horizontal and vertical deformations (Table 4.3). The stress relief process reduces the stress acting on the tunnel lining which then produces less deformation, as expected. Table 4.3 also depicts that the deformation is more significant for the full-slip condition.

Table. 4.3 Horizontal and vertical deformations of tunnel lining for different stress relaxation coefficients.

| λ | Horizontal deformation (cm) | | Vertical deformation (cm) | |
|-----------|-----------------------------|-----------|---------------------------|-----------|
| | No-slip | Full-slip | No-slip | Full-slip |
| 0 | 0.52 | 0.63 | 0.62 | 0.73 |
| 0.35 | 0.49 | 0.59 | 0.58 | 0.68 |
| 0.5 | 0.38 | 0.46 | 0.45 | 0.53 |
| 0.7 | 0.24 | 0.29 | 0.28 | 0.33 |

The mobilization of the earth pressure around the tunnel for different stress relaxation coefficients is presented in Fig. 4.10, in terms of normalized vertical (σ_1/σ_v) and horizontal stress (σ_3/σ_v) calculated along the tunnel centerline. The values of σ_1/σ_v and σ_3/σ_v decrease around the tunnel due to the stress relief process, with the maximum reduction occurs at $\lambda=0.7$. Larger lateral earth pressure coefficients (σ_3/σ_v) are predicted for higher λ at some positions, due to the soils are in a passive state when moving towards the tunnel.

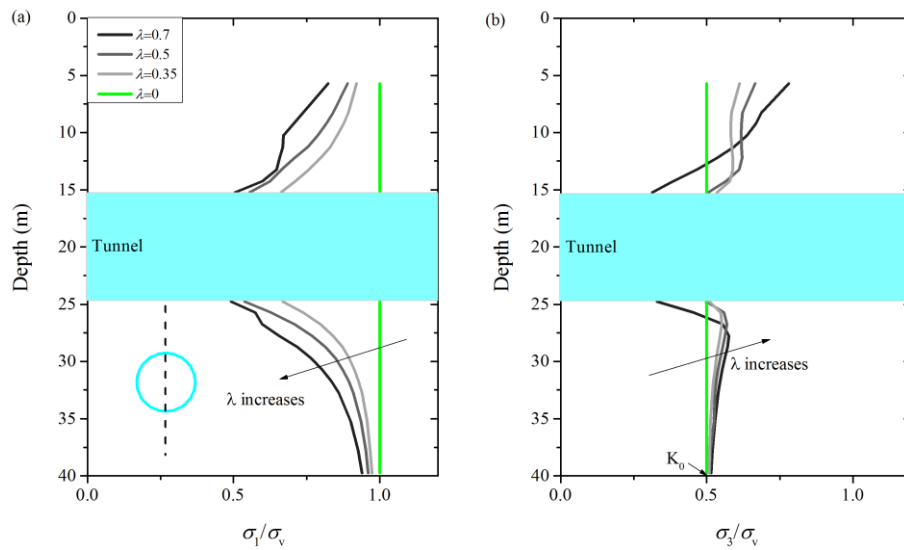


Fig. 4.10 Normalized vertical and horizontal stresses around the tunnel.

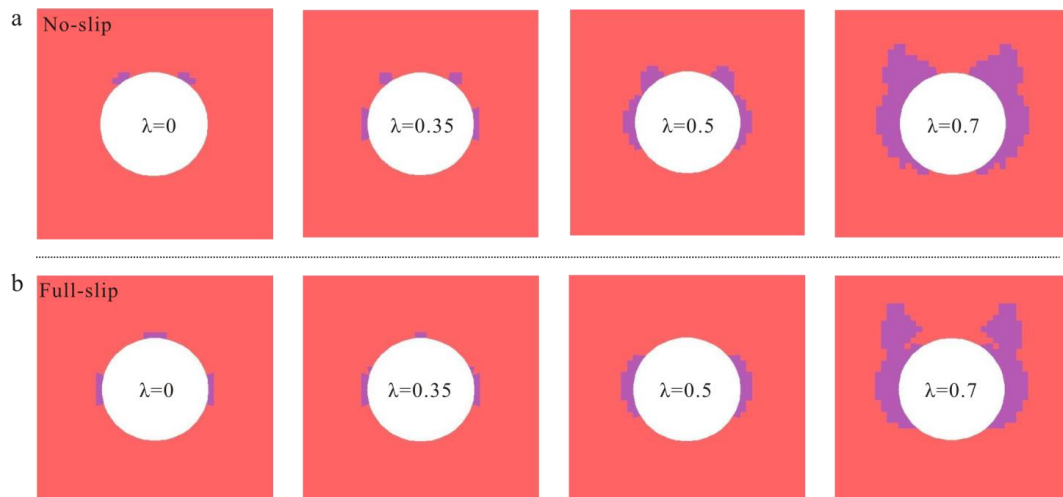


Fig. 4.11. Plastic zones after the lining installation versus the stress relaxation coefficients: (a) no-slip case; and (b) full-slip case.

Fig. 4.11 presents the plastic zones in the surrounding soil versus four stress relaxation

coefficients for the no-slip and full-slip cases. As can be seen, the plastic zone becomes larger as the stress relaxation coefficient increases, particularly for the tunnel sides and shoulders. It is attributed to the displacement of soil around the tunnel boundary becomes progressively larger as the stress relaxation coefficient increases (Fig. 4.2). When $\lambda < 0.35$, most of the surrounding soil elements do not reach the plastic state and, stay in an elastic state. It seems that the no-slip case induces a slightly larger plastic zone than the full-slip case. However, as compared to the stress relief process, the effect of soil-tunnel interface conditions on the plastic zone is secondary.

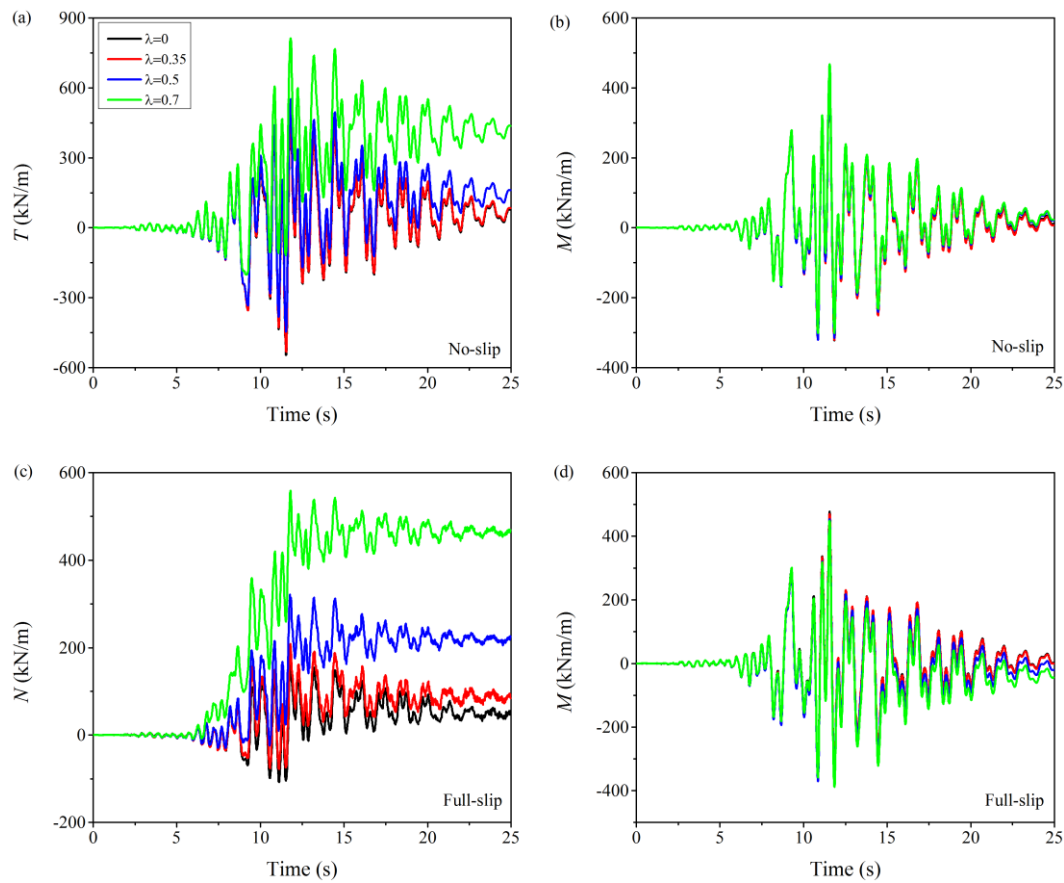


Fig. 4.12 Time histories of the seismic internal force increments: (a) axial force, no-slip; (b) bending moment, no-slip; (c) axial force, full-slip; and (d) bending moment, full-slip.

4.4.2 Seismic analysis

After the installation of the tunnel lining, various ground motions are then applied to investigate the tunnel seismic response under different initial stress states. Fig. 4.12 presents

the time histories of seismic-induced internal forces (total internal forces minus static ones) at the tunnel right shoulder ($\theta=45^\circ$) for the Kobe earthquake with an amplitude of $PGA=0.4\text{ g}$.

The axial force increases at the beginning of the earthquake due to the input motion intensity increases, especially for the higher stress relaxation coefficient ($\lambda=0.7$). At the end of the earthquake, a significant residual axial force is left on the lining due to the irreversible plasticity deformations of soil (Cilingir and Madabhushi, 2011a; Kontoe *et al.*, 2011; Tsinidis *et al.*, 2016b). This is more evident when a larger stress relaxation coefficient is employed. However, the stress relief process has a minor influence on the bending moment time histories, and no clear trend is found, as shown in Figs. 4.12b and 4.12d.

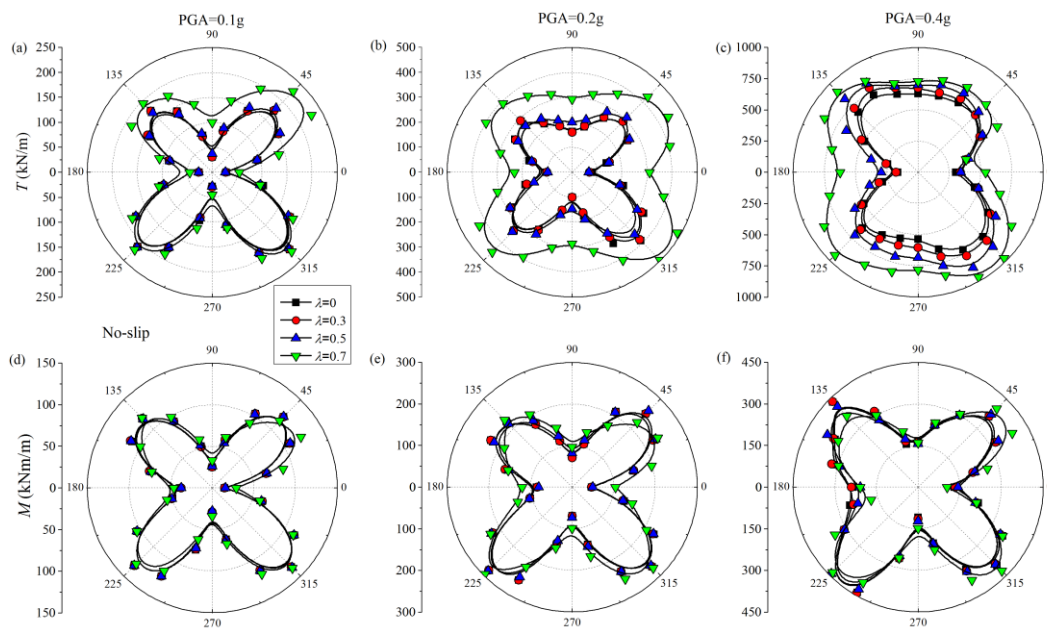


Fig. 4.13. Distribution of the maximum seismic internal force increments for no-slip cases: (a)~(c) axial forces; and (d)~(f) bending moments.

Figs. 4.13 and 4.14 respectively compare the distributions of the maximum absolute internal force increments induced by the Kobe earthquake under various λ values and $PGAs$, for the no-slip and full-slip cases. All the analyses illustrate that a noticeable seismic internal force increment appears near the shoulder and the arch for the no-slip case and the bending moment for the full-slip case. However, similar to the static analysis results, the seismic axial force increments are relatively uniform along the tunnel circumference for the full-slip case.

Sedarat *et al.* (2009) studied the effect of soil-tunnel contact conditions on the response of tunnels based on a Coulomb friction law. They stated that the axial force almost stays constant in the case of tunnel ovaling without friction (corresponding to the full-slip case here). Higher stress relaxation coefficient leads to a larger seismic axial force increment, while the bending moments are slightly influenced by the stress relief process.

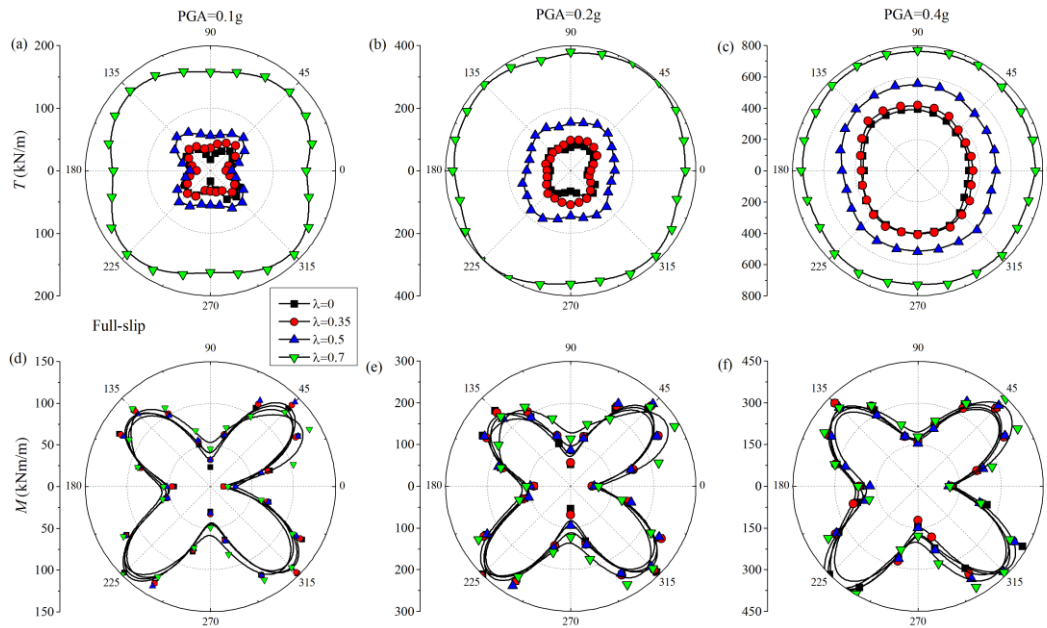


Fig. 4.14 Distribution of the maximum seismic internal force increments for full-slip cases: (a)~(c) axial forces; and (d)~(f) bending moments.

Fig. 4.15 shows the typical plastic zones in the surrounding soil at the end of the Kobe earthquake. The plastic zone is becoming progressively larger as the stress relaxation coefficients and motion intensities increase. Consistent with the static results, the no-slip case generally results in larger plastic zones relative to the full-slip case. The results have underlined that the soil-tunnel interface condition, to a certain degree, affects the soil plasticity as well. Huo *et al.* (2005) and Tsinidis *et al.* (2016b) also reported that the “strong” connection between the soil and the lining increased the soil plastic strain around the flexible tunnel while the plastic strain decreased for the full-slip condition.

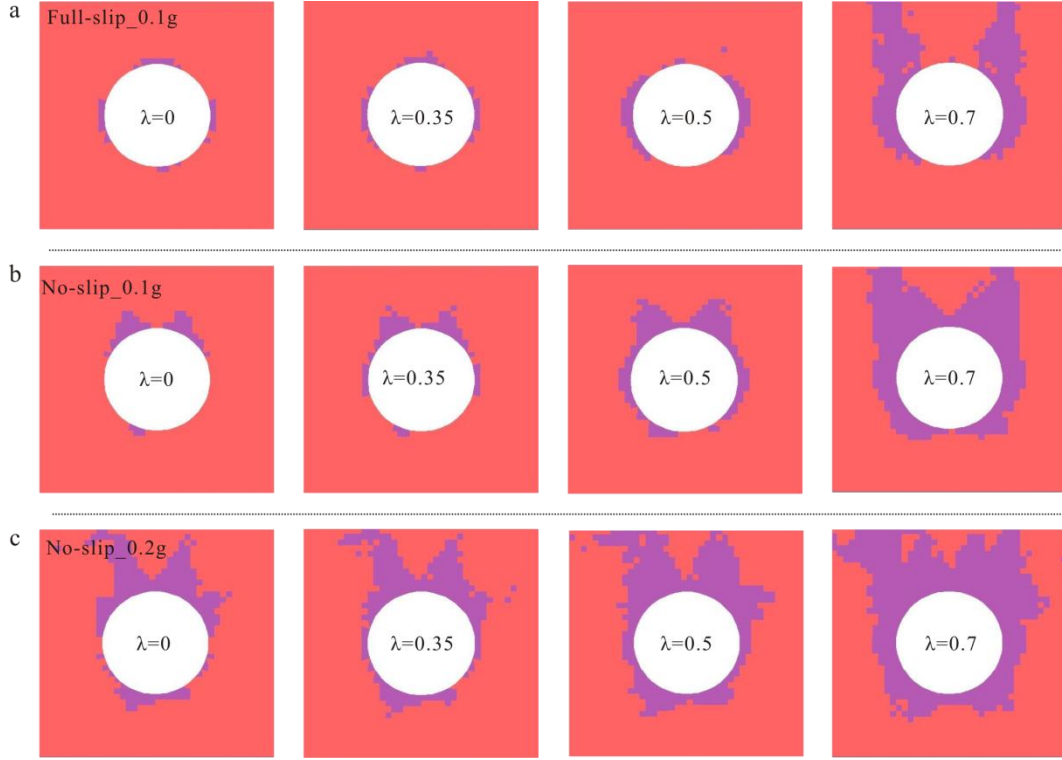


Fig. 4.15 Plastic zones around the tunnel at the end of the Kobe earthquake: (a) full-slip, 0.1g; (b) no-slip, 0.1g; and (c) no-slip, 0.2g.

To quantify the effect of the stress relief process on the seismic-induced internal force increments, two normalized parameters are defined:

$$R_T = \frac{N_{seismic_{\lambda_i}}}{N_{static_{\lambda_i}}} \quad (4.7)$$

$$SR_T = \frac{N_{seismic_{\lambda_i}}}{N_{seismic_{\lambda_0}}} \quad (4.8)$$

where R_T is the ratio of the seismic axial force increment compared to the static one at the same stress relaxation coefficient λ_i , SR_T is the ratio of the seismic axial force increment at the specific stress relaxation coefficient λ_i compared to the one in the case of $\lambda=0$. The definition of these coefficients for the bending moment is the same as the ones for the axial forces.

Fig. 4.16 shows the R_T and R_M ratios versus the stress relaxation coefficients for the no-slip and full-slip cases, corresponding to six ground motions and three motion intensities. Different ground motions capture similar trends. The much larger R_M ratios are calculated due to the relatively lower static bending moment (Fig. 4.7). The effect becomes progressively larger as the stress relaxation coefficients and the input motion intensities increase,

particularly for the no-slip case. The maximum R_M ratio increases up to 12 while it is around 2.5 for the R_T ratio. Similar to the static analysis results, the changes in the R_T and R_M ratios are negligible when the value of λ is smaller than 0.35, while the ratios rapidly increase when larger λ values are utilized. The results of this study have confirmed the findings of [Gomes \(2013\)](#) under no-slip condition.

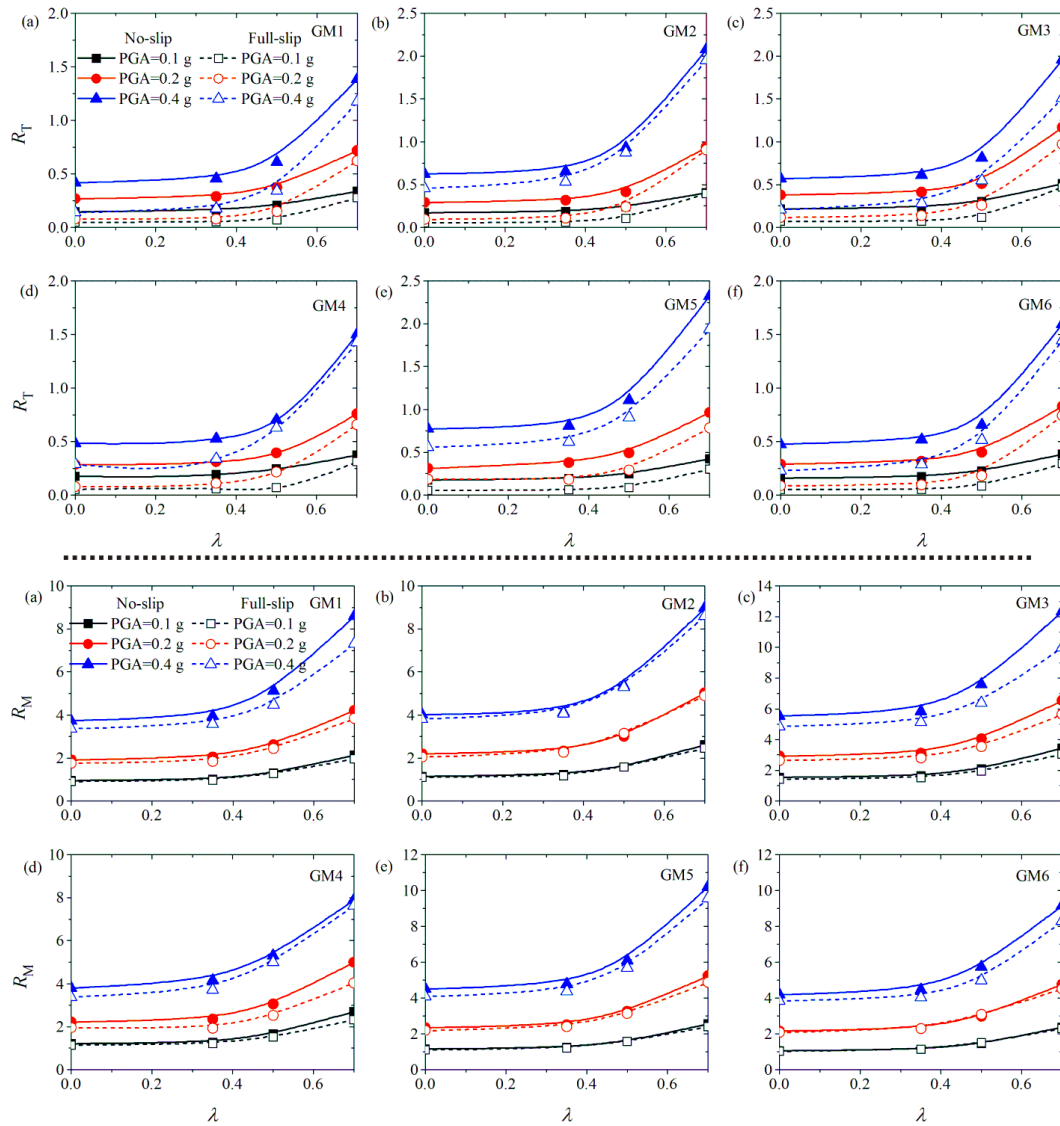


Fig. 4.16 R_T and R_M ratios versus λ for different ground motions and motion intensities.

The ratios (e.g., SR) between the maximum seismic-induced internal force increments at a specific stress relaxation coefficient and the ones at $\lambda=0$ are respectively presented in Figs. [4.17](#) and [4.18](#) for the no-slip and full-slip cases. The SR_T ratio increases with increasing stress

relaxation coefficient for the two soil-tunnel interaction conditions. For the no-slip case, the ratio varies from 1.0 to 1.5, while it changes from 1.0 to 4.5 for the full-slip case. This contributes to a lower axial force increment is calculated in the case of $\lambda=0$ for the full-slip condition (Fig. 4.14a~4.14c). Concerning the bending moments, the stress relief process shows a minor influence on the SR_M ratios, and no clear trend is observed. The no-slip conditions predict the SR_M ratios change from 0.95 to 1.05, while a slightly larger variation (0.9~1.1) is observed for the full-slip conditions.

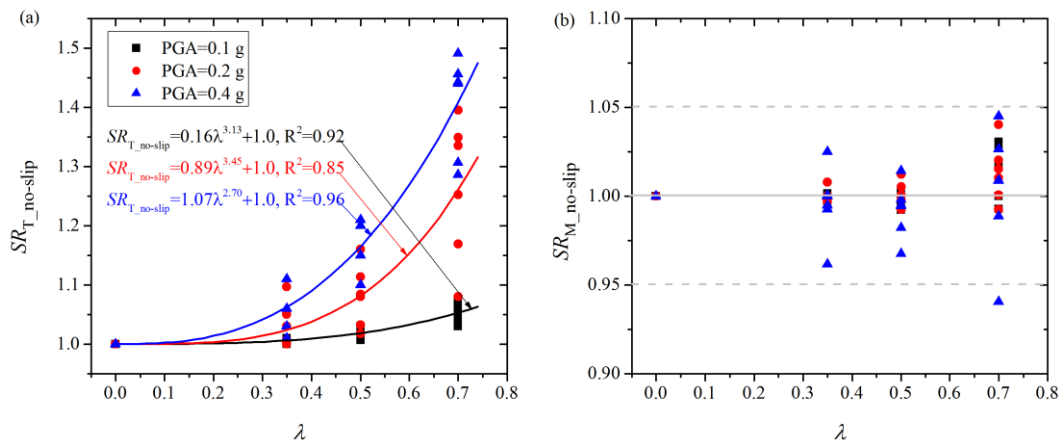


Fig. 4.17 Relationship between the SR ratios and the λ values for no-slip cases: (a) axial forces; and (b) bending moments.

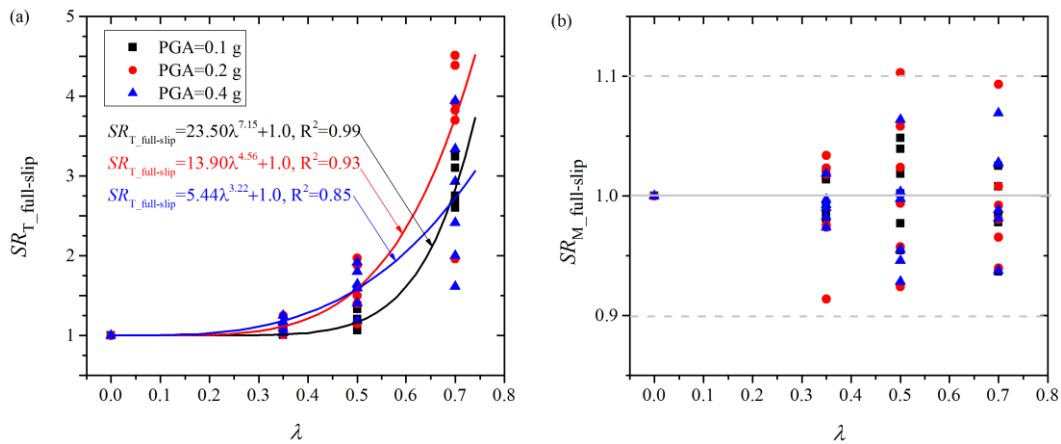


Fig. 4.18. Relationship between the SR ratios and the λ values for full-slip cases: (a) axial forces; and (b) bending moments.

Higher input motion intensity leads to larger R_T ratios, but the SR_T ratios do not always vary in the same trend. The SR_T ratios appear to increase with the increase of the motion intensities

for the no-slip conditions (Fig. 4.17a), and the effect is becoming progressively larger as the stress relaxation coefficient increases. However, the full-slip conditions present the same trend only for the stress relaxation coefficient $\lambda < 0.5$, while the maximum ratio is reported when $PGA = 0.2$ g in the case of stress relaxation coefficient $\lambda = 0.7$ (Fig. 4.18a). This phenomenon can be due to the larger axial force increment caused by the earthquake in the case of $PGA = 0.4$ g when no stress relief is considered, as shown in Fig. 4.14c.

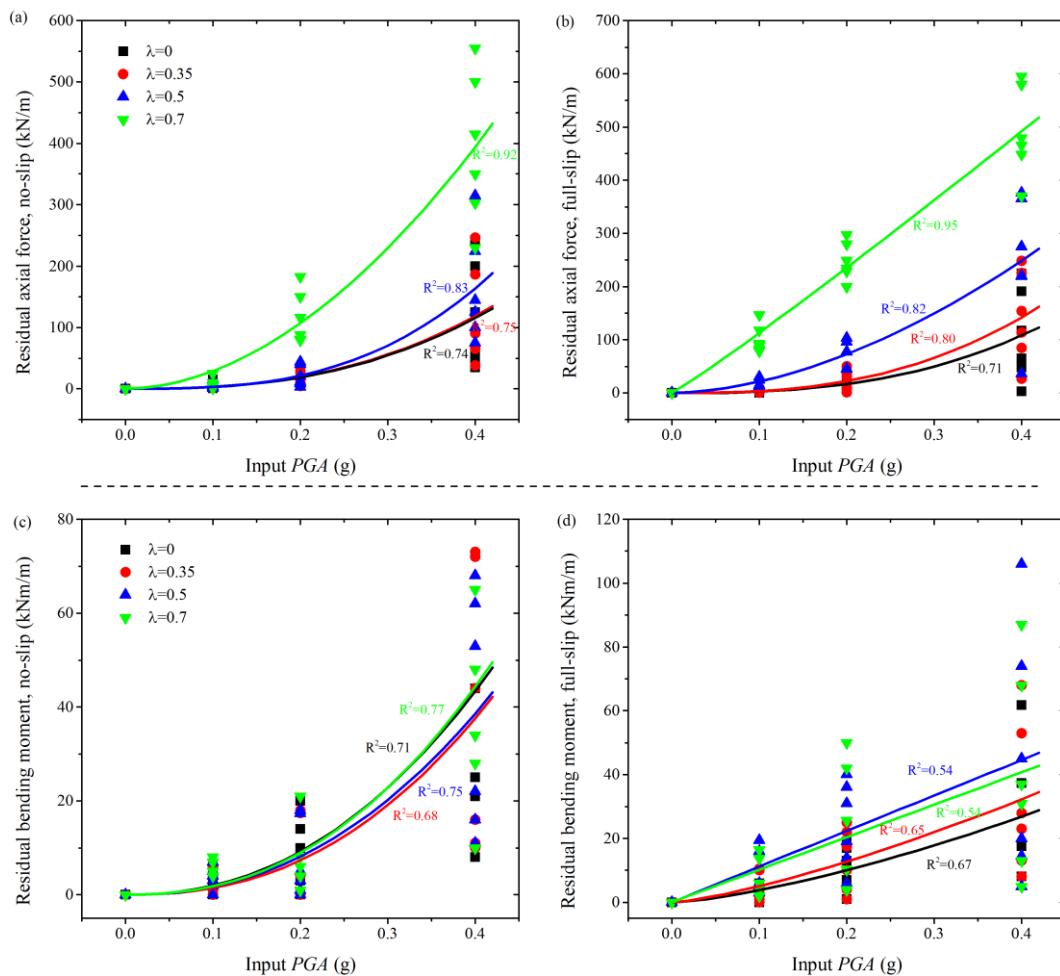


Fig. 4.19 Relationship between the residual internal forces and the λ values: (a) axial forces, no-slip; (b) axial forces, full-slip; (c) bending moments, no-slip; and (d) bending moments, full-slip.

Fig. 4.19 summarizes the residual axial forces and residual bending moments at the end of the earthquakes for all the examined cases. Similarly, the stress relaxation coefficients pronouncedly affect the calculated residual axial forces rather than the residual bending moments. The residual axial forces also increase as the stress relaxation coefficients increase.

This is more evident for the larger motion intensity (Amorosi and Boldini, 2009). However, the residual bending moments seem to be less sensitive to the stress relief process, since a weak relationship between the stress relaxation coefficients and the residual bending moments. An increase in the residual bending moment with increasing input motion intensity is observed for the two interface conditions, as expected. The results indicate that the stress relief process will, to some extent, aggravate the residual internal forces.

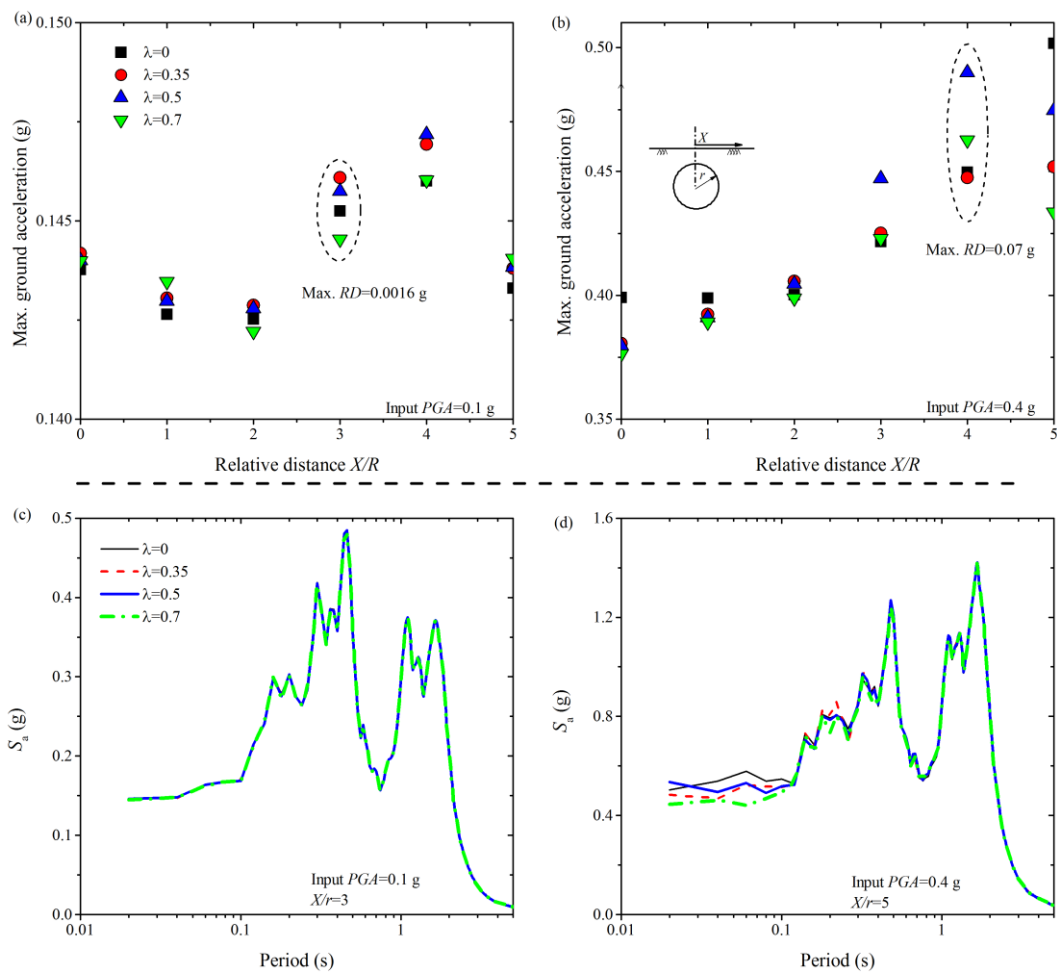


Fig. 4.20 Surface ground motions: (a) maximum ground acceleration, 0.1 g; (b) maximum ground acceleration, 0.4 g; (c) spectral acceleration, 0.1 g; and (d) spectral acceleration, 0.4 g (no-slip case, Kobe earthquake).

4.4.3 Surface ground motions

Researches on the seismic wave scattering produced by tunnels mainly focus on two aspects. The first set of works concentrates on determining the dynamic behaviour of tunnels subjected to seismic waves. The present study belongs to this set. The second set of works

focus on the diffracting effects of tunnels on the surface ground motion. To this end, here we discuss whether the stress relief during tunnelling can significantly influence the surface ground motion.

The maximum ground accelerations at various relative positions (X/r) are showed in Fig. 4.20a and 4.20b. The relative differences (RD) of the maximum ground accelerations computed by various stress relaxation coefficients are negligible with a maximum RD is equal to 0.0016 g for $PGA=0.1$ g and it is 0.07 g for the 0.4 g case. It should be noted that the stress relief process tends to slightly reduce acceleration amplitudes at the positions of $X/r=0$ and 1. This could be partly attributed to higher stress relief leads to a larger plastic zone, thus the response in the high frequency range will be filtered out because of the softening of the soil. This filtering effect can be examined according to the spectral acceleration of the ground motion, as shown in Fig. 4.20c and 4.20d. For the higher motion intensity, In general, higher stress relief levels result in slightly smaller spectral accelerations over a short period range while no difference is observed over a long period range. Another finding from this figure is that, relative to the stress relief, the surface ground motion tends to be significantly influenced by the presence of a tunnel.

4.4.4 Depth-dependent G/G_{\max} curve

The above numerical model adopts a single shear modulus reduction (G/G_{\max}) curve. It is a fact that these types of curves for soils are strongly dependent on the mean effective stress. High mean stress will result in less modulus reduction. By making the hysteretic damping depth-dependent, the simulation can be more realistic. Hence, the depth-dependent G/G_{\max} curves are used to compare its potential influence on the numerical predictions. Fig. 4.21 presents the experimental data (Bilotta *et al.*, 2014), the adopted curves, and the fitting parameters.

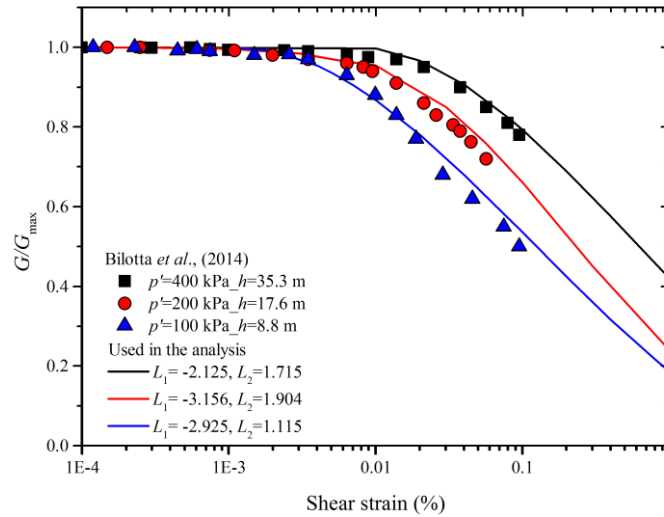


Fig. 4.21 Depth-dependent G/G_{\max} curves.

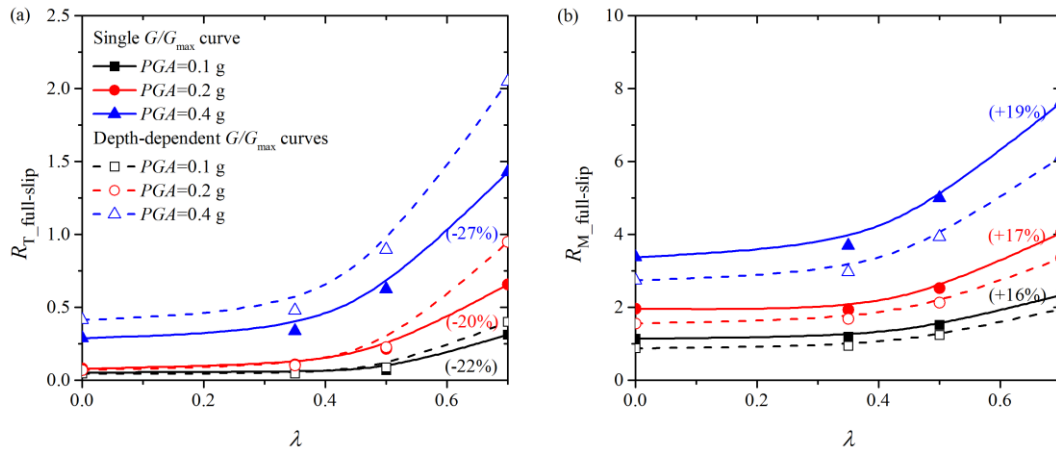


Fig. 4.22 R_T and R_M for full-slip case: (a) axial forces; and (b) bending moments.

Fig. 4.22 presents the comparison for the full-slip case in terms of R_T and R_M ratios, corresponding to Northridge ground motion. Two scenarios (i.e., single curve and depth-dependent curves) capture similar relationships between the R_T (or R_M) ratios with stress relaxation coefficients under different ground motion intensities. The results calculated by the depth-dependent G/G_{\max} curves are in well agreement with the ones of the single curve for the smaller stress relaxation coefficients and lower ground motion intensities. The difference is becoming progressively larger as the stress relaxation coefficients and ground motion intensities increase, reaching respectively differences of 27% and 19% for axial forces and bending moments. It can be concluded that the effect of the hysteretic formulation on the numerical predictions depends on the initial shear stress state (i.e., stress relaxation

coefficients) and the modulus reduction levels (i.e., ground motion intensities).

4.5 Conclusions

This chapter presents a set of two-dimensional dynamic nonlinear time-history analyses to assess the influence of the excavation-induced stress relief process on the seismic behaviour of tunnels. The soil nonlinearity is characterized through an elastic perfectly plastic model that follows the Mohr-Coulomb shear failure criterion, in combination with a built-in hysteretic model to account for the soil stiffness degradation at small strains. The convergence-confinement method is utilized to simulate the stress relief process during the tunnel excavation. Four stress relaxation coefficients, considering a range from 0 to 0.7, are selected to consider different initial stress states. The soil-tunnel interface is also considered using a series of normal and tangential springs in two extreme cases, namely the no-slip and full-slip conditions.

Before the seismic analysis, the influence of the excavation-induced stress relief on the tunnel lining forces and the surrounding soil stress states are investigated under static conditions. Increasing the stress relaxation coefficient reduces the lining forces and deformations of the tunnel whereas it increases the plastic zone in the surrounding soil. Concerning the soil-tunnel interface influence, the no-slip case corresponds to the larger axial forces and slightly larger plastic zones.

Then, six ground motions with diverse frequency characteristics and motion intensities are employed to conduct the dynamic time-history analyses. Opposite to static internal forces, the stress relief process produces substantial seismic axial force increments whereas the effect is negligible for the seismic bending moment increments. Two normalized ratios (R and SR) are introduced to quantify the stress relief influence on the seismic internal force increments.

Concerning the R ratio, the stress relief process has a more pronounced effect on the bending moments rather than on the axial forces. The effect becomes progressively larger as the stress

relaxation coefficient and the motion intensity increase. In general, the no-slip condition predicts slightly larger R_T and R_M ratios relative to the full-slip conditions. For the SR ratios, the SR_T ratio increases with increasing the stress relaxation coefficient. However, there is no clear trend between the SR_M ratios with the λ values. The residual axial forces in both the no-slip and the full-slip conditions appear to increase with the increase of the stress relaxation coefficient and ground motion intensities. The residual bending moments seem to be less sensitive to the stress relaxation coefficient.

The stress relief process has a negligible influence on the maximum ground accelerations, but the spectral acceleration in the high frequency range seems to be slightly reduced for large stress relief levels. Besides, the G/G_{\max} curve has an important influence on the numerical predictions, particularly for the larger stress relaxation coefficients and higher ground motion intensities. In general, a depth-dependent G/G_{\max} curve tends to predict larger R_T and low R_M ratios for the analyzed cases.

Chapter 5

Underlying soft soil layer-tunnel seismic interaction

5.1 Introduction

In some sites, tunnels will be excavated close to or have to pass through grounds comprising a soft soil layer. For tunnels built in such unfavourable geological conditions, special attention is required to the tunnel design due to its small elastic modulus and low strength. Historical cases as well as previous research studies have emphasized the devastating consequences of soft soil layers for the tunnel stability during its construction and operation stages (Chu and Lin, 2007; Huang *et al.*, 2013).

Earthquake damages to tunnels have demonstrated that ground condition (e.g., rock joints, faults, liquefiable layers) is one of the major factors influencing the seismic performance of tunnels (Hashash *et al.*, 2001). Some studies suggested that seismic actions on tunnels could be aggravated in unfavourable ground conditions. For example, Zhuang *et al.* (2009) observed an increase of the deformations and internal forces when a soft layer intersected a subway station. Saeid *et al.* (2015) showed that faults could influence the seismic stability of underground caverns by extending the plastic zone and increasing the displacements in the rock mass. Gomes *et al.* (2015) investigated the tunnel seismic response in a two-layered ground and the increased lining forces were observed. Yoo *et al.* (2017) stated that the presence of joints could significantly increase the tunnel bending moments, which could be 20 times higher than the ones in intact rock.

On the other hand, the presence of a soft soil layer will influence the propagation of the incoming seismic waves from bedrock, in terms of amplitude and frequency components. Opposite to the amplification effect of the surface soft soil layers, buried soft soil layers tend to attenuate the motions from bedrock in certain conditions (Bilotta *et al.*, 2015; Rayhani and El Naggar, 2008; Takahashi *et al.*, 2006). The degree of this reduction depends mainly on the buried depth, thickness, stiffness of the soft layer, and the input ground motion.

Understanding the soft soil layer-tunnel seismic interaction in a multi-layered ground is an important issue for a safe seismic design. In particular, to our knowledge, no study has considered the influence of an underlying soft soil layer on the tunnel seismic behaviour (Fig. 5.1). To fill this gap, this chapter aims:

- To provide a theoretical understanding of the mechanical mechanism behinds the soft soil layer-tunnel interaction under seismic loading from the wave motion perspective.
- To further examine how the soft soil layer affects the propagation of the ground motions in terms of acceleration, spectral acceleration, shear strain, and Arias intensity through a nonlinear seismic site response analysis.
- To obtain the possible relationships between the soft soil layer parameters and the seismic internal force increments for engineering purposes.

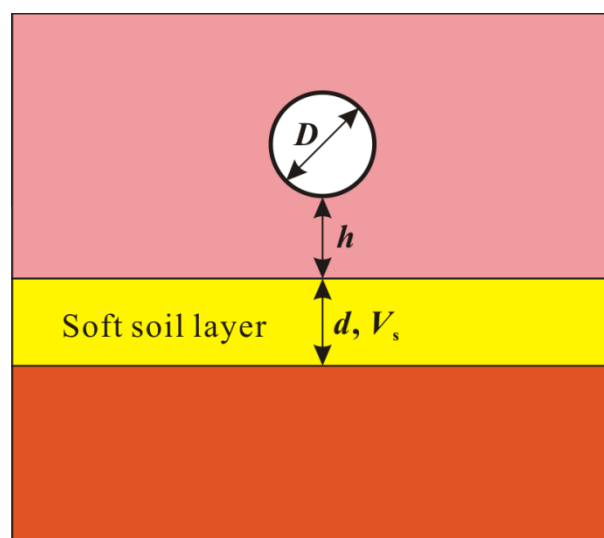


Fig. 5.1 Schematic representation of the underlying soft soil layer-tunnel interaction.

This chapter begins with an analytical study of the plane SH wave propagating through a three-layered elastic soil. It allows exploring how an elastic soft interlayer affects the incident wave. Then, nonlinear seismic site responses are performed by dynamic time-history analyses, to indicate the potential effect of a soft soil layer on the propagation of ground motions with various intensities. Subsequently, parametric analyses are conducted to investigate the seismic response of tunnels considering the variation of soft layer parameters including its thickness, shear wave velocity, and position. The last part of this chapter explores abnormal responses observed in dynamic numerical analyses and attempts to provide possible explanations.

5.2 Plane SH wave propagation in a three-layered elastic medium

5.2.1 Analytical solution

The dynamic equilibrium equations of wave propagation in an infinitely isotropic elastic medium are as follows (Liao, 2002; Xu *et al.*, 2003):

$$\begin{cases} \rho \frac{\partial^2 U_x}{\partial t^2} = (\lambda + G) \frac{\partial}{\partial x} \left(\frac{\partial U_x}{\partial x} + \frac{\partial U_y}{\partial y} + \frac{\partial U_z}{\partial z} \right) + G \nabla^2 U_x \\ \rho \frac{\partial^2 U_y}{\partial t^2} = (\lambda + G) \frac{\partial}{\partial y} \left(\frac{\partial U_x}{\partial x} + \frac{\partial U_y}{\partial y} + \frac{\partial U_z}{\partial z} \right) + G \nabla^2 U_y \\ \rho \frac{\partial^2 U_z}{\partial t^2} = (\lambda + G) \frac{\partial}{\partial z} \left(\frac{\partial U_x}{\partial x} + \frac{\partial U_y}{\partial y} + \frac{\partial U_z}{\partial z} \right) + G \nabla^2 U_z \end{cases} \quad (5.1)$$

where U_x , U_y , U_z is the displacement in the x -, y -, and z -direction respectively; λ is the Lamé constant, ρ is the density; G is the shear modulus; ∇^2 is the Laplace operator.

For the plane SH wave,

$$U_x = U_y = 0 \quad (5.2)$$

Hence, Eq. 5.1 can be simplified:

$$\rho \frac{\partial^2 U_z}{\partial t^2} = G \nabla^2 U_z \quad (5.3)$$

For the plane SH wave passing through the three-layered elastic medium, as shown in Fig. 5.2, the displacement in the medium 1, medium 2, and medium 3 can be derived as follows:

$$\begin{cases} U_{z1} = A_1 e^{ik(y+P_1x-ct)} + B_1 e^{ik(y-P_1x-ct)} & X \leq 0 \\ U_{z2} = A_2 e^{ik(y+P_2x-ct)} + B_2 e^{ik(y-P_2x-ct)} & 0 \leq X \leq d \\ U_{z3} = A_3 e^{ik(y+P_3x-ct)} & X \geq d \end{cases} \quad (5.4)$$

$$c = \omega/k \quad (5.5)$$

$$\omega = 2\pi f \quad (5.6)$$

$$\begin{cases} P_1^2 = \frac{c^2}{V_{s1}^2} - 1 \\ P_2^2 = \frac{c^2}{V_{s2}^2} - 1 \\ P_3^2 = \frac{c^2}{V_{s3}^2} - 1 \end{cases} \quad (5.7)$$

where U_{z1} , U_{z2} , U_{z3} , is the displacement of the wave in the medium 1, 2, and 3, respectively; $i = \sqrt{-1}$; A_1 , B_1 , is the amplitude of the incident wave, reflected wave in the medium 1 respectively; A_2 , B_2 , is the amplitude of the refracted wave, reflected wave in the medium 2 respectively; A_3 is the amplitude of the transmitted wave in the medium 3; V_{s1} , V_{s2} , V_{s3} is the shear wave velocity in the medium 1, medium 2, and medium 3 respectively.

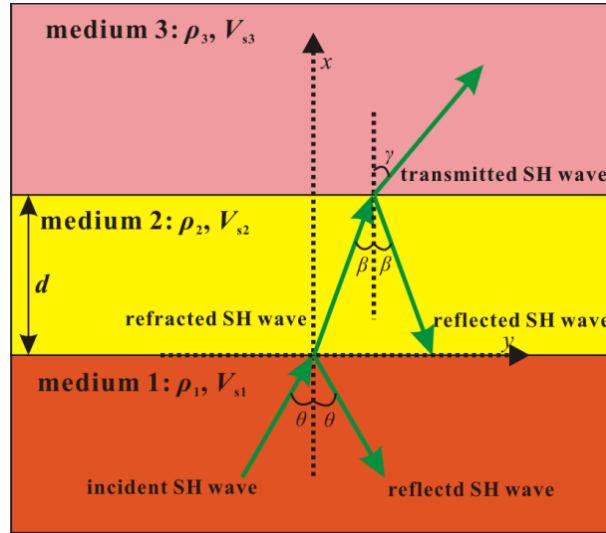


Fig. 5.2 Propagation path of plane *SH* wave.

Five unknown parameters (A_1 , A_2 , A_3 , B_1 , and B_2) in Eq. 5.4 which can be determined based on the conditions at the interfaces. At the interfaces between medium 1 and medium 2, medium 2 and medium 3, stress equilibrium and displacement continuity must be satisfied, as presented in Fig. 5.3. At the interface between medium 1 and medium 2 ($x=0$, $y=0$):

$$\begin{cases} A_1 + B_1 = A_2 + B_2 \\ \rho_1 V_{s1}^2 (A_1 P_1 - B_1 P_1) = \rho_2 V_{s2}^2 (A_2 P_2 - B_2 P_2) \end{cases} \quad (5.8)$$

At the interface between medium 2 and medium 3 ($x=d$, $y=0$):

$$\begin{cases} A_2 e^{-ikP_2 d} + B_2 e^{-ikP_2 d} = A_3 e^{-ikP_3 d} \\ \rho_2 V_{s2}^2 (A_2 P_2 e^{-ikP_2 d} - B_2 P_2 e^{-ikP_2 d}) = \rho_3 V_{s3}^2 A_3 P_3 e^{-ikP_3 d} \end{cases} \quad (5.9)$$

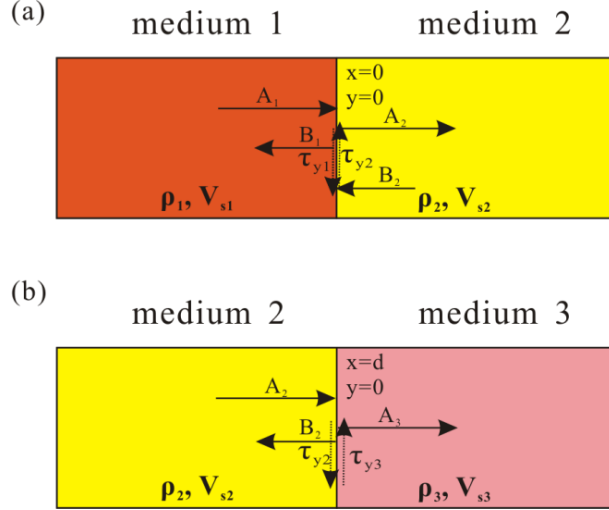


Fig. 5.3 Interface conditions: (a) medium 1 and medium 2; and (b) medium 2 and medium 3.

Hence, by calculating Eqs. 5.8 and 5.9, the transmission coefficient, defined as the ratio between the amplitude of the transmitted wave and the one of the vertically incident *SH* wave ($\theta=0^\circ$) can be derived:

$$\frac{A_3}{A_1} = \frac{4a_5 e^{-i\omega d(m_1+m_2)/V_{s1}}}{a_2 a_3 e^{-2i\omega d m_1/V_{s1}} + a_1 a_4} \quad (5.10)$$

And,

$$\begin{cases} a_1 = 1 - \frac{\rho_2 V_{s2}}{\rho_1 V_{s1}} \\ a_2 = \frac{\rho_2 V_{s2} + \rho_3 V_{s3}}{\rho_1 V_{s1}} \\ a_3 = 1 + \frac{\rho_2 V_{s2}}{\rho_1 V_{s1}} \\ a_4 = \frac{\rho_2 V_{s2} - \rho_3 V_{s3}}{\rho_1 V_{s1}} \\ a_5 = \frac{\rho_2 V_{s2}}{\rho_1 V_{s1}} \end{cases} \quad (5.11)$$

Based on Eqs. 5.10 and 5.11, the relationships between the transmission coefficient and the interlayer parameters (i.e., V_{s2} , ρ_2 , d) for various incident wave frequencies (i.e., f) can be examined.

5.2.2 Parametric analysis

The parameters adopted for the medium 1 and medium 3 are as follows: $\rho_1=\rho_3=1900 \text{ kg/m}^3$, $V_{s1}=V_{s3}=1000 \text{ m/s}$, while the parameters of the interlayer will vary according to the study

cases.

- To investigate the relationships between the transmission coefficient and the interlayer thickness, the following parameters are assumed: $\rho_2=1600 \text{ kg/m}^3$, $V_{s2}=50$, 200 m/s , f varies from 0.5 to 20 Hz , and d changes from 0 to 15 m (Fig. 5.4).
- To investigate the relationships between the transmission coefficient and the interlayer shear wave velocity, the following parameters are assumed: $\rho_2=1600 \text{ kg/m}^3$, $d=5 \text{ m}$, $\rho_2=800, 1600 \text{ kg/m}^3$, f varies from 0.5 to 20 Hz and V_{s2} changes from 50 to 800 m/s (Fig. 5.5).
- To investigate the relationships between the transmission coefficient and the interlayer density, the following parameters are assumed: $\rho_2=1600 \text{ kg/m}^3$, $d=5 \text{ m}$, $f=8$, 20 Hz , ρ_2 varies from 800 to 1900 kg/m^3 , and V_{s2} changes from 50 to 800 m/s (Fig. 5.6).

It should be noted that a dimensionless parameter is introduced here to normalize the relationship between the frequency, thickness, and shear wave velocity. The normalized wavelength is calculated as follows:

$$d/\lambda_w = d \cdot f/V_{s2} \quad (5.12)$$

Fig. 5.4 shows that the transmission coefficients dramatically decrease with increasing interlayer thickness, particularly for $V_{s2}=50 \text{ m/s}$ case. In this case, transmission coefficients show less sensitive to the thickness and the frequency. Oppositely, the transmission coefficients gradually decrease with the increase of both thickness and frequency ($V_{s2}=200 \text{ m/s}$). Larger transmission coefficients are observed for some pairs of (d, f) , due to the interlayer thickness is an integer multiple of the half-wavelength (i.e., $d/\lambda_w=0.5, 1.0, 1.5$). The results have demonstrated that the interlayers with different thicknesses will have an identical effect on the incident waves with various frequencies if the normalized wavelengths are the same.

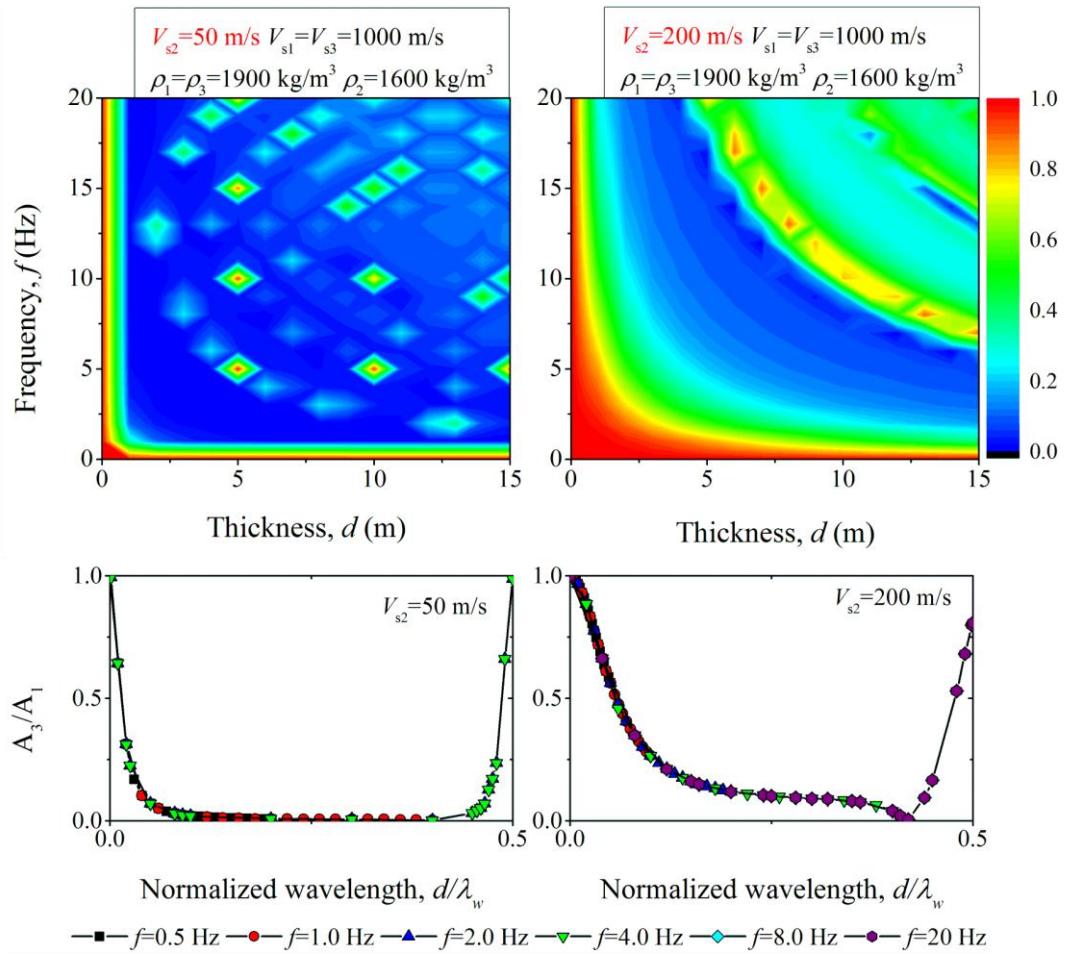


Fig. 5.4 Effect of the interlayer thickness on the transmission coefficients.

The relationships between the transmission coefficient and the interlayer shear wave velocity for various incident wave frequencies are presented in Fig. 5.5. In general, the transmission coefficients increase with increasing interlayer shear wave velocity. This is more evident for a larger density case ($\rho_2=1600 \text{ kg/m}^3$). For the same V_{s2} , high frequency incident wave tends to be de-amplified. Fig. 5.6 presents the relationships between the transmission coefficient and the density for various soil shear wave velocities. As can be seen, with the increase of the density, the transmission coefficients slightly increase and its influence is relatively secondary compared to the shear wave velocity.

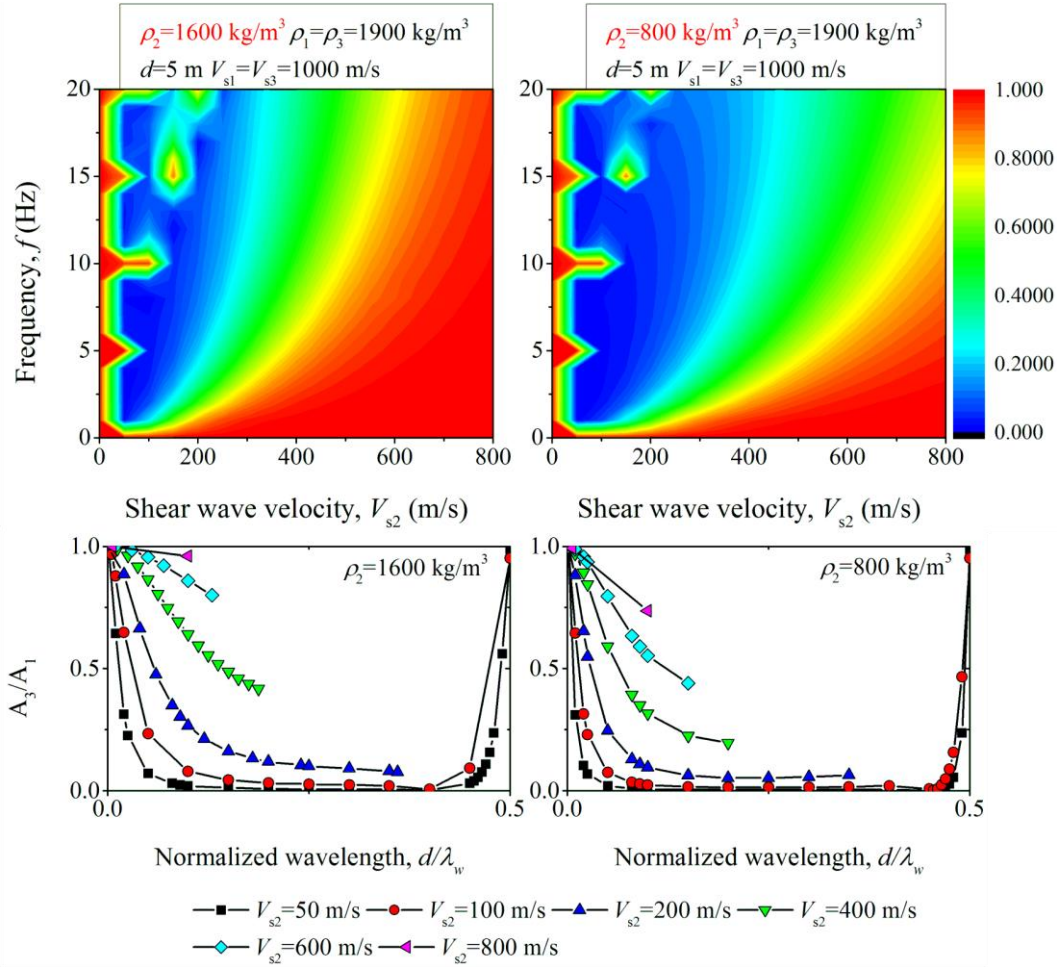


Fig. 5.5 Effect of the interlayer shear wave velocity on the transmission coefficients.

The analytical work provides a basic understanding of how an elastic soft interlayer affects wave propagation. In general, a soft interlayer can effectively reduce the amplitude of the transmitted wave in a certain range of the frequency, depending mainly on the interlayer thickness, density, and shear wave velocity. On the other hand, soil presents shear stiffness degradation and damping buildup in a seismic condition; meanwhile, the real ground motions covering a wide range of the frequency component. The amplification or de-amplification of the ground motion also appears during the wave propagation, which depends heavily on the site conditions, soil parameters, and characteristics of the input motions, etc. These factors complicate the propagation characteristic of the wave passing through a soft soil layer in the nonlinear medium. The presence of a soft soil layer is expected to modify the propagation of incoming waves from the bedrock and changes the soil dynamic behaviour, thus the seismic

behavior of the tunnels buried in the soil is undoubtedly influenced. Hence, this issue will be examined by the dynamic time-history analysis in the following parts.

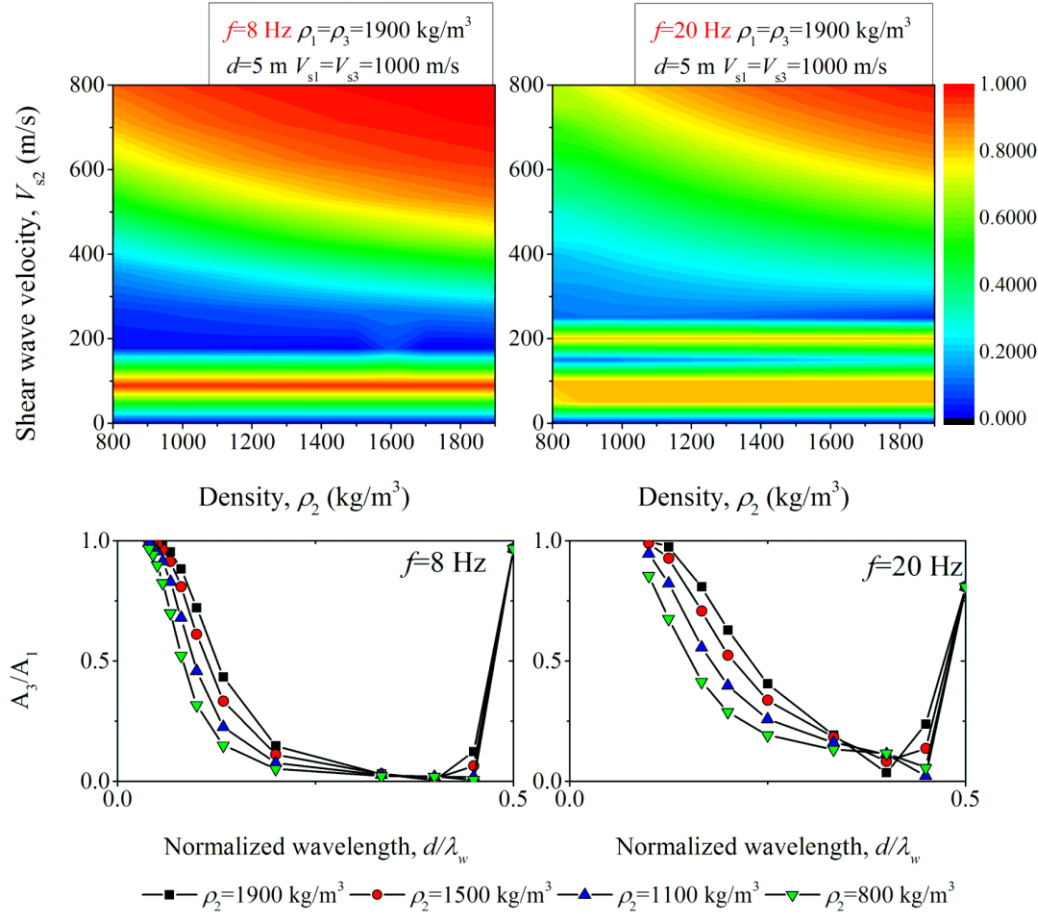


Fig. 5.6 Effect of the interlayer density on the transmission coefficients.

5.3 Soft soil layer-tunnel system

5.3.1 Outline of the idealized problem

An ideal deposit of soil, which is characterized by a nonlinear shear stiffness G_0 increasing with depth adopting the Eq. 5.13 (Viggiani and Atkinson, 1995), is assumed as the reference soil profile.

$$\frac{G_0}{p_r} = A \cdot \left(\frac{p'}{p_r}\right)^n \cdot R_0^m \quad (5.13)$$

where p_r is a reference pressure taken equal to 1 kPa, p' is the mean effective pressure, A , n ,

and m are the soil parameters related to the plasticity index and over-consolidation ratio. Their values are respectively equal to 1400, 0.85, and 0.35 based on the recommendation (Viggiani and Atkinson, 1995). The corresponding shear wave velocity profile is shown in Fig. 5.7 (black line), an example of a site comprising a soft layer is presented as well (red line). The subsoil profile used here is similar to the one adopted in the previous studies (Amorosi and Boldini, 2009; Visone *et al.*, 2009).

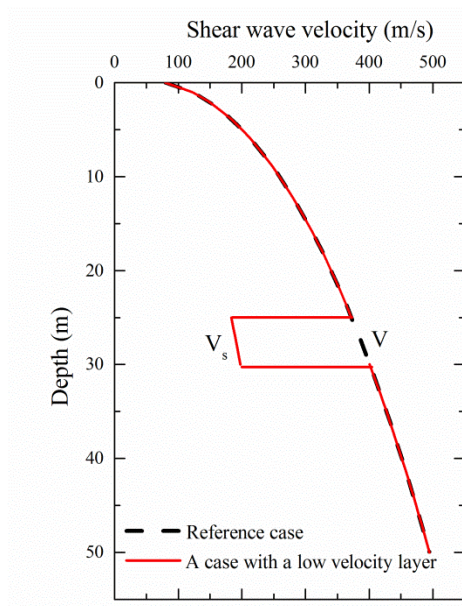


Fig. 5.7 Schematic representation of the shear wave velocity profile.

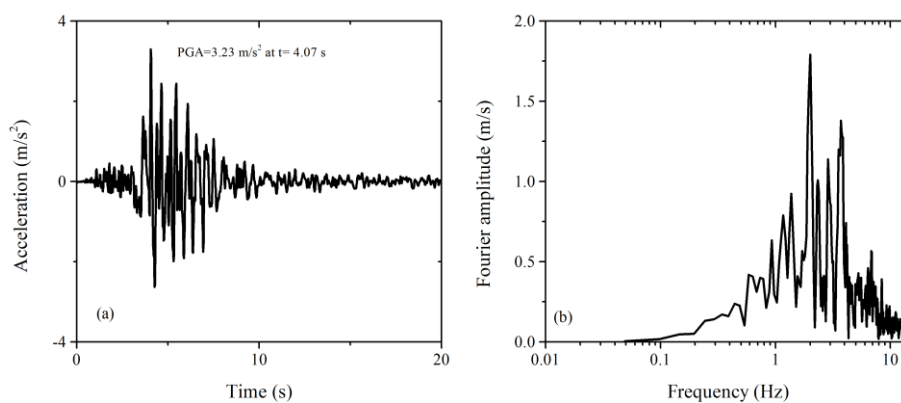


Fig. 5.8 Seismic input motion: (a) acceleration time-history; and (b) Fourier spectrum.

The seismic input motion selected in this study for the dynamic time-history analysis is the accelerometer registration at the Tolmezzo station of the Friuli earthquake (Italy) on May 6th,

1976. The peak acceleration of the original acceleration is 0.35 g with a duration time of 36.32 s. The higher energy of this motion is focused on the frequency ranges from 1 to 4 Hz with a predominant frequency at 2 Hz. Only the first 20 seconds are selected and the frequencies higher than 10 Hz (Fig. 5.8) are filtered out to limit the minimum element size adopted in the numerical model.

5.3.2 Model details

The two-dimensional numerical model with a height of 50 m and a width of 100 m is built, as shown in Fig. 5.9. As a relatively shallow circular tunnel is more vulnerable than a deep tunnel under earthquake loading, the buried depth of the tunnel centre is defined as 15 m.

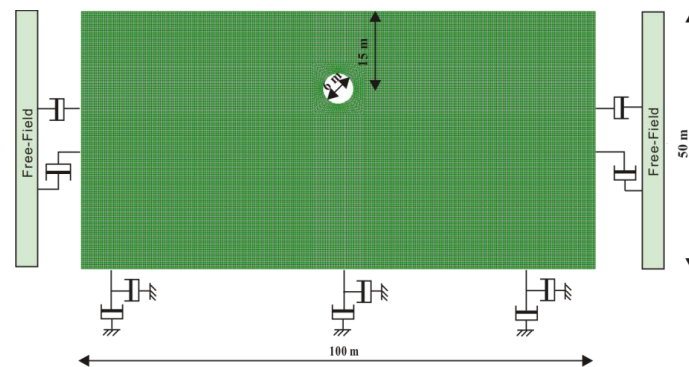


Fig. 5.9 Numerical model used in the dynamic analysis.

The boundary condition, seismic input method, soil-tunnel interface model, and the constitutive models for soil and the tunnel structure are the same as the ones used in the previous chapters, which are not presented here for the sake of the brevity. The soil and tunnel parameters used for analysis are taken from the literature and correspond to real soil parameter values (Bilotta *et al.*, 2015; Rayhani and El Naggar, 2008), as shown in Table 5.1. The tunnel excavation process is simulated using the convergence-confinement method with 20% of stress relaxation.

Table 5.1 Properties of the soil and tunnel lining.

| Parameters | Reference case | Soft soil case | Tunnel lining |
|--|-----------------|----------------|---------------|
| <i>Property of the soil</i> | | | |
| Unit weight, ρ (kN/m ³) | 19 | 19 | |
| Shear wave velocity, V_s (m/s ²) | Fig. 5.7 | Table 5.2 | |
| Poisson's ratio, ν_s | 0.3 | 0.32 | |
| Internal friction angle, φ (°) | 20 | 15 | |
| Cohesion, c (kPa) | 8 | 5 | |
| Lateral earth pressure coefficient, K_0 | 0.5 | 0.5 | |
| <i>Property of the tunnel</i> | | | |
| Young's modulus E_1 (GPa) | | | 30 |
| Poisson's ratio, ν_1 | | | 0.2 |
| Lining thickness, t (m) | | | 0.3 |
| Diameter, D (m) | | | 6 |
| <i>Property of the soil-tunnel interface</i> | | | |
| Normal spring stiffness, K_n (N/m) | 4×10^9 | | |
| Tangential spring stiffness, K_s (N/m) | 4×10^9 | | |

The hysteretic damping and the Rayleigh damping are also employed in the numerical model. Similarly, the shear modulus reduction of clay proposed by Sun *et al.* (1988) is used for matching the “default” hysteretic model implemented in the numerical code. In this chapter, a relatively smaller damping ratio (0.2%) is utilized to remove the possible high frequency noise and to minimize the negative effect on the numerical predictions caused by the misuse of improper damping parameters (Sun and Dias, 2018). This is appropriate when additional hysteretic damping as well as a quiet boundary condition is incorporated in the numerical model (Itasca, 2011).

Table 5.2 Analysis cases in the numerical model.

| Cases | Parameters |
|---------------------------------------|------------------------------|
| Location, h/D | 0.5; 1.0; 1.5; 2.0 |
| Relative thickness, d/D | 0; 1/6; 0.5; 1.0; 1.5; 2.0 |
| Relative shear wave velocity, V_s/V | 0.2; 0.3; 0.4; 0.5; 0.7; 1.0 |
| Peak ground acceleration, PGA (g) | 0.1; 0.2; 0.3 |

The analysis cases listed in Table 5.2 are performed to investigate how an underlying soft

layer affects the propagation of the ground motion and the seismic internal force increments in the tunnel lining. The examined parameters (Fig. 5.1) including the soft soil layer relative location h/D ; the relative soft soil layer thickness d/D ; the relative shear wave velocity V_s/V ; and the input motion intensities PGA .

5.4 Numerical results

The first part investigates the seismic response of a site comprising a soft layer, corresponding to the case of $h/D=d/D=1.0$, $PGA=0.1, 0.2, \text{ and } 0.3 \text{ g}$. The shear wave velocity of the soft layer is considered as a variable ($V_s/V=0.3, 0.5, 0.7, 1.0$). The second part investigates the influence of an underlying soft soil layer on the seismic response of a tunnel in terms of the seismic-induced internal forces in the tunnel lining, considering the cases listed in Table 5.2.

5.4.1 Free-field case

Representative numerical predictions at the ground surface for four V_s/V values in the case of $PGA=0.1 \text{ g}$ are shown in Fig. 5.10, in terms of the spectral accelerations (5% damping, Fig. 5.10a) and spectral ratios (Fig. 5.10b). The soft layer tends to reduce the maximum response spectra amplitude with the effect is becoming gradually larger as the relative shear wave velocity decreases. The peak amplitude decreases from 18 m/s^2 for a homogenous site to 7 m/s^2 for a site with $V_s/V=0.3$. Besides, the response spectra amplitude moves toward longer periods and a multi-peak phenomenon of the response spectra appears as the relative velocity decreases. This could be attributed to the increase of the fundamental period due to the presence of the soft soil layer.

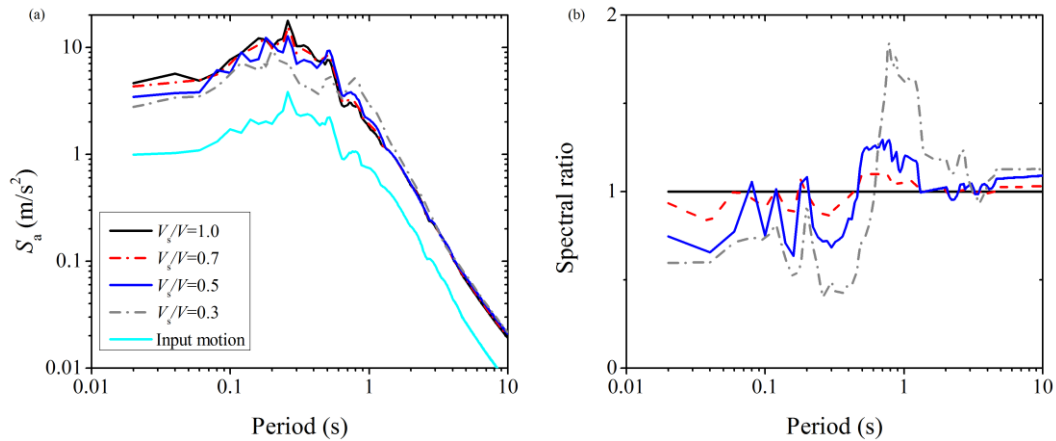


Fig. 5.10 Effects of a soft soil layer on the spectral accelerations and spectral ratios.

Although the soft soil layer attenuates response at the short period of ground motion, significant amplification at the longer period is observed as the spectral ratio progressively increases from 1 for a homogenous site to a maximum ratio of 1.8, as noted in Fig. 5.10b. It indicates that the soft soil layer is not always reducing the acceleration response, which is related strongly to the frequency components of the input ground motions. This is in agreement with the findings of the theoretical study.

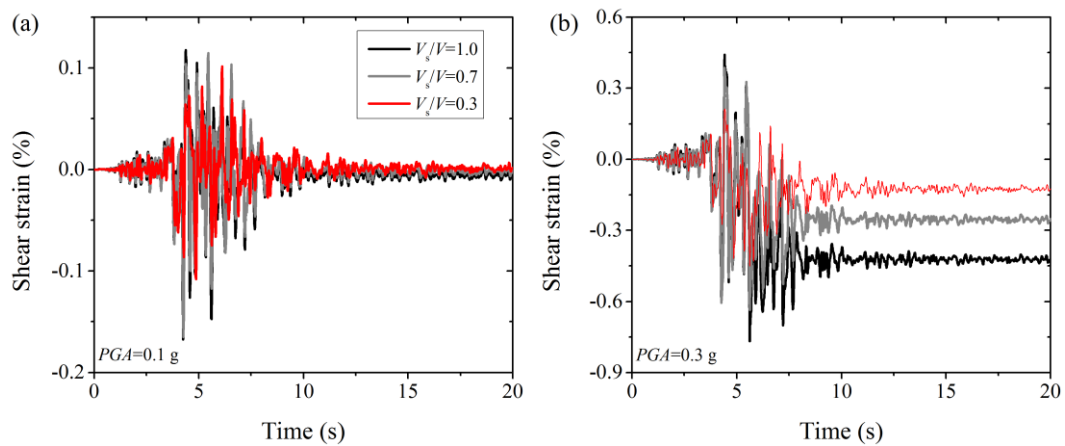


Fig. 5.11 Shear strain time-histories for three relative velocities: (a) $PGA=0.1$ g; and (b) $PGA=0.3$ g.

Fig. 5.11 plots the shear strain time-histories at depth equals to 2 m (where the maximum shear strain appears) for different relative shear wave velocities. The results indicate that the soft soil layer can reduce both the maximum shear strains and the residual shear strains, particularly for the higher motion intensity. In this case, the residual shear strain is decreased

by about 75%, from 0.0042 for a homogenous soil layer to 0.0013 for a site with $V_s/V=0.3$. The residual shear strain appears at the end of the earthquake event produces significant residual internal forces in the tunnel lining due to the irreversible plastic deformation of soil (Amorosi and Boldini, 2009). Thus, it can be speculated that a reduction of the residual internal forces at the end of an earthquake occurs due to the presence of a soft soil layer.

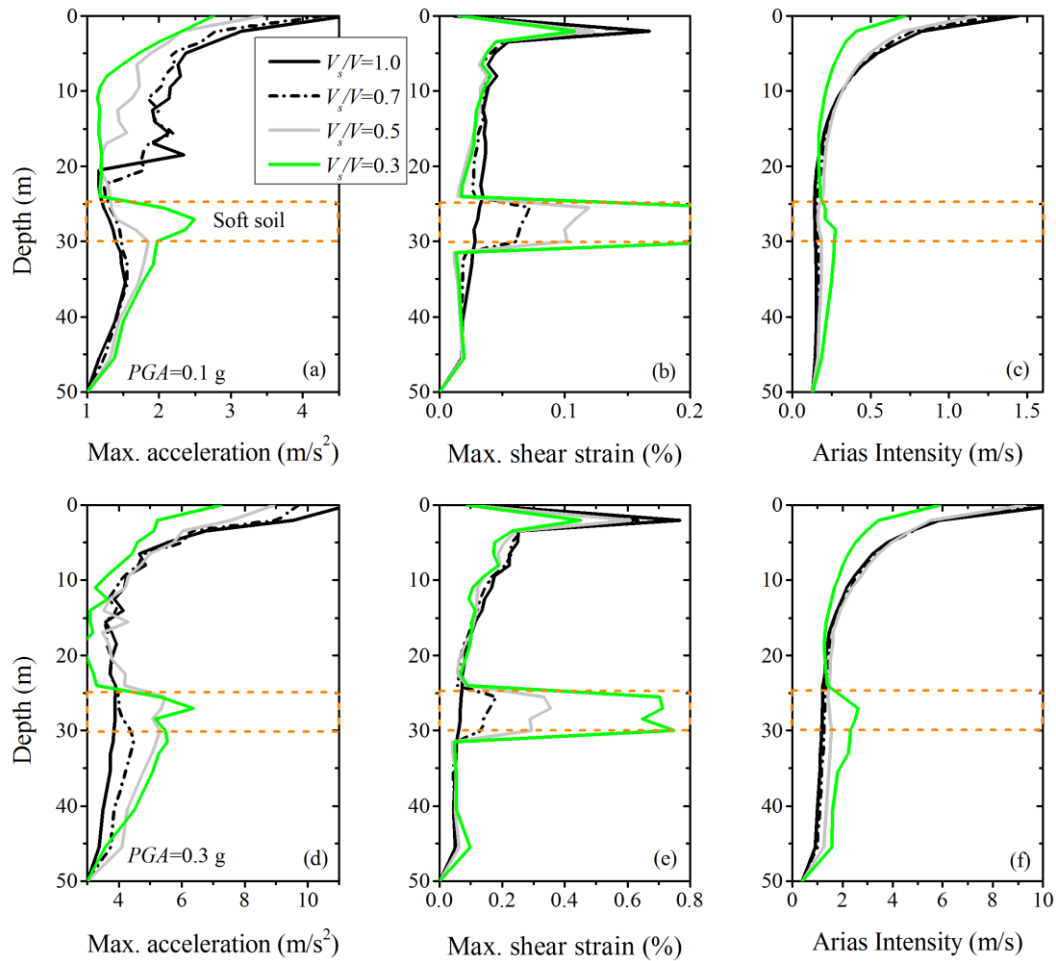


Fig. 5.12 Profiles of the maximum acceleration, maximum shear strains, and Arias intensity.

The responses in terms of maximum acceleration, maximum shear strains, and Arias intensity are shown in Fig. 5.12. The figures indicate that the presence of the soft soil layer tends to amplify the acceleration and Arias intensity for the soil beneath the soft soil layer (depth 30~50 m). This may be due to the reflection of the incident wave occurring at the interface between the upper soft soil layer and the lower stiff soil layer (depth 30 m); hence, more energy is accumulated in this area. Inside the soft soil layer (24~30 m), significant

amplification on the three calculated parameters is observed due to the low soil shear modulus. This is more evident for the shear strains in comparison with acceleration and Arias intensity. For response in the top 24 m, the presence of a soft soil layer reduces the acceleration, strains, and Arias intensity responses as compared to the homogenous site. In general, the soft soil layer effect is more pronounced when the relative shear wave velocity is smaller. Different motion intensities capture a similar trend, and a maximum reduction of ~40% for maximum acceleration and around 50% for Arias intensity at the ground surface is observed for a weak motion (0.1 g). A strong motion (0.3 g) seems to induce a relatively small amplification of maximum acceleration (32%) and Arias intensity (45%), because of a larger soil damping.

In summary, the comparisons of the free-field case highlight the potential beneficial effect of the soft soil layer on the responses of acceleration, shear strain, and Arias intensity (above the soft soil layer). Besides the soil stiffness degradation, the presence of a soft soil layer further increases the fundamental period of the site. Therefore, the response at a long period is amplified and the response at a short period is suppressed. Moreover, the soft soil layer will dissipate more earthquake energy due to the increased soil damping. On the other hand, the impedance ratio between the soft soil layer and the underlying stiff soil layer results in the reflection of the input motion, rather than transmission to the upper layers. Hence, the energy is probably trapped inside the soft soil layer due to wave reflection and refraction, leading to a significant increase of the accelerations, strains, and Arias intensity of the soft soil layer. Similar evidence was provided in the centrifuge tests performed by [Rayhani and El Naggar \(2008\)](#), which demonstrated that a soft soil trapped between stiff layers was responsible for reducing the peak ground acceleration. However, it is worth noticing that the soft soil layer amplifies the response at long periods, particularly for a very soft soil layer.

5.4.2 Soil-tunnel system

In this section, various cases (see Table [5.2](#)) are investigated through the parametric numerical analysis. The distributions of the seismic internal force increments and the modification ratios of the lining forces caused by the underlying soft soil layer are presented.

5.4.2.1 Effect of the relative velocity

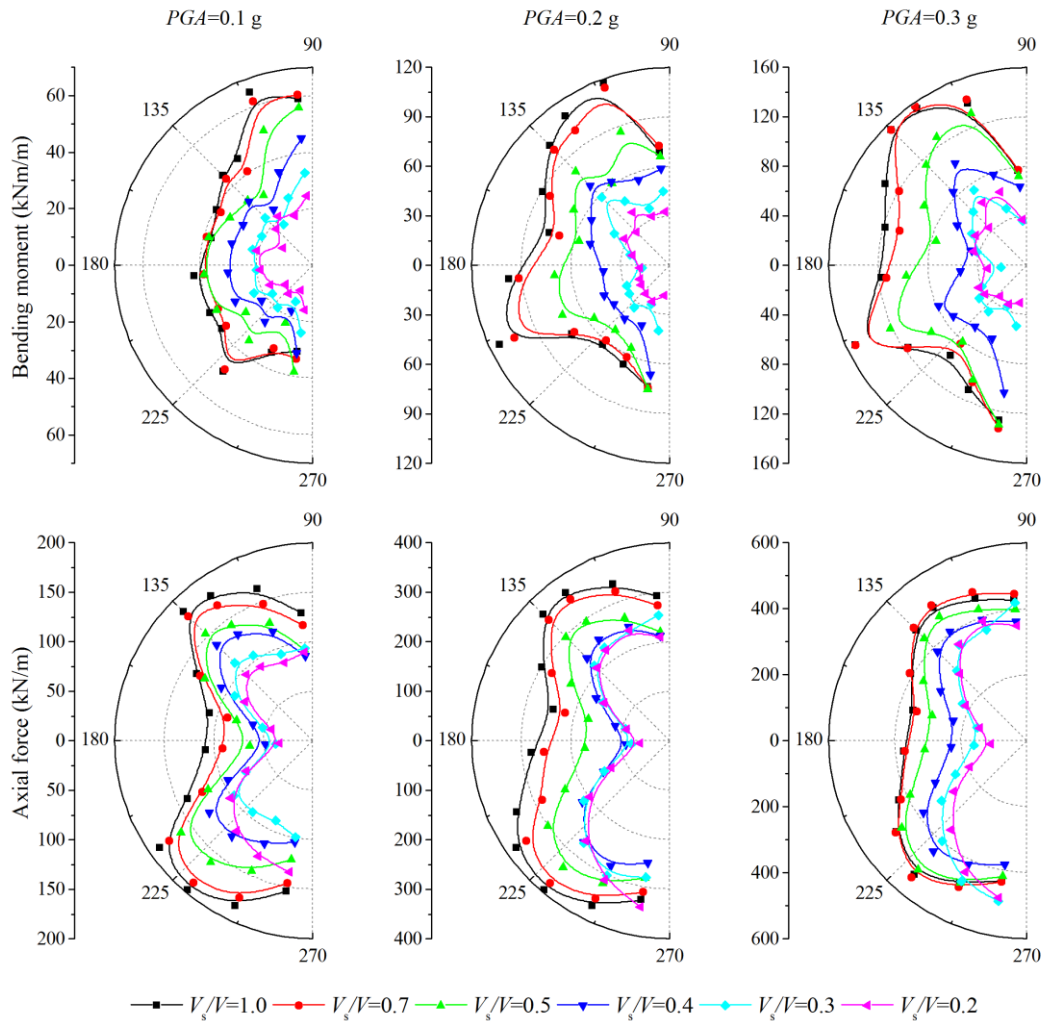


Fig. 5.13 Distributions of the seismic internal force increments for different relative shear wave velocities.

Fig. 5.13 presents the typical distribution of the seismic internal force increments for various V_s/V values, corresponding to $h/D=d/D=1.0$, and $PGA=0.1, 0.2$, and 0.3 g. The stress redistribution around the tunnel caused by the irreversible soil plastic deformations produces a complicated distribution of internal force. The soft layer tends to modify the lining forces in terms of distribution and magnitude with the effect is becoming gradually larger as the relative shear wave velocity decreases. In general, the maximum dynamic internal forces decrease due to the presence of the soft soil layer. For the 0.1 g case, the bending moment at $\theta=135^\circ$ increases from 13 kNm/m for $V_s/V=0.2$ to 50 kNm/m for the homogenous site whereas the axial force varies from 120 kN/m to around 200 kN/m. It is worth remarking that

the maximum axial force is observed around the tunnel invert for a very soft soil case (i.e., $V_s/V=0.2$). This is different from the distribution of axial force in other cases. It could be attributed to the fact that a soft soil layer with very low stiffness is more vulnerable to yielding and causes large plastic deformation near the tunnel invert even at small motion intensities (Amorosi and Boldini, 2009).

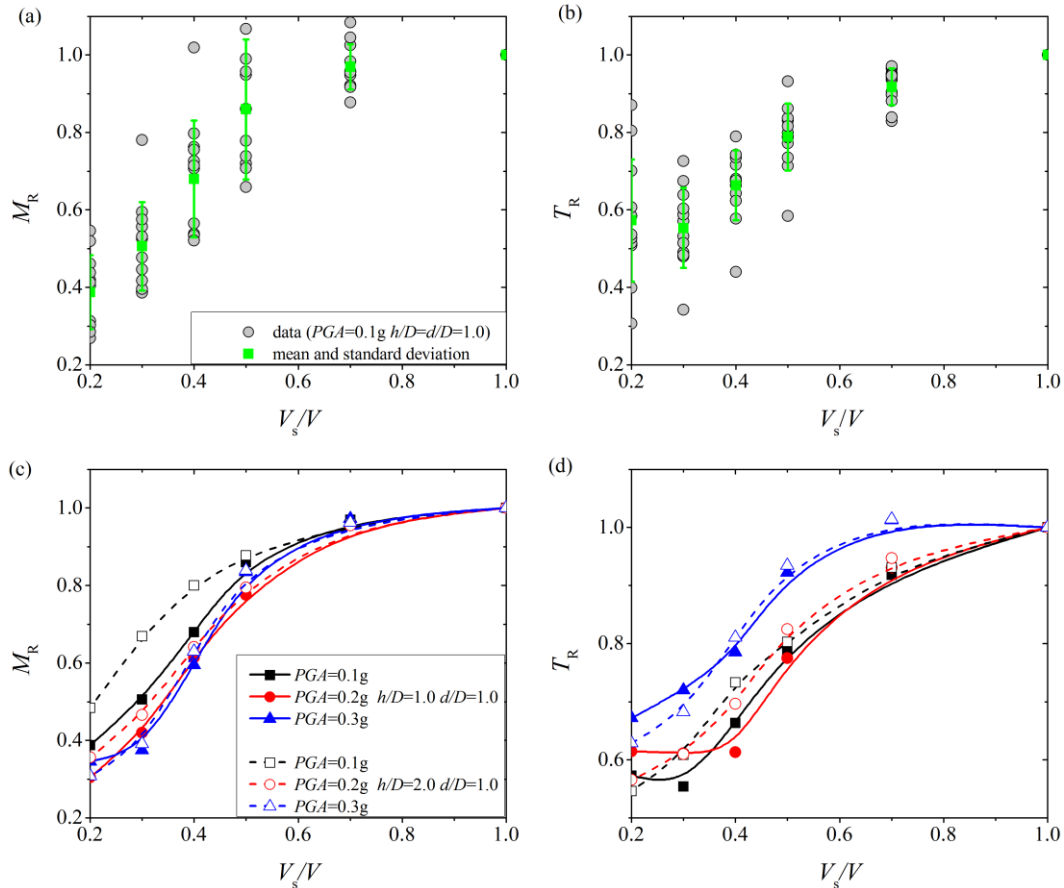


Fig. 5.14 Modification ratios versus relative shear wave velocities.

To quantify the effect of a soft soil layer on the seismic internal force increments, the modification ratio of the seismic internal force increments is introduced, which is defined as the ratio of the seismic internal force increments for the soft soil layered site to the ones for the homogenous case. It should be noted that the modification ratio is averaged from twelve calculated lining forces, to avoid the impact of abnormal results observed at tunnel invert for some cases. As an example, the values of M_R and T_R versus V_s/V are presented respectively in Figs. 5.14a and 5.14b, corresponding to the results shown in Fig. 5.13.

Figs. 5.14c and 5.14d present the modification ratios of the axial forces and bending moments for different relative shear wave velocities, corresponding to $d/D=1.0$, $h/D=1.0$, and 2.0 , $PGA=0.1$, 0.2 , and 0.3 g. The values of M_R and T_R increase with increasing relative shear wave velocity. A rapid increase is found when the V_s/V changes from 0.2 to 0.5 and the changes become gradually smaller when the V_s/V increases from 0.5 to 1.0 . Although the values of M_R and T_R show a similar trend, larger T_R ratios are reported compared to the M_R . It indicates that the relative shear wave velocity has a more significant effect on the bending moment rather than on the axial force.

The location of the soft soil layer effect (i.e., h/D) on the internal force cannot be ignored. Moving the soft soil layer close to the tunnel (a distance of one-time tunnel diameter) will lead to an additional reduction of the lining forces. The effect becomes progressively unimportant as the relative shear wave velocity increases. The results also report that larger motion intensity (i.e., 0.3 g) leads to a smaller ratio of the bending moment and a larger ratio of the axial force. The discrepancy of the M_R values arisen by the motion intensity becomes minor with the increase of V_s/V . Thus, it can be concluded that the reduction effect of the soft soil layer on the seismic internal force increment is gradually decreasing with increasing shear wave velocity of the soft soil layer. This is consistent with the findings in the theoretical study and the free-field case.

5.4.2.2 Effect of the relative thickness

Figs. 5.15 and 5.16 present the relationships between the relative thickness (i.e., d/D) of the soft soil layer and seismic internal force increments. The distributions of the seismic internal force increments are shown in Fig. 5.15 ($h/D=1.0$, $V_s/V=0.3$, $PGA=0.1$, 0.2 , and 0.3 g) while Fig. 5.16 presents the modification ratios of the lining force versus the relative thickness corresponding to $h/D=1.0$, $V_s/V=0.3$, and 0.7 , $PGA=0.1$, 0.2 , and 0.3 g.

As can be seen in Fig. 5.15, the maximum lining force is not always decreasing linearly as the relative thickness increase, while the $d/D=2.0$ case induces larger internal forces than the ones

calculated in $d/D=1.0$ case for weak ground motions (i.e., 0.1 g). As the motion intensity increases, the difference of the lining forces between $d/D=1.0$ and $d/D=2.0$ generally becomes minor. The reasons for this abnormal tunnel response will be explored in section 5.5.

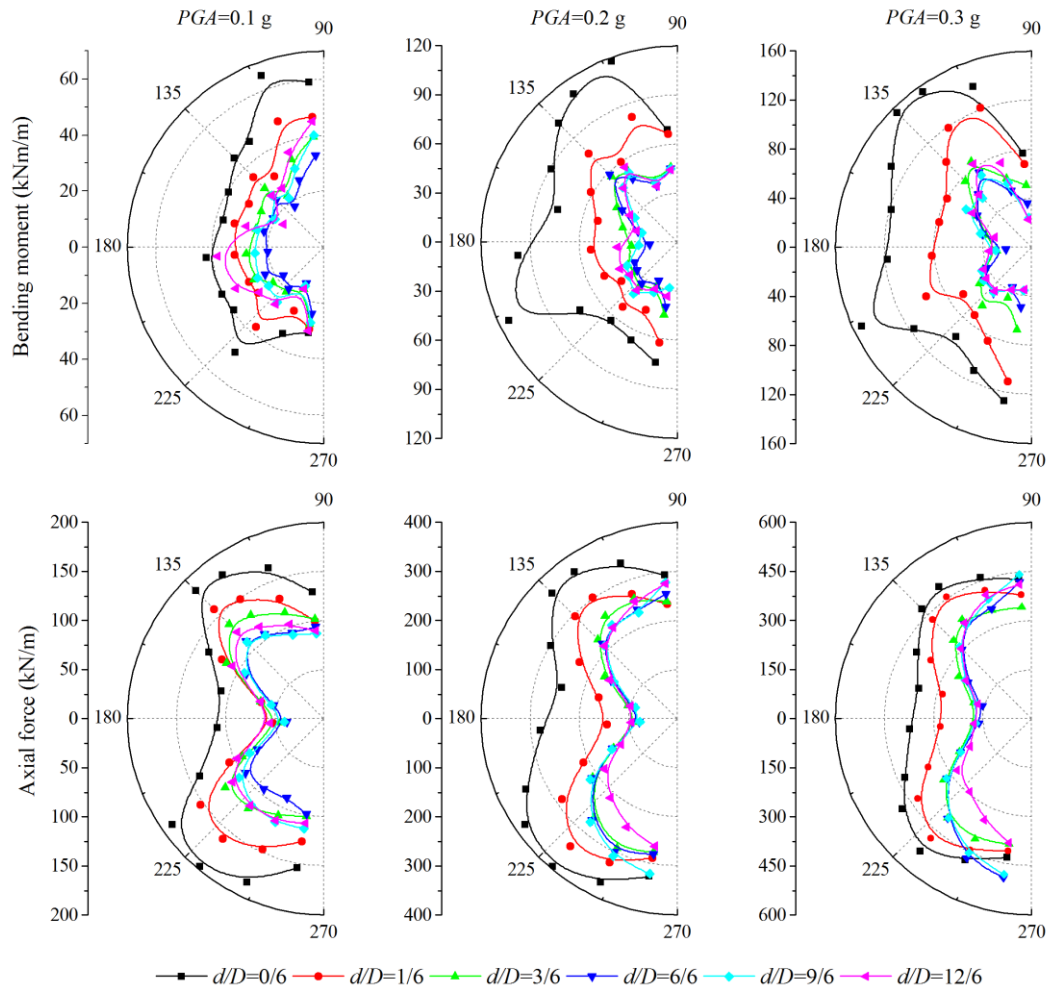


Fig. 5.15 Distributions of the seismic internal force increments for different relative thicknesses.

Concerning the modification ratios, the $V_s/V=0.3$ case permits a rapid decrease of modification ratios of the bending moment and axial force when the soft soil layer thickness increases to 0.5 times the tunnel diameter. Similarly, this is more evident for the bending moment rather than for the axial force. An additional increase in the soft soil layer thickness is found to have an insignificant effect on the calculated dynamic internal force ($PGA=0.2$ and 0.3 g). However, a slight increase in the ratios of M_R and T_R is observed when the relative thickness is greater than 1.0 for the case of $PGA=0.1$ g. The relative thickness effect on the tunnel response is negligible for $V_s/V=0.7$, although a linear decrease in both bending moment

and axial force is reported. This is in good agreement with the findings in Fig. 5.5, in which a slow decrease in transmission coefficient with increasing normalized wavelength is observed for a large interlayer velocity case.

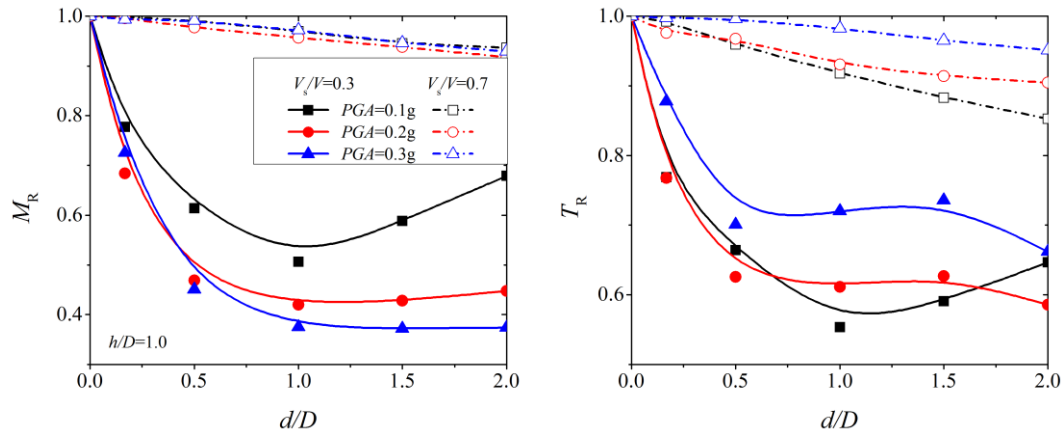


Fig. 5.16 Modification ratios versus relative thicknesses.

The theoretical study and the numerical simulation results indicate that a critical thickness exists which leads to a more pronounced reduction of the lining forces. For the case considered here, it is about the same as the tunnel diameter (i.e., $d/D=1.0$). For this critical thickness, the soft soil layer could effectively reduce the amplitude of the transmitted wave. However, beyond this thickness range, the seismic isolation effect of a soft soil layer will not be increased greatly. This depends on the input motion intensity, relative shear wave velocity, and frequency of the input motion, etc.

5.4.2.3 Effect of the relative distance

The effects of the soft soil layer position with respect to the tunnel on the seismic internal force increments distributions are presented in Fig. 5.17 ($d/D=1.0$, $V_s/V=0.3$, $PGA=0.1, 0.2$, and 0.3 g). Generally, different locations of the soft soil layer induce similar distributions, although a slightly large response is reported for $h/D=2.0$ than for $h/D=1.0$ especially for 0.1 g case (the possible reasons will be presented in section 5.5). However, compared to the results obtained for relative shear wave velocity and relative thickness, the distribution form, and amplitude of the lining forces are less insensitive to the position of a soft soil layer.

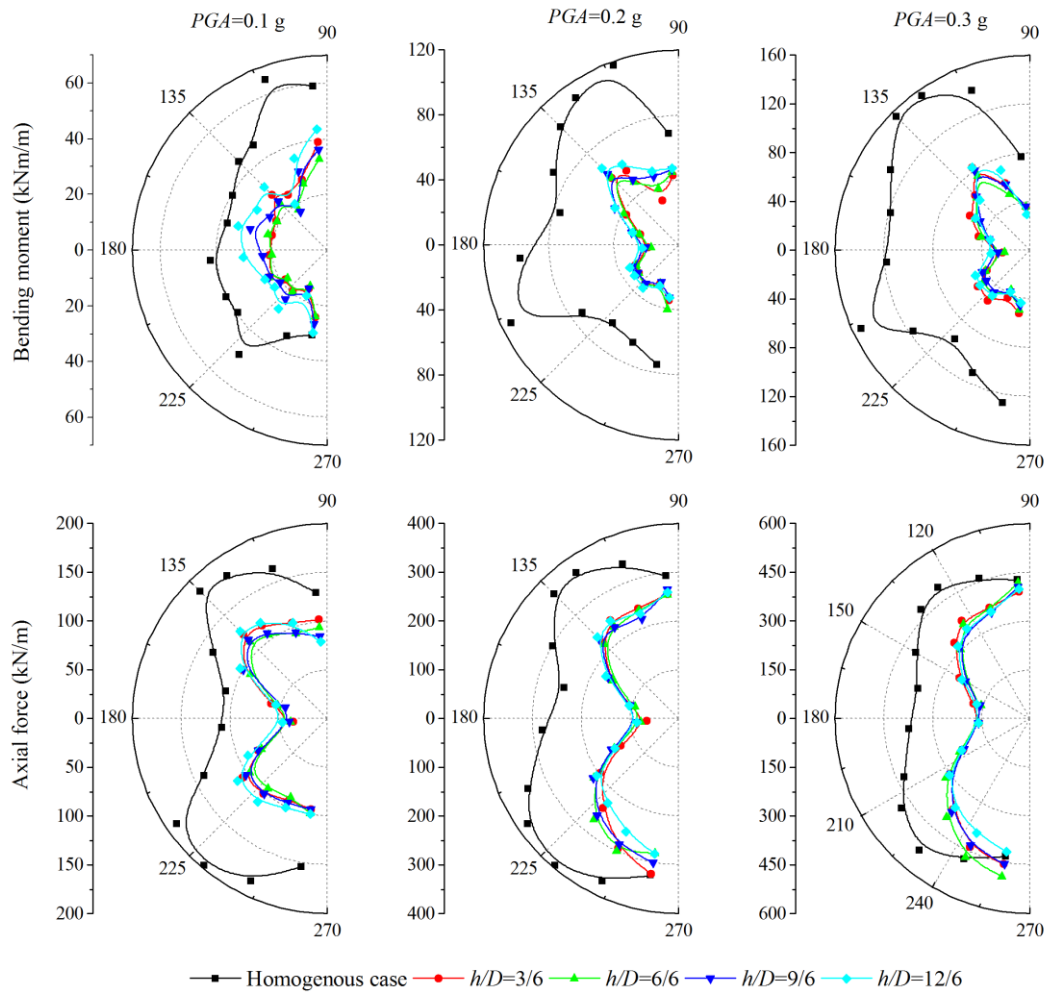


Fig. 5.17 Distributions of the seismic internal force increments for different relative distances.

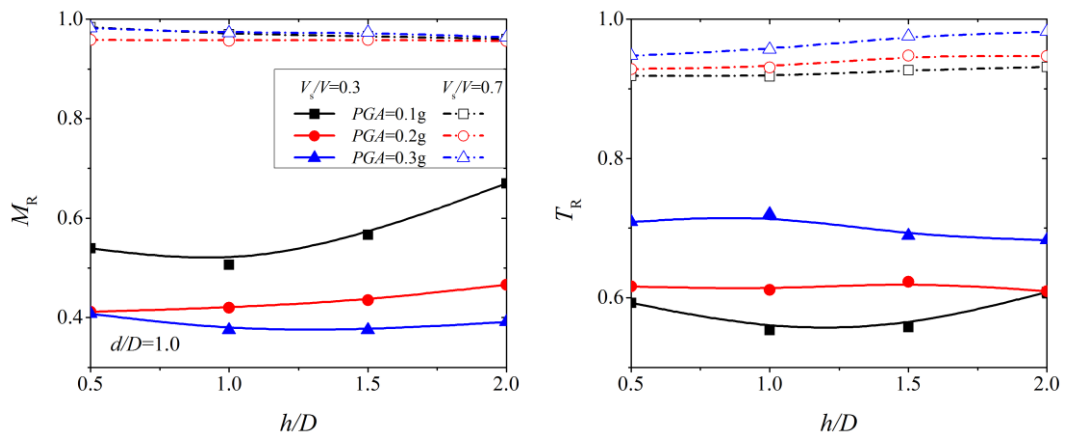


Fig. 5.18 Modification ratios versus relative distances.

Fig. 5.18 presents the modification ratios of the seismic internal force increments versus the relative distances of the soft soil layer. The analyses corresponding to $d/D=1.0$, $V_s/V=0.3$, and

0.7, $PGA=0.1, 0.2,$ and 0.3 g. Results of the $V_s/V=0.3$ case indicate that the ratios of bending moments and axial forces seem to stay constant as the relative distance increases, except for bending moments in the case of $PGA=0.1$ g. Similarly, the effect on the bending moment is increased with the motion intensity increases whereas the effect on the thrust holds an opposite trend. It is found that the effects of relative distance on the M_R and T_R ratios are also negligible for the $V_s/V=0.7$ case.

5.5 Discussion

As mentioned above, the cases of $h/D=2.0, d/D=1.0, V_s/V=0.3$ (see Fig. 5.16a) and $h/D=1.0, d/D=2.0, V_s/V=0.3$ (see Fig. 5.18a) present abnormal results as compared to other cases for weak motion intensity (i.e., 0.1 g). It is found that the lower boundary of two soft soil layers is the same (36 m below the surface), as shown in Fig. 5.19.

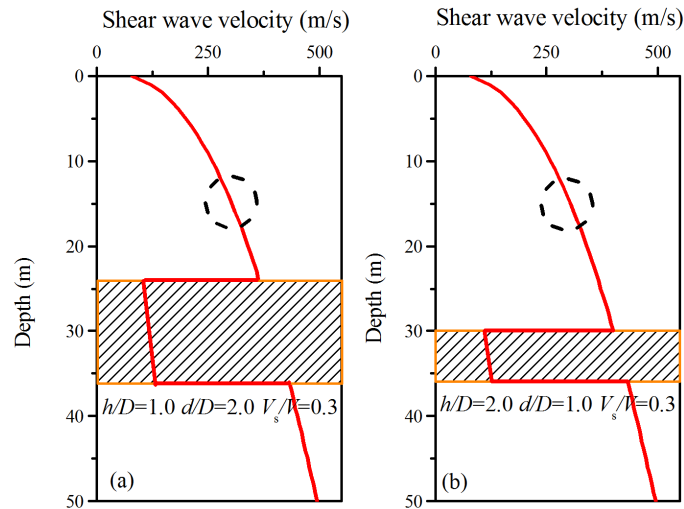


Fig. 5.19 Two soil profiles corresponding to the cases of abnormal results.

As the layer thickness increases, the actual distance between the tunnel and the centre of the soft soil layer also increases. The abnormal results of the dynamic internal forces can be attributed to the locations of the soft soil layer. Hence, this section attempts to examine this hypothesis in the time domain and frequency domain by varying the relative distance (i.e., h/D) of the soft soil layer. The numerical models correspond to $t/D=1.0$ and $V_s/V=0.3$, while

the values of h/D are equal to 1.0, 2.0, 4.0, the intensities of the input motions with 0.1 g and 0.3 g are considered.

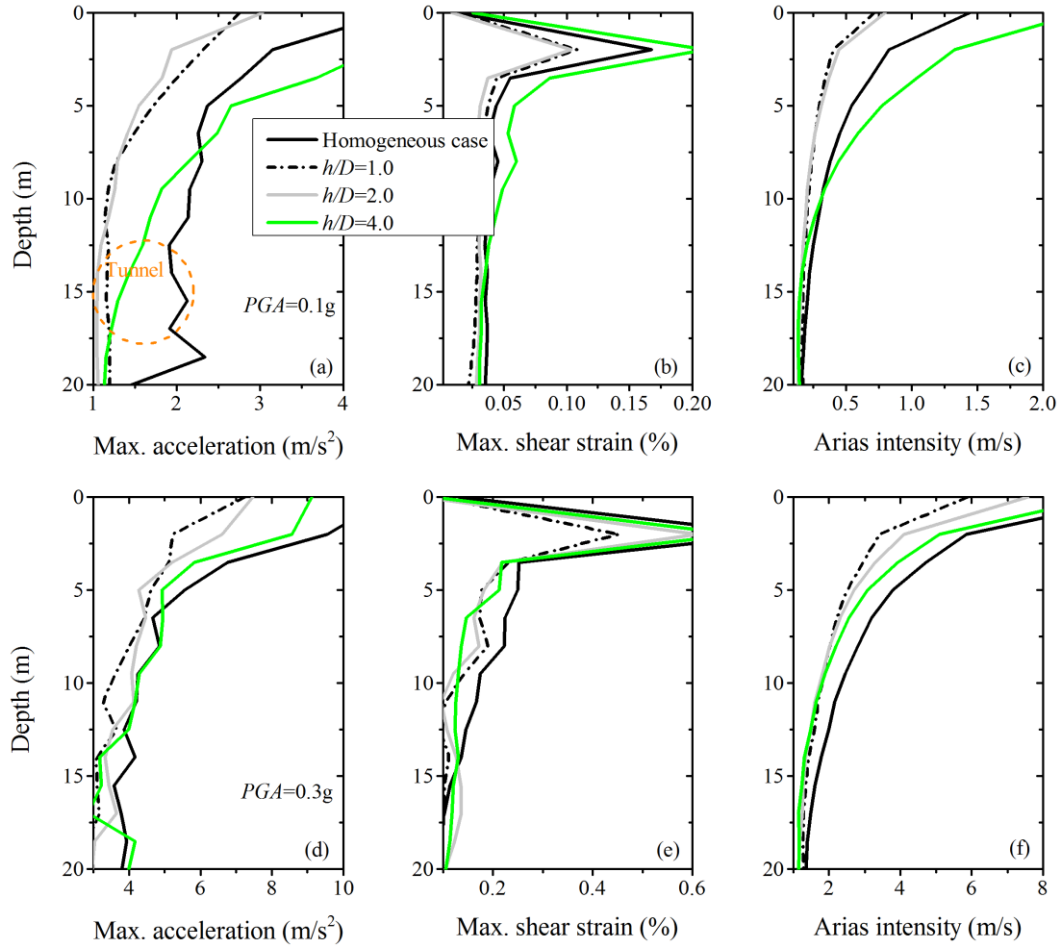


Fig. 5.20 Variations of the response with depth for the acceleration, shear strains, and Arias intensity.

Time-domain: The comparisons of the variation of the maximum acceleration, maximum shear strain, and Arias intensity with depth (top 20 m), are presented in Fig. 5.20. The results of the weak motion case are shown in Figs. 5.20a~5.20c while Figs. 5.20d~5.20f present the response for the strong motion. For the 0.1 g case, the soft layer reduces the response at the tunnel centre position compared to the homogeneous case, particularly for the acceleration response. The relationships between the h/D with the acceleration and strain responses show a nonlinear reduction, while larger acceleration and strain responses are reported for the case of $h/D=4.0$ in comparison with the $h/D=1.0$ and 2.0 cases. Higher imposed ground strains or the accelerations generally cause larger deformations of the tunnel lining thus result in the larger

calculated bending moment. This may be one of the reasons for the abnormal results observed in section 5.4.

The results also indicate that the difference in acceleration response (Fig. 5.20d) caused by the relative distance is not pronounced for strong motions (i.e., 0.3 g). This may be partially explained by the increased soil nonlinearity effect. In general, an increase of the input motion intensity permits to reduce the amplification ratio of the peak ground acceleration and to modify the amplification frequency due to the degradation of the shear modulus and increase of the damping (Finn and Eeri, 2016). This also reduces the stiffness difference between the soft soil layer and the nearby stiff soil and to some extent, weakens the effect of the soft soil layer. Hence, insignificant differences in the dynamic internal forces are shown in Figs. 5.17 and 5.18.

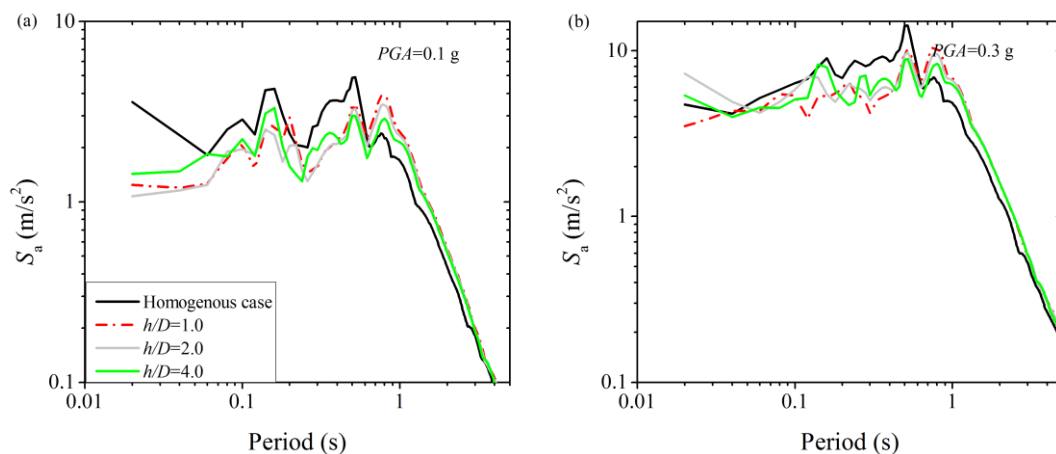


Fig. 5.21 The spectral accelerations at the position of tunnel center for different relative distances.

Frequency domain: Fig. 5.21 presents the spectral accelerations at the tunnel centre position (i.e., 15 m) for various relative distances. Similar to the findings of Fig. 5.10, the soft layer increases the response at a long period (>0.6 s) while reduces the response at short period compared to the homogenous case. As for the short period, the minimum response is observed in the case of $h/D=2.0$, rather than the case of $h/D=4.0$. It is also worth remarking that high ground motion intensity tends to eliminate the difference caused by the soft soil layer over the short period range, as shown in Fig. 5.21b.

On the other hand, the dynamic amplification of stress waves affecting a tunnel is generally negligible when the wavelength is more than eight times larger than the tunnel diameter (Bobet, 2010; Hashash *et al.*, 2001). The short period corresponds to a small wavelength could much affect the seismic tunnel behavior than the long period. The soft soil layer leads to a reduction of the lining forces because the spectral acceleration decreases over the short period range. Although the spectral acceleration for long periods is amplified, the tunnel is less sensitive to this period range. It explains why the $h/D=4.0$ case results in the largest response than other soft soil layer cases (Fig. 5.20a). It also clarifies why the small difference of the lining forces is observed for different relative distances at larger ground motion intensities (Figs. 5.17 and 5.18).

5.6 Conclusion

This chapter highlights the potential beneficial effect of an underlying soft soil layer on the tunnel seismic behaviour. The theoretical study as well as the numerical analysis is presented first to provide a basic understanding of the wave propagation through a soft soil layer. Then, dynamic time-history analyses are performed considering various soft soil layer parameters, including the relative thickness, relative shear wave velocity, and relative distance. The effect of motion intensity is also considered. The results are compared in terms of distribution and modification ratios of the maximum seismic internal force increments.

According to the wave motion theory, the propagation characteristic of the plane SH wave in a three-layered elastic medium is investigated analytically. The theoretical work verifies that a weak interlayer will reduce the transmission coefficient of the incident wave, depending on the interlayer density, shear wave velocity, thickness, and wave frequency. In this study, it is found that the influence of a weak interlayer is concentrated in the range of a normalized wavelength (i.e., d/λ_w) lower than 0.5.

Furthermore, the numerical results of a free-field case reveal that the presence of a soft soil layer tends to amplify the spectral acceleration amplitude at the long periods whereas it

attenuates the response over the short period range. As compared to a homogenous case, reductions of the acceleration, strain, and Arias intensity caused by the soft soil layer are also observed at the tunnel centre position.

The seismic internal force increments in the tunnel lining are reduced due to the presence of a soft soil layer, particularly for the bending moments when subjected to a strong motion. The relative shear wave velocity in the range of 0.2~0.5 has a more pronounced effect on the modification ratios of the lining forces. The effect becomes progressively smaller as the relative shear wave velocity increases. This study also finds a critical thickness that can effectively reduce the seismic actions on the tunnel lining. For the case considered here, it is about one tunnel diameter (i.e., $d/D=1.0$). Concerning the relative distance, it leads to a slight change in the lining forces in comparison with the effect of the shear wave velocity and thickness.

Chapter 6

Probabilistic seismic response of tunnels in random soils: Sensitivity analysis

6.1 Introduction

Due to the inherent uncertainty in nature and the presence of measurement errors, soil parameters inevitably present variation and uncertainty (Fenton, 1999; Phoon and Kulhawy, 1999a, 1999b). The soil properties can spatially vary along the tunnel axis and this can affect the tunnel behaviour as different materials will transmit differently the waves (Manolis *et al.*, 2020; Nedjar *et al.*, 2007). Thus, the prediction of the tunnel seismic response is highly uncertain. Contrary to deterministic analyses, probabilistic concepts provide a more rational way of quantifying the uncertainties in soil-tunnel systems. For any probabilistic analyses, the identification of the important variables is in general a basic step. An input parameter can be considered as deterministic if it has a small influence on the response output and it should be considered as probabilistic if a significant influence appears. In this regard, sensitivity analyses proved to be able to effectively quantify the relative importance of each variable on the variance of the predicted model response (Mahmoudi *et al.*, 2019; Nariman *et al.*, 2019). With the help of sensitivity analyses, probabilistic analyses and design works will be simplified by discarding unimportant variables.

Numerous techniques are nowadays used to perform sensitivity analysis, which can be grouped into two categories (Sobol and Levitan, 1999; Sudret, 2008; Sudret and Mai, 2015):

local sensitivity analysis (i.e., *LSA*) and global sensitivity analysis (i.e., *GSA*). *LSA* focuses on the local impact of input parameters on the model by computing the response gradient with respect to its parameters around a nominal value. Methods such as the Tornado diagram, *FORM*, and Monte Carlo simulation (Calabrese and Lai, 2016; Na *et al.*, 2008, 2009) are typical representatives. However, *LSA* ignores the interaction influence between variables and may compute inaccurate sensitivity indices in the presence of a strongly nonlinear dependency between variables. Besides, increased variable numbers will lead to a dramatic increase in computational costs. Oppositely, *GSA* is an attractive and powerful tool since it can effectively tackle these limitations. This technique offers extensive possibilities for ranking the individual and interaction effects of variables simultaneously. In practice, *GSA* can be applied solely or can freely incorporate with other advanced uncertainty quantification methods (Sudret, 2008; Nariman *et al.*, 2019). Quite recently, many efforts are devoted to enhancing the efficiency of *GSA* using surrogate models since they permit to provide accurate sensitivity indices with relatively small computational costs (i.e., the original computationally expensive models are substituted by surrogate models (Al-Bittar *et al.*, 2018; Ferrario *et al.*, 2017; Pan and Dias, 2017). Among the most widely used surrogate techniques, the sparse polynomial chaos expansions (*SPCE*) method is the more representative one. Once the surrogate model is properly trained, the sensitivity index of each input variable could be analytically calculated based on the *SPCE* coefficients (Sudret, 2008).

The *GSA* of a tunnel in seismic conditions is, however, rarely investigated in the literature (Nariman *et al.*, 2019). This could be attributed to the following reasons:

- The probabilistic concept is not widely used, the design of tunnels employed in modern seismic codes is based on deterministic soil properties.
- The record-to-record variability in terms of magnitude and frequency characteristic is expected to have a more pronounced influence since the prediction of a future earthquake for a specific site is always difficult.
- The third reason comes from the sophisticated and computationally expensive dynamic time-history numerical analyses, particularly for strong nonlinearity and high dimensional problems. In this situation, more realizations are required to

construct the surrogate model; however, many probabilistic methods fail to accurately represent the true model responses.

This chapter attempts to explore the capability of the sparse polynomial chaos expansions combined with the global sensitivity analysis (*SPCE-GSA*) for the tunnel seismic response considering strong nonlinearity and high dimensional cases. The final goal is to figure out the parameters that have the most or least influence on the variability in the tunnel seismic deformations. This chapter is organized as follows. First, the basic principles behind the *SPCE-GSA* method are simply introduced. Then, the deterministic numerical model and probabilistic models of seven variables are presented. Next, the accuracy of the *SPCE* model as well as the efficiency of the *SPCE-GSA* method is respectively validated. After that, sensitivity analyses are performed for a wide range of shear wave velocities, motion intensities, and coefficients of variation. Finally, the variability in the sensitivity indices caused by the sampling size, polynomial degree (to train the *SPCE* model), and ground motion characteristic is evaluated.

6.2 Method

6.2.1 Polynomial chaos expansion

The link between the input parameters and output responses can be defined by:

$$\mathbf{y} = M(\mathbf{X}) \quad (6.1)$$

where $\mathbf{X} = \{x^1, x^2, \dots, x^M\}$ is a random vector that parameterizes the variability of the input parameters with a dimension of M , and \mathbf{y} is the vector of model responses $\mathbf{y} = \{y^1, y^2, \dots, y^M\}$. In *PCE*, a surrogate model is built by expanding the system response on a suitable basis:

$$M(\mathbf{X}) = \sum_{\alpha \in \mathbb{N}^M} k_{\alpha} \Psi_{\alpha}(\mathbf{X}) \quad (6.2)$$

where the $\Psi_{\alpha}(\mathbf{X})$ are multivariate polynomials, $k_{\alpha} \in R$ are the unknown coefficients, $\alpha \in \mathbb{N}^M$ is a multidimensional index. The multivariate polynomials $\Psi_{\alpha}(\mathbf{X})$ is the tensor product of univariate orthonormal polynomials $\psi_{\alpha_i}(x_i)$. Hermite polynomials are selected for

representing the univariate polynomials (Mollon *et al.*, 2009, 2013; Pan and Dias, 2017). Considering a finite sum in Eq. 6.2, the truncated polynomial chaos expansion is introduced (Blatman and Sudret, 2011):

$$M(\mathbf{X}) \approx M^{PC}(\mathbf{X}) = \sum_{\alpha \in \mathcal{A}} k_{\alpha} \Psi_{\alpha}(\mathbf{X}) \quad (6.3)$$

where $\mathcal{A} \in \mathbb{N}^M$ is the set of selected multi-indices of multivariate polynomials. A hyperbolic (or q -norm) truncation scheme (Schöbi and Sudret, 2019), is adopted for selecting the multivariate polynomials $\Psi_{\alpha}(\mathbf{X})$:

$$\mathcal{A}^{M,p,q} = \left\{ \alpha \in \mathcal{A}^M : \|\alpha\|_q = \left(\sum_{i=1}^M a_i^q \right)^{1/q} \leq p \right\} \quad (0 < q \leq 1) \quad (6.4)$$

where the term p refers to the maximum degree of a *PCE* model. The maximum number of unknown coefficients equals to $\frac{(M+p)!}{M!p!}$. In this study, $q=0.75$ is adopted to reduce high order interaction terms (Schöbi and Sudret, 2019). The unknown coefficients $\{k_{\alpha}\}_{\alpha \in \mathcal{A}^{M,p,q}}$ can then be computed using the least-square minimization method (Blatman and Sudret, 2011):

$$\hat{\mathbf{y}} = \arg \min \mathbb{E}[(\mathbf{k}^T \Psi(\mathbf{X}) - M(\mathbf{X}))^2] \quad (6.5)$$

An adaptive *PCE* calculation strategy based on the Least Angle Regression (*LAR*) algorithm (Blatman and Sudret, 2011) is applied to select the most important candidate polynomial basis while all the other coefficients are set to zero (i.e., sparse *PCE*). Furthermore, the *SPCE* used here allows adaptively choosing the best polynomial degree (p) from a degree range and almost without sacrificing accuracy (Blatman and Sudret, 2010; Lataiotis *et al.*, 2018a, 2018b; Sudret, 2008).

6.2.2 Sobol' indices

The sensitivity index measures the relative contribution of the partial variances D_{i_1, \dots, i_s} of each group of variables $\{x_{i_1}, \dots, x_{i_s}\}$ on the total variance D of all variables, is given by:

$$S_{i_1, \dots, i_s} = \frac{D_{i_1, \dots, i_s}}{D} \quad (6.6)$$

The first order Sobol' index S_i represents the effect of a single input variable alone, while the second order sensitivity indices S_{ij} , $i \neq j$, study the interaction effects of the variable i and

j on the output variance (Sobol and Levitan, 1999; Zoutat *et al.*, 2018). The total Sobol' index S_i^T is the sum of all the Sobol' indices involving variable i , which represents its individual effect and the combination effect with other variables on the output variance.

$$S_i^T = \sum_{\{i_1, \dots, i_s\}} S_{i_1, \dots, i_s} \quad (6.7)$$

Theoretically $0 \leq S_i \leq S_i^T \leq 1$, and $S_i = S_i^T = 0$ means that the model output does not depend on variable i while $S_i = S_i^T = 1$ means that the model output depends only on variable i .

6.2.3 Error estimation

The leave-one-out error ε_{LOO} , compares the *SPCE* ($M^{PC \setminus i}$) predictions on the excluded point x^i with the real value y^i . It can be written as (Blatman and Sudret, 2011):

$$\varepsilon_{LOO} = \frac{\sum_{i=1}^{N_{ED}} (M(x^i) - M^{PC \setminus i}(x^i))^2}{\sum_{i=1}^{N_{ED}} (M(x^i) - \mu_Y)^2}, i \in N_{ED} \quad (6.8)$$

where μ_Y is the sample mean of the experimental design response.

Another error estimator ε_{VAL} , is adopted by comparing the *SPCE* predictions with the true responses of additional deterministic models (i.e., N_{VAL} validation cases).

$$\varepsilon_{VAL} = \frac{\sum_{i=1}^{N_{VAL}} (M(x^i) - M^{PC}(x^i))^2 / N_{VAL}}{\text{Var}[\sum_{i=1}^{N_{VAL}} M(x^i)]}, i \in N_{VAL} \quad (6.9)$$

where $\text{Var}[\sum_{i=1}^{N_{VAL}} M(x^i)]$ is the variance of the true response of validation cases.

6.2.4 Numerical procedure

The main scheme to perform the sparse polynomial chaos expansions based global sensitivity analysis focuses on the following steps (Fig. 6.1):

- **Step 1:** Generation of a set of input parameters using the Latin hypercube sampling method.
- **Step 2:** Definition of the soil-tunnel numerical model.
- **Step 3:** Calculation of the tunnel seismic response.

- **Step 4:** Construction of the *SPCE* model until the target accuracy is satisfied.
- **Step 5:** Calculation of the Sobol' indices using *SPCE* coefficients.

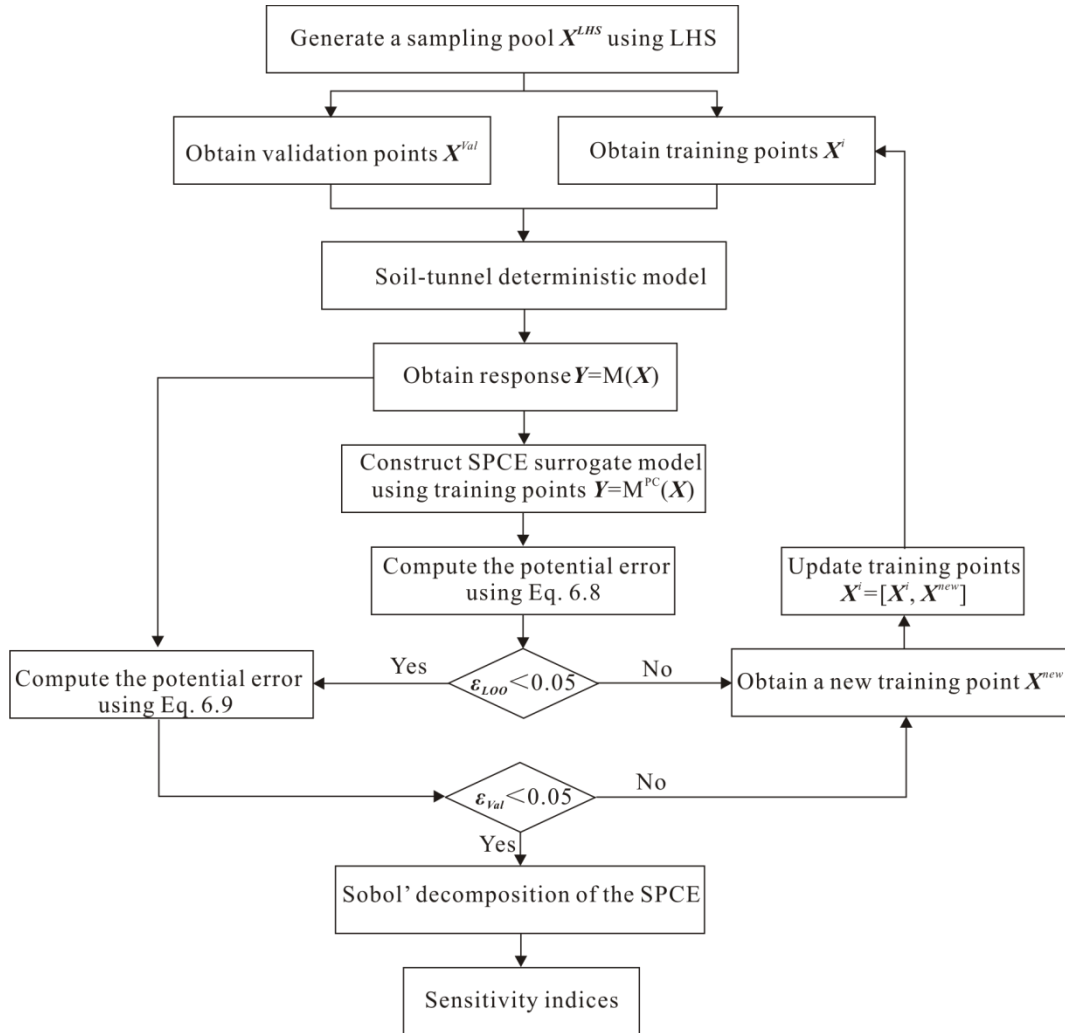


Fig. 6.1 Flowchart of the adopted *SPCE-GSA* method.

6.3 Computational model

6.3.1 Deterministic numerical model

The Bologna-Florence high-speed railway tunnel in Italy is selected as a reference case. Thus, the two-dimensional numerical model utilized in this chapter is the same as the one used in Chapter 3. It should be emphasized that:

- The mean shear wave velocity of this tunnel site is increased from 184 m/s to 200

m/s since the former value leads to numerical instability for some cases (lower values are generated when considering uncertainty).

- A perfect bonding between the soil and tunnel lining is assumed. This is not only due to the presence of interface elements that will significantly increase the computational cost, but also the difficulty in selecting the appropriate interface parameters in random soils.
- The Friuli ground motion is utilized (Figs. 6.2a and 6.2b) after a high frequency cutoff (10 Hz) and baseline correction. It is then transformed into a shear stress time-history and is applied at the model base (quiet boundary condition).

To determine the adequate model dimension and mesh size, a parametric analysis is performed. The results of Table 6.1 indicate that a numerical model width of 100 m (height of 40 m) with a mesh size of 0.8×0.8 m is sufficient to avoid boundary effects and maintain model stability, meanwhile significantly reduces the computational cost. It corresponds to a computational time of 310 s (Intel Xeon CPU E5-2620 v4 2.1 GHz, two processors), 6.5 times lower than the refined model. The final two-dimensional numerical model is presented in Fig. 6.2c.

This study focuses on the maximum tunnel deformation ΔD , which is defined as the relative maximum horizontal displacement between the tunnel top and bottom (red points in Fig. 6.2c). As an example, Fig. 6.2d respectively presents the deformation time-histories in deterministic analyses.

Table 6.1. Numerical model testing.

| Model width (m) | Mesh size (m) | Element number | Solution time (s) | ΔD (cm) |
|-----------------|---------------|----------------|-------------------|-----------------|
| 100 | 0.8×0.8 | 6000 | 310 | 2.45 |
| 100 | 0.5×0.5 | 16000 | 1306 | 2.43 |
| 150 | 0.5×0.5 | 24000 | 2325 | 2.30 |

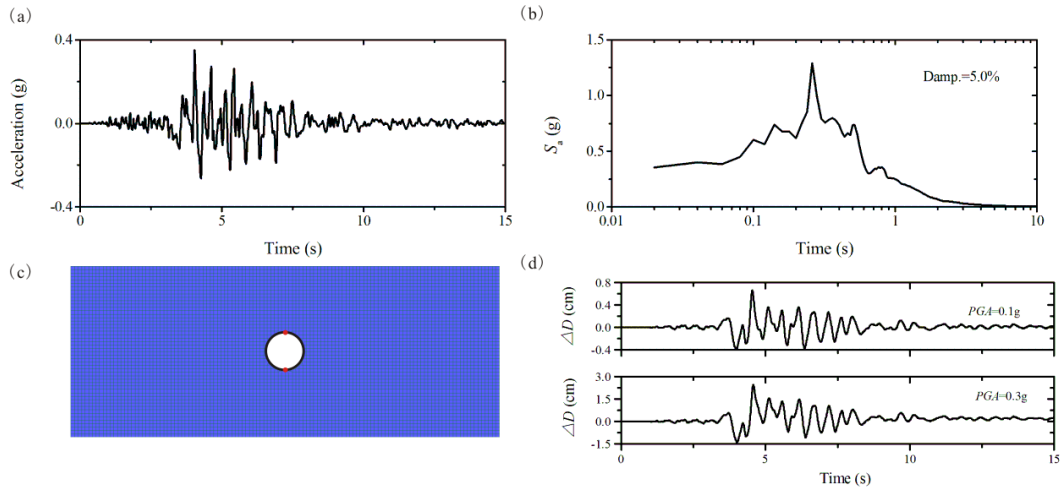


Fig. 6.2 Seismic input, numerical model, and deterministic seismic analysis.

6.3.2 Probabilistic modelling of variables

In a probabilistic analysis, each uncertain model parameter can be represented by a random variable and a corresponding probability density function (*PDF*). In this chapter, five soil parameters (density, shear wave velocity, Poisson's ratio, cohesion, and internal friction angle), and the modulus reduction factor M_s , and centre frequency f_{\min} of the Rayleigh damping are also considered as the random variables.

The probabilistic input models of five soil parameters in terms of coefficient of variation (*COV*) and distribution type are taken from the literature and correspond to real variability measured in the laboratory or in-situ tests (Fenton, 1999; Mollon *et al.*, 2009, 2013; Pan and Dias, 2017; Phoon and Kulhawy, 1999a, 1999b). To avoid the unrealistic values generation, the distribution tails need to be truncated to describe the variables in a meaningful way. In this study, the lower bound (*LB*) and the upper bound (*UB*) are respectively determined based on the mean ± 2 times of the standard deviation (Sun *et al.*, 2020). This step is critically important for the variable V_s since extremely low values will lead to a very dense mesh to maintain numerical stability (Kuhlemeyer and Lysmer, 1973). It will lead to a significant increase in computational cost. Besides, the variables are considered as inter-independent since the adopted Sobol' decomposition method is invalid for correlated variables.

Similarly, the empirical curve proposed by [Sun *et al.* \(1988\)](#) is also incorporated in the model, using the function suggested by [Hardin and Drnevich \(1972\)](#), as follows:

$$G/G_{max} = \frac{1}{1+\gamma/\gamma_{ref}} \quad (6.10)$$

The reference strain value γ_{ref} is determined from the strain at which the value of modulus reduction factor (i.e., M_s) equals 0.5, corresponding to a reference strain $\gamma_{ref}=0.234$ in this study.

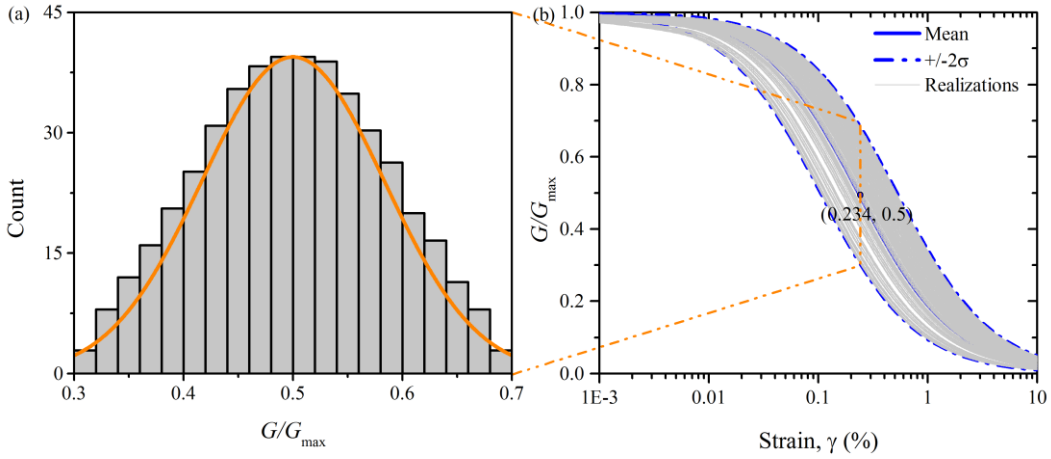


Fig. 6.3 Examples of random G/G_{max} curves used in the probabilistic analysis.

To consider its uncertainty, the empirical probability model of [Darendeli \(2001\)](#) which allows representing the most comprehensive investigation regarding the variability of nonlinear soil properties is used. This model assumes that the parameter G/G_{max} is normally distributed for a given strain level and that the strain-dependent standard deviation is given by the following expression:

$$\sigma_{G/G_{max}} = 0.015 + 0.16\sqrt{0.25 - (G/G_{max} - 0.5)^2} \quad (6.11)$$

This equation produces the smallest standard deviation (~ 0.015) when M_s value is equal to 0.0 or 1.0, and the largest standard deviation (~ 0.095) when $M_s=0.5$. Noted that this equation is proposed for generic soil conditions, whereas the standard deviation derived from laboratory tests on a specific soil is supposed to be smaller. The resulting modulus reduction curves for the reference case are schematically shown in Fig. 6.3.

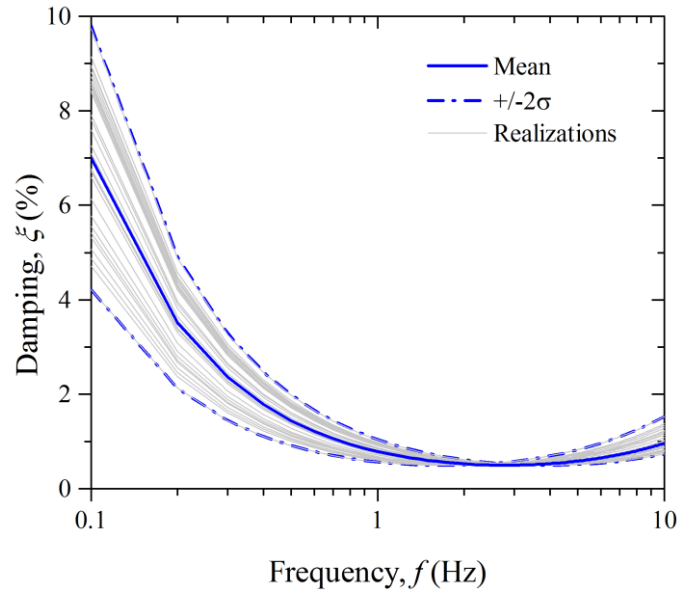


Fig. 6.4 Rayleigh damping realizations for the reference case.

Rayleigh damping parameters are determined based on the method proposed by [Kwok *et al.* \(2007\)](#). Based on Eq. 2.8 (see Chapter 2), it can be seen that the site fundamental frequency is related to the shear wave velocity and soil depth. Considering V_s as a random variable, the uncertainty of Rayleigh damping is automatically involved. Once the mean and truncated bounds of V_s are known, the parameters of the probabilistic input model of f_{\min} are determined accordingly ([Kwok *et al.*, 2007](#)). This indicates that the parameters f_{\min} and V_s are positively correlated. The uncorrelated assumption used here increases the f_{\min} variability and overestimates its sensitivity index (although its sensitivity index is really small, will be presented later).

In this study, the value of ξ_{\min} is equal to 0.5%. This small ξ_{\min} value permits to remove the possible high frequency noise without significantly reducing the timestep ([Sun and Dias, 2018](#)), particularly when the hysteretic damping is employed. Realizations of the Rayleigh damping curve in the reference case are shown in Fig. 6.4, as an illustration.

Table 6.2 lists the probabilistic input models of seven variables (benchmark case). The soil shear wave velocity will vary from 200 to 500 m/s to investigate the sensitivity indices evolution under different ground motion intensities ($PGA=0.1$ g, 0.2 g, 0.3 g). In the case of

$V_s = 200$ m/s, the influences of the *COV* of V_s (5%, 10%, and 20%) on the calculated sensitivity indices are discussed.

Table 6.2 Probabilistic input models of variables in the benchmark case.

| Parameters | Symbol | Unit | Mean | COV | Distribution | LB | UB |
|--------------------------|-----------|----------|------|------|--------------|------|------|
| Density | ρ | kN/m^3 | 17 | 0.05 | Normal | 15.3 | 18.7 |
| Shear wave velocity | V_s | m/s | 200 | 0.2 | Normal | 120 | 280 |
| Poisson's ratio | ν_s | - | 0.3 | 0.15 | Normal | 0.21 | 0.39 |
| Internal friction angle | φ | $^\circ$ | 37.0 | 0.2 | Normal | 22.2 | 51.8 |
| Cohesion | c | kPa | 5.0 | 0.3 | Normal | 2.0 | 8.0 |
| Modulus-reduction factor | M_s | - | 0.5 | 0.19 | Normal | 0.31 | 0.69 |
| Centre frequency | f_{min} | Hz | 2.75 | 0.18 | Normal | 1.65 | 3.85 |

6.4 Method verification

6.4.1 SPCE model

To demonstrate the efficiency of the adopted *SPCE-GSA* method in seismic conditions, the probabilistic input models listed in Table 6.2 are adopted to perform the global sensitivity analysis. The comparison is respectively performed for low and high levels of soil nonlinearity: one considering a ground motion intensity $PGA=0.1$ g and another considering a higher intensity with a $PGA=0.3$ g.

The comparisons between the probability density function (*PDF*), cumulative distribution function (*CDF*) of the 400 training points and *SPCE* predictions are respectively shown in Figs. 6.5a and 6.5c for $PGA=0.3$ g and 0.1 g. Two figures show that the *SPCE* model is a good substitute for the original computationally expensive numerical models. According to the *PDF* and *CDF* under the two studied intensities, it is possible to make some remarks. The deformation distribution is almost normal in the case of low intensity (Fig. 6.5c). The *SPCE* model reproduces well the response of training points (the corresponding error ϵ_{L00} is very small). On the contrary, the deformation distribution is more complex for $PGA=0.3$ g, having three peaks and a long tail towards left. The *SPCE* model is not able to reproduce these local features very well and results in a relatively large error. These local peaks result from the soil

nonlinearity and the increased interaction terms between variables.

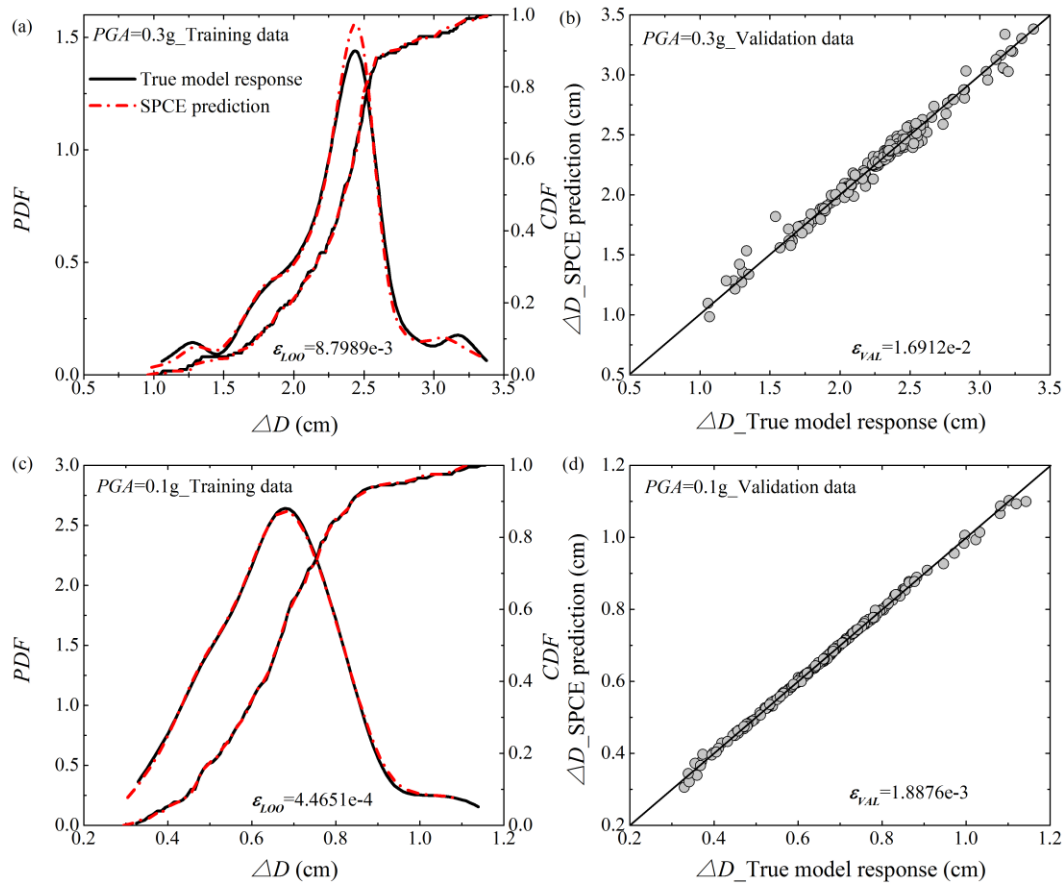


Fig. 6.5 Comparison between *PDF*, *CDF* of training points and *SPCE* predictions: (a) $PGA=0.3$ g; and (c) $PGA=0.1$ g; deformations of true numerical and *SPCE* predictions: (b) $PGA=0.3$ g; and (d) $PGA=0.1$ g.

The trained *SPCE* model is then employed to predict the tunnel deformation using 200 validation points. Figs. 6.5b and 6.5d respectively show the deformation predicted by the *SPCE* model and the true model responses for two intensity cases. The *SPCE* predictions agree well with the true deterministic model responses, particularly in the case of $PGA=0.1$ g.

On the other hand, the standard numerical procedure depicted in Fig. 6.1 shows that the final *SPCE* model is iteratively constructed until the target accuracy is reached. For the given training points, the *LAR* iteration (see Eq. 6.5) works by minimizing the value of ϵ_{LOO} (see Eq. 6.8) for selecting the best sparse candidate basis. This iteration procedure, however, leads to a drastic increase in the *SPCE* model construction time with the increase of the training points. Hence, one question is raised:

- How many training points can ensure the constructed surrogate models that satisfy the target accuracy in this study? This means that there is no need to update iteratively the surrogate model with increasing training points but only for the final training points.

To this end, 10000 deterministic time-history analyses are prepared, corresponding to the benchmark case and $PGA=0.3$ g (solution time is around 36 days). These results are primarily used to investigate the influences of the polynomial degree and sampling size on the variability in the computed Sobol' indices (see Discussion). The polynomial degree is adaptively chosen from a range of degrees specified *a priori* (1 to 12 in this study) given the specific training points. N training points are selected from the 9800 sampling pools while the remaining 200 samples are used for validation purposes. For each experimental design, 200 replications are applied (i.e., 200 final *SPCE* models for each N).

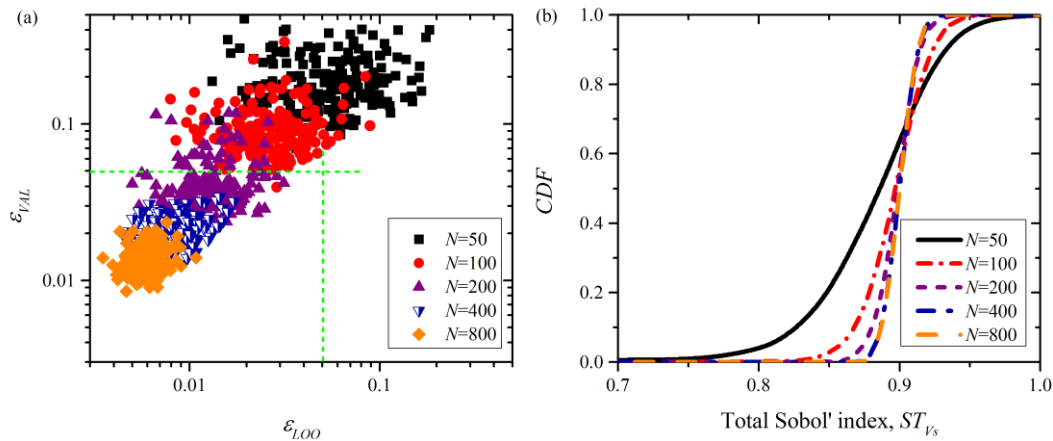


Fig. 6.6 Comparison of (a) values of ϵ_{VAL} and ϵ_{LOO} for different sampling sizes; and (b) the corresponding *CDF* plots of total Sobol' index of V_s .

Fig. 6.6a shows the accuracy of the constructed *SPCE* model with different initial training points ($N=50, 100, 200, 400, 800$) while the corresponding *CDF* plots of the total Sobol' index of V_s are depicted in Fig. 6.6b. It appears that increased training points result in decreased model errors. 400 training points are adequate to ensure that each random realization satisfies the target accuracy. It also provides a very close estimation of the total Sobol' index of V_s calculated with $N=800$. Thus, $N=400$ experimental design is directly used in the following analysis if not specified.

6.4.2 Sensitivity indices

A Monte Carlo simulation based stochastic analysis is performed to have a direct look at the tunnel deformation variability and determine the relative importance of each variable in the framework of *LSA*. The idea behinds the Monte Carlo simulation based *LSA* method is simple and straightforward: the change in the model output is evaluated for all sampling points, and the input variable which causes the largest change in the model output is given the highest rank in the sensitivity analysis. Its sensitivity analysis strategy is to vary one input variable at a time while remaining other variables constant (i.e., mean values), the sensitivity index of each variable can then be respectively calculated.

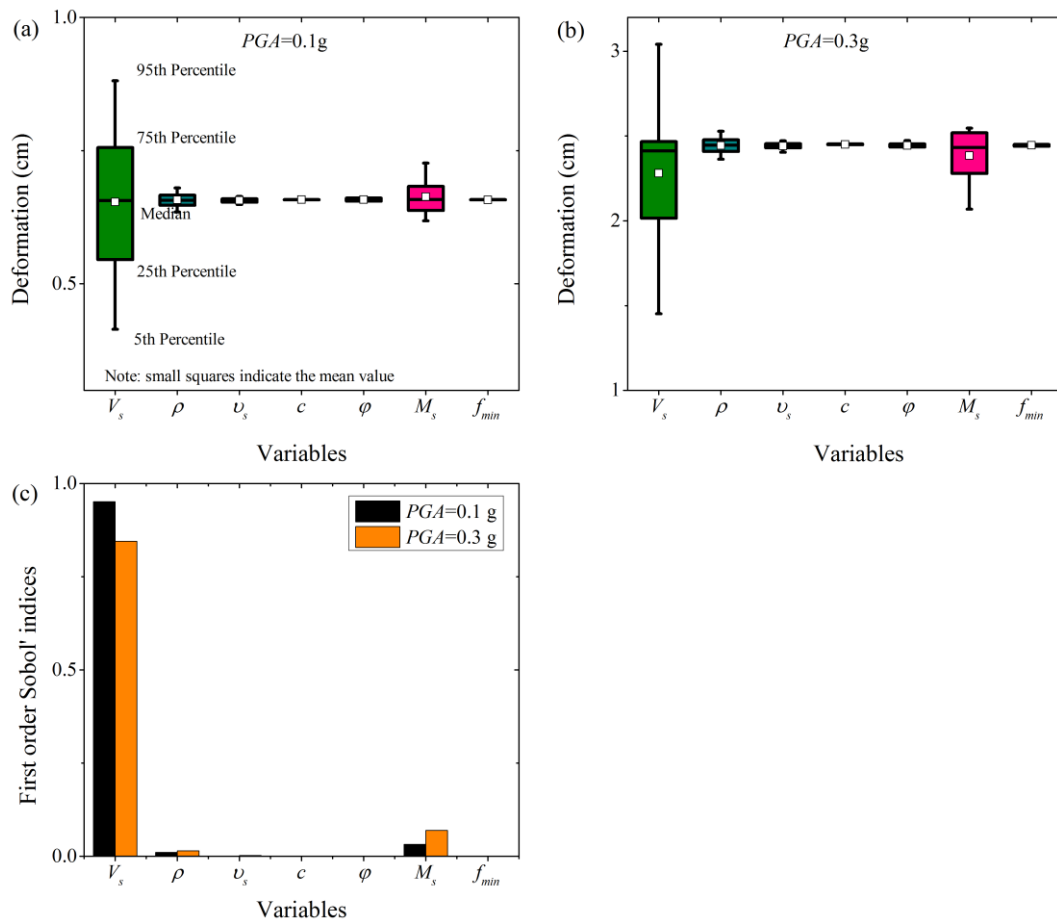


Fig. 6.7 Tunnel deformations corresponding to all variables or a single variable: (a) *PGA=0.1g*; (b) *PGA=0.3 g*; and (c) first order Sobol' indices calculated by *SPCE-GSA* method.

The analyzed scenarios correspond to the probabilistic input models listed in Table 6.2 (case of *PGA=0.1 g* and *0.3 g*). For each case, 500 Monte Carlo simulations are performed (stable

results can be obtained). It means that 7000 ($500 \times 7 \times 2$) deterministic time-history numerical analyses are conducted. Also, for computing the Sobol' sensitivity indices via the *SPCE-GSA* method, 800 samples (400×2) are additionally generated, bringing the total simulation runs to 7800 (~28 days).

The tunnel deformation ranges for different cases computed with the Monte-Carlo simulation are shown in Figs. 6.7a and 6.7b. The large variability in the deformation could be attributed to the uncertainty of the shear wave velocity and the modulus reduction factor (Fig. 6.7a), while the centre frequency, Poisson's ratio, cohesion, and internal friction angle have ignorable importance. The *SPCE-GSA* method quantitatively provides the same relative importance of each variable, but using less numerical runs, as shown in Fig. 6.7c.

6.5 Sensitivity analysis

In this section, representative results in terms of the first order and total Sobol' indices for different scenarios, e.g., soil shear wave velocities, ground motion intensities, and coefficients of variation are evaluated and discussed in detail.

6.5.1 Soil type and motion intensity

The soil type (i.e., shear wave velocity, V_s) and ground motion intensity (i.e., *PGA*) have a direct and pronounced influence on the deformation response of tunnels. Three values of V_s , from 200 m/s to 500 m/s corresponding respectively to soft, medium, and stiff soils (Zoutat *et al.*, 2018) in practice are investigated. Besides, the ground motion intensity varies from 0.1 g to 0.3 g to consider different soil nonlinearity levels. The probabilistic input model of each variable is listed in Table 6.2 except the values of V_s and f_{min} , which are varied parametrically.

Table 6.3 presents the first order and total Sobol' indices for all the analyzed scenarios, while the high order indices indicating the interaction effects are not presented due to their great number. However, the interaction effect between the variables can be estimated based on the

difference between the first order and total indices: the larger the difference, the stronger the interaction.

Table 6.3 Sensitivity indices for different soil conditions and motion intensities.

| PGA (g) | Parameters | Soft soil ($V_s=200$ m/s) | | Medium soil ($V_s=350$ m/s) | | Stiff soil ($V_s=500$ m/s) | |
|---------|------------|----------------------------|-------------|------------------------------|-------------|-----------------------------|-------------|
| | | Total | First order | Total | First order | Total | First order |
| 0.1 | V_s | 0.9560 | 0.9514 | 0.9902 | 0.9863 | 0.9932 | 0.9892 |
| | ρ | 0.0119 | 0.0100 | 0.0029 | 0.0028 | 0.0048 | 0.0036 |
| | v_s | 0.0012 | 0.0011 | 8.377E-4 | 7.574E-4 | 0.0010 | 8.332E-4 |
| | c | 6.558E-5 | 0 | 2.841E-5 | 0 | 6.590E-5 | 8.308E-7 |
| | φ | 4.443E-4 | 2.309E-4 | 4.771E-4 | 1.9827E-4 | 0.0019 | 4.169E-4 |
| | M_s | 0.0354 | 0.0326 | 0.0095 | 0.0060 | 0.0032 | 0.0019 |
| | f_{min} | 1.228E-4 | 0 | 4.898E-5 | 1.629E-5 | 6.159E-5 | 1.701E-5 |
| | V_s | 0.9081 | 0.8945 | 0.9767 | 0.9634 | 0.9640 | 0.9568 |
| 0.2 | ρ | 0.0128 | 0.0123 | 0.0022 | 0.0020 | 0.0042 | 0.0026 |
| | v_s | 0.0022 | 0.0018 | 7.546E-4 | 5.765E-4 | 0.0020 | 0.0013 |
| | c | 2.062E-4 | 0 | 2.111E-4 | 8.574E-7 | 7.732E-4 | 0 |
| | φ | 0.0044 | 4.622E-4 | 0.0087 | 0.0046 | 0.0327 | 0.0282 |
| | M_s | 0.0868 | 0.0761 | 0.0257 | 0.0156 | 0.0061 | 0.0033 |
| | f_{min} | 0.0012 | 1.740E-4 | 1.750E-4 | 1.341E-5 | 4.561E-4 | 0 |
| | V_s | 0.9063 | 0.8452 | 0.9620 | 0.9475 | 0.8384 | 0.8280 |
| | ρ | 0.0164 | 0.0141 | 0.0032 | 0.0027 | 0.0133 | 0.0113 |
| 0.3 | v_s | 0.0027 | 0.0017 | 0.0012 | 6.1431E-4 | 0.0012 | 5.578E-4 |
| | c | 0.0023 | 0 | 3.748E-4 | 0 | 9.776E-4 | 3.319E-4 |
| | φ | 0.0160 | 0.0014 | 0.0250 | 0.0189 | 0.1550 | 0.1460 |
| | M_s | 0.1285 | 0.072 | 0.0254 | 0.0151 | 0.0051 | 0.0025 |
| | f_{min} | 0.0012 | 0 | 1.990E-4 | 0 | 3.200E-4 | 0 |
| | V_s | 0.8452 | 0.8280 | 0.9620 | 0.9475 | 0.8384 | 0.8280 |
| | ρ | 0.0141 | 0.0113 | 0.0032 | 0.0027 | 0.0133 | 0.0113 |
| | v_s | 0.0017 | 0.0013 | 0.0012 | 6.1431E-4 | 0.0012 | 5.578E-4 |

In the case of $PGA=0.1$ g, the soil shear wave velocity dominates tunnel deformations and the corresponding first order Sobol' index varies from 0.9514 to 0.9892 as the value of V_s increases, indicating a slight increase effect for the stiffer soil. The sensitivity indices of other variables are very small, showing a negligible influence on the tunnel deformations for this scenario. Increasing the ground motion intensity to 0.3 g, the influence of V_s is gradually decreasing, particularly for the soft and stiff soil cases (respectively with a first order index of 0.8452 and 0.828). This phenomenon could be attributed to shear modulus reduction and soil plasticity. As can be observed, the total index of M_s in the soft soil increases from 0.0354 to 0.1285 while the total index of φ in the stiff soil greatly increases from 0.0019 to 0.155.

It is worth noticing that the differences between the first order and total Sobol' indices of the variables in all the analyzed scenarios are not obvious, except for the V_s and M_s in the soft soil subjected to strong ground motions. This is because the interaction effect occurs between these two variables, as shown in Fig. 6.8. The second Sobol' index of (V_s, M_s) is around 0.05 while they respectively show very weak interaction effects. A reduction in the sensitivity index of M_s with increasing of V_s is observed, which is more evident in the case of $PGA=0.3$ g (decrease from 0.1285 to 0.0051). The dependence of M_s on the value of V_s is not surprising because the higher the value of V_s , the lower the possibility of soil stiffness degradation. The effect of the internal friction angle (φ) uncertainty on the deformation response increases with the increase of V_s value. A maximum total sensitivity index of 0.155 corresponds to $V_s=500$ m/s and $PGA=0.3$ g. This observation is related to the soil plasticity. Compared to φ , the cohesion (c) sensitivity index is smaller although the larger variation degree ($COV=30$ %). This is because the values of φ greatly influence the Mohr-Coulomb failure envelope while the influences of c values are minor due to the small absolute value (Mollon *et al.*, 2009, 2013).

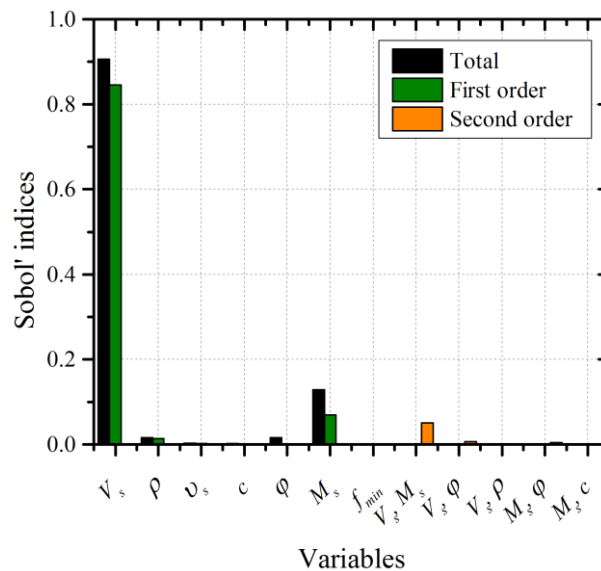


Fig. 6.8 Total, first, and second order Sobol' indices for all the variables ($V_s=200$ m/s and $PGA=0.3$ g).

Another interesting observation is the uncertainty in the Rayleigh damping centre frequency (f_{min}) has almost no effect on the tunnel deformations. This is because the frequency interval is defined according to the recommendation of Kwok *et al.* (2007), which permits to produce

almost the frequency-independent damping ratios in the frequency range of interest. Besides, the reduced f_{min} influence on the seismic response of tunnels appears in the cases of small damping ratios and high soil nonlinearity, as reported in (Chapter 3). The f_{min} sensitivity index may increase if it is randomly defined without any selection criteria or the higher damping ratios are adopted.

6.5.2 Coefficient of variation

The *COV*, which defines the variation level of a variable, is another important parameter in a probabilistic input model (Fang *et al.*, 2020; Mollon *et al.*, 2009, 2013; Pan and Dias, 2017; Phoon and Kulhawy, 1999a, 1999b). This subsection aims to shed light on the *COV* effect on the sensitivity index of each variable to the tunnel deformations. The analysis corresponds to the probabilistic input model listed in Table 6.2 except the variation level of the shear wave velocity. The sensitivity analyses are performed considering three variation levels (i.e., *COV*=5%, 10%, and 20%), in the case of *PGA*=0.1 g and 0.3 g.

Figs. 6.9a to 6.9c respectively show the total and first order Sobol' indices of each variable under *PGA*=0.1g, while the results for *PGA*=0.3 g are presented in Figs. 6.9b and 6.9d. In the case of *PGA*=0.1 g, the soil shear wave velocity is the most important variable even for a smaller variation degree (i.e., *COV*=5%). With the values of *COV* increase from 5% to 20%, the V_s is gradually dominating the tunnel deformation variance with an increase of the first order index from 0.523 to 0.951 (~ 81.8% increase) and the corresponding total index varies from 0.525 to 0.956 (~ 82.1% increase). The minor differences between the first order and the total Sobol' indices indicate a negligible interaction effect between variables. The increase in the sensitivity index of V_s caused by the larger variation level leads to a reduction in the sensitivity indices of the other variables. However, the increase or decrease in the sensitivity indices does not alter the relative importance of each variable in this analyzed scenario and they could be ordered as follows: shear wave velocity V_s , modulus reduction factor M_s , density ρ , Poisson's ratio ν_s , internal friction angle φ , cohesion c , and centre frequency f_{min} .

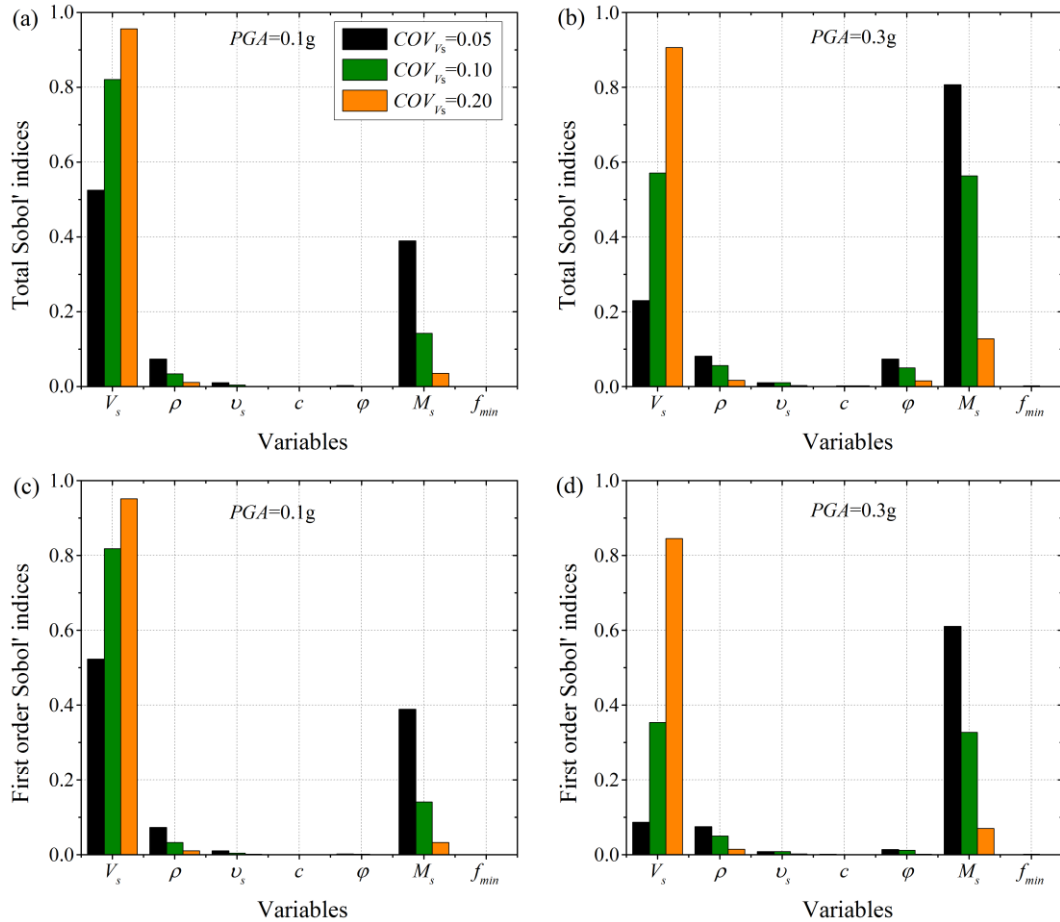


Fig. 6.9 Influences of the COV on the total Sobol' indices: (a) $PGA=0.1$ g; and (b) $PGA=0.3$ g; and on the first order indices: (c) $PGA=0.1$ g; and (d) $PGA=0.3$ g.

For $PGA=0.3$ g, two major differences are found compared to the observations for a $PGA=0.1$ g. Firstly, the modulus reduction factor M_s , rather than V_s , has a more pronounced influence when the $COV=5\%$. This significant increase in the sensitivity index of M_s could be attributed to the soil stiffness degradation appear under a strong ground motion and the relatively large variation level of M_s . Secondly, the differences between the first order and total Sobol' indices of the V_s , M_s and φ in all the analyzed scenarios are obvious, meaning that the interaction effect occurs. The interaction effect is more evident when the variation of V_s is smaller. This is because two strong interaction effects (M_s and V_s , M_s and φ) appear in the case of $COV=5\%$ while the interaction effect between M_s and φ gradually vanishes and the main effect of V_s tends to dominate the sensitivity index with the increasing variation level of V_s (e.g., $COV=20\%$). The interaction effect, on the other hand, increases the total Sobol' indices of φ . In general, the order of variables does not change in comparison with the observation for

weak ground motions, except in the case of $COV=5\%$.

As a conclusion, this comparison shows the significant influence of the coefficient of variation on the sensitivity index, which is related to the ground motion intensity. A reduced variation degree of a variable theoretically reduces its sensitivity index. However, it does not indicate the variable is less important (and vice versa), the influence is sometimes decisive as highlighted in Fig. 6.9a and 6.9c. The sensitivity index of a variable also depends on the variation degree of the other variables since the sensitivity analysis essentially quantifies the relative importance of a variable.

6.6 Discussion

6.6.1 Variability in the computed Sobol' indices

It appears from the above study that the Sobol' indices predicted by the *SPCE-GSA* method is related to the constructed surrogate model (Sudret, 2008). The accuracy of the *SPCE* depends on the sampling size, polynomial degree, and stop criterion. In this study, an algorithm to choose adaptively the optimal polynomial degree in the range from 1 to 12, combined with a target accuracy of 0.05 is used to train the surrogate model. To better understand the role of the polynomial degree and sampling size, and to evaluate the variability in the calculated sensitivity indices, 10000 deterministic dynamic time-history analyses are performed. These analyses correspond to the benchmark case (Table 6.2), subjected to a ground motion with a magnitude of 0.3 g. A range of sampling size N , from 50 to 800, is randomly selected from this 10000 sampling pool, and for each sampling size, 1000 replications are applied. Then the *SPCE* (turning off the adaptive algorithm) of different degrees p , from 1 to 10, is accordingly trained. It means that for each p order *SPCE*, 1000 surrogate models are constructed which correspond to 1000 sensitivity indices of each variable.

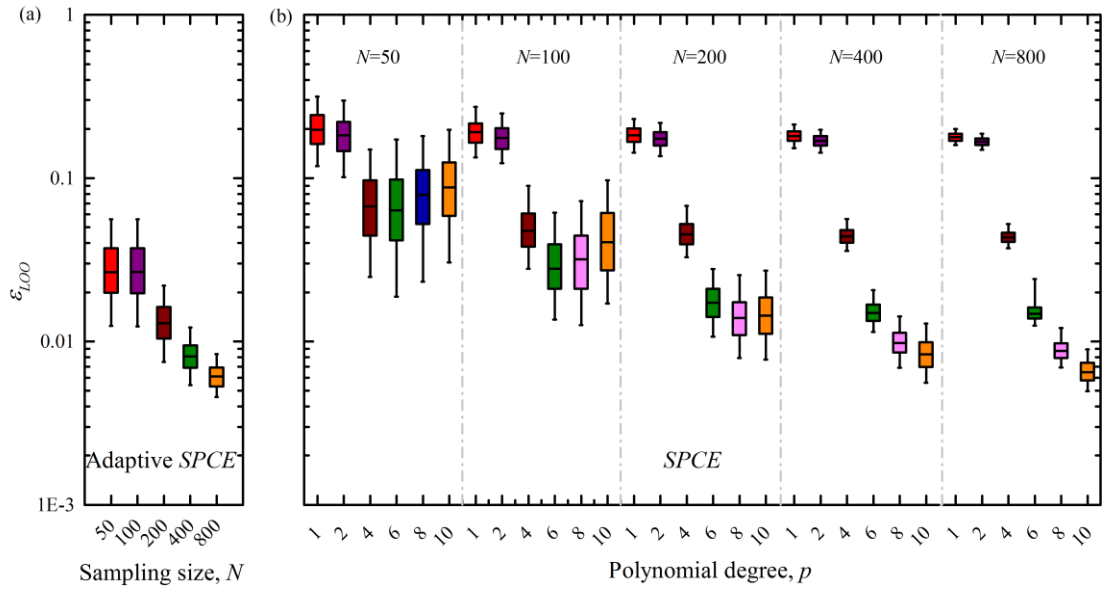


Fig. 6.10 Evolution of ε_{LOO} with the sampling size and polynomial degree: (a) adaptive *SPCE*; and (b) *SPCE*.

Fig. 6.10a shows the evolution of ε_{LOO} with the sampling size using the adaptive *SPCE* while the results of various orders *SPCE* are presented in Fig. 6.10b. The percentile ranges in the box plots are the same as those in Fig. 6.7. For the adaptive *SPCE* used in this study, the model error decreases with the increase of the sampling size N and it permits to construct the surrogate model more explicitly even with less N (i.e., 200). As shown in Fig. 6.10b, the first and second order *SPCE* models always produce larger errors, indicating that they cannot represent the complex numerical response even for a large number of training points (i.e., 800). Increasing the polynomial degree p , the *SPCE* tends to perform well if N is large enough to train the surrogate model because as the p increases, the number of unknown coefficients in the *SPCE* greatly increases (Eq. 6.4). This explains why high order *SPCE* models still result in large errors in the case of $N=50$ and 100.

Once 1000 surrogate models are constructed for each analyzed scenario, the sensitivity analysis is performed accordingly. The variations of the total Sobol' index of the shear wave velocity V_s and density ρ with the sampling size for different polynomial degrees are presented respectively in Figs. 6.11a and 6.11b. The detailed results of the total Sobol' index of V_s are given in Fig. 6.12 while the results of other parameters are not presented for the sake of brevity. It appears that the sensitivity index variability generally decreases with the

increase of the sampling size and polynomial degree. When the sampling size is small ($N=50$ and 100), the sensitivity indices predicted by different order $SPCE$ models show a large variation. This comes from the large model error and associated variation of the model error, as shown in Fig. 6.10.

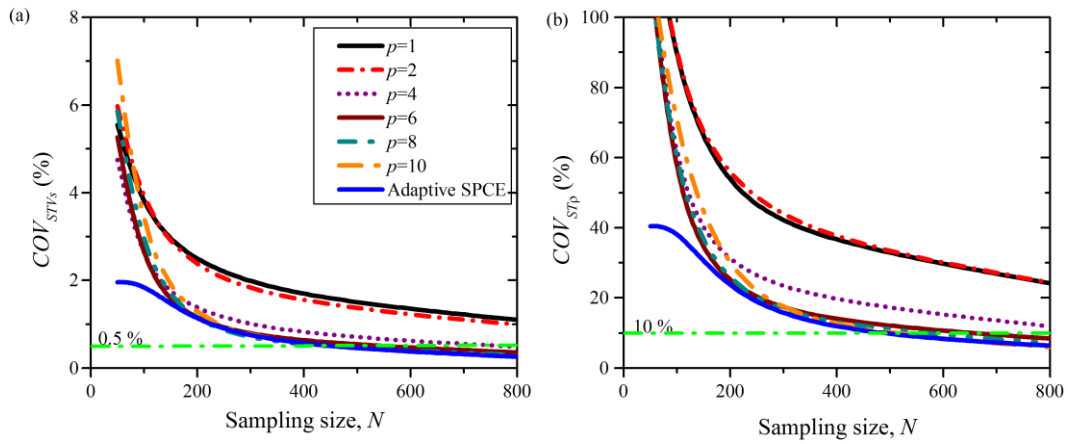


Fig. 6.11 Variation of the total Sobol' indices: (a) shear wave velocity; and (b) density for different sampling sizes and polynomial degrees.

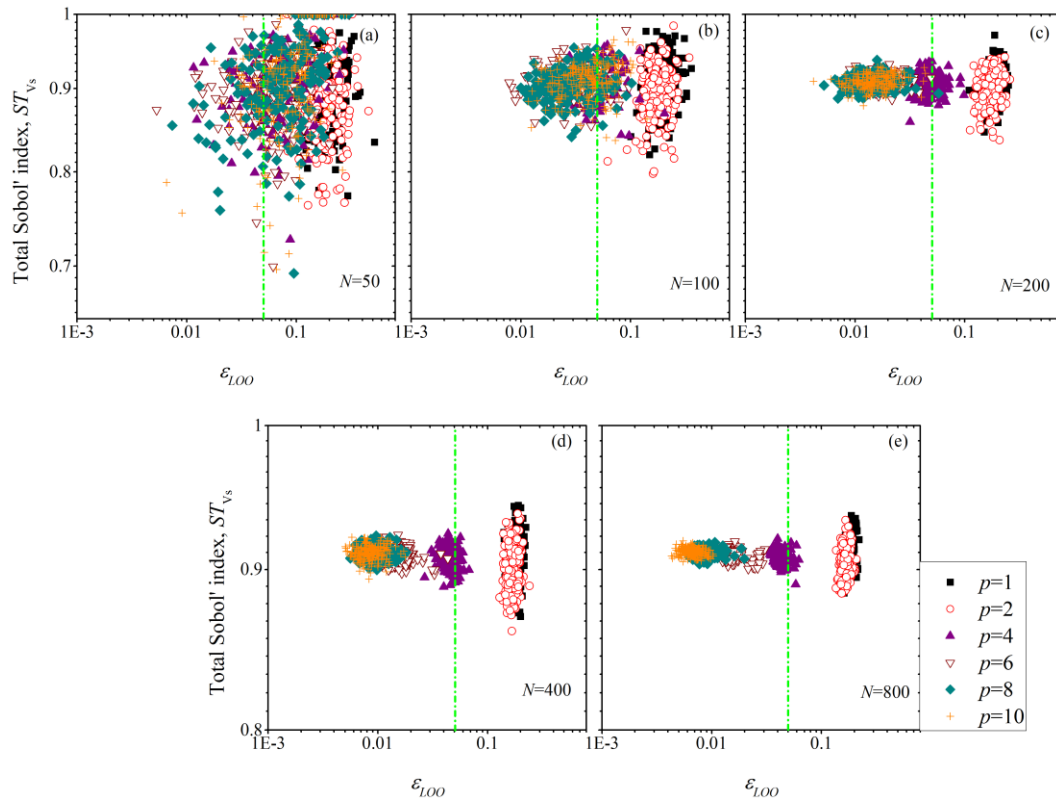


Fig. 6.12 Scatter plots comparing the total Sobol' index of V_s for different sampling sizes and polynomial degrees.

An over-fitting frequently occurs when fewer training data is used. This leads to calculation errors and a wrong ranking of the sensitivity index of each variable even if a small model error is observed. An illustrative example of over-fitting which appears during the sensitivity analysis is presented in Fig. 6.13 (corresponding to sampling size $N=50$ and motion intensity $PGA=0.3$ g). With the increased sampling size, higher order *SPCE* models greatly reduce the variability in the calculated sensitivity indices, since the over-fitting is effectively avoided and the surrogate model permits to accurately predict the true numerical responses.

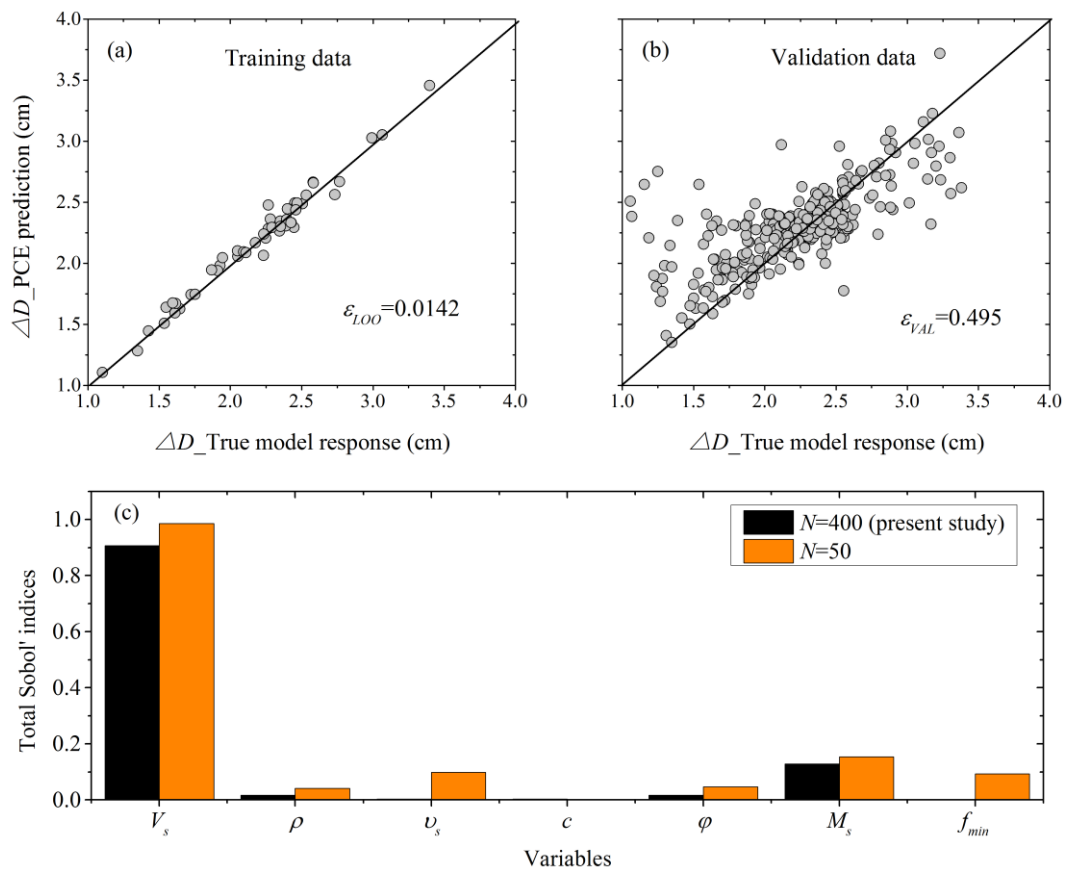


Fig. 6.13 An illustrative example of over-fitting due to insufficient training data and the corresponding total Sobol' indices.

Although the model error (ϵ_{LOO}) appears to decrease with increasing polynomial degree p , the convergences of *COV* of two variables are obtained as soon as $p \geq 6$. This indicates that a sixth order *SPCE* is possible to accurately substitute the true numerical predictions when the sampling size is sufficient. For the adaptive *SPCE-GSA* method with a sampling size $N=400$, the variability in the total Sobol' indices of V_s and ρ is respectively equal to 0.5% and 10%. Larger variations are observed for the total index of density, which is however not a problem

since the absolute value of the index makes this variable unimportant (0.0164, see Table 6.3).

In summary, the best optimal manner to reduce the variability in the calculated sensitivity index is to get more training points and select an appropriate polynomial degree. For the former, this in general is practically difficult due to the limits of computational cost. Also, this is not a cost-effective way since the greatly increased sampling size corresponds to a slow decrease in the sensitivity index variability when the threshold is exceeded, as depicted in Fig. 6.11. For the latter, it is difficult to, *a priori*, know which *SPCE* order can exactly represent the true model response while high order surrogate models induce more training points. Thus, an algorithm to choose adaptively the optimal polynomial degree is important.

6.6.2 Input ground motion characteristics

To gain insights into the ground motion characteristics influence on the computed Sobol' indices, three additional recorded accelerations, e.g., Nice, Northridge, and Kobe are selected. The acceleration time-histories and the corresponding Arias intensities in the case of $PGA=0.1$ g are presented in Fig. 6.14a and 6.14b. The energy of the Kobe ground motion is about twice the Nice one. The analyses are performed in the benchmark case (Table 6.2) with PGA amplitudes equal to 0.1 g and 0.3 g. The evolutions of the total Sobol' indices for different input ground motions considering weak and strong intensities are respectively presented in Fig. 6.14c and 6.14d.

For the case of a $PGA=0.1$ g, V_s is always the most important variable and the Sobol' indices of each variable for different ground motions are almost identical. The input ground motion influences on the calculated sensitivity indices are strengthened with the increase of the motion intensity (i.e., 0.3 g), because of the different soil nonlinearity levels. The Northridge ground motion induces the maximum V_s sensitivity index, while the Kobe ground motion the minimum one is found. This could be attributed to the fact that the Kobe ground motion has the largest energy and induces significant soil plasticity, thus it enhances the role of the related variables (i.e., v_s , c , φ , M_s). Moreover, strong interaction effects between different

variables appear for the Kobe ground motion (i.e., the sum of the total Sobol' indices is larger than 1). In summary, the ground motion characteristics have an unimportant influence on the computed sensitivity indices when the soil behaviour is linear. However, an influence appears and increases with the soil nonlinearity increasing levels. For the cases analyzed, V_s and M_s are the two most important variables for each ground motion.

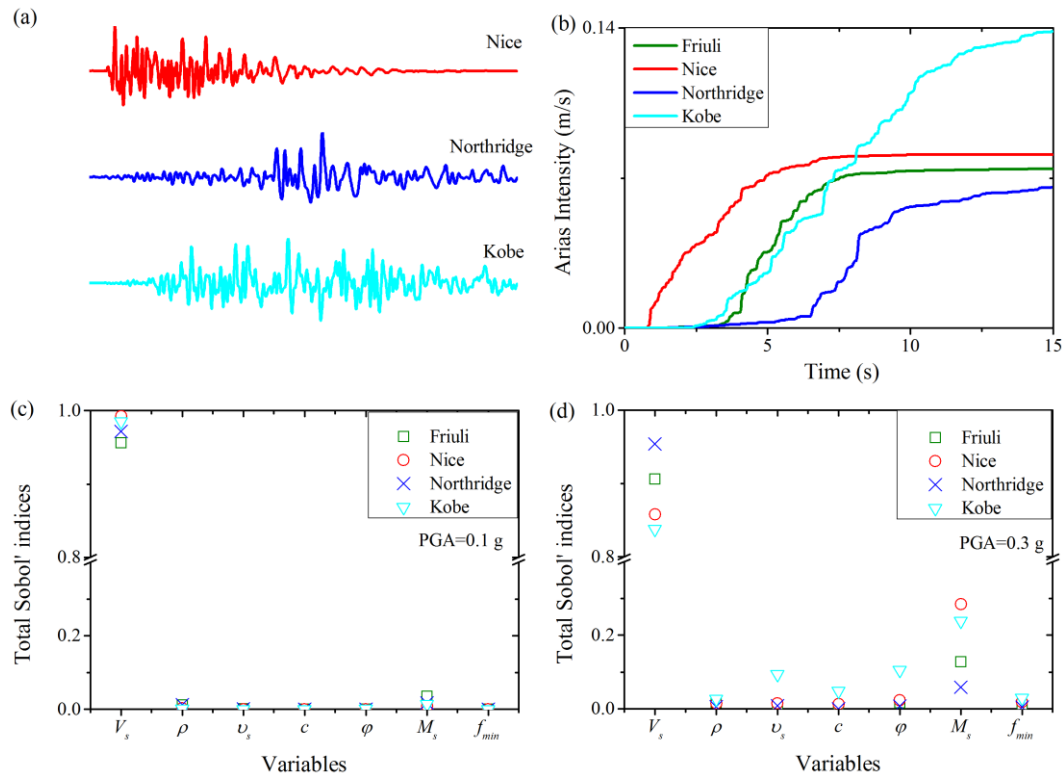


Fig. 6.14 Influences of the input ground motions: (a) acceleration time-histories (scaled to 0.1 g, the acceleration time-history of Friuli can be seen Fig. 6.2a); (b) Arias intensities of input ground motions with an amplitude of 0.1 g; (c) Total Sobol' indices for $PGA=0.1$ g; and (d) Total Sobol' indices for $PGA=0.3$ g.

6.7 Conclusions

This chapter presents a global sensitivity analysis based on the sparse polynomial chaos expansions method to investigate the relative importance of seven variables on the variability in the tunnel seismic deformations. The analyses are performed in a wide range of cases, to fully consider the possible probabilistic scenarios of a real tunnel project. The results illustrate the accuracy and efficiency of the *SPCE-GSA* method for the tunnel seismic analysis.

Following the procedure presented herein, shows that this method has the capability of performing sensitivity analyses of other more realistic cases.

The study reveals that V_s dominates the tunnel seismic deformations for weak motion cases. Increasing the motion intensity, the influence of V_s gradually decreases while the influences of M_s for the soft soil and φ for the stiff soil greatly increase. This is due to the shear modulus reduction and soil plasticity. The influences of other random variables are generally minor, thus they should be considered as deterministic ones. The interactions between V_s and M_s , M_s , and φ in the soft soil subjected to strong motions appear especially when the variation degree of V_s is not high. Moreover, the decreased variation degree of a variable generally leads to a reduction in its sensitivity index. However, a relatively small variation of the variable can still have a pronounced influence (Fig. 6.9). Furthermore, the influences of the ground motion characteristics on the computed sensitivity indices increase with increasing the soil nonlinearity level.

The Sobol' indices predicted by the *SPCE-GSA* method are related to the accuracy of the constructed surrogate model. Getting more training points and selecting an appropriate polynomial degree could guarantee that the constructed surrogate models can well represent the true numerical responses. It, therefore, decreases the variability in the calculated sensitivity indices.

Chapter 7

Probabilistic seismic response of tunnels in random soils:

Statistical analysis

7.1 Introduction

In the current seismic analysis and design practice, the seismic response of a tunnel is evaluated using a deterministic approach. This kind of analysis, however, has no capability of considering the soil parameters uncertainties and quantifying their influences on the tunnel seismic response. Because of the lack of information and the inherent soil properties uncertainty, the accurate prediction of the seismic response of tunnels is often challenging. Therefore, considering the uncertainty of the soil-tunnel system and variability in the tunnel seismic response appears to more rational.

This chapter aims to quantify the variability in the tunnel seismic deformations caused by uncertain soil and damping model parameters. The statistical characteristics in terms of mean, variance, and coefficient of variation of the tunnel deformations are examined through two-dimensional plane strain nonlinear finite difference models (i.e., the same as the one used in Chapter 6) combined with Monte Carlo simulations. To address some limitations of the existing studies, several uncertain scenarios are investigated. Analyses are performed for a wide range of soil shear wave velocities, ground motion intensities, lining Young's moduli, correlation structures, distribution types, and coefficients of variation. Finally, the impact on a reliability-based seismic design of tunnels is discussed.

7.2 Monte Carlo simulation

This section first introduces an advanced sampling method named Latin hypercube sampling, to improve the sampling quality (i.e., speed up calculation convergence). Then, the sample size to guarantee the calculation accuracy is discussed.

7.2.1 Latin hypercube sampling

When employing the Monte Carlo simulation, the challenge lies in how to improve the calculation efficiency. To do so, the Latin hypercube sampling (*LHS*) technique (Iman, 1999) is used to generate the input samples.

LHS uses a stratified sampling scheme to improve the coverage of the input space. The stratification is accomplished by dividing the graph vertical axis of the cumulative distribution function (*CDF*) of a random variable into n non-overlapping intervals of equal length, where n is the sample size. Then, the *LHS* scheme requires a random value selection within each of the n intervals. Exactly one value will be selected from the corresponding intervals on the horizontal axis. Each interval for each variable is sampled only once, and the univariate sample values are randomly matched across all the variables to form the n sample points by permuting each factor column in the design. It is found that the computational cost saving in sampling is reduced by a factor of 20 to 100 when using *LHS* rather than a simpler random sampling to estimate the mean and standard deviation of the model responses (Iman, 1999; Toufigh and Pahlavani, 2018).

To help to understand, Fig. 7.1 shows 50 sampling points for a set of two variables using the random sampling and *LHS* methods, where variables (x_1, x_2) are independent and uniformly distributed on the interval $(0, 1)$. As observed, the points generated by the random sampling method are not uniformly distributed and some points are replicated, whereas *LHS* improves the sampling quality.

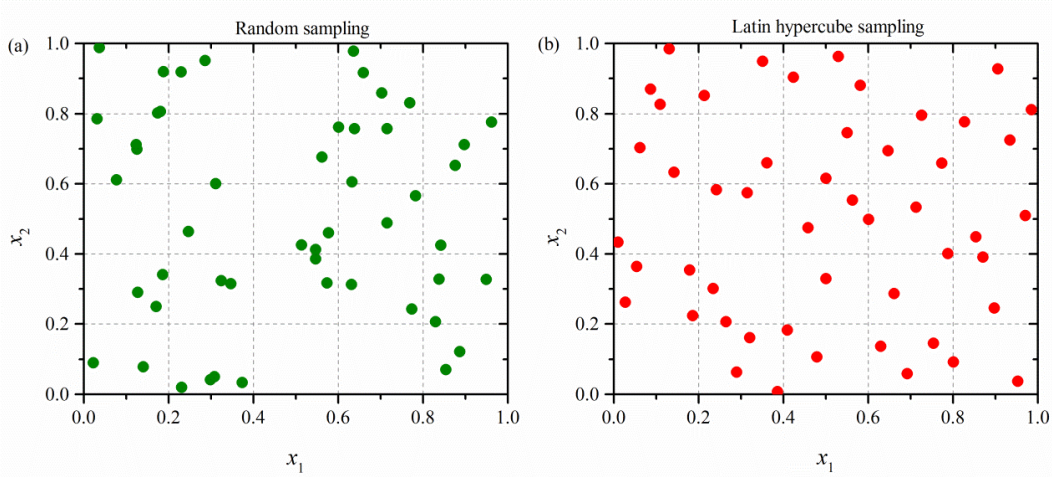


Fig. 7.1 Comparison of sampling point distributions generated by two sampling methods in 2D: (a) random sampling; and (b) Latin hypercube sampling.

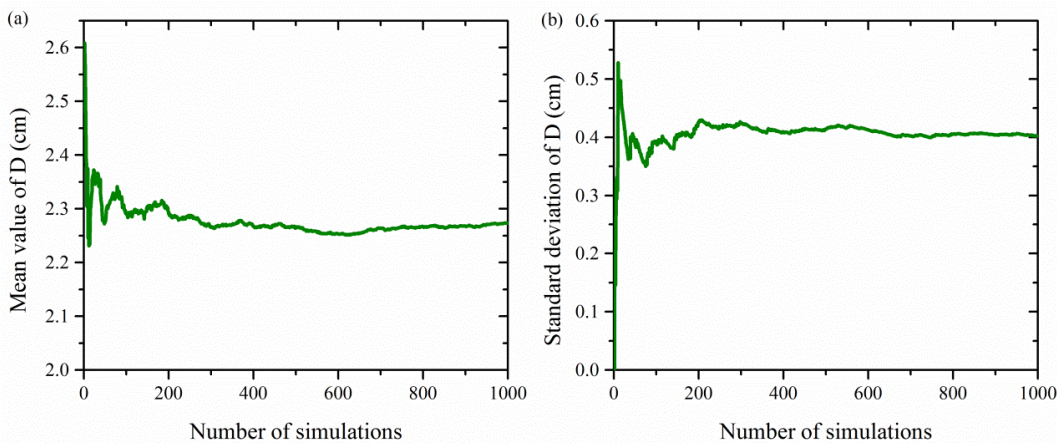


Fig. 7.2 Mean and standard deviation of the tunnel deformation as a function of the number of simulations for the reference case when $PGA=0.3g$: (a) mean value; and (b) standard deviation.

7.2.2 Sample size

To obtain reliable statistical results, the sample size should be determined first. Fig. 7.2 shows the mean value and standard deviation of the tunnel maximum deformation as a function of the number of simulations for the reference case subjected to a strong ground motion ($PGA=0.3 g$). It can be observed that stable results are obtained as the simulation number reaches 500, and the corresponding statistical moments are very close to the ones of 1000 simulations. Therefore, stochastic analyses are performed by adopting 500 deterministic realizations. This number is used as a default in the following work if it is not specifically pointed out.

7.2.3 Probabilistic models

The deterministic numerical model used in this chapter is the same as the one used in Chapter 6. The probabilistic input models of the seven studied variables as tabulated in Table 6.2 are used as the reference case. In this chapter, only Friuli ground motion is selected as the seismic input. More details are not presented in this section, readers can refer to the content of section 6.3. Fig. 7.3 shows the main scheme to quantify the statistical characteristic of the tunnel seismic deformation in the framework of Monte Carlo simulations. It includes the uncertainty inputs, a 2D soil-tunnel numerical model, and the uncertainty propagation process.

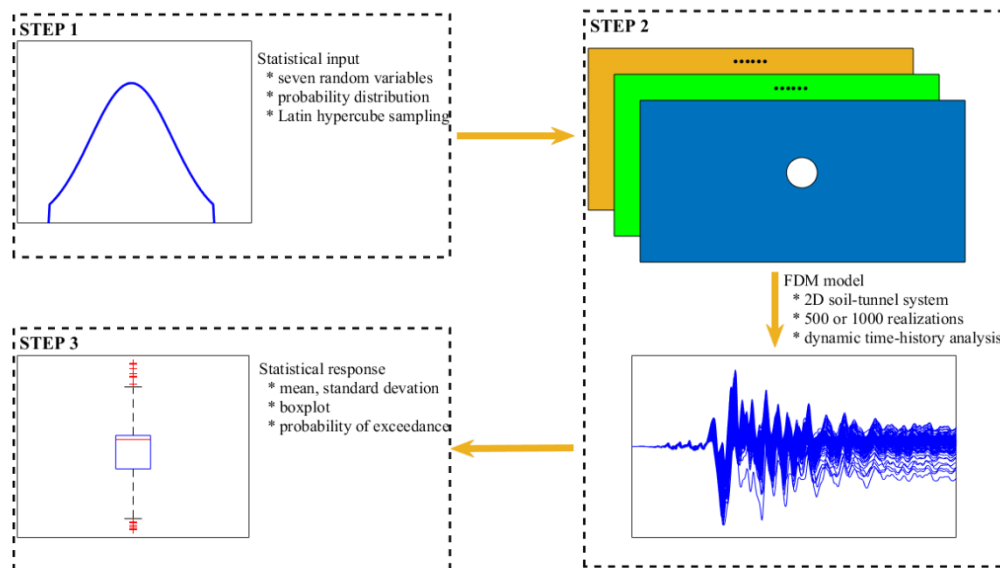


Fig.7.3 Uncertainty quantification in the framework of Monte Carlo.

7.3 Results of the reference case

The probabilistic analysis of the reference case (Table 6.2), which allows showing the basic deformation characteristic of a tunnel in random soils is presented. In this study, a link between *FLAC* and *MATLAB* software is built to automatically exchange the data (variables input and responses processing). To consider different levels of soil nonlinearity, the amplitude of the Friuli ground motion varies from 0.05 g to 0.3 g.

Fig. 7.4 shows the computed tunnel deformations time-histories, histograms of the maximum tunnel deformation, and the corresponding probability of exceedance (*POE*, the probability of a stochastic process exceeds a critical value) for two ground motion intensities. Three types of probability distributions (e.g., normal, lognormal, and gamma) are adopted to fit the computed deformation responses. The majority of the tunnel responses are in the elastic range for $PGA=0.1$ g, leading to a small variability in the computed deformation time-histories, as shown in Fig. 7.4a. The maximum deformations appear to be symmetrical and result in a smooth *POE* curve. Increasing the ground motion intensity to 0.3 g, the soil nonlinearity influence increases, and the deformation time-histories show a larger variability. Furthermore, the deformation histogram is found to be more complex, having multi-peaks and a heavy left tail. Hence, the deformation responses are difficult to characterize by simple probability distributions, as observed in Fig. 7.4f.

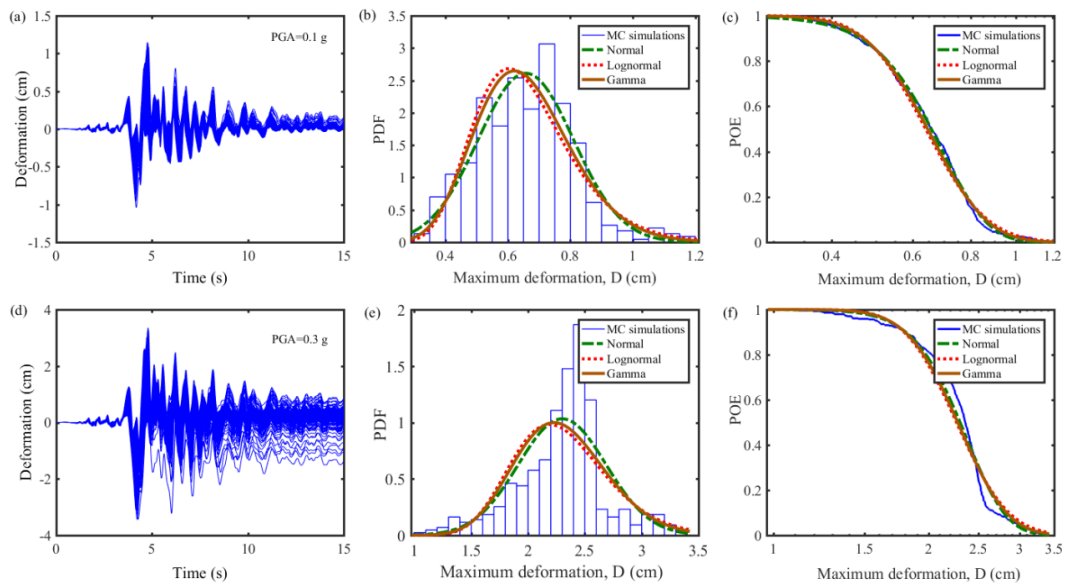


Fig. 7.4 Computed deformation time-histories and histograms of the maximum deformation and the corresponding probability of exceedance (500 MCs are also respectively fitted by normal, lognormal, and gamma distribution):

(a)~(c) $PGA=0.1$ g; and (d)~(f) $PGA=0.3$ g.

The deterministic value D_d , mean μ_D , standard deviation σ_D , coefficient of variation COV ($=\sigma_D/\mu_D$), skewness of the *PDF* curve for different motion intensities are shown in Table 7.1. For the weak motions (i.e., $PGA=0.05$ g, and 0.1 g), the mean values of the stochastic responses are identical to the deterministic results. It implies that the soil parameters

uncertainty introduces an unbiased effect on the tunnel deformations. The Kolmogorov-Smirnov test shows that the computed tunnel deformations follow a normal distribution with a significance level of 0.05. For the higher intensities (i.e., $PGA=0.2$ g, and 0.3 g), the mean values are lower than the deterministic ones. A small portion of lower deformation values is predicted (Fig. 7.4e), corresponding to a negative skewness value (Table 7.1). As a result, the maximum deformation cannot pass the $K-S$ test for normality. It is found that the standard deviations appear to increase with the increase of ground motion intensities. However, the $COVs$ of the maximum deformations slightly decrease as the ground motion intensity increases, with values approximately constant and equal to 0.2.

Table 7.1 Statistic moments of the reference case.

| PGA (g) | D_d (cm) | μ_D (cm) | σ_D (cm) | COV | Skewness | $K-S$ test |
|-----------|------------|--------------|-----------------|-------|----------|------------|
| 0.05 | 0.311 | 0.311 | 0.071 | 0.227 | 0.234 | Normal |
| 0.1 | 0.658 | 0.658 | 0.153 | 0.233 | 0.340 | Normal |
| 0.2 | 1.479 | 1.445 | 0.296 | 0.205 | 0.012 | - |
| 0.3 | 2.449 | 2.300 | 0.387 | 0.168 | -0.332 | - |

7.4 Parametric study

This section aims to further reveal the statistical moments of the maximum tunnel deformations under different scenarios. Additional stochastic analyses are performed for a wide range of soil types, lining Young's moduli, coefficients of variations, distribution types, and correlation structures.

7.4.1 Soil type and lining stiffness

Numerous deterministic studies have illustrated that the relative flexibility between the soil and tunnel lining (i.e., flexibility ratio) has a direct effect on the seismic-induced tunnel deformations (Bilotta *et al.*, 2014; Bobet, 2010). To summarize the statistical characteristics of deformations in a wider range, complementary studies are performed for a range of shear wave velocities (V_s) and Young's moduli of the lining (E_l). The V_s values vary from 200 m/s to 500 m/s, which corresponds to soft and stiff soils (Zoutat *et al.*, 2018). Meanwhile, the value

of E_l is respectively equal to 20 GPa, 35 GPa, and 70 GPa, which depends on the lining material (e.g., concrete, reinforced concrete and, cast iron) to consider flexible and rigid tunnels. The mean, upper, and lower limits in the probability distributions of V_s and f_{\min} vary in the exception of the variation degrees (Table 6.2). The other parameters are the same as the ones adopted in the reference case. Considering all the combinations of V_s , E_l , and PGA , a total of 14500 (i.e., $3 \times 3 \times 500$) dynamic time-history analyses are performed, requiring around 1200 computational hours.

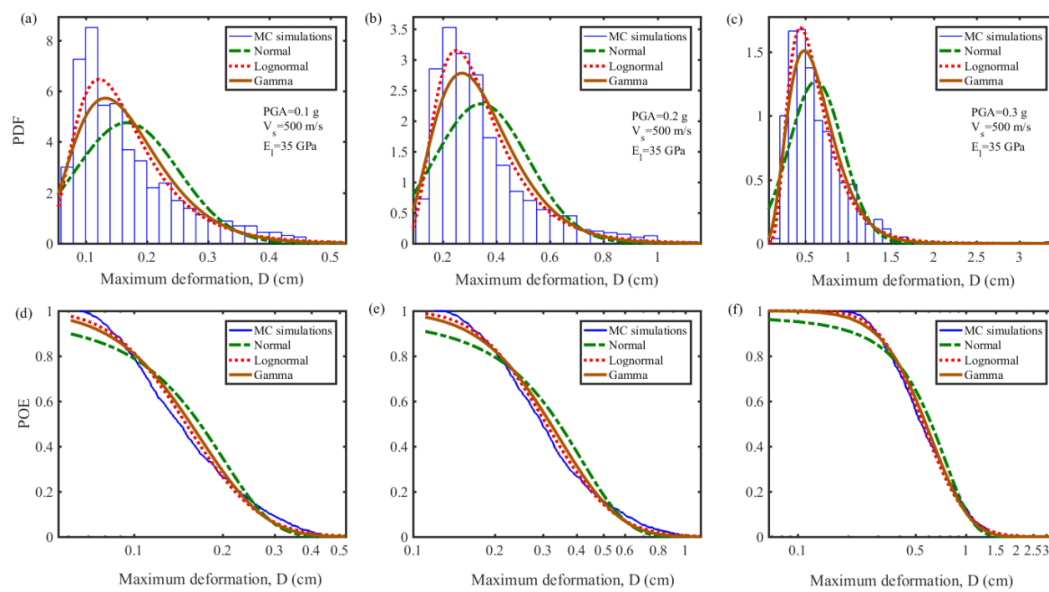


Fig. 7.5 Histograms of the maximum deformations and corresponding probability of exceedance in the case of $V_s=500$ m/s and $E_l=35$ GPa (results of 500 MCs respectively fitted by normal, lognormal, and gamma distribution): (a) and (d) $PGA=0.1$ g; (b) and (e) $PGA=0.2$ g; (c) and (f) $PGA=0.3$ g.

Fig. 7.5 shows the representative results in terms of deformations histogram and POE , corresponding to the cases of $E_l=35$ GPa, $V_s=500$ m/s, and three PGA s. Three major differences can be seen when a comparison with the $V_s=200$ m/s (Fig. 7.4e) case is done. Firstly, larger V_s will reduce the tunnel deformation ranges (i.e., [minimum, maximum]) for the same lining stiffness and ground motion intensity, since the tunnel deformation depends heavily on the surrounding soil responses (the stiffer the soil, the lower the deformation). Secondly, the histograms show a long tail towards their right (i.e., larger deformations) and this is more evident for higher ground motion intensities. This could be attributed to the soil profiles generated with lower V_s values in the stochastic analysis. Thirdly, the lognormal

distribution matches well the deformation responses (Figs. 7.5d~7.5f).

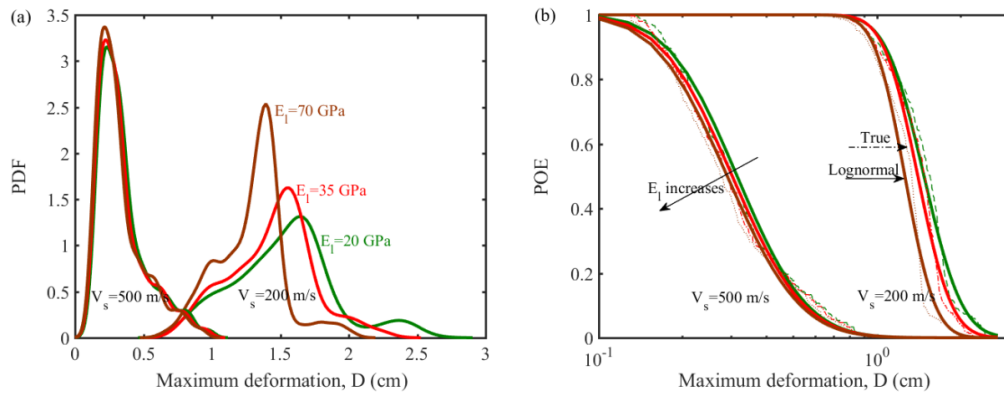


Fig. 7.6 Probability density function and the corresponding POE for different values of E_l , in the case of $V_s=200$ and 500 m/s, $PGA=0.2$ g: (a) PDF ; and (b) POE of the model response and lognormal fittings.

Fig. 7.6 shows the $PDFs$ and $POEs$ of the deformations computed with three lining Young's moduli. The comparisons correspond to $V_s=200$ m/s and 500 m/s, with a $PGA=0.2$ g. It is found that, for the soft soil (i.e., $V_s=200$ m/s), when E_l increases, the small deformations probability increases. The PDF decreases in width as E_l increases, due to the decreased upper deformation limit. However, for the stiffer soil (i.e., $V_s=500$ m/s), when the lining stiffness increases, both the $PDFs$ and $POEs$ are slightly modified. It means E_l has an insignificant effect on the computed tunnel deformations for stiff soils, whereas extremely high deformations usually occur for flexible tunnels in soft soils.

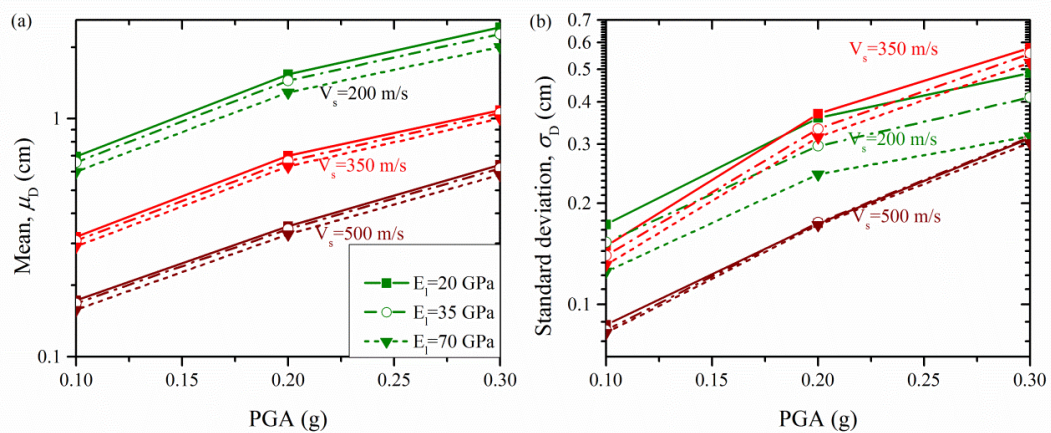


Fig. 7.7 Statistical moments of the computed deformations for different V_s , E_l , and PGA values: (a) mean; and (b) standard deviation.

Fig. 7.7 shows the results obtained for different values of V_s , E_l , and PGA , in terms of mean values and standard deviations. As observed, both the mean values and standard deviations increase with the PGA increases. The figure clearly shows that a tunnel with a lower stiffness buried in a soft soil will have a larger mean deformation than one with a higher stiffness buried in a stiff soil. This trend is observed for standard deviations only when the ground motion intensity is low (i.e., $PGA=0.1$ g). It is found that, for higher $PGAs$ (i.e., 0.2 g, and 0.3 g), the soil with a medium V_s value will induce the larger standard deviations than one that has a higher or a lower V_s value. This will be discussed in detail in Fig. 7.8. Additionally, it can be observed that the influence of E_l is insignificant for a stiff soil (i.e., $V_s=500$ m/s). For instance, the relationships of the mean and standard deviation versus the ground motion intensity for different E_l values are almost identical.

Table 7.2 Statistical moments for different values of V_s and E_l in the case of $PGA=0.3$ g.

| V_s (m/s) | E_l (GPa) | D_d (cm) | μ_D (cm) | COV | Skewness |
|-------------|-------------|------------|--------------|-------|----------|
| 200 | 20 | 2.584 | 2.422 | 0.201 | -0.120 |
| | 35 | 2.449 | 2.301 | 0.168 | -0.332 |
| | 70 | 2.148 | 2.000 | 0.158 | -0.193 |
| 350 | 20 | 0.881 | 1.086 | 0.534 | 1.235 |
| | 35 | 0.869 | 1.059 | 0.526 | 1.240 |
| | 70 | 0.847 | 1.004 | 0.522 | 1.100 |
| 500 | 20 | 0.533 | 0.640 | 0.486 | 0.972 |
| | 35 | 0.515 | 0.622 | 0.505 | 1.620 |
| | 70 | 0.479 | 0.582 | 0.519 | 1.135 |

Table 7.2 shows the results of computed tunnel deformations for different soil conditions and lining stiffness, in the case of $PGA=0.3$ g. For the soft soil (i.e., $V_s=200$ m/s), the mean deformation is lower than the one computed in the deterministic analysis. While for the other two soils (i.e., $V_s=350$ m/s, and 500 m/s), the computed mean deformations are larger than the deterministic ones. This could be attributed to the heavy left tails with small deformations for the soft soil, whereas the heavy right tails with larger deformations for the stiff soil, as shown in Figs. 7.4 and 7.5. The skewness values also confirm this finding (i.e., a negative value corresponds to a PDF towards the left or vice versa). Additionally, it can be observed from Table 7.2 that the lining stiffness influence on the $COVs$ is generally not pronounced. Its

effect becomes progressively smaller as the V_s increases, despite a relatively small COV is computed in the case of $V_s=200$ m/s.

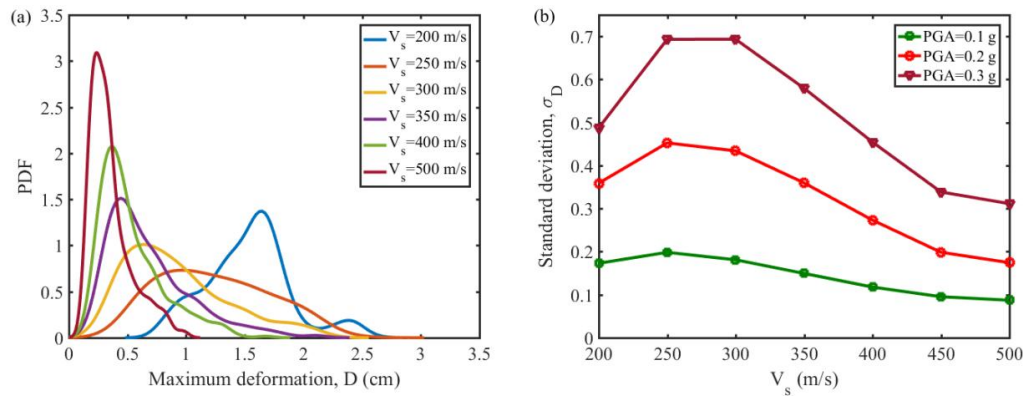


Fig. 7.8 Influences of V_s on the variability in the tunnel deformation: (a) PDF for different values of V_s in the case of $PGA=0.2$ g; and (b) standard deviations for different values of V_s and PGA , in the case of $E_t=20$ GPa.

The observation from Fig. 7.7b shows a nonlinear relationship between the standard deviation with the V_s value. To discuss in detail how the V_s value affects the standard deviation of deformations, a variety of V_s values, from 200 m/s to 500 m/s are investigated. The analyses (10500 numerical realizations) correspond to $E_t=20$ GPa and three $PGAs$. Fig. 7.8 presents the standard deviation evaluations with V_s and the corresponding $PDFs$ in the case of 0.2 g. The critical V_s that induces the maximum standard deviation is generally in the range between 250 m/s and 300 m/s. This is due to the high probability of generating both lower and higher V_s profiles during random realizations for medium soils. This results in a wider deformation interval as shown in Fig. 7.8a. Results also show that the standard deviation is more sensitive to the change of V_s for a higher PGA (i.e., 0.3 g), due to the increased influence of ground motion intensity on the soil deformations.

7.4.2 Correlation between c and φ

The input parameters are assumed to be independent in the previous analyses. In practice, a negative correlation between the cohesion c and the friction angle φ is widely reported (Al-Bibbar *et al.*, 2018; Fenton, 1999; Mollon *et al.*, 2009, 2013). The correlation coefficient

$\rho_{c,\varphi}$ is generally lower than -0.8 (Phoon and Kulhawy, 1999a, 1999b). Positive $\rho_{c,\varphi}$ values are also encountered for some soils, for instance, a $\rho_{c,\varphi}$ value of 0.25 (Wolff, 1985), and 0.6 (Guo et al., 2020). In this section, a range of $\rho_{c,\varphi}$ values, from -0.8 to 0.8, is investigated to gain insights into the influence of this parameter on the tunnel seismic deformations. The analyses are performed in two scenarios: scenario 1 accounts for seven variables (reference case); scenario 2 considers only the uncertainty of c and φ whereas other parameters are assumed to be constant. For two scenarios, the ground motion with an amplitude of $PGA=0.1$ g and 0.3 g are considered.

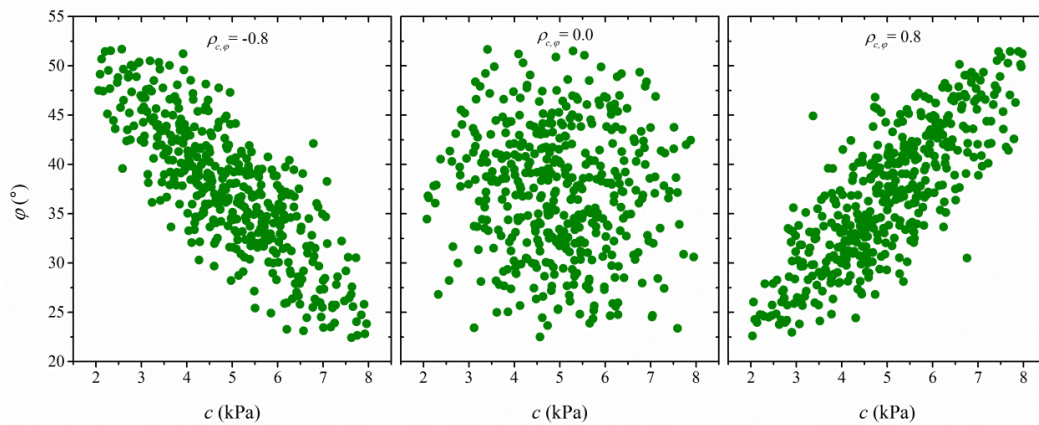


Fig. 7.9 500 pairs of c and φ sampled with different correlation coefficients: (a) $\rho_{c,\varphi}=-0.8$; (b) $\rho_{c,\varphi}=0.0$; and (c) $\rho_{c,\varphi}=0.8$.

Fig. 7.9 shows schematically 500 pairs of (c, φ) sampled with three different correlation coefficients ($\rho_{c,\varphi}=-0.8, 0$, and 0.8). As observed, for the negative correlation, a lower value of the c corresponds to a larger value of φ , whereas a positive correlation leads to an increase of the φ value as the c value increases. When the c and φ are assumed to be independent (i.e., $\rho_{c,\varphi}=0$), these two parameters are randomly generated without any trend.

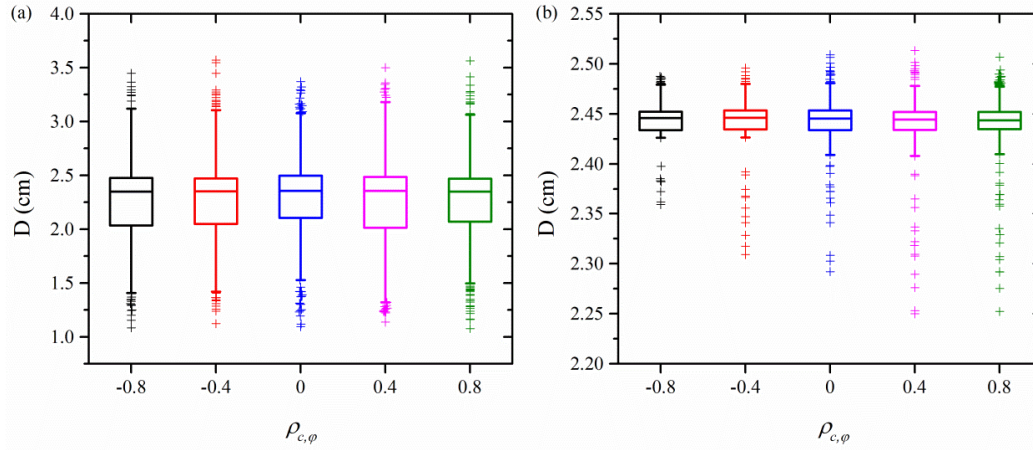


Fig. 7.10 Computed maximum tunnel deformations considering different correlation coefficients in two scenarios: (a) seven variables are considered; and (b) c and φ are only considered as variables.

Fig. 7.10 shows box-and-whisker plots of maximum tunnel deformations considering different correlation coefficients in the case of $PGA=0.3$ g. The horizontal lines inside the boxes indicate the median value, whereas boxes' extremes indicate the first and third quartiles of the computed deformation distribution. The whiskers in Fig. 7.10 extend to points that are within 1.5 times the inter-quartile range, and deformations that exceed that range are explicitly presented using cross symbols. For scenario 1, Fig. 7.10a shows that the variability in the deformations is not sensitive to the correlation coefficients change. As the $\rho_{c,\varphi}$ increases, the median, maximum, and minimum responses tend to remain the same. However, when cohesion and friction angle uncertainties are only considered (scenario 2), the variability in the computed deformations increases as the correlation coefficient increases, as shown in Fig. 7.10b. For instance, the positive correlations lead to longer tails than negative ones while the medium value is less influenced.

Table 7.3 illustrates the mean and standard deviations of the deformations, for different correlation coefficients and ground motion intensities. The results show that computed mean deformations of correlated cases ($\rho_{c,\varphi} \neq 0$) tend to be close or identical to the independent case ones ($\rho_{c,\varphi} = 0$) for all the investigated cases. The correlation coefficients have also a negligible influence on the standard deviations for scenario 1. When the variability in the tunnel deformations is only induced by the uncertainties of c and φ (scenario 2), the standard

deviations increase with the correlation coefficients increase (Mollon *et al.*, 2009), especially for the large ground motion intensities. The different observations from these two scenarios are due to the soil shear wave velocity (V_s) rather than the shear strength parameters (c , ϕ) which control the tunnel deformation responses, as shown in Fig. 7.11.

Table 7.3 Statistical moments for correlation coefficients $\rho_{c,\phi}$.

| | Mean | | | | Standard deviation | | | |
|--------|------------|-------|------------|-------|--------------------|-------|------------|-------|
| | Scenario 1 | | Scenario 2 | | Scenario 1 | | Scenario 2 | |
| ρ | 0.1 g | 0.3 g | 0.1 g | 0.3 g | 0.1 g | 0.3 g | 0.1 g | 0.3 g |
| -0.8 | 0.653 | 2.261 | 0.658 | 2.444 | 0.152 | 0.419 | 0.0027 | 0.015 |
| -0.4 | 0.658 | 2.273 | 0.658 | 2.444 | 0.157 | 0.427 | 0.0028 | 0.020 |
| 0 | 0.657 | 2.301 | 0.658 | 2.443 | 0.153 | 0.387 | 0.0031 | 0.023 |
| 0.4 | 0.657 | 2.267 | 0.658 | 2.440 | 0.154 | 0.418 | 0.0033 | 0.028 |
| 0.8 | 0.657 | 2.267 | 0.658 | 2.442 | 0.152 | 0.415 | 0.0034 | 0.029 |

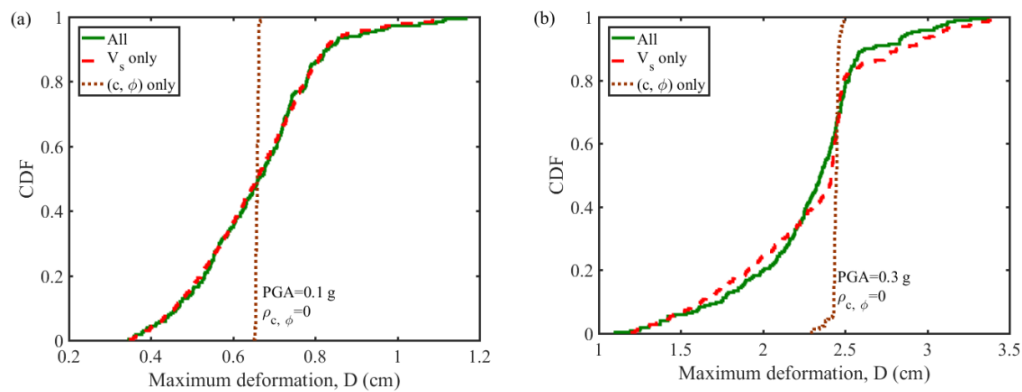


Fig. 7.11 CDFs of the maximum tunnel deformations for two ground motion intensities (All: considering seven variables, V_s : only V_s is considered as variable, (c, ϕ) : cohesion and friction angle are considered as variables with $\rho_{c,\phi}=0.0$).

As observed in Fig. 7.11, the CDFs computed with only the V_s uncertainty are almost identical to the ones where seven variables are simultaneously considered. When only considering c and ϕ uncertainties, the CDF shows a steeper gradient. The influence of the c and ϕ uncertainties on the tunnel deformations is insignificant regardless of the correlation coefficients. Negative correlations tend to produce similar deformations for different probabilistic analysis realizations. It then reduces the standard deviation of deformations. This is due to the “averaging effect” which appears for negative correlation coefficients (i.e., large c combined with small ϕ or vice versa, thus the soil for each realization is not easily close to a

plastic state, Fig. 7.9a). For positive correlation coefficients, this averaging effect is not present and the computed deformations are more sensitive to the (c, φ) pairs on the distribution tails. Specifically, small c combined with small φ or vice versa, thus some soil profiles are in an elastic state whereas others may experience a plastic state, the difference between each realization is supposed to be larger (Fig. 7.9c).

7.4.3 Probability distribution and COV

Despite the normal distribution has been employed to characterize the uncertainty of soil properties in many studies (Fenton, 1999; Guo *et al.*, 2020; Jimenez and Sitar, 2009; Phoon and Kulhawy, 1999a, 1999b, Toufigh and Pahlavani, 2018), the soil properties can also follow a beta or lognormal distribution (or other distributions). Furthermore, the use of normal distribution inevitably generates soil parameters without physical meaning in some cases. The beta and lognormal distributions allow to naturally generate non-negative values. It is more appropriate to describe the uncertainty of soil parameters. Three different types of probability distributions (beta, lognormal, and normal) are employed to characterize the soil parameters uncertainty. In this section, only the shear wave velocity is characterized as a random variable, because of its significant influence. The parametric analyses correspond to $V_s = 500$ m/s, $E_f = 20$ GPa, and $PGA = 0.3$ g.

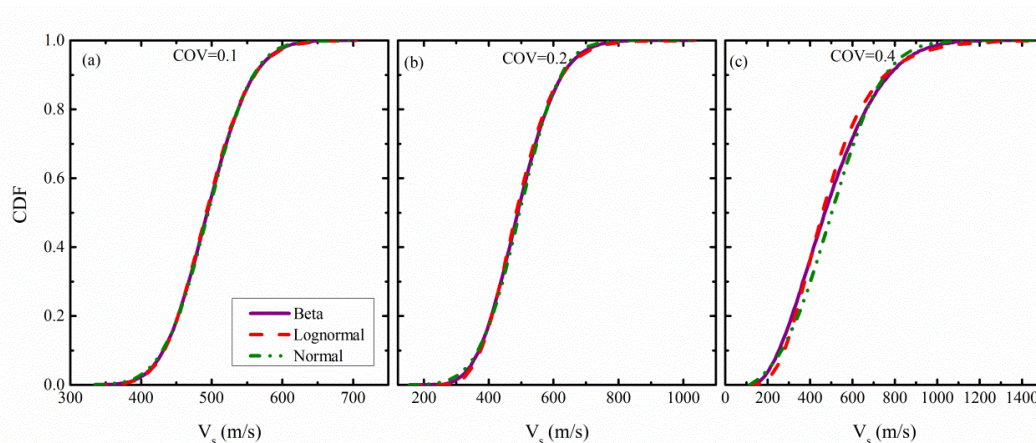


Fig. 7.12 Comparison between beta, lognormal, and normal distributions: (a) $COV=0.1$; (b) $COV=0.2$; and (c) $COV=0.4$.

For each distribution type, four coefficients of variation (i.e., COV), varying from 0.1 to 0.4 are considered. These values of COV are thought to be representative of the V_s variability ranges for typical soils (Rathje *et al.*, 2010; Sun *et al.*, 2020; Toro, 1995). To visually demonstrate the relative ranges of V_s generated, Fig. 7.12 presents a comparison between the cumulative density functions (CDF) of the beta, lognormal, and normal distributions for $COV=0.1, 0.2,$ and 0.4 . A lower bound (i.e., V_s value of 120 m/s) is adopted to maintain numerical stability for each probability distribution. As observed, negligible differences between distributions appear for small coefficients of variation (i.e., $COV=0.1$), and the differences increase with increasing $COVs$. Considering all the combinations of distribution types and coefficients of variation, 12000 (i.e., $3 \times 4 \times 1000$, around 1033 computational hours) dynamic numerical analyses are performed. The number of numerical realizations (i.e., 1000) in this case is higher than before (i.e., 500), to accurately capture the tail response.

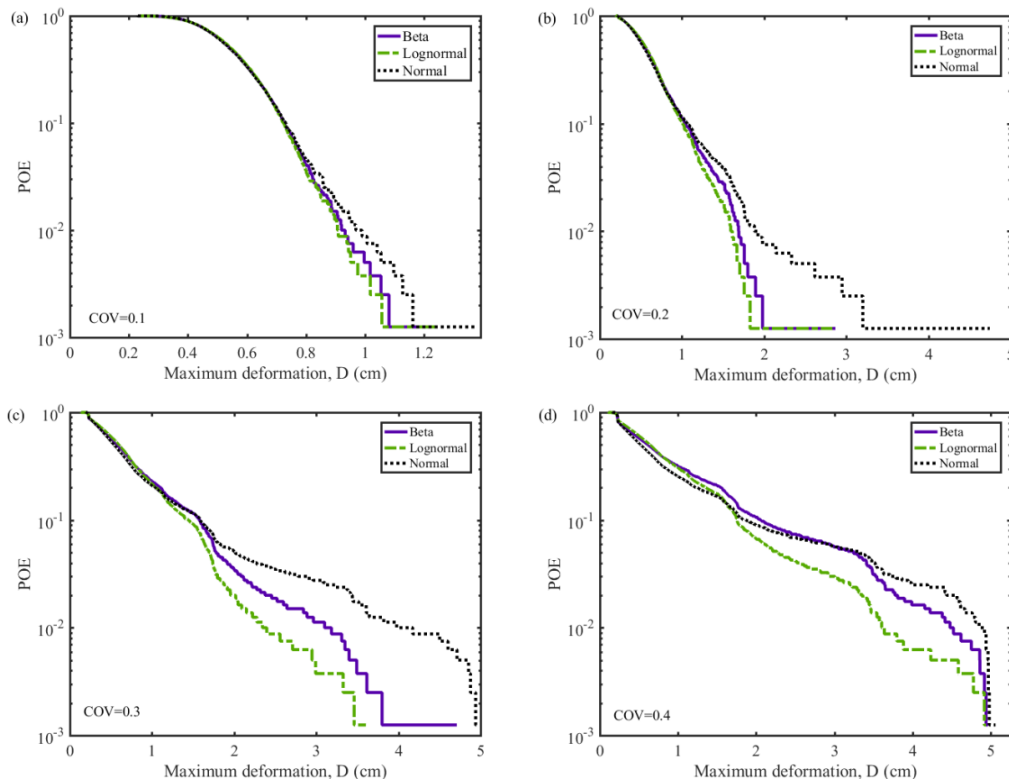


Fig. 7.13 Computed $POEs$ for different distribution types and $COVs$.

Fig. 7.13 shows the $POEs$ for different distribution types and coefficients of variation. As observed, the differences of $POEs$ computed by different distributions increase with the $COVs$

increase. For a small variation degree (i.e., 0.1), the tunnel deformations are not sensitive to the distribution types since the corresponding *CDFs* are almost identical (Fig. 7.12a). In this case, it appears that the values of *POE* are slightly affected by distribution types only when *POEs* are small (i.e., $<10^{-2}$). For larger variation degrees, the distribution types have an increased effect on the tunnel deformations as the *CDFs* of the input variable are more different (Fig. 7.12c). This is due to the different tail-behavior of the beta, lognormal, and normal distributions. Additionally, it leads to an increase in the influenced *POE* range. For instance, Fig. 7.13c shows that *POE* values lower than 0.1 appear to be significantly influenced by the distribution types. The normal distribution has the largest probability of generating smaller V_s values at the left tail, and these smaller values correspond to higher tunnel deformations. For $COV=0.4$, the maximum deformations calculated by the three distributions are identical ($D=5$ cm) because the lower bounds of V_s are reached (i.e., 120 m/s). Due to the removed smaller V_s values, the differences in the small *POE* ranges appear to decrease (Fig. 7.13d). The *POE* values show an increased difference for *POEs* greater than 0.1 (corresponding to larger V_s , Fig. 7.12c).

Results also show that for small *POE* ranges (i.e., $<10^{-2}$), normal distributions induce the highest *POE* value while lognormal distribution the lowest one. This is generally more evident as the *COV* increases. Normal distributions predict a conservative *POE* value compared to non-normal ones. It can be considered as the worst distribution (Mollon *et al.*, 2009; Pan and Dias, 2017). It means that the use of normal distribution to model the uncertainty of soil parameters in this study stays on the safe side from the reliability viewpoint.

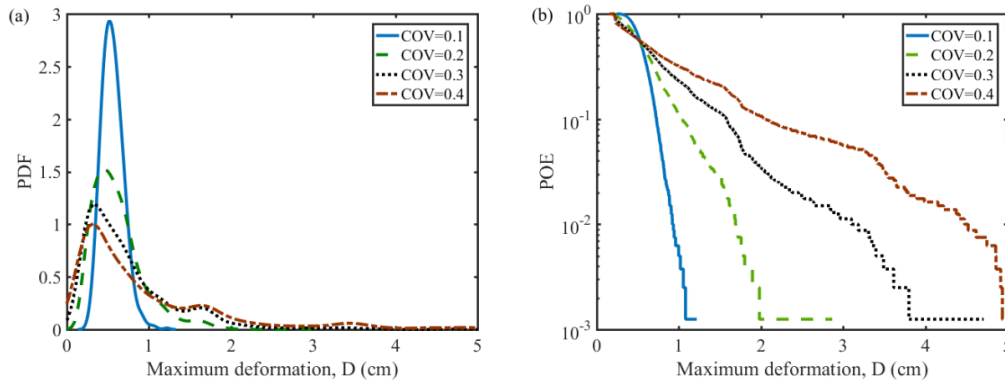


Fig. 7.14 Effects of *COV* on tunnel deformations computed with the lognormal distribution: (a) *PDFs*; and (b) *POEs*.

To increase the understanding of the *COV* influence on the tunnel deformations, the corresponding *PDFs* and *POEs* of deformations for four *COVs* are respectively shown in Figs. 7.14a and 7.14b, assuming that the shear wave velocity follows a lognormal distribution. The deformations with a lower *COV* (i.e., 0.1) vary in a narrower range and have a steeper gradient than the ones with a higher *COV*. Additionally, it appears that with the *COV* increases, the *PDF* of deformations increases in width, and has a tail towards the right. Therefore, for higher *COVs*, the *POE* values are larger (i.e., higher probabilities of failure). For instance, the *POE* computed with a *COV*=0.4 can be about two orders of magnitude higher than the *POE* with *COV*=0.1 in the case of allowed maximum deformation $D=1$ cm.

Table 7.4 summarizes the mean and standard deviation of computed tunnel deformations for different distribution types and *COVs*. When the uncertainty of V_s increases (i.e., *COV* increases), the computed mean deformations tend to increase. This is due to the larger deformations that result from smaller V_s values (Fig. 7.14a). Results also show that the distributions have an insignificant influence on the computed mean deformations for small *COVs* while the influence will gradually increase as the uncertainty increases. Beta distribution produces mean deformations that can be up to 9% higher than the ones computed with lognormal distributions. For the normal distribution, the mean deformation is 6% higher than the one computed with the lognormal distribution. Similarly, the standard deviation of deformations also increases with the *COVs* increase. The distribution types can have a significant influence on the variability in the deformations for larger *COVs*. For instance, the

standard deviation of deformation with the beta distribution is 23% higher than the one computed with the lognormal distribution. The standard deviation computed with the normal distribution can be up to 46% higher than the one computed with the lognormal distribution.

Table 7.4 Mean and standard deviation for different distribution types and *COVs*.

| Distributions | Statistic moments | COV | | | |
|---------------|--------------------|-------|-------|-------|-------|
| | | 0.1 | 0.2 | 0.3 | 0.4 |
| Beta | Mean | 0.556 | 0.622 | 0.750 | 0.949 |
| Lognormal | | 0.556 | 0.612 | 0.724 | 0.874 |
| Normal | | 0.557 | 0.631 | 0.766 | 0.877 |
| Beta | Standard deviation | 0.134 | 0.322 | 0.584 | 0.927 |
| Lognormal | | 0.132 | 0.301 | 0.495 | 0.754 |
| Normal | | 0.139 | 0.388 | 0.724 | 0.956 |

7.5 Implications on tunnel seismic design

The tunnel will damage if the deformation exceeds a certain threshold. In current seismic codes, the allowed maximum deformations are recommended for different serviceability limit states in a deterministic framework, ignoring the variability associated with the tunnel deformations. The uncertainty of soil properties, however, as in many studies (Al-Bittar *et al.*, 2018; Fenton, 1999; Guo *et al.*, 2020; Mollon *et al.*, 2009, 2013; Nedjar *et al.*, 2007) showed great importance for the reliability of geotechnical structures.

To consider the effects of soil properties uncertainty on the tunnel seismic design, a factor of safety (*FS*) could be employed to link the target probability of exceedance POE_T with the deterministic deformations (D_d) or allowable deformation through the following equation:

$$POE_T = P[D > FS \cdot D_d] \quad (7.1)$$

The target POE_T may depend on the importance index and damage requirement of a specific tunnel project. To illustrate in detail the relationships between the target POE_T and required *FS*, the results of Fig. 7.7 ($V_s=200$ m/s, $PGA=0.3$ g) and Fig. 7.14 are revisited.

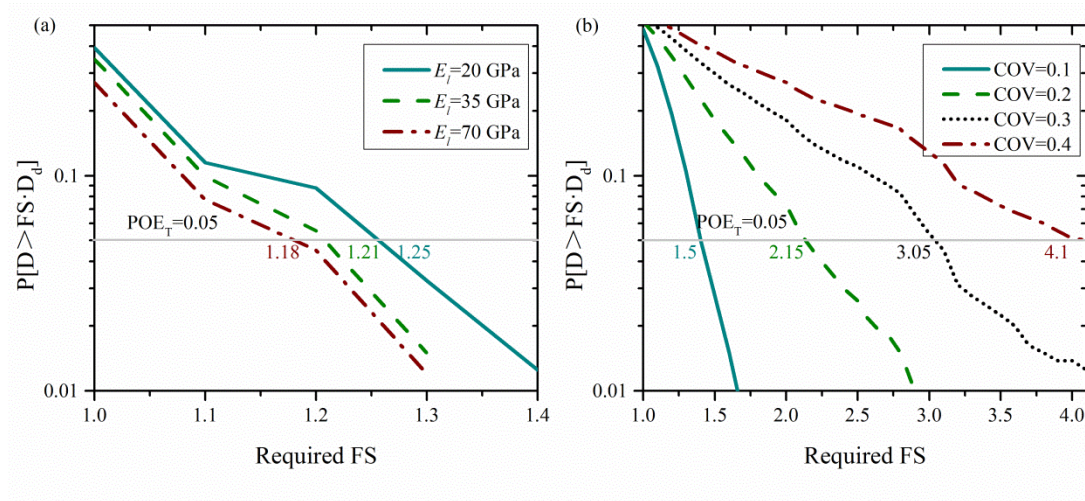


Fig. 7.15 Relationship between the target POE and required FS : (a) E_i ; and (b) COV .

Fig. 7.15 can be used to choose a required factor of safety to satisfy the target probability of exceedance for these two cases. Results show that a larger factor of safety is generally required for flexible tunnels. For instance, if a target POE_T of 0.05 is needed for a tunnel with $E_i = 20$ GPa, a factor of safety of at least $FS = 1.25$ would be required. For a tunnel considering the value of $E_i = 70$ GPa, the required factor would be at least 1.18. If the FS is determined based on a flexible tunnel, it will result in a conservative seismic design when this factor is directly applied to a rigid tunnel. Additionally, Fig. 7.15b illustrates that the required FS will be significantly reduced as the soil parameters uncertainty decreases. For instance, the required FS decreases obviously from 4.1 to 1.5 when the COV varies from 0.4 to 0.1. To this end, high-quality in-situ and laboratory tests are necessary to accurately characterize the soil properties needed for seismic design, to further reduce the soil properties variability.

7.6 Conclusions

This chapter presents the uncertainty quantification of seismic-induced deformations to characterize the response variability caused by random soil properties. To this end, 2D nonlinear finite difference numerical models combined with Monte Carlo simulations are employed to perform stochastic dynamic time-history analyses of a soil-tunnel system. Analyses are performed for a wide range of soil shear wave velocities, ground motion intensities, lining Young's moduli, probability distribution types, coefficients of variation, and

correlation structures.

The random soil properties can have an important influence on tunnel deformations under seismic loadings. The mean and standard deviations of deformations increase when the ground motion intensities increase. Concerning the lining stiffness, the larger mean and standard deviations are observed for flexible tunnels. However, the lining stiffness influence is generally insignificant for tunnels in stiff soils. A critical shear wave velocity V_s that causes the highest deformations variability is observed. In this study, these values vary from 250 m/s to 300 m/s. Generally, the correlation between the c and φ has an insignificant influence on the statistical characteristics of deformations, since the deformations are less influenced by the soil shear strength parameters. However, when considering only the c and φ uncertainty, positive correlation coefficients can lead to slightly larger standard deviations.

The study also investigates the effects of using different distribution types to characterize the V_s uncertainty, assuming different variation degrees. It appears that the distribution types can have an important influence on the tunnel deformations only when the variation degree is high. This is due to the different *CDF* tails of the input variable. Compared to the other two distributions, a lognormal distribution tends to produce the lowest mean, standard deviation, and *POE* value in a small range. The normal distribution can be considered as the worst one in terms of *POE*. The variation degree has a more pronounced influence on the tunnel deformations, particularly for the *POE* values.

The uncertainty of soil properties on the seismic tunnel deformations can be properly considered by introducing a safety factor that corresponds to a target *POE*. For preliminary designs, it will not be possible to conduct direct Monte Carlo simulations to quantify the variability of the seismic tunnel response due to the computational burden. Like the racking ratio-flexibility ratio relationships (Bobet, 2010) employed for a quick estimation of the tunnel deformations, the *POE* can be directly estimated if the statistical moments of deformation distributions are known with confidence. In this case, the computationally expensive stochastic numerical analysis will be avoided. Hence, to fully consider the

uncertainty of the soil properties in a probabilistic-based design, a probabilistic chart should be proposed in the future. It will guide the selection of an appropriate safety factor for a target *POE*.

Chapter 8

Conclusion

8.1 Summary and results

The purpose of this research work was to investigate the seismic response of tunnels considering a dynamic time-history analysis within deterministic and probabilistic frameworks. The main goal was to address several limitations of the previous studies that cannot represent the actual soil-tunnel conditions such as the tunnel construction consequence, multi-layered soils, as well as the inherent uncertainty of geotechnical parameters.

First, numerical investigations for the seismic analysis of tunnels were reviewed in frameworks of deterministic and probabilistic (Chapter 2). The discussion was limited to a brief presentation of two categories of numerical methods, namely the quasi-static and dynamic time-history analyses. Despite great efforts that have been devoted to gaining a better understanding of the earthquake effects on tunnels in various conditions, several key questions required further research. Special attention was given to the frequency-dependent Rayleigh damping that was commonly utilized in most nonlinear models to simulate damping at small strains or to remain numerical stability. Different damping selection criteria and determination approaches were proposed in the literature. However, the users determined damping parameters with a certain degree of arbitrariness since there is no consensus regarding the optimal approach.

This is why the importance of Rayleigh damping in nonlinear tunnel seismic analysis was

evaluated in Chapter 3. It included three critical issues associated with the damping model type (full, simplified or, extended), target damping ratio (ξ_{tar}), and matching frequencies (f_1 , f_2). A full Rayleigh damping formulation was considered throughout this work. Five damping determination approaches and six ξ_{tar} values (from 0.2% to 10%) were adopted in two-dimensional plane strain numerical models that incorporated a linear elastic-perfectly plastic constitutive model (Mohr-Coulomb shear strength criteria).

The influence of the damping determination approaches generally increased with increasing ξ_{tar} and motion intensity. It was commonly believed that an increased ξ_{tar} led to a reduced tunnel seismic response. The average results ($T/T_{0.2}$) obtained in this work were consistent with this point of view, especially for weak ground motions. However, opposite trends were observed for strong ground motions due to the modified soil nonlinearity by the value of ξ_{tar} . The influences of the damping determination approach and the target damping ratio were more evident for high frequency components (Group A). Using solely the soil fundamental frequency to determine the damping parameters conceptually underestimated the tunnel seismic response. However, for some ground motions, this method appeared to calculate the maximum tunnel response among other approaches for high target damping ratios and strong nonlinearity cases. Besides, the use of an improper stiffness-proportional damping coefficient resulted in a substantial increase in computational cost.

Then, excavation-induced stress disturbance influences on the tunnel seismic response under no-slip and full-slip soil/lining interface conditions were assessed in Chapter 4, with the help of the convergence-confinement method. The construction consequence affected tunnel static behaviour and soil plastic zones. The results of the dynamic analyses revealed that the stress relief significantly increased the seismic axial forces but had a negligible influence on the seismic bending moments. Compared to the no-stress relief case, additional seismic axial force increments were more evident for large relaxation coefficients under the full-slip case, with a maximum ratio (i.e., SR) of 4. Furthermore, the upper and lower limit relationships between the stress relaxation coefficients and the SR ratios were given for application purposes.

Chapter 5 investigated the underlying soft soil layer-tunnel seismic interaction. A theoretical study was first performed to understand the propagation characteristic of a plane SH wave propagated vertically through a three-layered elastic medium. The analytical results demonstrated that the transmission coefficient of the incident wave decreased with increasing the normalized wavelength (d/λ_w , in the range from 0 to 0.5), especially for an interlayer with a small stiffness. Then, parametric numerical analyses of an underlying soft soil layer-tunnel system were conducted. The presence of an underlying soft soil layer reduced the seismic internal force increments, worked as a natural damper. A critical thickness which was about one time the tunnel diameter (i.e., $d/D=1.0$) was observed in this work. Compared to relative stiffness and thickness, the relative position slightly affected the tunnel seismic response.

The variables that had the most or the least impact on the tunnel seismic deformation were examined in Chapter 6. Seven geotechnical parameters were considered as random variables and their probabilistic values were taken from the literature. In comparison with traditional local sensitivity analyses, the sparse polynomial chaos expansions based global sensitivity analysis ($SPCE-GSA$) provided satisfactory estimates with a lower computational cost. However, its accuracy was related to the sample size and polynomial degrees used for constructing the $SPCE$ model. The analyses revealed that the soil shear wave velocity (V_s) dominated the tunnel seismic deformations, particularly in the case of weak ground motions. Nevertheless, the role of the modulus reduction factor (M_s) increased for strong soil nonlinearity cases and could even be the most important one when the COV of V_s was relatively low (i.e., 5%).

Finally, the variability in the tunnel seismic deformations caused by seven uncertain geotechnical parameters was quantified in Chapter 7. The statistical characteristics in terms of mean, variance, and coefficient of variation of the tunnel deformations were given for different uncertain scenarios through Monte Carlo simulations. The results highlighted the significant influence of uncertain geotechnical parameters on tunnel seismic deformations. Flexible tunnels induced the larger mean and standard deviations. The lining stiffness influence gradually vanished in stiff soils. Critical V_s that caused the highest variability was

observed. In this study, these values varied from 250 m/s to 300 m/s.

Generally, the correlation between the soil cohesion and friction angle had an insignificant influence on the calculated variability, since deformations were less influenced by the soil shear strength parameters. The distribution types of a variable (V_s) had an important influence on the tunnel deformations only for high variation levels, due to the significantly different tails of the cumulative density functions. A lognormal distribution appeared to produce the lowest mean, standard deviation, and probability of exceedance (*POE*) in a small range while a normal distribution was the worst case in terms of *POE*. The uncertain geotechnical parameters on the seismic tunnel deformations could be properly considered by introducing a safety factor that corresponded to a target *POE*.

8.2 Outlook

The four investigated aspects, including Rayleigh damping influence, tunnel construction consequence, underlying soft soil layer, and uncertainty of the geotechnical parameters, allowed to fulfill the initial objectives which were the motivation of this work. The following improvements should be conducted to address the limitations of this research or to extend the findings to a wider range of applications.

- The significance of the Rayleigh damping in a nonlinear numerical model was assessed in this work, using only one soil profile. Previous studies on site seismic response have demonstrated that the adverse effect caused by the improper use of Rayleigh damping was even large for a deep or/and a soft soil deposit. For this kind of geological configuration which is more complex than the studied one, the appropriate determination of Rayleigh damping is expected to be more important. The damping parameters should therefore be well-calibrated with caution. To circumvent the frequency-dependent, an alternative approach is to avoid the use of Rayleigh damping or to consider only a small target damping ratio when it has to be utilized. A question arises “*Is it possible to implement a frequency-independent*

damping model in the time-domain analysis?”.

- The tunnel excavation-induced stress perturbation was simulated with a linear elastic-perfectly plastic constitutive model for the soil. It cannot describe a real soil nonlinear behaviour under cyclic loadings, which may significantly influence the tunnel seismic response. Furthermore, stress relief leads to an excavation damaged zone around a tunnel and generally shows a time-dependent effect (i.e., rock, clay). It may be interesting to consider these construction consequences in future works.
- This work demonstrated that an underlying soil layer would effectively reduce the seismic actions on a tunnel. This soft soil layer worked as a natural damper that attenuates the propagated ground motion. Analogically, *Controlled Low Strength Materials*, *Rubber-Sand Mixture*, and *Expanded Polystyrene Composite Soil* are expected to protect buried structures from the destroying earthquakes in the framework of the geotechnical seismic isolation (*GSI*). Besides, the synthetic and optimal design (i.e., *Metasoil* concept) of mechanical and geometry properties of the *GSI* can be conducted according to the required safety level.
- Uncertainties associated with geotechnical parameters were considered in a soil-tunnel system using random variables. Despite the probability distributions and properties that were taken from the literature, site-specific models are supposed to improve the engineering insights. During this research, the spatial variability of soil properties was discarded. To characterize this feature, a random field method should be preferred. On the other hand, a sophisticated soil constitutive model generally performs better than a simpler one to predict the tunnel seismic response. The main problem is the fact that a more complex constitutive model has more parameters; nevertheless, some of them are not easy to be determined based on laboratory tests, they will then be subjected to uncertainty. For soil models with different levels of complexity, a comparative study is therefore needed to tradeoff the high-fidelity and robustness in random soils.
- This work was limited to statistical characteristics (i.e., mean, standard deviation, and *COV*) of the calculated tunnel deformations under seismic loading. Oppositely, the probability of failure at a rare event (i.e., $10^{-3}\sim 10^{-5}$) is generally the quantities of

interest when dealing with the uncertain quantification under static conditions. To estimate the failure probability of a tunnel for a given intensity measure (i.e., PGA , S_a), seismic fragility curves were proposed in practice considering the record-to-record variability. Hence, two key questions emerge from the above: “*Uncertainty of geotechnical parameters and variability of the ground motions, which is the more important one ?*”. And “*Is it necessary to consider small failure probabilities for tunnels under earthquake loadings?*”.

Appendix A

Table A.1. Input ground motions.

| Group A | | | | | | | |
|----------------|-----------------------|------|------------------------------|-----------|--------------------|------------------|--------------------|
| ID | Earthquake Name | Year | Station Name | Magnitude | Mechanism | R_{jb} (km) | V_{s30} (m/s) |
| 1 | San Fernando | 1971 | Fairmont Dam | 6.61 | Reverse | 25.58 | 634.33 |
| 2 | San Fernando | 1971 | Lake Hughes #9 | 6.61 | Reverse | 17.22 | 670.84 |
| 3 | San Fernando | 1971 | Pearblossom Pump | 6.61 | Reverse | 35.54 | 529.09 |
| 4 | Friuli_ Italy-02 | 1976 | San Rocco | 5.91 | Reverse | 14.37 | 649.67 |
| 5 | Coyote Lake | 1979 | Gilroy Array #1 | 5.74 | strike slip | 10.21 | 1428.14 |
| 6 | Livermore-01 | 1980 | APEEL 3E Hayward SUH | 5.8 | strike slip | 29.19 | 517.06 |
| 7 | Mammoth Lakes-06 | 1980 | Bishop - Paradise Lodge | 5.94 | strike slip | 18.85 | 585.12 |
| 8 | Irpinia_ Italy-02 | 1980 | Brienza | 6.2 | Normal | 41.73 | 561.04 |
| 9 | Coalinga-03 | 1983 | Sulphur Baths (temp) | 5.38 | Reverse | 12.77 | 617.43 |
| 10 | Coalinga-05 | 1983 | Sulphur Baths (temp) | 5.77 | Reverse | 9.75 | 617.43 |
| 11 | Morgan Hill | 1984 | Gilroy - Gavilan Coll | 6.19 | strike slip | 14.83 | 729.65 |
| 12 | Morgan Hill | 1984 | Gilroy Array #1 | 6.19 | strike slip | 14.9 | 1428.14 |
| 13 | Morgan Hill | 1984 | San Justo Dam (R Abut) | 6.19 | strike slip | 31.88 | 543.63 |
| 14 | Lazio-Abruzzo | 1984 | Atina | 5.8 | Normal | 12.8 | 585.04 |
| 15 | Hollister-04 | 1986 | SAGO South - Surface | 5.45 | strike slip | 11.15 | 608.67 |
| 16 | Chalfant Valley-01 | 1986 | Bishop - Paradise Lodge | 5.77 | strike slip | 14.99 | 585.12 |
| 17 | Loma Prieta | 1989 | Bear Valley #7_ Pinnacles | 6.93 | Reverse Oblique | 68.22 | 509.87 |
| Group B | | | | | | | |
| 1 | San Fernando | 1971 | Fairmont Dam | 6.61 | Reverse | 25.58 | 634.33 |
| 2 | Mammoth Lakes-03 | 1980 | Long Valley Dam (Downst) | 5.91 | strike slip | 10.31 | 537.16 |
| 3 | Mammoth Lakes-03 | 1980 | Long Valley Dam (L Abut) | 5.91 | strike slip | 10.31 | 537.16 |
| 4 | Mammoth Lakes-04 | 1980 | Long Valley Dam (L Abut) | 5.7 | strike slip | 12.75 | 537.16 |
| 5 | Coalinga-01 | 1983 | Parkfield - Fault Zone 11 | 6.36 | Reverse | 27.1 | 541.73 |
| 6 | Coalinga-01 | 1983 | Parkfield - Gold Hill 3W | 6.36 | Reverse | 38.1 | 510.92 |
| 7 | Morgan Hill | 1984 | UCSC Lick Observatory | 6.19 | strike slip | 45.47 | 713.59 |
| 8 | Chalfant Valley-02 | 1986 | Long Valley Dam (Downst) | 6.19 | strike slip | 18.3 | 537.16 |
| 9 | Chalfant Valley-02 | 1986 | Long Valley Dam (LAbut) | 6.19 | strike slip | 18.3 | 537.16 |
| 10 | Chalfant | 1986 | Mammoth Lakes Sheriff | 6.19 | strike slip | 34.92 | 529.39 |

| | Valley-02 | | Subst | | | | |
|----|------------------------|------|------------------------------------|------|--------------------|-------|---------|
| 11 | Whittier Narrows-01 | 1987 | Baldwin Park - N Holly | 5.99 | Reverse Oblique | 4.34 | 544.68 |
| 12 | New Zealand-02 | 1987 | Matahina Dam | 6.6 | Normal | 16.09 | 551.3 |
| 13 | Loma Prieta | 1989 | Belmont - Envirotech | 6.93 | Reverse Oblique | 43.94 | 627.59 |
| 14 | Loma Prieta | 1989 | Golden Gate Bridge | 6.93 | Reverse Oblique | 79.71 | 584.17 |
| 15 | Loma Prieta | 1989 | Piedmont Jr High School Grounds | 6.93 | Reverse Oblique | 72.9 | 895.36 |
| 16 | Loma Prieta | 1989 | Point Bonita | 6.93 | Reverse Oblique | 83.37 | 1315.92 |
| 17 | Loma Prieta | 1989 | SF - Cliff House | 6.93 | Reverse Oblique | 78.58 | 614.57 |
| 18 | Loma Prieta | 1989 | SF - Diamond Heights | 6.93 | Reverse Oblique | 71.23 | 582.9 |
| 19 | Loma Prieta | 1989 | SF - Presidio | 6.93 | Reverse Oblique | 77.34 | 594.47 |
| 20 | Loma Prieta | 1989 | SF - Rincon Hill | 6.93 | Reverse Oblique | 74.04 | 873.1 |
| 21 | Loma Prieta | 1989 | So. San Francisco_ Sierra Pt. | 6.93 | Reverse Oblique | 63.03 | 1020.62 |
| 22 | Northridge-01 | 1994 | LA - Chalon Rd | 6.69 | Reverse | 9.87 | 740.05 |
| 23 | Northridge-01 | 1994 | Vasquez Rocks Park | 6.69 | Reverse | 23.1 | 996.43 |
| 24 | Hector Mine | 1999 | Hector | 7.13 | strike slip | 10.35 | 726 |
| 25 | Chi-Chi_ Taiwan-03 | 1999 | CHY086 | 6.2 | Reverse | 49.69 | 665.2 |
| 26 | Chi-Chi_ Taiwan-03 | 1999 | TCU075 | 6.2 | Reverse | 18.47 | 573.02 |
| 27 | Chi-Chi_ Taiwan-03 | 1999 | TCU138 | 6.2 | Reverse | 21.11 | 652.85 |
| 28 | Chi-Chi_ Taiwan-04 | 1999 | CHY042 | 6.2 | strike slip | 34.1 | 665.2 |
| 29 | Chi-Chi_ Taiwan-04 | 1999 | CHY086 | 6.2 | strike slip | 33.63 | 665.2 |
| 30 | Chi-Chi_ Taiwan-06 | 1999 | CHY035 | 6.3 | Reverse | 40.36 | 573.04 |
| 31 | Chi-Chi_ Taiwan-06 | 1999 | CHY086 | 6.3 | Reverse | 53.5 | 665.2 |
| 32 | Cape Mendocino | 1992 | Butler Valley Station 2 | 7.01 | Reverse | 43.82 | 525.26 |
| 33 | Chuetsu-oki_ Japan | 2007 | Iizuna Mure | 6.8 | Reverse | 66.1 | 526.13 |

Appendix B

This Appendix summarizes the equations employed by the two analytical solutions for calculating the axial forces and bending moments for the no-slip assumption at the interface in static conditions.

Bakker method (Bakker, 2003):

$$T = -\frac{(\sigma_v + \sigma_h)}{2} \cdot r + \frac{(\sigma_v - \sigma_h)}{2} \cdot r \cdot \cos(2\theta) \quad (\text{B.1})$$

$$M = -\frac{(\sigma_v + \sigma_h)}{4} \cdot r^2 \cdot \cos(2\theta) \quad (\text{B.2})$$

Erdmann method (Erdmann, 1983):

The maximum normal force T_{\max} and the maximum bending moment M_{\max} are respectively given by the following equation:

$$T_{\max} = \frac{\alpha r}{\alpha + \beta + \frac{\alpha \beta}{1 + \nu_s}} \cdot \frac{(\sigma_v + \sigma_h)}{2} + \frac{\left(1 + \frac{\alpha}{12(1 + \nu_s)} + \frac{\beta}{4(1 + \nu_s)}\right) r}{1 + \frac{\alpha(3 - 2\nu_s)}{12(3 - 4\nu_s)(1 + \nu_s)} + \frac{\beta(5 - 6\nu_s)}{4(3 - 4\nu_s)(1 + \nu_s)} + \frac{\alpha \beta}{12(3 - 4\nu_s)(1 + \nu_s)^2}} \cdot \frac{(\sigma_v - \sigma_h)}{2} \quad (\text{B.3})$$

$$M_{\max} = \frac{\left(1 + \frac{\beta}{2(1 + \nu_s)}\right) r^2}{2 + \frac{\alpha(3 - 2\nu_s)}{6(3 - 4\nu_s)(1 + \nu_s)} + \frac{\beta(5 - 6\nu_s)}{4(3 - 4\nu_s)(1 + \nu_s)} + \frac{\alpha \beta}{6(3 - 4\nu_s)(1 + \nu_s)^2}} \cdot \frac{(\sigma_v - \sigma_h)}{2} \quad (\text{B.4})$$

$$\alpha = \frac{E_s r^3}{EI} \quad (\text{B.5})$$

$$\beta = \frac{E_s r}{EA} \quad (\text{B.6})$$

where σ_v and σ_h are respectively vertical and horizontal stresses at the tunnel center depth, r is the tunnel radius, θ is the orientation angle representing the position of observation points, ν_s is the soil Poisson's ratio, EI and EA are the flexural rigidity and the normal stiffness of the lining, E_s is the elasticity modulus of the soil.

Reference

- Al-Bittar, T., Soubra, A.H., Thajeel, J., 2018. Kriging-based reliability analysis of strip footings resting on spatially varying soils. *J Geotech Geoenviron Eng.* 144, 1-11.
- Amorosi, A., Boldini, D., 2009. Numerical modelling of the transverse dynamic behaviour of circular tunnels in clayey soils. *Soil Dyn. Earthq. Eng.* 29, 1059–1072.
- Amorosi, A., Boldini, D., Elia, G., 2010. Parametric study on seismic ground response by finite element modelling. *Comput. Geotech.* 37, 515–528.
- Amorosi, A., Boldini, D., Falcone, G., 2014. Numerical prediction of tunnel performance during centrifuge dynamic tests. *Acta Geotech.* 9, 581–596.
- Argyroudis, S.A., Ptilakis, K.D., 2012. Seismic fragility curves of shallow tunnels in alluvial deposits. *Soil Dyn. Earthq. Eng.* 35, 1–12.
- Bakker, K., 2003. Structural design of linings for bored tunnels in soft ground. *Heron* 48, 33-63.
- Blatman, G., Sudret, B., 2010. Efficient computation of global sensitivity indices using sparse polynomial chaos expansions. *Reliab Eng Syst Saf.* 95, 1216–1229.
- Blatman, G., Sudret, B., 2011. Adaptive sparse polynomial chaos expansion based on least angle regression. *J Comput Phys.* 230, 2345–2367.
- Bi, K., Hao, H., 2012. Influence of ground motion spatial variations and local soil conditions on the seismic responses of buried segmented pipelines. *Struct. Eng. Mech.* 44, 663–680.
- Bilotta, E., Lanzano, G., Madabhushi, S.P.G., Silvestri, F., 2014. A numerical Round Robin on tunnels under seismic actions. *Acta Geotech.* 9, 563–579.
- Bilotta, E., De Santis, L., Di Laora, R., D’Onofrio, A., Silvestri, F., 2015. Importance of seismic site response and soil-structure interaction in dynamic behavior of a tall building. *Géotechnique.* 65, 391-400.
- Bobet, A., Fernandez, G., Huo, H., Ramirez, J., 2008. A practical iterative procedure to estimate seismic-induced deformations of shallow rectangular structures. *Can. Geotech. J.* 45, 923–938.
- Bobet, A., 2010. Drained and undrained response of deep tunnels subjected to far-field shear loading. *Tunn. Undergr. Sp. Technol.* 25, 21–31.
- Cabangon, L.T., Elia, G., Rouainia, M., 2019. Modelling the transverse behaviour of circular tunnels in structured clayey soils during earthquakes. *Acta Geotech.* 14, 163–178.

- Cai, M., 2011. Rock Mass Characterization and Rock Property Variability Considerations for Tunnel and Cavern Design 379–399.
- Calabrese, A., Lai, C.G., 2016. Sensitivity analysis of the seismic response of gravity quay walls to perturbations of input parameters. *Soil Dyn Earthq Eng.* 82, 55–62.
- Chakraborty, D., Kumar, J., 2013. Stability of a long unsupported circular tunnel in soils with seismic forces. *Nat. Hazards* 68, 419–431.
- Chakraborty, S., Majumder, D., 2018. Hybrid Reliability Analysis Framework for Reliability Analysis of Tunnels *J. Comput. Civ. Eng.* 32, 1–9.
- Chen, Z., Wei, J., 2013. Correlation between ground motion parameters and lining damage indices for mountain tunnels. *Nat. Hazards* 65, 1683–1702.
- Chen, Z., Liang, S., He, C., 2017. Seismic performance of an immersed tunnel considering random soil properties and wave passage effects. *Struct. Infrastruct. Eng.* 2479, 1–15.
- Chu, B., Lin, Y., 2007. Mechanical behavior of a twin-tunnel in multi-layered formations. *Tunn Undergr Sp Technol.* 22, 351–62.
- Cilingir, U., Gopal Madabhushi, S.P., 2011a. A model study on the effects of input motion on the seismic behaviour of tunnels. *Soil Dyn. Earthq. Eng.* 31, 452–462.
- Cilingir, U., Madabhushi, S.P.G., 2011b. Effect of depth on seismic response of circular tunnels. *Can. Geotech. J.* 48, 117–127.
- Clough, G.W., Penzien, J., 1993. *Dynamics of structures*, 2nd Ed., McGraw-Hill, N.Y.
- Corigliano, M., Scandella, L., Lai, C.G., Paolucci, R., 2011. Seismic analysis of deep tunnels in near fault conditions: a case study in Southern Italy. *Bull. Earthq. Eng.* 9, 975-995.
- Conti, R., Viggiani, G.M.B., Perugini, F., 2014. Numerical modelling of centrifuge dynamic tests of circular tunnels in dry sand. *Acta Geotech.* 9, 597–612.
- Croce, A., 2011. *Analisi dati di monitoraggio del rivestimento della galleria del passante ferroviario di Bologna*. PhD Thesis, Polytechnics of Torino, Torino.
- Cui, Z., Sheng, Q., Leng, X., 2018. Effects of a controlling geological discontinuity on the seismic stability of an underground cavern subjected to near-fault ground motions. *Bull. Eng. Geol. Environ.* 77, 265–282.
- Darendeli, M.B., 2001. *Development of a new family of normalized modulus reduction and material damping curves*. Ph.D. Thesis, University of Texas, Austin.

- Debiasi, E., Gajo, A., Zonta, D., 2013. On the seismic response of shallow-buried rectangular structures. *Tunn. Undergr. Sp. Technol.* 38, 99–113.
- Dias, D., Kastner, R., 2013. Movements caused by the excavation of tunnels using face pressurized shields-analysis of monitoring and numerical modelling results. *Eng. Geol.* 152, 17-25.
- Do, N.A., Dias, D., Oreste, P., Djeran-Maigre, I., 2014. 2D tunnel numerical investigation: the influence of the simplified excavation method on tunnel behaviour. *Geotech. Geol. Eng.* 32, 43-58.
- Do, N.A., Dias, D., Oreste, P., Djeran-Maigre, I., 2015a. Behaviour of segmental tunnel linings under seismic loads studied with the hyperstatic reaction method. *Soil Dyn. Earthq. Eng.* 79, 108–117.
- Do, N.A., Dias, D., Oreste, P., Djeran-Maigre, I., 2015b. 2D numerical investigation of segmental tunnel lining under seismic loading. *Soil Dyn. Earthq. Eng.* 72, 66–76.
- Emeriault, F., Breyse, D., Kastner, R., Denis, A., 2004. Geotechnical survey and mechanical parameters in urban soils: Modelling soil variability and inferring representative values using the extension of Lyon subway line D as a case study. *Can. Geotech. J.* 41, 773–786.
- EPRI, 1993. Guidelines for determining design basis ground motions. Electric Power Research Institute, Palo Alto, Calif.
- Erdmann, J., 1983. Comparison of two-dimensional and development of three-dimensional analysis methods for tunnels. Report Institute of Statics, TU Braunschweig, 83-403.
- Fang, Y.B., Su, Y.H., 2020. On the use of the global sensitivity analysis in the reliability-based design: Insights from a tunnel support case. *Comput Geotech.* 117, 103280.
- Fabozzi, S., Bilotta, E., 2016. Behaviour of a Segmental Tunnel Lining under Seismic Actions. *Procedia Eng.* 158, 230–235.
- Fabozzi, S., Bilotta, E., Yu, H., Yuan, Y., 2018. Effects of the asynchronism of ground motion on the longitudinal behaviour of a circular tunnel. *Tunn. Undergr. Sp. Technol.* 82, 529–541.
- Fenton, G.A., 1999. Estimation for stochastic soil models. *J Geotech Geoenviron Eng.* 125, 470-485.
- Ferrario, E., Pedroni, N., Zio, E., Lopez-Caballero, F., 2017. Bootstrapped Artificial Neural Networks for the seismic analysis of structural systems. *Struct Saf.* 67, 70-84.
- Finn, W.D.L., Eeri, M., 2016. Amplification effects of thin soft-surface layers. *Earthq Spectra.* 32, 2109–26.
- Franza, A., Marshall, A.M., 2019. Centrifuge and real-time hybrid testing of tunneling beneath piles

- and piled buildings. *J. Geotech. Geoenviron. Eng.* 145, 04018110.
- Goh, A.T.C., Kulhawy, F.H., 2003. Neural network approach to model the limit state surface for reliability analysis. *Can. Geotech. J.* 40, 1235–1244.
- Gomes, R.C., 2013. Effect of stress disturbance induced by construction on the seismic response of shallow bored tunnels. *Comput. Geotech.* 49, 338-351.
- Gomes, R.C., 2014. Numerical simulation of the seismic response of tunnels in sand with an elastoplastic model. *Acta Geotech.* 9, 613–629.
- Gomes, R.C., Gouveia, F., Torcato, D., Santos, J., 2015. Seismic response of shallow circular tunnels in two-layered ground. *Soil Dyn. Earthq. Eng.* 75, 37–43.
- Gong, W., Juang, C.H., Martin, J.R., Tang, H., Wang, Q., Huang, H., 2018. Probabilistic analysis of tunnel longitudinal performance based upon conditional random field simulation of soil properties. *Tunn. Undergr. Sp. Technol.* 73, 1–14.
- Guo, X.F., Sun, Q.Q., Dias, D., Antoient, E., 2020. Probabilistic assessment of an earth dam stability design using the adaptive polynomial chaos expansion. *Bull Eng Geol Environ.* doi: 10.1007/s10064-020-01847-2.
- Griffiths, S.C., Cox, B.R., Rathje, E.M., 2016. Challenges associated with site response analyses for soft soils subjected to high-intensity input ground motions. *Soil Dyn. Earthq. Eng.* 85, 1–10.
- Hall, J.F., 2006. Problems encountered from the use (or misuse) of Rayleigh damping. *Earthq. Eng. Struct. Dyn.* 35, 525–545.
- Hall, J.F., 2018. Performance of viscous damping in inelastic seismic analysis of moment-frame buildings. *Earthq. Eng. Struct. Dyn.* 47, 2756–2776.
- Hamrouni, A., Dias, D., Sbartai, B., 2019. Probability analysis of shallow circular tunnels in homogeneous soil using the surface response methodology optimized by a genetic algorithm. *Tunn. Undergr. Sp. Technol.* 86, 22–33.
- Hardin, B.O., Drnevich, V.P., 1972. Shear modulus and damping in soils: design equations and curves. *J Soil Mech Found Div.* 7, 667-691.
- Hashash, Y.M.A., Park, D., 2001. Non-linear one-dimensional seismic ground motion propagation in the Mississippi embayment. *Eng. Geol.* 62, 185–206.
- Hashash, Y.M.A., Hook, J.J., Schmidt, B., I-Chiang Yao, J., 2001. Seismic design and analysis of underground structures. *Tunn. Undergr. Sp. Technol.* 16, 247–293.

- Hashash, Y.M.A., Park, D., 2002. Viscous damping formulation and high frequency motion propagation in non-linear site response analysis. *Soil Dyn. Earthq. Eng.* 22, 611–624.
- Hashash, Y.M.A., Park, D., Yao, J.I.C., 2005. Ovaling deformations of circular tunnels under seismic loading, an update on seismic design and analysis of underground structures. *Tunn. Undergr. Sp. Technol.* 20, 435–441.
- Hatzigeorgiou George D., G.D., Beskos, D.E., 2010. Soil-structure interaction effects on seismic inelastic analysis of 3-D tunnels. *Soil Dyn. Earthq. Eng.* 30, 851–861.
- Hleibieh, J., Wegener, D., Herle, I., 2014. Numerical simulation of a tunnel surrounded by sand under earthquake using a hypoplastic model. *Acta Geotech.* 9, 631–640.
- Huang, F., Zhu, H., Xu, Q., Cai, Y., Zhuang, X., 2013. The effect of weak interlayer on the failure pattern of rock mass around tunnel – Scaled model tests and numerical analysis. *Tunn Undergr Sp Technol.* 35, 207–18.
- Huang, J., Zhao, X., Zhao, M., Du, X., Wang, Y., Zhang, Chengming, Zhang, Chiyu, 2020. Effect of peak ground parameters on the nonlinear seismic response of long lined tunnels. *Tunn. Undergr. Sp. Technol.* 95, 103175.
- Hudson, M., Idriss, I.M., Beikae, M., 1994. QUAD4M-A computer program to evaluate the seismic response of soil structures using finite element procedures and incorporating a compliant base. Univ. of Calif., Davis, Calif.
- Huh, J., Tran, Q.H., Haldar, A., Park, I., Ahn, J.H., 2017. Seismic vulnerability assessment of a shallow two-story underground RC box structure. *Appl. Sci.* 7, paper ID735.
- Huo, H.B., Bobet, A., Fernandez, G., Ramirez, J., 2005. Load transfer mechanisms between underground structure and surrounding ground: evaluation of the failure of the Daikai station. *J. Geotech. Geoenviron. Eng.* 131, 1522-1533.
- Huo, H., Bobet, A., Fernández, G., Ramírez, J., 2006. Analytical solution for deep rectangular structures subjected to far-field shear stresses. *Tunn. Undergr. Sp. Technol.* 21, 613–625.
- Hwang, J.H., Lu, C.C., 2007. Seismic capacity assessment of old Sanyi railway tunnels. *Tunn. Undergr. Sp. Technol.* 22, 433–449.
- Iai, S., 2005. International standard (ISO) on seismic actions for designing geotechnical works - An overview. *Soil Dyn. Earthq. Eng.* 25, 605–615.
- Idriss, I.M., Lysmer, J., Hwang, R., Seed, H.B., 1973. QUAD4: a computer program for evaluating the

- seismic response of soil structures by variable damping finite element procedures. Univ. of Calif., Berkeley, Calif.
- Iida, H., Hiroto, T., Yoshida, N., Iwafujiii, M., 1996. Damage to Daikai subway station. *Soils Found. Special Issue*, 283–300.
- Iman, R.L., 1999. Latin hypercube sampling. *Encyclopedia of Statistical Sciences, Update Volume 3*, John Wiley & Sons, New York.
- ITA, 1988. Guidelines for the design of tunnels. *Tunn. Undergr. Sp. Technol.* 3, 237-249.
- Itasca, 2011. *FLAC – Fast Lagrangian Analysis of Continua – Version 7.0 User’s Guide*. Itasca Consulting Group, Minneapolis.
- Jimenez, R., Sitar, N., 2009. The importance of distribution types on finite element analyses of foundation settlement. *Comput Geotech*, 36, 474-483.
- Jehel, P., 2014. A critical look into Rayleigh damping forces for seismic performance assessment of inelastic structures. *Eng. Struct.* 78, 28–40.
- Kampas, G., Knappett, J.A., Brown, M.J., Anastasopoulos, I., Nikitas, N., Fuentes, R., 2020. Implications of volume loss on the seismic response of tunnels in coarse-grained soils. *Tunn. Undergr. Sp. Technol.* 95, 103127.
- Kampas, G., Knappett, J.A., Brown, M.J., Anastasopoulos, I., Nikitas, N., Fuentes, R., 2019. The effect of tunnel lining modelling approaches on the seismic response of sprayed concrete tunnels in coarse-grained soils. *Soil Dyn. Earthq. Eng.* 117, 122–137.
- Karakostas, C.Z., Manolis, G.D., 2000. Dynamic response of unlined tunnels in soil with random properties. *Eng. Struct.* 22, 1013–1027.
- Karakostas, C.Z., Manolis, G.D., 2002. Dynamic response of tunnels in stochastic soils by the boundary element method. *Eng. Anal. Bound. Elem.* 26, 667–680.
- Karakus, M., 2007. Appraising the methods accounting for 3D tunnelling effects in 2D plane strain FE analysis. *Tunn. Undergr. Sp. Technol.* 22, 47-56.
- Karakus, M., Fowell, R.J., 2003. Effects of different tunnel face advance excavation on the settlement by FEM. *Tunn. Undergr. Sp. Technol.* 18, 513-523.
- Katona, M.G., 2010. *Seismic Design and Analysis of Buried Culverts and Structures*. *J. Pipeline Syst. Eng. Pract.* 1, 111–119.
- Kausel, E., 2014. Damping matrices revisited. *J. Eng. Mech.* 140, 1–4.

- Kontoe, S., Zdravkovic, L., Potts, D.M., Menkiti, C.O., 2008. Case study on seismic tunnel response. *Can. Geotech. J.* 45, 1743–1764.
- Kontoe, S., Zdravkovic, L., Potts, D.M., Menkiti, C.O., 2011. On the relative merits of simple and advanced constitutive models in dynamic analysis of tunnels. *Géotechnique* 61, 815–829.
- Kontoe, S., Avgerinos, V., Potts, D.M., 2014. Numerical validation of analytical solutions and their use for equivalent-linear seismic analysis of circular tunnels. *Soil Dyn. Earthq. Eng.* 66, 206–219.
- Kouretzis, G.P., Sloan, S.W., Carter, J.P., 2013. Effect of interface friction on tunnel liner internal forces due to seismic S- and P-wave propagation. *Soil Dyn. Earthq. Eng.* 46, 41–51.
- Kramer, S.L., 1996. *Geotechnical earthquake engineering*, Prentice-Hall, Englewood Cliffs, N.J.
- Kroetz, H.M., Do, N.A., Dias, D., Beck, A.T., 2018. Reliability of tunnel lining design using the Hyperstatic Reaction Method. *Tunn. Undergr. Sp. Technol.* 77, 59–67.
- Kuhlemeyer, R.L., Lysmer, J., 1973. Finite element method accuracy for wave propagation problems. *J. Soil Mech. Found. Div.* 99, 421-427.
- Kwok, A.O.L., Stewart, J.P., Hashash, Y.M.A., Matasovic, N., Pyke, R., Wang, Z., Yang, Z., 2007. Use of exact solutions of wave propagation problems to guide implementation of nonlinear seismic ground response analysis procedures. *J. Geotech. Geoenviron. Eng.* 133, 1385–1398.
- Lataniotis, C., Marelli, S., Sudret, B., 2018a. UQLab user manual – the Input module, Report UQLab-V1.1-102, Chair of Risk, Safety & Uncertainty Quantification, ETH Zurich.
- Lataniotis, C., Marelli, S., Sudret, B., 2018b. UQLab user manual – the Model module, Report UQLab-V1.1-102, Chair of Risk, Safety & Uncertainty Quantification, ETH Zurich.
- Lanzo, G., Pagliaroli, A., D’Elia, B., 2003. Numerical study on the frequency-dependent viscous damping in dynamic response analyses of ground. In: *Proc. of IV Int. Conf. Earthq. Resist. Eng. Struct.*, Ancona, 315-324.
- Lanzano, G., Bilotta, E., Russo, G., Silvestri, F., Madabhushi, S.P.G., 2012. Centrifuge modeling of seismic loading on tunnels in sand. *Geotech. Test. J.* 35, 1-16.
- Lanzano, G., Bilotta, E., Russo, G., Silvestri, F., 2015. Experimental and numerical study on circular tunnels under seismic loading. *Eur. J. Environ. Civ. Eng.* 19, 539-563.
- Lee, T.H., Park, D., Nguyen, D.D., Park, J.S., 2016. Damage analysis of cut-and-cover tunnel structures under seismic loading. *Bull. Earthq. Eng.* 14, 413–431.

- Li, D.Q., Jiang, S.H., Chen, Y.F., Zhou, C.B., 2014. Reliability analysis of serviceability performance for an underground cavern using a non-intrusive stochastic method. *Environ. Earth Sci.* 71, 1169–1182.
- Li, H.Z., Low, B.K., 2010. Computers and Geotechnics Reliability analysis of circular tunnel under hydrostatic stress field. *Comput. Geotech.* 37, 50–58.
- Li, T.Z., Yang, X.L., 2018. Probabilistic Stability Analysis of Subway Tunnels Combining Multiple Failure Mechanisms and Response Surface Method. *Int. J. Geomech.* 18, 04018167.
- Liao, Z.P., 2002. Introduction to Wave Motion. Science Press, Beijing (in Chinese).
- Lim, K., Cassidy, M.J., Li, A.J., Lyamin, A.V., 2016. Mean parametric Monte Carlo study of fill slopes. *Int J Geomech*, 04016105.
- Liu, J., Wang, W., Dasgupta, G., 2014. Pushover analysis of underground structures: Method and application. *Sci. China Technol. Sci.* 57, 423–437.
- Liu, W., Li, J., 2008. Seismic response evaluation of the impact of corrosion on buried pipelines based on the Markov process Abstract : *Earthq. Eng. Eng. Vib.* 7, 295–303.
- Lu, C.C., Hwang, J.H., 2017. Implementation of the modified cross-section racking deformation method using explicit FDM program : A critical assessment. *Tunn. Undergr. Sp. Technol.* 68, 58–73.
- Lu, C.C., Hwang, J.H., 2018. Damage analysis of the new Sanyi railway tunnel in the 1999 Chi-Chi earthquake: Necessity of second lining reinforcement. *Tunn. Undergr. Sp. Technol.* 73, 48–59.
- Lu, C.C., Hwang, J.H., 2019. Nonlinear collapse simulation of Daikai Subway in the 1995 Kobe earthquake: Necessity of dynamic analysis for a shallow tunnel. *Tunn. Undergr. Sp. Technol.* 87, 78–90.
- Luco, J.E., 2008. A note on classical damping matrices. *Earthq. Eng. Struct. Dyn.* 37, 615–626.
- Lv, Q., Sun, H.Y., Low, B.K., 2011. Reliability analysis of ground -support interaction in circular tunnels using the response surface method. *Int. J. Rock Mech. Min. Sci.* 48, 1329–1343.
- Lv, Q., Chan, C.L., Low, B.K., 2013. System Reliability Assessment for a Rock Tunnel with Multiple Failure Modes. *Roc* 46, 821–833.
- Lv, Q., Xiao, Z., Ji, J., Zheng, J., Shang, Y.Q., 2017a. Moving least squares method for reliability assessment of rock tunnel excavation considering ground-support interaction. *Comput. Geotech.* 84, 88–100.

- Lv, Q., Xiao, Z.P., Ji, J., Zheng, J., 2017b. Reliability based design optimization for a rock tunnel support system with multiple failure modes using response surface method. *Tunn Undergr Sp Technol.* 70, 1-10.
- Lysmer, J., Seed, H.B., Schnabel, P.B., 1971. Influence of base-rock characteristics on ground response. *Bull. Seismol. Soc. Am.* 61, 1213–1232.
- Ma, C., Lu, D.C., Du, X.L., Qi, C.Z., 2018. Effect of buried depth on seismic response of rectangular underground structures considering the influence of ground loss. *Soil Dyn. Earthq. Eng.* 106, 278-297.
- Madabhushi, S.S.C., Haigh, S.K., Madabhushi, G.S.P., 2018. LEAP-GWU-2015: Centrifuge and numerical modelling of slope liquefaction at the University of Cambridge. *Soil Dyn. Earthq. Eng.* 113, 671-681.
- Mahmoudi, E., Hötter, R., Georgieva, R., König, M., Schanz, T., 2019. On the global sensitivity analysis methods in geotechnical engineering: a comparative study on a rock salt energy storage. *Int J Civ Eng.* 17, 131–43.
- Mánica, M., Ovando, E., Botero, E., 2014. Assessment of damping models in FLAC. *Comput. Geotech.* 59, 12–20.
- Manolis, G.D., Stefanou, G., Markou, A.A., 2020. Dynamic response of buried pipelines in randomly structured soil. *Soil Dyn. Earthq. Eng.* 128, 105873.
- Matasovic, N., 1993. Seismic response of composite horizontally-layered soil deposits. Ph.D. Thesis, Univ. of Calif. Los Angeles.
- Mollon, G., Dias, D., Soubra, A., 2009. Probabilistic Analysis and Design of Circular Tunnels against Face Stability. *Int. J. Geomech.* 9, 237–249.
- Mollon, G., Dias, D., Soubra, A., 2011. Probabilistic Analysis of Pressurized Tunnels against Face Stability Using Collocation-Based Stochastic Response Surface Method. *J. Geotech. Geoenvironmental Eng.* 137, 385–397.
- Mollon, G., Dias, D., Soubra, A.H., 2013. Probabilistic analyses of tunneling-induced ground movements. *Acta Geotech.* 8, 181–199.
- Na, U.J., Chaudhuri, S.R., Shinozuka, M., 2008. Probabilistic assessment for seismic performance of port structures. *Soil Dyn Earthq Eng.* 28, 147–158.

- Na, U.J., Ray, Chaudhuri, S.R., Shinozuka, M., 2009. Effects of spatial variation of soil properties on seismic performance of port structures. *Soil Dyn Earthq Eng.* 29, 537–545.
- Nariman, N.A., Hussain, R.R., Mohammad, II., Karampour, P., 2019. Global sensitivity analysis of certain and uncertain factors for a circular tunnel under seismic action. *Front Struct Civ Eng.* 13, 1289–1300.
- Naseem, A., Kashif, M., Iqbal, N., Schotte, K., De Backer, H., 2020. Seismic behavior of triple tunnel complex in soft soil subjected to transverse shaking. *Appl. Sci.* 10, papered 334.
- Nedjar, D., Hamane, M., Bensafi, M., Elachachi, S.M., Breysse, D., 2007. Seismic response analysis of pipes by a probabilistic approach. *Soil Dyn. Earthq. Eng.* 27, 111–115.
- Nielsen, A.H., 2009. On the use of Rayleigh damping for seismic analysis. *Eng. Comput. Mech.* 162, 215–220.
- Nguyen, D.D., Park, D., Shamsheer, S., Nguyen, V.Q., Lee, T.H., 2019. Seismic vulnerability assessment of rectangular cut-and-cover subway tunnels. *Tunn. Undergr. Sp. Technol.* 86, 247–261.
- Pan, Q.J., Dias, D., 2017. Probabilistic evaluation of tunnel face stability in spatially random soils using sparse polynomial chaos expansion with global sensitivity analysis. *Acta Geotech.* 12, 1415–1429.
- Pan, Q.J., Dias, D., 2018. Probabilistic analysis of a rock tunnel face using polynomial chaos expansion method. *Int. J. Geomech.* 18, 1–11.
- Papaspiliou, M., Kontoe, S., Bommer, J.J., 2012. An exploration of incorporating site response into PSHA-Part I: Issues related to site response analysis methods. *Soil Dyn. Earthq. Eng.* 42, 302–315.
- Park, D., Hashash, Y.M.A., 2004. Soil damping formulation in nonlinear time domain site response analysis. *J. Earthq. Eng.* 8, 249–274.
- Park, K.H., Tantayopin, K., Tontavanich, B., Owatsiriwong, A., 2009a. Analytical solution for seismic-induced ovaling of circular tunnel lining under no-slip interface conditions: A revisit. *Tunn. Undergr. Sp. Technol.* 24, 231–235.
- Park, D., Sagong, M., Kwak, D.Y., Jeong, C.G., 2009b. Simulation of tunnel response under spatially varying ground motion. *Soil Dyn. Earthq. Eng.* 29, 1417–1424.

- Patil, M., Choudhury, D., Ranjith, P.G., Zhao, J., 2018. Behavior of shallow tunnel in soft soil under seismic conditions. *Tunn. Undergr. Sp. Technol.* 82, 30–38.
- Penzien, J., 2000. Seismically induced racking of tunnel linings. *Earthq. Eng. Struct. Dyn.* 29, 683–691.
- Phillips, C., Hashash, Y.M.A., 2009. Damping formulation for nonlinear 1D site response analyses. *Soil Dyn. Earthq. Eng.* 29, 1143–1158.
- Phoon, K.K., Kulhawy, F.H., 1999a. Characterization of geotechnical variability. *Can Geotech J.* 36, 612-624.
- Phoon, K.K., Kulhawy, F.H., 1999b. Evaluation of geotechnical property variability. *Can Geotech J.* 36, 625-639.
- Priestley, M.J.N., Grant, D.N., 2005. Viscous damping in seismic design and analysis. *J. Earthq. Eng.* 9, 229–255.
- Phoon, K.K., Kulhawy, F.H., 1999. Evaluation of geotechnical property variability. *Can. Geotech. J.* 36, 625–639.
- Rathje, E.M., Kottke, A.R., Trent, W.L., 2010. Influence of input motion and site property variabilities on seismic site response analysis. *J Geotech Geoenviron Eng.* 136, 1385-1398.
- Rayhani, M.H.T., El Naggar, M.H., 2008. Numerical modeling of seismic response of rigid foundation on soft soil. *Int J Geomech, ASCE.* 8, 336–46.
- Saeid, A.L., Mahmoud, Y., Arya, A., 2015. Control of fault lay-out on seismic design of large underground caverns. *Tunn Undergr Sp Technol.* 50, 305–316.
- Sahoo, J.P., Kumar, J., 2012. Seismic stability of a long unsupported circular tunnel. *Comput. Geotech.* 44, 109–115.
- Sahoo, J.P., Kumar, J., 2014. Stability of a circular tunnel in presence of pseudo-static seismic body forces. *Tunn. Undergr. Sp. Technol.* 42, 264–276.
- Schöbi, R., Sudret, B., 2019. Global sensitivity analysis in the context of imprecise probabilities (p-boxes) using sparse polynomial chaos expansions. *Reliab Eng Syst Saf.* 187, 129–1241.
- Schweiger, H., Thurner, R., Pottler, R., 2001. Reliability Analysis in Geotechnics with Deterministic Finite Elements: Theoretical concepts and practical application. *Int. J. Geomech.* 1, 389–413.
- Sedarat, H., Kozak, A., Hashash, Y.M.A., Shamsabadi, A., Krimotat, A., 2009. Contact interface in seismic analysis of circular tunnels. *Tunn. Undergr. Sp. Technol.* 24, 482–490.

- Shahrour, I., Khoshnoudian, F., Sadek, M., Mroueh, H., 2010. Elastoplastic analysis of the seismic response of tunnels in soft soils. *Tunn. Undergr. Sp. Technol.* 25, 478–482.
- Shen, Y., Gao, B., Yang, X., Tao, S., 2014. Seismic damage mechanism and dynamic deformation characteristic analysis of mountain tunnel after Wenchuan earthquake. *Eng. Geol.* 180, 85–98.
- Singh, D.K., Mandal, A., Karumanchi, S.R., Murmu, A., Sivakumar, N., 2018. Seismic behaviour of damaged tunnel during aftershock. *Eng. Fail. Anal.* 93, 44–54.
- Sobol, I.M., Levitan, Y.L., 1999. On the use of variance reducing multipliers in Monte Carlo computations of a global sensitivity index. *Comput Phys Commun.* 117, 52–61.
- Song, K., Cho, G., Lee, S., 2011. Effects of spatially variable weathered rock properties on tunnel behavior. *Probabilistic Eng. Mech.* 26, 413–426.
- St John, C.M., Zahrah, T.F., 1987. Aseismic design of underground structures. *Tunn. Undergr. Sp. Technol.* 2, 165–197.
- Sudret, B., 2008. Global sensitivity analysis using polynomial chaos expansions. *Reliab Eng Syst Saf.* 93, 964–979.
- Sudret, B., Mai, C.V., 2015. Computing derivative-based global sensitivity measures using polynomial chaos expansions. *Reliab Eng Syst Saf.* 134, 241–250.
- Sun, B., Zhang, S., Deng, M., Wang, C., 2020a. Nonlinear dynamic analysis and damage evaluation of hydraulic arched tunnels under mainshock–aftershock ground motion sequences. *Tunn. Undergr. Sp. Technol.* 98, 103321.
- Sun, J.I., Golesorkhi, R., Seed, H.B., 1988. Dynamic moduli and damping ratios for cohesive soils. *Earthquake Engineering Univ. of Calif., Berkeley, Calif.*
- Sun, Q.Q., Dias, D., 2018. Significance of Rayleigh damping in nonlinear numerical seismic analysis of tunnels. *Soil Dyn Earthq Eng.* 115, 489–494.
- Sun, Q.Q., Guo, X.F., Dias, D., 2020. Evaluation of the seismic site response in randomized velocity profiles using a statistical model with Monte Carlo simulations. *Comput Geotech*, 120, 103442.
- Suwal, S., Pagliaroli, A., Lanzo, G., 2014. Comparative Study of 1D Codes for Site Response Analyses. *Int. J. Landslide Environ.* 2, 24–31.
- Takahashi, N., Hyodo, M., Hyde, A.F.L., Yamamoto, Y., Kimura, S., 2006. Online earthquake response test for stratified layers of clay and sand. *J Geotech Geoenviron Eng, ASCE.* 132, 611–621.

- Tiwari, G., Pandit, B., Gali, M.L., Babu, G.L.S., 2018. Analysis of Tunnel Support Requirements Using Deterministic and Probabilistic Approaches in Average Quality Rock Mass. *Int. J. Geomech.* 18, 04018017.
- Tiwari, G., Pandit, B., Latha, G.M., Babu, G.L.S., 2017. Probabilistic analysis of tunnels considering uncertainty in peak and post-peak strength parameters. *Tunn. Undergr. Sp. Technol.* 70, 375–387.
- Tsai, C.C., Park, D., Chen, C.W., 2014. Selection of the optimal frequencies of viscous damping formulation in nonlinear time-domain site response analysis. *Soil Dyn. Earthq. Eng.* 67, 353–358.
- Toro, G.R., 1995. Probabilistic models of site velocity profiles for generic and site-specific ground-motion amplification studies. Technical Rep. No. 779574, Brookhaven National Laboratory, NY.
- Toufigh, V., Pahlavani, H., 2018. Probabilistic-based analysis of MSE walls using the Latin hypercube sampling method. *Int J Geomech.* 18, 040118109.
- Tsinidis, G., Ptilakis, K., Trikalioti, A.D., 2014. Numerical simulation of round robin numerical test on tunnels using a simplified kinematic hardening model. *Acta Geotech.* 9, 641–659.
- Tsinidis, G., Ptilakis, K., Madabhushi, G., Heron, C., 2015. Dynamic response of flexible square tunnels: Centrifuge testing and validation of existing design methodologies. *Géotechnique* 65, 401–417.
- Tsinidis, G., Rovithis, E., Ptilakis, K., Chazelas, J.L., 2016a. Seismic response of box-type tunnels in soft soil: Experimental and numerical investigation. *Tunn. Undergr. Sp. Technol.* 59, 199–214.
- Tsinidis, G., Ptilakis, K., Anagnostopoulos, C., 2016b. Circular tunnels in sand: dynamic response and efficiency of seismic analysis methods at extreme lining flexibilities. *Bull. Earthq. Eng.* 14, 2903–2929.
- Uenishi, K., Sakurai, S., 2000. Characteristic of the vertical seismic waves associated with the 1995 Hyogo-ken Nanbu (Kobe), Japan earthquake estimated from the failure of the Daikai Underground Station. *Earthq. Eng. Struct. Dyn.* 29, 813–821.
- Viggiani, G., Atkinson, J.H., 1995. Stiffness of fine-grained soil at very small strains. *Geotechnique.* 45, 249-265.
- Visone, C., Bilotta, E., Santucci De Magistris, F., 2009. One-dimensional ground response as a preliminary tool for dynamic analyses in geotechnical earthquake engineering. *J. Earthq. Eng.* 14, 131–162.

- Wang, J.N., 1993. Seismic design of tunnels: a simple state-of-the-art design approach, Parsons, Brinckerhoff, Quade and Douglas Inc., N.Y.
- Wang, Y.X., Shan, S.B., Zhang, C., Guo, P.P., 2019a. Seismic response of tunnel lining structure in a thick expansive soil stratum. *Tunn. Undergr. Sp. Technol.* 88, 250–259.
- Wang, Z.Z., Jiang, Y.J., Zhu, C.A., 2019b. Seismic energy response and damage evolution of tunnel lining structures. *Eur. J. Environ. Civ. Eng.* 23, 758–770.
- Wolff, T.H., 1985. Analysis and design of embankment dam slopes: A probabilistic approach. Purdue University.
- Xu, H.Y., Chen, D, Y., Yang, X.J., Liang, B., 2003. Propagation characteristics of plane SH wave passing through elastic interlining in elastic medium. *Chinese J Rock Mech Eng.* 22, 304-308 (in Chinese).
- Yoo, J.K., Park, J.S., Park, D., Lee, S.W., 2017. Seismic response of tunnels in jointed rock. *KSCE J Civil Eng.* 0, 1-9.
- Yu, H., Yuan, Y., Bobet, A., 2013a. Multiscale method for long tunnels subjected to seismic loading. *Int. J. Numer. Anal. Methods Geomech.* 37, 374–398.
- Yu, H., Yuan, Y., Qiao, Z., Gu, Y., Yang, Z., Li, X., 2013b. Seismic analysis of a long tunnel based on multi-scale method. *Eng. Struct.* 49, 572–587.
- Yue, Q.X., Ang, A.H., 2016. Nonlinear response and reliability analysis of tunnels under strong earthquakes. *Struct. Infrastruct. Eng.* 12, 618–630.
- Yue, Q.X., Ang, A.H., 2017. 3D reliability evaluation of tunnels under strong-motion earthquakes considering spatial randomness. *Struct. Infrastruct. Eng.* 13, 882–893.
- Zerva, A., Ang, A.H., Wen, Y.K., 1988. Lifeline response to spatially variable ground motions. *Earthq. Eng. Struct. Dyn.* 16, 361–379.
- Zhang, L., Liu, Y., 2020. Numerical investigations on the seismic response of a subway tunnel embedded in spatially random clays. *Undergr. Sp.* 5, 43–52.
- Zhao, C.Y., Lavasan, A.A., Barciaga, T., Kamper, C., Mark, P., Schanz, T., 2017. Prediction of tunnel lining forces and deformations using analytical and numerical solutions. *Tunn. Undergr. Sp. Technol.* 64, 164-176.
- Zhuang, H.Y., Ren, J., Miao, Y., Jing, L., Yao, E., Xu, C., 2019. Seismic Performance Levels of a Large Underground Subway Station in Different Soil Foundations. *J. Earthq. Eng.* 0, 1–26.

- Zhuang, H.Y., Wang, X.X., Chen, G.X., 2009. Earthquake responses of subway station with different depths of soft soil. *Chinese J Geotech Eng.* 31, 1258-1266 (in Chinese).
- Zou, Y., Liu, H., Jing, L., Cui, J., 2017. A pseudo-static method for seismic responses of underground frame structures subjected to increasing excitations. *Tunn. Undergr. Sp. Technol.* 65, 106–120.
- Zoutat, M., Elachachi, S.M., Mekki, M., Hamane, M., 2018. Global sensitivity analysis of soil structure interaction system using N2-SSI method. *Eur J Environ Civ Eng.* 22, 192–211.